



Forschungszentrum Karlsruhe
in der Helmholtz-Gemeinschaft

Wissenschaftliche Berichte
FZKA 7307

Results of the QUENCH-12 Experiment on Reflood of a VVER-type Bundle

**J. Stuckert, A. Goryachev, M. Große,
M. Heck, I. Ivanova, G. Schanz, L. Sepold,
U. Stegmaier, M. Steinbrück**

**Institut für Materialforschung
Programm Nukleare Sicherheitsforschung**

September 2008

Forschungszentrum Karlsruhe

in der Helmholtz-Gemeinschaft

Wissenschaftliche Berichte

FZKA 7307

Results of the QUENCH-12 Experiment on Reflood of a VVER-type Bundle

J. Stuckert, A. Goryachev*, M. Große, M. Heck, I. Ivanova*, G. Schanz,
L. Sepold, U. Stegmaier, M. Steinbrück

Institut für Materialforschung
Programm Nukleare Sicherheitsforschung

*RIAR (FSUE SSC-RIAR) Dimitrovgrad, Russland

Forschungszentrum Karlsruhe GmbH, Karlsruhe

2008

Für diesen Bericht behalten wir uns alle Rechte vor

Forschungszentrum Karlsruhe GmbH
Postfach 3640, 76021 Karlsruhe

Mitglied der Hermann von Helmholtz-Gemeinschaft
Deutscher Forschungszentren (HGF)

ISSN 0947-8620

urn:nbn:de:0005-073076

Zusammenfassung

Ergebnisse des Experiments QUENCH-12

Die Quench-Experimente untersuchen den Wasserstoffquellterm bei der Einspeisung von Notkühlwasser in einen trockenen, überhitzten Reaktorkern eines Leichtwasserreaktors. Das QUENCH-Versuchsbündel mit einer Gesamtlänge von etwa 2,5 m besteht üblicherweise aus 21 Brennstabsimulatoren im quadratischen Gitter, die der DWR-Geometrie westlicher Bauart entsprechen. Mit dem QUENCH-12-Versuch sollte jedoch der Einfluss von VVER-Materialien und -Bündelgeometrie auf das Fluten des Reaktorkerns untersucht werden. Das QUENCH-12-Versuchsbündel bestand daher aus 31 Brennstabsimulatoren im hexagonalen Gitter, von denen 18 beheizt waren (mittels Wolfram-Heizern, die sich im Zentrum der Stäbe befinden). Alle Brennstabhüllen, Eckstäbe und Abstandshalter waren aus Zr1%Nb (E110) und das Dampfführungsrohr (Shroud) aus Zr2.5%Nb (E125) gefertigt. Als Referenzversuch für den Vergleich mit der Bündel-Geometrie eines westlichen Druckwasserreaktors (DWR) wurde das QUENCH-06-Experiment (ISP-45) ausgewählt.

QUENCH-12 wurde am 27. September 2006 im Forschungszentrum Karlsruhe (FZK) im Rahmen des von der EU unterstützten ISTC-Programms 1648.2 durchgeführt. Der Versuch ist von FZK in Abstimmung mit RIAR Dimitrovgrad und IBRAE Moskau (beide Russland) vorgeschlagen und mittels Vorausrechnungen durch das Paul-Scherrer-Institut (PSI, Schweiz) und das Kurchatov-Institut Moskau (Russland) sowie IRSN Cadarache (Frankreich) unterstützt worden. Dem Hauptexperiment war am 25. August 2006 ein Vorversuch (bis zu einer Maximaltemperatur von 1073 K) vorausgegangen, um das thermohydraulische Bündelverhalten zu ermitteln. Mit dem Ergebnis des Vorversuchs sollten die Eingabedaten für die Rechenprogramme und damit die Vorausrechnungen verbessert werden.

Nach der Stabilisierung der Versuchsanlage bei 873 K wurde die Voroxidation bei ~1470 K für eine Zeitspanne von ~3400 s durchgeführt, um die angestrebte maximale Oxidschichtdicke von etwa 200 μm zu erhalten. Auf die Voroxidation folgte die transiente Phase mit einem Temperaturanstieg bis ~2050 K. Dann wurde das Abschrecken des Versuchsbündels mit einem Wasserfluss von 48 g/s eingeleitet, wodurch nach ~5 min wieder Umgebungstemperatur erreicht war.

Das Fluten mit Wasser hatte eine moderate Temperatureskalation von ~50 K zu Folge, die etwas länger dauerte als im Versuch QUENCH-06. Die Temperaturen in den Bündelhöhen 850 mm bis 1050 mm überstiegen die Schmelztemperatur des β -Zr, d. h. 2130 K.

Während des Versuchs wurde eine Wasserstoffmenge von insgesamt 58 g erzeugt (QUENCH-06: 36 g). Davon wurden 24 g während des Flutens freigesetzt (QUENCH-06: 4 g). Zusätzlich zum Wasserstoff, der durch die starke Oxidation des Zirkoniums während der Temperatureskalation bzw. zum Beginn der Flutphase erzeugt wurde, wurde höchstwahrscheinlich eine größere Menge des in der Hülle absorbierten Wasserstoffs freigesetzt.

Drei Eckstäbe wurden aus dem Bündel gezogen: ein erster zum Ende der Voroxidation, ein zweiter während der transienten Phase und ein dritter nach dem Versuch. Alle Eckstäbe

zeigen Effekte der sog. Breakaway-Oxidation, d. h. starkes Abplatzen der Oxidschichten. Deutliche Spuren der Breakaway-Oxidation zeigten sich darüber hinaus an allen Oberflächen der Hüllrohre und des Shrouds, wenngleich die Breakaway-Oxidation an den Oberflächen der Eckstäbe ausgeprägter waren. Mögliche Gründe für diese Unterschiede könnten in den unterschiedlichen mechanischen Eigenschaften von Rohr und massivem Stab sowie in unterschiedlicher Oberflächengüte von Brennstabhülle und Eckstab liegen.

Breakaway-Oxidation in Verbindung mit lokaler Schmelzebildung und -oxidation sowie die etwas längere Verweildauer des QUENCH-12-Bündels auf höherer Temperatur werden als Grund für die gegenüber dem QUENCH-06-Experiment erhöhte Wasserstoffproduktion angesehen.

Abstract

The QUENCH experiments are to investigate the hydrogen source term resulting from the water injection into an uncovered core of a Light-Water Reactor. The QUENCH test bundle with a total length of approximately 2.5 m usually consists of 21 fuel rod simulators of Western PWR (Pressurized Water Reactor) geometry. The QUENCH-12 test bundle, however, which was set up to investigate the effects of VVER materials and bundle geometry (hexagonal lattice) on core reflood consisted of 31 fuel rod simulators. 18 rods of which were electrically heated using tungsten heaters in the rod center. All claddings, corner rods and grid spacers were made of Zr1%Nb (E110) and the shroud of Zr2.5%Nb (E125). For comparison, the QUENCH-06 test (ISP-45) with Western PWR geometry (square lattice) was chosen as reference.

QUENCH-12 conducted at the Forschungszentrum Karlsruhe (FZK, Karlsruhe Research Center) on 27 September, 2006 in the frame of the EC-supported ISTC program 1648.2 was proposed by FZK together with RIAR Dimitrovgrad and IBRAE Moscow (Russia), and supported by pretest calculations performed by PSI (Switzerland) and the Kurchatov Institute Moscow (Russia) together with IRSN Cadarache (France). It had been preceded by a low-temperature (maximum 1073 K) pretest on 25 August, 2006 to characterize the bundle thermal hydraulic performance and to provide data to assess the code models used for pretest calculational support.

After a stabilization period at 873 K pre-oxidation took place at ~1470 K for ~3400 s to achieve a maximum oxide thickness of about 200 μm . A transient phase followed with a temperature rise to ~2050 K. Then quenching of the bundle by a water flow of 48 g/s was initiated cooling the bundle to ambient temperature in ~5 min.

Following reflood initiation, a moderate temperature excursion of ~50 K was observed, over a longer period than in QUENCH-06. The temperatures at elevations between 850 mm and 1050 mm exceeded the melting temperature of β -Zr, i.e. 2130 K.

The total hydrogen production in QUENCH-12 was 58 g (QUENCH-06: 36 g). During reflood 24 g of hydrogen were released (QUENCH-06: 4 g). Additionally to the hydrogen produced by the strong oxidation of zirconium during temperature escalation and at the beginning of the reflood phase, respectively, a large amount of hydrogen previously absorbed in the metal is assumed to be released at that time.

Three corner rods were withdrawn during the experiment, one at the end of preoxidation, a second one during the transient phase and a third one after the test. All corner rods showed breakaway oxidation effects, i.e. strong spalling of oxide scales. In addition to the corner rods, the surfaces of the rod simulators and shroud show intensive breakaway oxidation although the breakaway is more pronounced at the surfaces of the corner rods. Possible reasons for the differences could be different mechanical properties of tube and massive rod and other surface preparation of cladding and corner rods.

Breakaway oxidation together with local melt formation and subsequent melt oxidation as well as a longer exposure time at temperature in QUENCH-12 compared to QUENCH-06 is

considered as reason for a higher hydrogen generation compared to the QUENCH-06 experiment.

Contents

List of Tables	1
List of Figures	2
Introduction.....	11
1 Description of the Test Facility	13
2 Test Bundle Instrumentation	15
3 Hydrogen Measurement Devices	16
4 Data Acquisition and Process Control.....	17
5 Test Conduct and Pertinent Results.....	17
6 Posttest Examination.....	20
6.1 Posttest Appearance of Shroud During Bundle Dismounting	20
6.2 Videoscope Inspection.....	20
6.3 Appearance of the Withdrawn Corner Rods	21
6.4 Encapsulation and Sectioning of the Test Bundle	21
6.5 Metallographic Examination.....	22
6.5.1 Investigation Procedures	22
6.5.2 Documentation and Interpretation of the Bundle Status	23
6.5.3 Oxidation of the Withdrawn Corner Rods	29
6.5.4 Lateral and Axial Distribution of ZrO ₂ Scale and α-Zr(O) Layer Thickness.....	30
6.5.5 Analysis of the Spalled Fraction of the Oxide Scales	33
6.6 Measurements of thicknesses of residual metal layers and comparison with QUENCH-06	33
6.7 Results of Metallographic Posttest Examinations by RIAR	34
6.7.1 Introduction	34
6.7.2 Examination of the Cross Sections.....	35
6.7.3 Measurement of Oxidation of the Corner Rods Withdrawn	36
6.7.4 Conclusions	37
6.8 Analysis of the Hydrogen Absorbed in the Corner Rods	37
7 Summary	41
References	43

List of Tables

- Table 1: QUENCH test matrix
- Table 2: Design characteristics of the QUENCH-VVER test bundle
- Table 3: Comparison of some physical/chemical properties of different zirconium alloys
- Table 4: Properties of zirconia fiber insulating boards of type ZYFB3
- Table 5: Diameters of the materials used for the QUENCH high-temperature thermocouples (mm)
- Table 6: Main characteristics of the HfO₂ thermocouple insulator
- Table 7: Main characteristics of the ZrO₂ pellet material, yttria-stabilized, type FZY
- Table 8: List of instrumentation for the QUENCH-12 test bundle.
- Table 9: QUENCH-12; Bundle thermocouples positions
- Table 10: QUENCH-12; Failure of thermocouples
- Table 11: QUENCH-12; Electrical resistances of circuits, contacts, and cables
- Table 12: QUENCH-12; Sequence of events for test
- Table 13: QUENCH-12; Maximum measured test bundle and shroud temperatures evaluated for upper elevations
- Table 14: QUENCH-12; Water/steam balance
- Table 15: QUENCH-12; Quench front progression
- Table 16: QUENCH-12; Results of bundle filling with epoxy resin
- Table 17: QUENCH-12; Cross sections for the metallographic examination
- Table 18: QUENCH-12; Oxide layers, α -layers and residual metal of withdrawn corner rods D, F, B.
- Table 19: Estimation of complete oxide layer thicknesses on corner rods withdrawn from the QUENCH-12 test bundle
- Table 20: Average layer thicknesses measured by FZK at lower cross sections of the QUENCH-12 test bundle
- Table 21: Average layer thicknesses measured by FZK at upper cross sections of the QUENCH-12 test bundle
- Table 22: Average layer thicknesses measured by RIAR at different cross sections of the QUENCH-12 test bundle
- Table 23: Detailed results of metallographic measurement performed by RIAR at withdrawn corner rods

List of Figures

- Fig. 1: QUENCH Facility - Main components.
- Fig. 2: Flow diagram of the QUENCH test facility.
- Fig. 3: QUENCH Facility; Containment and test section.
- Fig. 4: QUENCH-12; Test section with flow lines.
- Fig. 5: QUENCH-12; VVER fuel rod simulator bundle (cross section, top view) including rod group numbers.
- Fig. 6: QUENCH-12; Heated VVER fuel rod simulator.
- Fig. 7: QUENCH-12; Unheated VVER fuel rod simulator.
- Fig. 8: QUENCH-12; Unheated VVER-type central rod.
- Fig. 9: Principal locations of the different types of thermocouples used in the QUENCH-12 test bundle (top view) together with rod designations.
- Fig. 10: QUENCH-12; Axial temperature measurement locations in the test section
- Fig. 11: QUENCH-12; High-temperature thermocouple.
- Fig. 12: QUENCH-12; Concept for fastening of cladding outer surface thermocouples.
- Fig. 13: QUENCH-12; Arrangement of the thermocouples inside the corner rods.
- Fig. 14: QUENCH Facility; H₂ measurement with the GAM 300 mass spectrometer.
- Fig. 15: Mass spectrometer sampling position at the off-gas pipe of the QUENCH test facility.
- Fig. 16: Hydrogen measurement with the CALDOS analyzer connected to the exhaust gas pipe of the QUENCH facility
- Fig. 17: QUENCH-12; Top view of the off-gas pipe with the sampling line of the mass spectrometer and the standard orifice (F 601) between the two flanges.
- Fig. 18: QUENCH-12; Comparison of power and temperature profiles for QUENCH-12 and QUENCH-06.
- Fig. 19: QUENCH-12; Test conduct (schematics of histories of bundle temperature, power, argon and steam flow rate and hydrogen production rate).
- Fig. 20: QUENCH-12; Averaged axial temperature profile of all TFS thermocouples, left, and axial oxide layer profile of corner rod F for elevations 700-1120 mm, right, at time of rod pulling, i.e. 7175 s (transient phase).
- Fig. 21: QUENCH-12; Quench water injection rate and rise of water level in the test bundle.

- Fig. 22: QUENCH-12; Selected readings of the bundle thermocouples demonstrate the quench front propagation during the quench phase.
- Fig. 23: QUENCH-12; Spalling of outer scales of oxide layers at corner rods D, F, and B.
- Fig. 24: QUENCH-12; Comparison of hydrogen release during QUENCH-12 and QUENCH-06.
- Fig. 25: QUENCH-12; Radial temperature distributions (bundle and shroud) for three time points: 1) 5960 s (1st corner rod removed), 2) 7150 s (2nd corner rod removed), 3) 7265 s (before reflood), and at three levels, i.e. 850 mm, bottom, 950 mm, center, and 1050 mm, top.
- Fig. 26: QUENCH-12; Comparison of axial temperature distribution versus the unwound shroud for two time points: a) before withdrawal of 2nd corner rod, top, b) before reflood, bottom.
- Fig. 27: Temperatures at elevation 850 mm of bundles QUENCH-06 and QUENCH-12 during transient and quench phases.
- Fig. 28: Temperatures at elevation 950 mm of bundles QUENCH-06 and QUENCH-12 during transient and quench phases.
- Fig. 29: Axial shroud temperature profiles for QUENCH-06 and QUENCH-12 on beginning and end of transient phase.
- Fig. 30: Axial bundle temperature profiles for QUENCH-06 and QUENCH-12 on beginning and end of transient phase.
- Fig. 31: QUENCH-12; Posttest appearance of the hot zone of shroud and test bundle (~750-1150 mm) at orientations 0, 90, 180, and 270 degrees (from left).
- Fig. 32: QUENCH-12; Piece of upper shroud that broke off during dismantling.
- Fig. 33: Debris transported to the inlet section of the off-gas tube during the QUENCH-12 test.
- Fig. 34: QUENCH-12; Videoscope monitoring at the empty position of the withdrawn corner rod D, viewed from bottom to top.
- Fig. 35: QUENCH-12; Videoscope monitoring at the empty position of the withdrawn corner rod D, viewed from bottom to top; cont'd.
- Fig. 36: QUENCH-12; Videoscope monitoring (side view) at the empty position of the withdrawn corner rod D.
- Fig. 37: QUENCH-12; local melt formation at 850 mm and the position of corner rod B withdrawn after the test.
- Fig. 38: QUENCH-12; Photographs of corner rod D, 622-751 mm.
- Fig. 39: QUENCH-12; Photographs of corner rod D 821-1003 mm.
- Fig. 40: QUENCH-12; Photographs of corner rod D 1038-1159 mm.
- Fig. 41: QUENCH-12; Photographs of corner rod F 609-766 mm.

- Fig. 42: QUENCH-12; Photographs of corner rod F, 847-1038 mm.
- Fig. 43: QUENCH-12; Photographs of corner rod F, 1062-1159 mm.
- Fig. 44: QUENCH-12; Photographs of corner rod B, 552-701 mm.
- Fig. 45: QUENCH-12; Photographs of corner rod B, 697-884 mm.
- Fig. 46: QUENCH-12; Typical morphology of spalled oxide scale of corner rod (laminated structure).
- Fig. 47: QUENCH-12; Epoxying process of the tested bundle.
- Fig. 48: QUENCH-12; Cross sections at 535 mm, 550 mm, 554 mm, and 570 mm.
- Fig. 49: QUENCH-12; Cross sections at 634 mm, 650 mm, 654 mm, and 670 mm.
- Fig. 50: QUENCH-12; Cross sections at 734 mm, 750 mm, 754 mm, and 770 mm.
- Fig. 51: QUENCH-12; Cross sections at 834 mm, 850 mm, 854 mm, and 870 mm.
- Fig. 52: QUENCH-12; Cross sections at 934 mm, 950 mm, 954 mm, and 970 mm.
- Fig. 53: QUENCH-12; Cross sections at 1034 mm, 1050 mm, 1134 mm, and 1150 mm.
- Fig. 54: QUENCH-12-1, level 550 mm; cross section overview.
- Fig. 55: QUENCH-12-1, level 550 mm; cladding oxidation of the central rod.
- Fig. 56: QUENCH-12-1, level 550 mm; cladding oxidation of rod 5 (inner ring, heated).
- Fig. 57: QUENCH-12-1, level 550 mm; cladding oxidation of rod 19 (second ring, unheated).
- Fig. 58: QUENCH-12-1, level 550 mm; relocated cladding debris, showing both-sided oxidation.
- Fig. 59: QUENCH-12-1, level 550 mm; oxidation state of corner rod A.
- Fig. 60: QUENCH-12-1, level 550 mm; oxidation state of corner rod C.
- Fig. 61: QUENCH-12-3, level 650 mm; cross section overview.
- Fig. 62: QUENCH-12-3, level 650 mm; cladding oxidation of the central rod.
- Fig. 63: QUENCH-12-3, level 650 mm; cladding oxidation of rod 4 (inner ring, heated).
- Fig. 64: QUENCH-12-3, level 650 mm; cladding oxidation of rod 18 (second ring, unheated).
- Fig. 65: QUENCH-12-3, level 650 mm; oxidation state of corner rod A.
- Fig. 66: QUENCH-12-3, level 650 mm; oxidation state of corner rod C.
- Fig. 67: QUENCH-12-3, level 650 mm; oxidation state of corner rod E.

- Fig. 68: QUENCH-12-1 and -3, levels 550 and 650 mm; oxidation of the shroud (inner side).
- Fig. 69: QUENCH-12-5, level 750 mm; cross section overview.
- Fig. 70: QUENCH-12-5, level 750 mm; cladding oxidation of the central rod.
- Fig. 71: QUENCH-12-5, level 750 mm; cladding oxidation of rods 2 and 7 (inner ring, heated).
- Fig. 72: QUENCH-12-5, level 750 mm; cladding oxidation of rods 10 and 17 (second ring, unheated).
- Fig. 73: QUENCH-12-5, level 750 mm; cladding oxidation of rods 24 and 30 (outer ring, heated).
- Fig. 74: QUENCH-12-5, level 750 mm; oxidation state of corner rod A.
- Fig. 75: QUENCH-12-5, level 750 mm; oxidation state of corner rod C.
- Fig. 76: QUENCH-12-5, level 750 mm; oxidation state of corner rod E towards west.
- Fig. 77: QUENCH-12-5, level 750 mm; oxidation state of corner rod E towards east.
- Fig. 78: QUENCH-12-7, level 850 mm; cross section overview.
- Fig. 79: QUENCH-12-7, level 850 mm; macrographs of rods towards SE, illustrating advanced oxidation and losses of cladding due to fracture.
- Fig. 80: QUENCH-12-7, level 850 mm; cladding oxidation of rod 7 (inner ring, heated).
- Fig. 81: QUENCH-12-7, level 850 mm; cladding oxidation of rod 15 (second ring, unheated).
- Fig. 82: QUENCH-12-7, level 850 mm; cladding oxidation of rod 30 (outer ring, heated).
- Fig. 83: QUENCH-12-7, level 850 mm; microstructure of melt pool in contact to rod 25.
- Fig. 84: QUENCH-12-7, level 850 mm; oxide scale around pool of relocated melt.
- Fig. 85: QUENCH-12-7, level 850 mm; oxidation state of corner rod C.
- Fig. 86: QUENCH-12-7, level 850 mm; oxidation state of corner rod E.
- Fig. 87: QUENCH-12-7 and -5, levels 850 and 750 mm; oxidation of the shroud (inner side).
- Fig. 88: QUENCH-12-9, level 950 mm; cross section overview.
- Fig. 89: QUENCH-12-9, level 950 mm; macrographs of rods towards S, illustrating formation and oxidation of melt pools via the necking mechanism.
- Fig. 90: QUENCH-12-9, level 950 mm; macrographs of rods towards N, illustrating melt pool formation and melt re-distribution.
- Fig. 91: QUENCH-12-9, level 950 mm; macrographs of rods towards W, illustrating complete oxidation of residual melt.

- Fig. 92: QUENCH-12-9, level 950 mm; macrographs of rods towards E, illustrating a triangular melt pool with embedded scales and an inactive dry neck.
- Fig. 93: QUENCH-12-9, level 950 mm; dissolution trend of scale of rod 8, embedded by the triangular melt pool (see previous figure).
- Fig. 94: QUENCH-12-9, level 950 mm; oxidation state of rod 8 at the steam exposed opposite side.
- Fig. 95: QUENCH-12-9, level 950 mm; state of total oxidation of rod 7, indicating the history of different contributions.
- Fig. 96: QUENCH-12-9, level 950 mm; oxidation state of corner rod A, showing massive oxide and duplex melt microstructure.
- Fig. 97: QUENCH-12-9, level 950 mm; oxidation state of corner rod X, a massive relocated fragment, most probably of corner rod A origin.
- Fig. 98: QUENCH-12-9, level 950 mm; state of total oxidation of corner rod C remnants.
- Fig. 99: QUENCH-12-9, level 950 mm; macrographs, depicting the remnants of the shroud.
- Fig. 100: QUENCH-12-9, level 950 mm; thick shroud remnant, composed of outer part with duplex microstructure, metallic core, and inner scale.
- Fig. 101: QUENCH-12-9, level 950 mm; thin shroud remnant, composed of outer part with duplex microstructure, and fully oxidized inner part.
- Fig. 102: QUENCH-12; Cross-sections of inner rod simulators at elevation 1050 mm.
- Fig. 103: QUENCH-12; Cross-sections of unheated rods (left part of the bundle) at elevation 1050 mm.
- Fig. 104: QUENCH-12; Cross-sections of unheated rods (right part of the bundle) at elevation 1050 mm.
- Fig. 105: QUENCH-12; Cross-sections of heated and corner rods (left part of the bundle) at elevation 1050 mm.
- Fig. 106: QUENCH-12; Cross-sections of heated and corner rods (right part of the bundle) at elevation 1050 mm.
- Fig. 107: QUENCH-12; Microstructure of cladding tube of unheated rods 1 (intensive initial pre-oxidation; left column) and 13 (moderate initial pre-oxidation; right column) at elevation 1050 mm.
- Fig. 108: QUENCH-12; Pronounced breakaway structure of corner rods oxide layers at elevation 1050 mm; cross-section of relocated corner rod A corresponds to an upper bundle elevation.
- Fig. 109: QUENCH-12; Cross-sections of inner rod simulators at elevation 1150 mm.

- Fig. 110: QUENCH-12; Cross-sections of unheated rods (left part of the bundle) at elevation 1150 mm.
- Fig. 111: QUENCH-12; Cross-sections of unheated rods (right part of the bundle) at elevation 1150 mm.
- Fig. 112: QUENCH-12; Cross-sections of heated and corner rods (left part of the bundle) at elevation 1150 mm.
- Fig. 113: QUENCH-12; Cross-sections of heated and corner rods (right part of the bundle) at elevation 1150 mm.
- Fig. 114: QUENCH-12; Microstructure of cladding tubes of unheated rod 12 and heated rod 21 at elevation 1150 mm.
- Fig. 115: QUENCH-12; Pronounced breakaway structure of corner rods oxide layers at elevation 1150 mm; cross-section of relocated corner rod A corresponds to an upper bundle elevation.
- Fig. 116: QUENCH-12, level 700 mm; oxidation of withdrawn corner rod D, representing the end of the pre-oxidation phase.
- Fig. 117: QUENCH-12, level 940 mm; oxidation of withdrawn corner rod D, representing the end of the pre-oxidation phase.
- Fig. 118: QUENCH-12, level 1120 mm; oxidation of withdrawn corner rod D, representing the end of the pre-oxidation phase.
- Fig. 119: QUENCH-12, level 700 mm; oxidation of withdrawn corner rod F, representing the state just before quenching.
- Fig. 120: QUENCH-12, level 940 mm; oxidation of withdrawn corner rod F, representing the state just before quenching.
- Fig. 121: QUENCH-12, level 1120 mm; oxidation of withdrawn corner rod F, representing the state just before quenching.
- Fig. 122: QUENCH-12, level 700 mm; oxidation of withdrawn corner rod B, representing the whole test exposure.
- Fig. 123: QUENCH-12, level 820 mm; oxidation of withdrawn corner rod B, representing the whole test exposure
- Fig. 124: QUENCH-12; Structure of the residual oxide layer on the surface of three withdrawn corner rods at different bundle elevations.
- Fig. 125: QUENCH-12; oxide and α -layer thickness at bundle elevation 550 mm (Cross section QUE-12-01).
- Fig. 126: QUENCH-12; Oxide and α -layer thickness at bundle elevation 650 mm (Cross section QUE-12-03).

- Fig. 127: QUENCH-12; Oxide and α -layer thickness at bundle elevation 750 mm (Cross section QUE-12-05).
- Fig. 128: QUENCH-12; Oxide and α -layer thickness at bundle elevation 850 mm (Cross section QUE-12-07).
- Fig. 129: QUENCH-12; Oxide and metal layer thickness at bundle elevation 950 mm (Cross section QUE-12-09).
- Fig. 130: QUENCH-12; Oxide and α -layer thickness at bundle elevation 1050 mm (Cross section QUE-12-12).
- Fig. 131: QUENCH-12; oxide and α -layer thickness at bundle elevation 1150 mm (Cross section QUE-12-11).
- Fig. 132: QUENCH-12; measured axial layers profiles, bundle, top, and rod simulators, bottom.
- Fig. 133: QUENCH-12; Degree of cladding oxide layer spalling for different bundle elevations, total oxide layer calculated on the base of residual metal.
- Fig. 134: QUENCH-12; Posttest axial distribution of the oxide layer of the cladding tube surfaces.
- Fig. 135: QUENCH-12; Results of metallographical examination of residual cladding metal thickness at bundle elevation 550 mm.
- Fig. 136: QUENCH-12; Results of metallographical examination of residual cladding metal thickness at bundle elevation 650 mm.
- Fig. 137: QUENCH-12; Results of metallographical examination of residual cladding metal thickness at bundle elevation 750 mm.
- Fig. 138: QUENCH-12; Results of metallographical examination of residual cladding metal thickness at bundle elevation 850 mm.
- Fig. 139: QUENCH-12; Results of metallographical examination of residual cladding metal thickness at bundle elevation 1150 mm.
- Fig. 140: Comparison of oxide thicknesses at bundle elevation 550 mm of QUENCH-12 (values estimated from residual metal) with QUENCH-06 (measured values).
- Fig. 141: Comparison of oxide thicknesses at bundle elevation 750 mm of QUENCH-12 (values estimated from residual metal) with QUENCH-06 (measured values).
- Fig. 142: Comparison of oxide thicknesses at bundle elevation 850 mm of QUENCH-12 (values estimated from residual metal) with QUENCH-06 (measured values).
- Fig. 143: Comparison of oxide thicknesses at bundle elevation 1150 mm of QUENCH-12 (values estimated from residual metal) with QUENCH-06 (measured values).
- Fig. 144: QUENCH-12; Radial distribution of cladding oxide layer thicknesses calculated on the base of residual metallic layers (from bottom to top: elevations 550 mm, 650 mm, 750 mm).

- Fig. 145: QUENCH12; Temperature distributions at elevation 550 mm for three time points (top) and corresponding distribution of cladding oxide layer thicknesses after test completion calculated on the basis of residual metallic layers (bottom).
- Fig. 146: QUENCH-12; Structure of the simulator claddings in cross section 554 mm.
- Fig. 147: QUENCH-12; Structure of the simulator claddings in cross section 654 mm.
- Fig. 148: QUENCH-12; Structure of the simulator claddings in cross section 754 mm.
- Fig. 149: QUENCH-12; Structure of the simulator claddings in cross section 854 mm.
- Fig. 150: QUENCH-12; Macrographs of the simulators in cross section 954 mm.
- Fig. 151: QUENCH-12; Melt structure in cross section 954 mm.
- Fig. 152: QUENCH-12; Variation in thickness of the metal part of the simulator claddings in the examined cross sections.
- Fig. 153: QUENCH-12; Variation in thickness of α -Zr(O) in the examined cross sections.
- Fig. 154: QUENCH-12; Pictures of corner rod cross sections from 20 mm segments (polished at top) examined by RIAR.
- Fig. 155: QUENCH-12; Neutron radiographs and visual appearance of selected axial positions of corner rod D.
- Fig. 156: QUENCH-12; Normalized radial intensity distribution of five axial positions of corner rod D.
- Fig. 157: QUENCH-12; Axial distribution of the hydrogen content for the three investigated corner rods.
- Fig. 158: QUENCH-12; Ratio between the values of hydrogen concentration determined by hot extraction (HE) and neutron radiography (NR) for withdrawn corner rods.
- Fig. 159: QUENCH-12; Fit of axial temperature distribution, determined hydrogen content, and calculated hydrogen partial pressure for corner rod D.
- Fig. 160: QUENCH-12; Micrographs of details taken from cross sections at different axial positions of corner rod D.
- Fig. 161: QUENCH-12; Comparison of axial variation of the hydrogen content and the macroscopic appearance of the upper part of the shroud.
- Fig. 162: Comparison of the hydrogen concentrations in cladding rod segments and in corner rod B.
- Fig. 163: QUENCH-12; Neutron radiograph of the upper end of the lower part of corner rod B (x axis is the position of the transmission graph).
- Fig. 164: Comparison of hydrogen absorbed by cladding during QUENCH-12 and QUENCH-06 tests.

Introduction

The most important accident management measure to terminate a severe accident transient in a Light Water Reactor (LWR) is the injection of water to cool the uncovered degraded core. Analysis of the TMI-2 [1] accident and the results of integral out-of-pile (CORA [2, 3]) and in-pile experiments (LOFT [4], PHEBUS [5]) have shown that before the water succeeds in cooling the fuel pins there may be an enhanced oxidation of the zircaloy cladding that in turn causes a sharp increase in temperature, hydrogen production, and fission product release.

Besides, quenching is considered as a worst-case accident scenario regarding hydrogen release to the containment. For licensing and safety analyses one has to prove that the hydrogen release rate and total amount do not exceed limits for the considered power plant. The hydrogen generation rate must be known to design appropriately accident mitigation measures like passive autocatalytic recombiners and ignitors.

The physical and chemical phenomena of the hydrogen release are, however, not sufficiently well understood. The increased hydrogen production during quenching cannot be completely explained on the basis of the available zircaloy/steam oxidation correlations [6]. In most of the code systems describing severe fuel damage, phenomena, e.g. melt oxidation and steam starvation prior to flooding, which lead to an enhanced oxidation and hydrogen generation are either not considered or only modeled in a simplified empirical manner.

In addition, no sophisticated models were available to predict correctly the thermal-hydraulic and the clad behavior particularly during the quenching processes in the CORA and LOFT LP-FP-2 tests. An extensive experimental database is therefore needed as a basis for model development and code improvement.

The QUENCH program on the investigation of coolability and determination of the hydrogen source term has therefore been launched at the Forschungszentrum Karlsruhe with the following main objectives.

- The provision of an extensive experimental database for the development of detailed mechanistic models,
- The examination of the physico-chemical behavior of overheated fuel elements under different flooding conditions and at different stages of core degradation,
- The determination of cladding failure criteria, cracking of oxide layers, exposure of new metallic surfaces to steam,
- The investigation of the oxide layer degradation under steam starvation conditions and influence of this phenomenon on subsequent flooding,
- The investigation of the melt oxidation process,
- The determination of the hydrogen source term.

The QUENCH program began with small-scale experiments using short zircaloy fuel rod segments [7-9]. On the basis of these results well-instrumented large-scale bundle experiments with fuel rod simulators under nearly adiabatic conditions are performed in the QUENCH facility of the Forschungszentrum Karlsruhe. The large-scale bundle experiments are more representative of prototypic reactor accident conditions than are the single-rod experiments. Important parameters of the bundle test program (see [Table 1](#)) are: quench medium, i.e. water or steam, fluid injection rate, cladding oxide layer thickness, and the temperature at onset of flooding.

VVER bundle experiment QUENCH-12 was set up to test a fuel element simulator of a hexagonal lattice and containing fuel rod claddings made of Zr1%Nb (E 110) as used in eastern VVER reactors. Its main objective was to compare the bundle behavior with that of a western PWR bundle during a severe accident scenario including quenching with water from the bottom. Test QUENCH-06 [10-11] was chosen as reference for the western PWR-type bundle. This involved pre-oxidation to a maximum of about 200 μm oxide thickness.

To set up the test conduct of QUENCH-12 it was necessary to compare the geometrical parameters of the QUENCH-12 (VVER) bundle with the QUENCH-06 (PWR) bundle:

1) The ratio of coolant channel QUENCH-12/QUENCH-06 is 1.09. So, to obtain the same flow velocity the fluid flow rate should be 9 % higher for the QUENCH-12 bundle than for the QUENCH-06 bundle.

2) The ratio of metallic surface QUENCH-12/QUENCH-06 is 1.22, i.e. the chemical energy production for the VVER bundle due to exothermic steam-metal reaction is higher by 22 %.

3) The ratio of bundle material mass QUENCH-12/QUENCH-06 is ~ 0.97 . Thus, the electrical power input for the VVER bundle should be slightly lower than that used for the QUENCH-06 bundle.

QUENCH-12 had been preceded by a low-temperature (maximum 1073 K) pretest on 25 August, 2006 to characterize the bundle thermal hydraulic performance and to provide data on which to assess the code models used for pretest calculations.

A complete set of temperature data of all axial levels was provided in the Quick Look Report (internal) on the QUENCH-12 experiment [24]. Therefore, only selected temperature plots are given in this report which describes besides test facility and test bundle the main results of the QUENCH-12 experiment with emphasis on the posttest examination. The QUENCH-12 bundle behavior is to a certain extent compared to that of reference test QUENCH-06. The analytical support for the preparation of the test by using the SCDAP/RELAP5 and MELCOR codes [12] and ICARE/CATHARE V1 Code [13] was carried out by Paul-Scherrer-Institut (PSI Switzerland) and by the Kurchatov Institute Moscow, respectively. The final calculations, which took advantage of the pre-experiment data, were performed by PSI using the SCDAP-based codes. Posttest calculations using the SVECHA/QUENCH code are as well not documented in this report but reported in [14].

1 Description of the Test Facility

The main components of the QUENCH test facility are presented in [Fig. 1](#). The test section is enclosed by a safety containment with a wall thickness of 5.6 mm and an inner diameter of 801.8 mm. The facility can be operated in two modes: a forced-convection mode depicted in the flow diagram of [Fig. 2](#) and a boil-off mode. In the forced-convection mode (relevant for QUENCH-12) superheated steam from the steam generator and superheater together with argon as a carrier gas enter the test bundle at the bottom ([Figs. 3 and 4](#)). The system pressure in the test section is around 0.2 MPa. The argon, steam, and hydrogen produced in the zirconium-steam reaction flow upward inside the bundle and from the outlet at the top through a water-cooled off-gas pipe to the condenser where the steam not consumed is separated from the non-condensable gases, usually argon and hydrogen. The water cooling circuits for bundle head and off-gas pipe are temperature-controlled to guarantee that the steam/gas temperature is high enough so that condensation at test section outlet and inside the off-gas pipe can be avoided. The temperature at the bundle head is kept at 348 K, and the flow rate of the cooling water is ~250 g/s. The off-gas pipe consists of a water-cooled inner pipe with a countercurrent flow and a flow rate of ~370 g/s. The water inlet temperature is controlled at 393 K. Between the off-gas pipe and inner cooling jacket there is stagnant off-gas. The main dimensions of the tubes that make up the off-gas pipe are:

Inner pipe:	outer diameter 139.7 mm, wall thickness 4.5 mm total length 3256 mm, material: stainless steel
Inner cooling jacket:	outer diameter 154 mm, wall thickness 2 mm, material: stainless steel
Outer cooling jacket:	outer diameter 168.3 mm, wall thickness 5 mm, material: stainless steel

The quenching water is injected through a separate line marked “bottom quenching” in [Fig. 4](#).

The design characteristics of the VVER test bundle are listed in [Table 2](#). The test bundle is approximately 2.5 m long and is made up of 18 heated and 13 unheated fuel rod simulators ([Fig. 5](#)), each with a length of approximately 2.5 m. Heating is electric by 4 mm diameter tungsten heaters installed in the rod center, and the heated length is 1024 mm (see heated rod in [Fig. 6](#) and unheated rods in [Figs. 7 and 8](#)). Electrodes of molybdenum/copper are connected to the tungsten heaters at one end and to the cable leading to the DC electrical power supply at the other end. The total heating power is distributed between two groups of heated rods as follows: 33 % of the power is released in the six inner fuel rod simulators, 67 % in the twelve outer fuel rod simulators. Electrical resistances of inner and outer ring (without cables on both ends) as well as of a single heater and a single slide contact at the copper electrode can be taken from [Table 11](#).

The fuel rod simulators are held in position by seven grid spacers, all made of Zr1%Nb. Its length is 20 mm. Furthermore, the thickness of the spacer is 0.25 mm and the mass of one grid spacer was measured to be 46.5 g.

The tungsten heaters of 4 mm diameter are installed in the center of the rods are surrounded by annular ZrO₂ pellets (bore size 4,15 mm). The unheated fuel rod simulator ([Fig. 7](#)) is filled with ZrO₂ pellets (bore size 2.5 mm).

The tungsten heaters are connected to electrodes made of molybdenum and copper at each end of the heater. The molybdenum and copper electrodes were joined by high-frequency/high-temperature brazing under vacuum (2×10^{-3} mbar) using an AuNi 18 powder (particle size <105 μm). For electrical insulation the surfaces of both types of electrodes were plasma-coated with 0.2 mm ZrO₂. To protect the copper electrodes and the O-ring-sealed wall penetrations against excessive heat they are water-cooled (lower and upper cooling chambers filled with demineralized water). The copper electrodes are connected to the DC electric power supply by means of special sliding contacts at the top and bottom.

The rod claddings of the heated and unheated fuel rod simulators are identical to those used in VVERs with respect to material and dimensions (Zr1%Nb, 9.13 mm outside diameter, 0.7 mm wall thickness; see also Table 2). Heated rods were filled with Ar5%Kr and unheated test rods, including the central one, were filled with He, each rod at a pressure of approx. 0.22 MPa. The different fill gases allow observation of a first cladding failure which then can be distinguished between heated and unheated test rod.

Six Zr1%Nb corner rods were installed in the bundle. Three of them, i.e. rods "A", "C", and "E" were made of a solid Zr1%Nb rod at the upper part and a Zr1%Nb tube at the lower part and were used for thermocouple instrumentation whereas the other three corner rods, i.e. rods "B", "D", and "F", were made of solid Zr1%Nb rods of 6 mm diameter to be able to be withdrawn from the bundle for checks of the amounts of ZrO₂ oxidation and hydrogen uptake at pre-defined times.

The test bundle was surrounded by a shroud of Zr2.5%Nb (E 125) with a 37 mm thick ZrO₂ fiber insulation extending from the bottom to the upper end of the heated zone and a double-walled cooling jacket of stainless steel over the entire length. The annulus between shroud and cooling jacket was purged (after several cycles of evacuation) and then filled with stagnant argon of 0.22 MPa. The annulus was connected to a flow- and pressure-controlled argon feeding system in order to keep the pressure constant at the target of 0.22 MPa (beyond this pressure gas is released) and to prevent an access of steam to the annulus after shroud failure (argon feeding below the target value). The 6.7 mm annulus of the cooling jacket was cooled by an argon flow. Both the absence of an ZrO₂ insulation above the heated region and the water cooling of the bundle head are to avoid overheating in that bundle region.

2 Test Bundle Instrumentation

The test bundle was instrumented with sheathed thermocouples (TC) attached to the rod claddings at 17 different elevations between -250 mm and 1350 mm and at different orientations according to [Fig. 10](#). The elevations of the surface-mounted shroud thermocouples are from -250 mm to 1250 mm. In the lower bundle region, i.e. up to the 550 mm elevation, NiCr/Ni thermocouples (1 mm diameter, stainless steel sheath 1.4541, MgO insulation) are used for temperature measurement of rod cladding and shroud. The thermocouples of the hot zone are high-temperature thermocouples with W-5Re/W-26Re wires, HfO₂ insulation, and a duplex sheath of tantalum (internal)/Zirconium with an outside diameter of 2.1 mm (see [Fig. 11](#) and [Table 5](#)). Additional information on the characteristics of the HfO₂ insulation are provided in [Table 6](#).

The thermocouple attachment technique for the surface-mounted high-temperature TCs is illustrated in [Fig. 12](#). The TC tip is held in place by two clamps of zirconium (0.2 mm thick). As these clamps are prone to oxidation and embrittlement in a steam environment an Ir-Rh wire of 0.25 mm diameter is additionally used in the experiments with pre-oxidation as was the case in test QUENCH-12. The leads of the thermocouples from the -250 mm to the 850 mm level leave the test section at the bottom whereas the TCs above 850 mm are routed to the top avoiding to route TC cables through the hot zone. Additionally, the cables of shroud thermocouples (designated TSH xx/x "1") were routed toward outside the shroud insulation to avoid heat transfer from the shroud into the TC cable, apart from the TC junction. The designations of the surface-mounted cladding thermocouples are "TFSH" for the heated rods and "TFSU" for the unheated rods, those of the centerline thermocouples inside the unheated rods are "TFC" ([Fig. 9](#)). This includes the unheated central rod of the QUENCH-12 bundle instrumented with two centerline high-temperature thermocouples (W/Re, \varnothing 2.1 mm), i.e. TFC 12 (at 850 mm, routed to bottom) and TFC 13 (at 950 mm, routed to top). Shroud thermocouples are designated "TSH".

The wall of the inner tube of the cooling jacket is instrumented between -250 mm and 1150 mm with NiCr/Ni thermocouples (designation "TCI"). The thermocouples that are fixed at the outer surface of the outer tube of the cooling jacket (designation "TCO") are also of the NiCr/Ni type due to the lower temperature regime. The designation of the centerline thermocouples inside the Zircaloy corner rods is "TIT". According to [Fig. 13](#) three of the six corner rods of the QUENCH-12 test bundle are instrumented as follows:

- Rod A: W/Re, 2.1 mm diameter, Zr/Ta duplex sheath, 950 mm elevation (TIT A/13)
- Rod C: W/Re, 2.1 mm diameter, Zr/Ta duplex sheath, 850 mm elevation (TIT C/12).
- Rod E: W/Re, 2.1 mm diameter, Zr/Ta duplex sheath, 750 mm elevation (TIT E/11).

A list of all instruments for experiment QUENCH-12 installed in the test section and at the test loop are given in [Table 8](#). The positions of the bundle thermocouples are given in [Table 9](#). The thermocouples that failed prior or during the test are listed in [Table 10](#).

3 Hydrogen Measurement Devices

The released hydrogen is analyzed by two different measurement systems: (1) a Balzers mass spectrometer (MS) "GAM 300" (Fig. 14) and (2) a hydrogen detection system "Caldos 7 G" (Fig. 16) located in a bypass to the off-gas line downstream the condenser. Due to their different locations in the facility the mass spectrometer "GAM 300" responds almost immediately (less than 5 s) to a change in the gas composition whereas the Caldos device has a delay time of about 80-100 s.

The mass spectrometer "BALZERS GAM 300" used is a completely computer-controlled quadrupole MS with an 8 mm rod system which allows quantitative measurement of gas concentrations down to about 10 ppm. For the MS measurement a sampling tube is inserted in the off-gas pipe located approx. 2.7 m downstream from the test section outlet (see also Fig. 17). It has several holes at different elevations to guarantee that the sampling of the gas to be analyzed is representative (see Fig. 15). To avoid steam condensation in the gas pipes between the sampling position and the MS the temperature of the gas at the MS inlet is controlled by heating tapes to be between 110 °C and 150 °C (the upper operating temperature of the MS inlet valves). This allows the MS to analyze the steam production rate. Besides, the concentrations of the following species were continuously measured by the mass spectrometer during all test phases: argon, hydrogen, steam, nitrogen, oxygen, krypton, and helium.

The temperature and pressure of the analyzed gas are measured near the inlet valve of the MS. The MS was calibrated for hydrogen with a well-defined argon/hydrogen mixture and for steam with mixtures of argon and steam supplied by a Bronkhorst controlled evaporator mixing (CEM) device. The MS off-gas is released into the atmosphere because the amount of hydrogen taken out of the system is negligible. A heated measuring gas pump was used to ensure a continuous flow of the steam-gas mixture from the off-gas pipe to the mass spectrometer.

The principle of measurement of the Caldos system is based on the different heat conductivities of different gases. The Caldos device is calibrated for the hydrogen-argon gas mixture. To avoid any moisture in the analyzed gas a gas cooler, which is controlled at 276 K, is connected to the gas analyzer (see also Fig. 16). The response time of the gas analyzer is documented by the manufacturer to be 2 s, i.e. a time in which 90 % of the final value should be reached. In contrast to the mass spectrometer the Caldos device only measures the hydrogen content. Gases other than H₂ cannot be analyzed by this system.

For the Caldos device as well as for the MS the hydrogen mass flow rate is calculated by referring the measured H₂ concentration to the known argon mass flow rate according to equation (1):

$$\dot{m}_{H_2} = \frac{M_{H_2}}{M_{Ar}} \cdot \frac{C_{H_2}}{C_{Ar}} \cdot \dot{m}_{Ar} \quad (1)$$

with M representing the molecular masses, C the concentrations in vol-% and \dot{m} the mass flow rates of the corresponding gases.

With an argon-hydrogen (two-component) mixture that in fact exists at the location of the Caldos analyzer equation (1) can be written as follows:

$$\dot{m}_{H_2} = \frac{M_{H_2}}{M_{Ar}} \cdot \frac{C_{H_2}}{100 - C_{H_2}} \cdot \dot{m}_{Ar} \quad (2)$$

4 Data Acquisition and Process Control

A computer-based control and data acquisition system is used in the QUENCH facility. Data acquisition, data storage, online visualization as well as process control, control engineering and system protection are accomplished by three computer systems that are linked in a network.

The data acquisition system allows recording of about 200 measurement channels at a maximum frequency of 25 Hz per channel. The experimental data and the date and time of the data acquisition are stored as raw data in binary format. After the experiment the raw data are converted into SI units and stored as ASCII data.

For process control, a system flow chart with the most important actual measurement values is displayed on the computer screen. Furthermore, the operating mode of the active components (pumps, steam generator, superheater, DC power system, valves) is indicated. Blocking systems and limit switches ensure safe plant operation. Operating test phases, e.g. heating or quenching phases, are pre-programmed and can be started on demand during the experiment. The parameter settings of the control circuits and devices can be modified online.

Online visualization allows to observe and to document the current values of selected measurement positions in the form of tables or plots. Eight diagrams with six curves each can be displayed as graphs. This means that altogether 48 measurement channels can be selected and displayed online during the course of the experiment.

The data of the main data acquisition system and of the mass spectrometers were stored on different computers. Both computers were synchronized. The data of the main acquisition system were stored at a frequency of 1 Hz for all test phases. The data of the mass spectrometer were collected with a frequency of 0.33 Hz and afterwards interpolated to 1 Hz to be compatible with all other data.

5 Test Conduct and Pertinent Results

Prior to the QUENCH-12 main test a pre-test needed to support pretest modelling was run: After stabilization at 873 K the electrical bundle power was increased from 3.7 kW to 5.45 kW initiating a heatup to a maximum temperature of 1063 K (TFC 1/13, centerline TC in central rod at 950 mm) resulting in negligible oxidation: less than 5 μm oxide layer thickness. The layer thickness was measured at corner rod B by an eddy-current device. The total hydrogen generated during the pretest was 0.9 g. Prior to the main test, corner rod B was re-inserted into the test bundle.

The electrical power input during the main QUENCH-12 test corresponds completely to the values calculated pretest, up to reflood phase. The temperature history at the hot region is very similar to the QUENCH-06 temperature history, particularly during pre-oxidation, as can be seen in [Fig. 18](#). The QUENCH-12 test phases can be summarized as follows.

- Stabilization at 873 K
- Phase I **Pre-oxidation** at ~1470 K for ~3400 s to achieve a maximum oxide thickness of about 200 μm
- Phase II **Transient** with a temperature rise of ~0.3 K/s (1500-1750K) and ~1.3 K/s (1750-1950 K) to a maximum temperature of ~2050 K
- Phase III **Quenching** of the bundle by a water flow of 48 g/s*)

*) Target: 46 g/s (based on flow area of 32.8 cm² compared to 42 g/s with 30.07 cm² in QUENCH-06).

As planned three corner rods were withdrawn from the bundle during the course of QUENCH-12: rod D at the end of preoxidation, rod F during the transient phase and rod B after the test. The illustration of the pulling times of rods D and F is included in [Fig. 19](#) which depicts the QUENCH-12 test conduct.

The sequence of events of the QUENCH-12 main test is listed in [Table 12](#).

A complete set of temperature data of all axial levels is provided in the Quick Look Report (internal) on the QUENCH-12 experiment [24]. Therefore, only selected temperature plots are given in this report. According to [Fig. 19](#) the experiment started with an application of electrical bundle power of ca. 3.5 kW, which was ramped step-wise to 9.9 kW over approx. 2300 s to achieve the desired pre-oxidation temperature at bundle peak position of 1473 K, in a flow of 3.3 g/s argon and 3.3 g/s steam. Pre-oxidation continued to the test time of 6000 s. At about this time corner rod D was withdrawn to check the oxidation level. The power was then ramped at a rate of 5.1 W/s to cause a temperature increase until the desired maximum temperature before quench of 2073 K was reached. Corner rod F was withdrawn after about 900 s from the start of the transient phase, when the bundle temperature was about 1823 K at the 950 mm level. [Fig. 20](#) compares the axial temperature distribution at that time with the measured axial oxide layer profile.

Reflood with 48 g/s of water (at room temperature) was initiated with help of the fast injection system. In [Fig. 21](#) the flow rate of the quench pump is given together with the rising water level in the bundle (L 501). The first spike of the L 501 signal is an indication of the fast water injection filling the lower bundle plenum rapidly. The spike at the beginning of the quench phase corresponds to the decrease in temperature responses at the different elevations shown in [Fig. 22](#). From this diagram it can also be seen that cooling to saturation level takes about 300 s.

The electrical power was reduced to 4 kW during the reflood phase, approximating effective decay heat levels. Following reflood initiation, a moderate temperature excursion of around 50 K was observed, over a longer period than in QUENCH-06. The temperatures at

elevations between 850 mm and 1050 mm exceeded the melting temperature of β -Zr, i.e. 2033 K.

Shroud failure was observed at around the initiation of reflood, while unheated and heated rods failed 20-30 s earlier, i.e. towards the end of the transient phase (exact failure times are given in Table 12). Rod failures were detected by internal pressure and by gas signals (He and Kr, respectively).

The third corner rod, i.e. rod B, was withdrawn after the test, again to check oxide levels and hydrogen absorption. All corner rods showed break-away oxidation effects, i.e. strong spalling of oxide scales (see [Fig. 23](#)). Corner rod B could only be withdrawn in two pieces with rod rupture at the bundle elevation of 880 mm. Besides the solid corner rods the entire test bundle resulted in severe damage of the surfaces of cladding and shroud due to breakaway oxidation. Spalling of the ZrO_2 scales of the rod claddings, however, is less pronounced than at the corner rods. Possible reasons could be (a) different mechanical properties of tube and solid rod; (b) different surface quality of cladding and rods.

The breakaway phenomenon will be discussed in more detail in the subsequent sections, i.e. posttest examination. This phenomenon together with local melt formation with subsequent melt oxidation as well as a longer exposure time at temperature is considered the reason for a higher hydrogen generation compared to the QUENCH-06 experiment.

From posttest examinations described in section 6.8 it is concluded that a large amount of hydrogen previously absorbed in the metal is released additionally to the hydrogen produced by the strong oxidation during temperature escalation and at the beginning of the reflood phase, respectively.

The total hydrogen production was 58 g (QUENCH-06: 36 g). During reflood 24 g of hydrogen were generated (QUENCH-06: 4 g). The amount of hydrogen is larger than the one in the QUENCH-06 experiment even if one takes into account the difference in the metallic clad surface which is 1.22 times larger in QUENCH-12 compared to the QUENCH-06 bundle (see [Fig. 24](#)).

The evaluation of the temperature data of the entire QUENCH-12 test revealed strong radial temperature differences in the bundle as can be seen for three different test times (5960, 7150, and 7265 s) and three different elevations (850, 950, and 1050 mm) in [Fig. 25](#). In the hot region bundle temperatures of the outer ring are elevated ([Fig. 26](#)) due to the strong oxidation of the shroud there, particularly at the end of the transient or beginning of quenching.

[Figs. 27, 28](#) illustrate similarity of bundle temperature profiles for QUENCH-12 and QUENCH-06 tests during transient and quench phases at hottest bundle elevations 850 mm 950 mm. However the increase of the corresponding shroud temperatures during end of transient is more pronounced for the QUENCH-12 test than for QUENCH-06. The probable reason can be loss of the protective effect of the shroud oxide layer due to nodular (local) breakaway oxidation at these bundle elevations (see chapter 6.2). The shroud temperatures at lower elevations were always about 50...100 K higher for the QUENCH-06 test in comparison to QUENCH-12 as shown in [Fig. 29](#). (The temperatures for elevations 1150 and

1250 mm are not shown for QUENCH-06 because of erroneous TC readings due to the “hot zone” effect as described in Appendix 2 of the FZKA 6829 report [15]).

The comparison of the axial bundle temperature profiles at the beginning and end of transient for two experiments (QUENCH-06 and QUENCH-12) is depicted in [Fig. 30](#). Each point is a result of averaging TC signals for the corresponding elevation. One can see that the bundle temperatures during the QUENCH-06 test were about 20...400 K higher than during the QUENCH-12 test for elevations below 1000 mm. This relationship is true for all elevations but changed for elevations 1000-1100 mm before reflood. The significant higher temperatures at elevation 750 mm for the QUENCH-06 test were also confirmed by comparing oxide layer thicknesses at this elevation for both tests ([Fig. 141](#)). At 750 mm the high oxidation values of the QUENCH-06 test bundle are due to breakaway oxidation of Zircaloy-4 in the preceding pre-oxidation phase (spalling of the oxide scale results in formation of additional metal surface).

6 Posttest Examination

6.1 Posttest Appearance of Shroud During Bundle Dismounting

After the experiment the QUENCH-12 test bundle and its shroud appear severely damaged particularly in the regions above ~800 mm elevation (see [Fig. 31](#)). Between ~850 and 1050 mm some part of the β -Zr of the outer shroud surface was partially molten and has reacted with the ZrO_2 fiber insulation resulting in a bulge typical for nearly all QUENCH bundles tested so far. After dismounting the upper part of the shroud was found to have been broken off at around 1000 mm elevation so that the piece of ~300 mm was removed before filling the bundle with epoxy resin (see [Fig. 32](#)).

Upon inspecting the inlet of the off-gas pipe, debris was found there ([Fig. 33](#)) after having been transported by steam/gas from the bundle to that location.

6.2 Videoscope Inspection

Spallation of the oxide scale was also observed with help of a videoscope (OLYMPUS IPLEX) inserted at the empty positions of the three withdrawn corner rods. Spalled oxide scales were even partially removed by pull-out of the videoscope from the bundle. [Figs. 34-36](#) show photographs of typical structures from different bundle elevations taken at the empty position of the withdrawn rod D. The lowest elevation where breakaway oxidation of cladding surface took place was at ~400 mm. The maximum temperature at this bundle position was about 1123 K. No spallation of oxide layer was observed at hottest bundle elevations between 800 and 1000 mm. However the shroud surface at these elevations was exposed to nodular breakaway oxidation. The majority of debris from claddings and shroud accumulated at the bottom of the bundle and upper edge of grid spacers. Particularly, the grid spacer at 550 mm elevation acted as a debris catcher. The initially coarse shroud surface revealed thicker spalled oxide scales, when compared to the simulator rod cladding.

Besides the breakaway effect at the outer surface, breaches of whole cladding were observed, which is typical for Zircaloy-4 cladding as well. Longitudinal and circumferential rod

cladding cracks were found in the hot bundle zone between 700 and 1000 mm (last photos in Figures 35 and 36).

Melt formations inside the bundle were observed only at some local positions, i.e. no massive melt had formed. An interesting effect was observed at the position of the corner rod B at an elevation above 850 mm. The neutron radiograph of the upper end of the lower withdrawn part of this rod is shown in [Fig. 37](#). It is comparable to the lower end of the upper part of this rod (both rod parts are to be seen in [Fig. 23](#)). The deep hole is clearly visible. The formation of these holes can be explained by the α - β phase composition of Zry-4. The α -Zr(O) phase at the outer regions and the β -Zr phase in the bulk of the rod formed during oxidation. Due to the lower melting temperature of the β -Zr phase (2128 K) compared to the oxygen stabilized α -Zr(O) phase (2248 K) a partial melting of the bulk occurs whereas the outer regions remain solid. After solidification, stresses and micro-cracks can be formed at the interface and the rod breaks along this interface.

6.3 Appearance of the Withdrawn Corner Rods

During inspection of the bundle it was noticed that the surface of the simulator rod claddings showed more regular and homogeneous structure of oxide layer than the surface of the massive corner rods. Both surfaces revealed breakaway oxidation but that of the corner rods is more pronounced ([Figs. 38-45](#)). A possible reason for it could be the different mechanical properties of cladding tubes and massive corner rods. The other possible reason could be the different initial rod surface condition: the surface of corner rods is generally coarser if compared with the anodized surface of the simulator rod cladding.

During the withdrawal and subsequent handling of the corner rods a certain amount of oxide scales fell off. This has to be taken into account with regard to the complete oxide layer thickness. Some of the thicker pieces were epoxied and ground, and [Fig. 46](#) shows their cross-sections. It illustrates how easy oxide scales can fall off during handling and that 100 μm in spalled oxide scale thickness is quite typical for the corner rod material.

6.4 Encapsulation and Sectioning of the Test Bundle

For encapsulation the test bundle and shroud are set up vertically. Prior to filling, a cap is placed over the bottom of the copper electrodes and a low-melting metal alloy (similar to Wood's metal containing 48 % Bi, 18 % Pb, 23 % In, 11 % Sn; density of $\sim 10 \text{ kg/dm}^3$; melting point of 331 K) is used to seal the bottom of the bundle. The low-melting metal is also used for sealing the bundle foot so that it can be re-used for the next experiment. For this purpose an inner cage is inserted into the bundle foot from the bottom. Filling of this auxiliary structure is from above the bundle foot, i.e. through holes in the shroud at elevations above -300 mm. Then a plexiglas® tube as mould with an inner diameter of 190 mm is put over test bundle with shroud and fixed at the flange of the bundle foot by a glue (see also schematic in [Fig. 47](#)). Encapsulation of the bundle is performed by filling the mould with the epoxy resin (Bakelite EPR 0273 with the pertinent hardener Bakelite EPH 350) from the bundle foot over the entire bundle length. The epoxying process generally shows a little heating due to the exothermal heat that develops during the curing stage and some shrinkage effect. Scale readings on the mass gain of epoxy resin per cm of filling are recorded and given in [Table 16](#), respectively. After epoxying the bundle the resin is allowed to harden for one week. Sectioning of the bundle is done by a saw with a diamond blade approximately 3 mm thick

and with an OD of 500 mm. The elevations of the cross sections are listed in [Table 17](#). [Figs. 48-53](#) present an overview of the QUENCH-12 cross sections available. They are described and interpreted in the subsequent sections.

6.5 Metallographic Examination

6.5.1 Investigation Procedures

The post-test examination of the bundle is based on the metallographic preparation of cross section slabs (top and bottom sides) by careful grinding and polishing, the visual inspection, and a comprehensive photo documentation of the top levels. The evaluation uses a selection of the available macrographs and micrographs for illustration within composed, thematic figures. The final bundle state is described, and an interpretation is given, as far as possible, of its behavior with respect to different aspects: The mechanisms of the physical-chemical interaction of the components and of their oxidation are deduced, paying special attention to the cladding oxidation and to consequences of the rising water level and the increasing evaporation during the final phase. The bundle is described from bottom to top, following the increase in extent of interactions with increasing temperature.

For the bundle itself, the scale thickness on the surfaces of the simulator rods and the corner rods (A, C, and E) as well as the inner and outer shroud surfaces was measured. This was done, if possible, in four directions around rods and shroud, and for all prepared cross sections. The results are described and illustrated in lateral scale thickness profiles and in axial profiles, given for the different components. The thickness of eventual sub-layers was separately tabulated (see [Tables 18-21](#)).

The oxidation of the withdrawn corner rods is addressed separately from the bundle. As already mentioned, corner rod B was withdrawn from the bundle after the QUENCH-12 pre-test for non-destructive oxide scale thickness measurement, re-inserted for the main test into the bundle, from which it was removed after the end of the experiment. Corner rod D was withdrawn from the bundle at the end of the pre-oxidation phase, corner rod F before the quench phase.

The quantitative results of the bundle oxidation are based on a comprehensive measurement scheme, comprising all rods, the remaining corner rods (A, C, and E), and the shroud. The oxide layer thickness and A_t at the top elevation of all cuts (levels 550, 650, 750, 850, 950, 1050 and 1150 mm) of the rods was determined at the four azimuthal orientations;. In addition, the thickness of the α -Zr(O) layer was determined at the same positions, wherever possible. At the microscope and in bright-field illumination this layer gives a hardly sufficient contrast against the prior β -Zr matrix. In cross polarization the image is too faint to allow the direct visual evaluation; respective micrograph photos reveal the microstructure by color contrast, but some α -Zr(O) grains continue beyond the layer boundary, which is defined by the oxygen diffusion profile. For those reasons some α -Zr(O) layer thickness results may be less reliable compared to oxide scale thickness data, which on the other hand are subject of eventual oxide loss errors. This is why control measurements of the thickness of the remaining metallic part were systematically performed. Those results with the inferior absolute precision of ca. 10 μm were used to calculate the β -Zr matrix by subtracting the α -Zr(O) result.

6.5.2 Documentation and Interpretation of the Bundle Status

Cross section slab QUE-12-01, bundle elevations 534 (bottom) and 550 mm (top)

Overviews of top and bottom side of the cross section slab are depicted in [Fig. 54](#). The macrograph of the bottom side (right) is shown mirror inverted for easier comparison with the top side, so that both cuts are seen in top view to south direction. (In the same way all overviews of the following elevations will be illustrated.) The cut at bottom elevation includes the spacer grid, providing the maintained rod arrangement, which consists of the instrumented central rod, the inner ring of six heated rods, the next ring of twelve unheated rods, the outer ring of twelve heated rods, and the corner rods A, C, and E. A few rubble fragments can be distinguished, in contrast to the top elevation, in which very much fragments are present, obviously collected on top of the spacer grid. The relocated rubble consists of partial cladding scale shells and fragments of partially oxidized cladding.

The details given in the following figures refer to the top elevation 550 mm. [Fig. 55](#) illustrates the cladding oxidation of the central rod in S direction and different magnifications. Accordingly, an earlier grown partial layer of the scale tends to spall from a thicker next one which is found split from the α -Zr(O) layer. By polarized light (top/right, compare to top/left) the contrast between the fine grained α -Zr(O) layer and the matrix of prior β -Zr phase is improved. [Fig. 56](#) shows the quite similar cladding oxidation state of rod 5. It is mentioned that an internally cracked scale layer is depicted brighter than a compact one due to diffusive light scattering, a valuable information in addition to that from bright-field illumination. [Fig. 57](#) depicts the oxidation state of rod 19, as example of the ring of unheated rods. The scale is thinner and not split into partial layers, compared to the previous figures; a lower temperature can explain the difference. [Fig. 58](#) deals with debris between rods 17 and 18, obviously relocated cladding pieces which are double-sided oxidized. The scales are thick and compact, the metallic matrix is α -Zr(O), many through-wall cracks are visible. A thin partial oxide layer remained only at a part of the surfaces of the bulk oxide. The oxidation state of corner rod A, illustrated in [Fig. 59](#) refers to W and N orientation, the assumed relatively hotter sides. An outer layer of scale fragments is detached from the α -Zr(O) layer, which supports only pieces of a thin additional oxide shell. According to [Fig. 60](#), the typical oxidation products of corner rod C in S and N orientation are fragments of scale, completely detached from the α -Zr(O) layer. For corner rod E it was not possible to correlate such scale fragments to their original surface position. Two micrographs concerning the oxidation of the shroud will be shown together with others from the next bundle elevation.

In total, the oxidation extent indicates some lateral temperature profile across the bundle, but the aspects of scale formation are common: The breakaway effect has given rise to the growth of layered partial scale, tending to spall in form of fragments from the α -Zr(O) layer. At the given elevation the temperature rise during the transient test phase was not sufficient to leave the breakaway regime later on.

Cross section slab QUE-12-03, bundle elevations 634 (bottom) and 650 mm (top)

The overviews are depicted in [Fig. 61](#) with the same conventions as described for the lower level. Considerable lateral rod movements due to rod bowing have distorted the arrangement and allowed several rod to rod contacts without noticeable consequences. By chance, a

relocated spacer grid fragment is kept at bottom level, but no other rubble is registered. The loss of the pellet of rod 18 is a preparation artifact.

The oxidation state is documented, starting with the central rod cladding in [Fig. 62](#). At the depicted N orientation the cladding cross section shows the typical thick scale. Especially the micrograph series in polarized light allows to distinguish details of the scale growth morphology: One or more thin top layers are lost by spalling from most surface positions. The next layer is compact and adherent, but according to its brightness it has to be interpreted as internally cracked post-transition scale. The inner and main part of the scale shows columnar crystallite growth, typical for the formation at high temperature above the breakaway regime. The growth of regular scale during the transient test phase starting from a pre-existing defective scale is a remarkable observation, and an important safety aspect. [Fig. 63](#) illustrates the very similar oxidation of rod 4, as example for the inner ring of heated rods. Again, top layer(s) spalling, adherence of a defective intermediate layer, and presence of a bulk oxide with columnar microstructure can be registered. In polarized light contrast the α -Zr(O) layer shows a coarse inner part below the fine grained outer part, which could be formed due to the presence of the more protective columnar oxide. Gradual differences are seen for rod 18 in [Fig. 64](#) as example for the ring of unheated rods. Here we observe stronger degradation tendencies of the post-transition scale and find a thinner partial layer of columnar scale.

According to the micrographs selected for [Fig. 65](#), corner rod A reveals a similar oxidation history: A more defective outer rim of the scale can be distinguished from an inner, intact part. Top layer(s) loss is not visible but it cannot be excluded. The N position of this corner rod, depicted by the two micrographs at bottom, includes the contour of the adjacent rod 10, which presents thicker and more defective scale. Corner rod C, presented in S and W orientation by [Fig. 66](#), shows splitting of layered oxide and also degradation tendencies of the α -Zr(O) layer. Corner rod E, depicted in [Fig. 67](#), shows mainly the fracturing and spalling of an outer oxide layer, whereas adherent residues of thin inner oxide can be detected. The series of illustrations shall be closed by [Fig. 68](#), the presentation of shroud scale in comparison with the 550 mm elevation. At both levels compact and intact scale and a fine-grained α -Zr(O) layer are registered.

Cross section slab QUE-12-05, bundle elevations 734 (bottom) and 750 mm (top)

The overview of the bundle, given in [Fig. 69](#) seems very similar to the previous level. No rubble is present, except a large spacer grid fragment, kept within the distorted arrangement of bowed rods.

[Fig. 70](#) shows that the central rod cladding was oxidized during (at least) two post-transition cycles after which the breakaway regime limit was left during the temperature increase of the transient experiment phase. After the more detailed description of similar observations at the previously considered bundle level 650 mm, this short interpretation of the oxidation history seems sufficient here, because the micrographs, especially those taken under polarized light are convincing enough. The growth of a very regular scale with columnar structure despite the local variation in the previous scale growth morphology is remarkable. [Fig. 71](#) compares the two rods 2 and 7 of the inner ring. The cladding oxidation state is similar for both; rod 7 shows a splitting tendency of the outer layer, which is not to be seen for rod 2. [Fig. 72](#) gives

another comparison between rods of a group, the unheated rods 10 and 17. Again the polarization effect helps to distinguish the more defective outer part of the scale from the intact inner one. It should be taken into account that preparation artifacts may have contributed somewhat to the final picture of partial scale degradation. In [Fig. 73](#) the two heated rods 24 and 30 of the outer ring are presented, which show comparable oxidation aspects. Most probably, a top oxide layer of rod 30 got lost from the depicted position.

The oxidation of corner rod A in S and E orientation is compared in [Fig. 74](#). The separation tendency of an outer scale layer from the younger oxide is registered for both rods. It is mentioned that such a partial layer is missed at the orientations N and W, which show comparable oxide fine structure, namely the layered sequence of older oxide on the columnar younger scale. For corner rod C the orientations W and E are compared in [Fig. 75](#). At west a fractured outer layer, an adherent intermediate layer and a columnar inner part can be distinguished, at east the anticipated top layer is lost and the intermediate layer is fractured. Corner rod E indicates a more variable behavior: As depicted in [Fig. 76](#), compact scale and regions with cracking into sub-layers prevail towards W. For the same rod [Fig. 77](#) shows several external partial layers of spalled oxide on the compact inner part of columnar scale, typically observed towards E. The number and thickness of the individual shells varies with the position. It is known from several breakaway studies that more localized forms of scale degradation may lead to thick lenses of multiply cracked oxide. At those positions the fast scale growth is accompanied by the thinning of the α -Zr(O) layer. Unfortunately this item cannot be used here, because the oxidation has continued during the experiment above the temperature limit of the breakaway regime. It is only clear that the pre-oxidation during the respective number of post-transition cycles is the reason for the breakaway-related morphology of the outer part of the scale. The sound inner part is quite comparable to the other rods, as reported above.

Cross section slab QUE-12-07, bundle elevations 834 (bottom) and 850 mm (top)

According to the overview, the bundle has experienced more important degradation at the elevation range depicted in [Fig. 78](#). At both levels the central rod is completely missing. At 834 mm, the lower side of the slab, all surrounding rods except rod 25 still show their cladding. At 850 mm three rods of the first ring (rods 3, 4, and 5) do not show any cladding residues. Concerning the second ring, rod 12 is seen to end within the translucent epoxy resin below and is missing at the 850 mm level, the pellet of rod 13 is present without any cladding residues, and the claddings of rods 10 and 14 are only partly present. In the outer ring no cladding residues of rods 21 to 24 are present. The stub of corner rod A ends below the 850 mm level and only its thermocouple is cut at this cross section. A lump of melt is cut at 850 mm in contact to rod 25, which does not reach down to the 834 mm level, but nevertheless this melt accumulation could have contributed to the cladding loss of rod 25 observed there. Obviously, the slab elevation range demonstrates both, the limit of serious fragmentation and that of melt accumulation.

In [Fig. 79](#) a choice of rods from the SE quarter of the bundle is depicted. The cladding of rod 3 is completely lost, only a part for rod 10 is at place. Because no other reason is obvious, those losses should be due to fragmentation and fragments relocation. The rod oxidation is described in three following figures. [Fig. 80](#) refers to rod 7. The two pairs of micrographs in bright field and polarization depict the massive scale (top) and the α -Zr(O)

layer (bottom) respectively. In bright field (top/left) the decoration of the grain columns of the inner part of the scale indicate a peak temperature above 1900 K; the polarization contrast (top/right) reveals the partial layers of the scale, which does not show a splitting tendency. The color contrast in polarization allows to detect the coarse grains of the α -Zr(O) layer, which grew inward beyond the limit of the oxygen-rich zone, for which some fractures can serve as indicators. [Fig. 81](#) shows for rod 15 a pair of micrographs of the oxide morphology (top) and one of the prior β -Zr matrix at the inner cladding rim. The oxide is similar to that of rod 7. (The irregular bright contrast above the regular oxide can be neglected because in this case it seems to result from rubble collection within a gap to the epoxy.) [Fig. 82](#) presents the cladding oxidation of rod 30, showing details of the oxide scale and the prior β -Zr matrix microstructure at the inner cladding rim. All three rods have shown consistent oxidation results.

The presence of a melt lump in contact to rod 25 is covered in the next two figures. [Fig. 83](#) is to inform about position and microstructure of this melt. The contact position at N of rod 25 supports the interpretation, that the melt should be a product of the meltdown of corner rod C, which could have provided sufficient mass of melt. However, the corner rod (massive at the given elevation and above) would be able to release melt with low oxygen content. The observed lump shows a duplex microstructure with distributed ZrO_2 precipitates, indicating considerable oxygen content. As illustrated in [Fig. 84](#) the melt is covered by an oxide scale which must have grown at place. According to the junction edge (top/left) scale has grown mainly at the free, steam exposed melt surface, but also at the contact to the embedded scale on the cladding of rod 25, which shows a thinning due to isolation from steam contact. The three other micrographs show the oxide morphology towards north. In total it is plausible to expect considerable oxygen enrichment of the melt bulk during such strong melt oxidation.

An impression of the oxidation of corner rod C in four directions shall be given in [Fig. 85](#) for which polarization contrast alone is sufficient. Common for all orientations is the contribution of scale growth, both within the breakaway regime and at high temperature, to the total scale (outer and inner part, respectively, as already described). The polarization contrast allows to distinguish the brighter, more defective outer from the darker inner part of the scales. At east orientation, assumed to have been the hottest side, the outer oxide part appears to reveal re-crystallized grains in contrast to all other positions, showing layered structure. For corner rod E [Fig. 86](#) uses micrographs in smaller magnification and confirms the distinction between the both oxide categories. The thickness of the inner part of the scale shows much more local variation for rod E than observed for rod C. It is clear that such growth variations must be the consequence of a variation of the protective properties of the pre-existing scale, which shows large local scatter in its thickness. Moreover, some non-detectable scale loss could have played a role. Unfortunately, no sufficiently complete interpretation can be given apart from those arguments.

The oxidation state of the shroud at its inner side is illustrated in [Fig. 87](#) (top) in comparison to the elevation 750 mm (bottom). At both elevations the scale is composed of a layered outer part and a columnar grown inner part, as described for the rods. At the higher level the scales are much thicker, the simple consequence of the higher temperature range.

Cross section slab QUE-12-09, bundle elevations 934 (bottom) and 950 mm (top)

The two overviews alone, depicted in [Fig. 88](#), give a quite informative impression of the bundle degradation state. On the one hand the cladding oxidation and the cladding brittleness are much more advanced than at the previously discussed level. When the melting temperature range of the cladding alloy matrix was exceeded, considerable chemical interaction between cladding and simulator pellets has set in, and the internal oxidation due to the resulting oxygen transfer from pellet to cladding has contributed to an improved structural stability of the rods. Indeed, the central rod is present in contrast to the lower level, and most of the cladding of the surrounding rods has remained as well. Moreover, most of the rods cannot be discussed individually, but have to be realized as members of a rod group, giving additional stability to the members. The groups came into contact by rod bending, neck formation along vertical contact lines, dissolution of embedded scale, and formation of common melt pools (so called necking mechanism). Lateral and axial melt re-distribution within rod groups is obvious at several positions, and will be demonstrated in more detail. In comparison of top and bottom elevation, the lower one seems to have the smaller net melt relocation loss (see e.g. the rod groups at NW and NE, and the shroud bulge towards NW). The state of the shroud remnants can be interpreted by mentioning the partial oxidation of the thick structure beginning from the inner side, shroud matrix melting, melt re-distribution leading to circumferential splitting, bulging, void and pocket formation. Neck formation between rods and parts of the inner shroud structure took place as well. Corner rod A is tentatively interpreted to be visible as relocated melt filled massive structure, denominated as rod X, typical for the rim position but non-typical for the elevation, and also as hollow remnant in contact with rods 9 and 10. Corner rods C and E can be identified at W and NE, respectively, according to the form of the ceramic remnants.

The more detailed bundle inspection is initiated with four illustrations for rod groups. [Fig. 89](#) shows a group towards south. The depicted rods including corner rod A are seen to be connected by contours of common scale, the residues of a melt pool after the loss of most of the melt: Rod A shows melt towards south, stabilized by an inner scale, which was formed after steam ingress. Some metallic melt remains at rods 9, 10, and 11, whereas most of the cladding of rod 3 and of the central rod is fully oxidized. The rounded shape of voids indicates loss of melt by downward relocation. Residual melt between rod 10 and the central rod contains embedded cladding scale. A very similar description can be given for the group of rods depicted in [Fig. 90](#). Here towards north, the rods 18 and 17 are fused together with corner rod E, and rod 29. The separate rod 28 indicates a previously formed junction to the shroud and the resulting penetration and loss of melt through the opening of the scale. [Fig. 91](#) shows towards west rods 13 and 25 (top) together with 14 and 26 (bottom) as well as the corner rod C. All residual cladding is completely oxidized, the former melt pool empty. At east in the bundle and according to [Fig. 92](#), released metallic melt, enclosed by rods 8, 31, and 19, is captured within the triangular space between the claddings (see at top/right). As seen in detail in [Fig. 93](#) for rod 8, the embedded scale segments have been thinned by oxygen transfer to the melt from outer and inner side. Towards north rod 8 indicates partial dissolution of the melt-covered external scale (bottom), and internal cladding melt oxidation in contact with the pellet (top/right).

The following figure concerning rod 8, member of the previously described group, leads over to the oxidation state at steam exposed surfaces. [Fig. 94](#) illustrates the external scale

(top/right) and the internal interaction of the cladding melt with the pellet (bottom). The interaction layer is found converted to the ceramic state. Rod 7 is illustrated as another example in [Fig. 95](#). The region towards south indicates previous local downward relocation of melt, and the contour of the void indicates the contribution of internal oxidation to the complete conversion of the remaining cladding material.

The oxidation state of corner rod A towards south is described with [Fig. 96](#). Accordingly, the outer part of the scale shows the coarse microstructure of high-temperature oxide (top/right), the following part seems to be disturbed, eventually due to interrupted presence of metallic melt (bottom/right), and the internal scale (bottom/left) indicates the access of steam into the split tube remnant. In comparison, rod X, interpreted according to its position as a relocated stub of the same rod A, shows a rather strange scale microstructure, which has to be explained by its history at changed elevation: As shown in [Fig. 97](#), the outermost part is a double layer of coarse grained oxide (top/right), next follows a series of partial layers of breakaway type (left, not depicted in more detail), and finally an again compact and protective oxide with variable layer thickness, formed at high temperature (bottom/right). Such composed oxide as depicted was found at the whole circumference of the rod according to archived photos. [Fig. 98](#) describes rod C towards west as fully oxidized tube, for which the external scale can be distinguished from the remnants of internal scale which was formed when metallic melt at the inner side came into contact with steam. It is mentioned without presenting an illustration that remnants of corner rod E are rather similar and fully oxidized as well.

The state of the shroud is documented in [Fig. 99](#) on basis of various macrographs from different sides. One has to keep in mind that partial melting of the shroud has allowed the splitting of an innermost scale from the molten part which oxidized further under formation of an additional partial scale. After the shroud rupture some steam was available at the outer surface as well, and this external oxidation formed a kind of crucible wall, stabilizing the melt. More detailed illustrations of two positions in south direction are given. [Fig. 100](#) depicts for one of them the inner part of the shroud at the boundary between metallic core and inner scale (bottom/left) together with the outer part, shown to have metallic/ceramic duplex microstructure (right). The other example in [Fig. 101](#) shows (top) the duplex metallic/ceramic microstructure towards the outer side of the shroud remnant in comparison with the ceramic inner part (bottom). The scale growth from the inner side has converted here the previously molten zone, indicated by the round-shaped voids from melt relocation. In the previous figure this zone has been shown to be thicker and not yet oxidized.

Cross section slab QUE-12-12, bundle elevation 1050 mm (top)

The heated rods at this elevation and above do not contain pellets because Mo electrodes are installed there. Five pictures ([Fig. 102-106](#)) show characteristic groups of rod simulators with corresponding temperature profiles. The temperatures during preoxidation phase were between 1300 and 1400 K, which corresponded to values above breakaway oxidation. The temperatures inside the unheated rods (TFC) were about 100 K higher than temperatures (TFS) at the rod surface ([Fig. 104](#), rod 12). The melting point of metallic Zircaloy was reached on the end of transient. All rod simulators evidenced melting of the residual cladding metal. This melt was partially relocated to the lower elevations. The accompanied local dissolution of external oxide layer is observed for few rod simulators. Also a local dissolution

of protective ZrO_2 layer on the surface of the Mo-electrodes was indicated. In spite of this no visible injury of electrodes was observed. A relatively thick internal oxide layer was formed by interaction of the melt with the pellet (Fig. 107). The structure of the oxide layer on the surface of massive corner rods evidenced intensive breakaway oxidation (Fig. 108). Such oxide structure was not observed on the surface of cladding tubes.

Cross section slab QUE-12-11, bundle elevation 1150 mm (top)

The rod simulators of the next elevation with the Mo electrodes inside heated rods are depicted in Fig. 109-113. The maximal temperature by this elevation was about 1700 K, i.e. the melting point of metallic Zircaloy was not reached. The protective ZrO_2 layer on the surface of the Mo electrodes remained intact. The surface thermocouples showed that the typical cladding temperatures during the pre-oxidation phase were between 1100 and 1250 K. It corresponds to the breakaway conditions. Indeed the cladding tube oxide layer evidenced a spalling of external thin scales (Fig. 114). Much more intensive oxide scales spalling was observed on the surface of massive corner rods (Fig. 115).

6.5.3 Oxidation of the Withdrawn Corner Rods

The oxidation state of the corner rods is described on basis of cuts at certain elevations, differing from the levels of the bundle cuts. A separate treatment including rod B for comparison should allow to identify eventual qualitative differences from the bundle behavior. Such deviations cannot be excluded because the corner rod fabrication could have exerted some influence on the oxidation under breakaway conditions even for identical composition as the fuel rod simulator cladding.

Fig. 116 shows the local variation of the oxidation of corner rod D at the end of the pre-oxidation test phase for the given elevation 700 mm. Whereas at some positions a compact and adherent scale is found, the rod shows at other positions the development of a few or several partial layers, split from each other but mostly remaining in loose local contact. The outermost partial layer or layers may have become lost as relocated fragments. The innermost partial layer shows the respective tendency of splitting away from the α -Zr(O) substrate layer. All those aspects of breakaway typical scale degradation are well known as well as the local variation in the progress of the effect. In the given case some temperature differences will have contributed to a larger variation range compared to more idealized conditions of separate effect tests on which the given interpretation is based. Fig. 117 illustrates the oxidation state of corner rod D at the 940 mm level. Compared to the previous level the temperature and the heating rate were higher. The breakaway regime has been almost avoided with the exposure conditions, the localized degradation features seem to indicate some surface defects or material weakness as trigger. Locally a thick compact scale has grown, whereas at other positions degradations occurred as rather early or later events (see right and bottom/left, respectively). In Fig. 118 breakaway specific layered oxide is obvious again for the 1120 mm level. The sequence of partial layers was formed by periodic cracking and thus scale growth stress relief, followed by growth of next partial layers until the critical failure stress level. Locally enhanced scale growth accompanied by thinner and more numerous partial layers is observed within lens-shaped oxide pustules. The moderate temperature at this elevation during the pre-oxidation phase is the reason for the breakaway typical scale growth morphology.

The following three figures are showing the oxidation state of corner rod F, representative for the pre-oxidized and heated condition before quenching. [Fig. 119](#) indicates the inhomogeneous oxidation at the 700 mm level, at which the breakaway transition did not yet occur everywhere around the rod circumference (top/left) compared to the post-transition morphology at other positions (bottom/left, and right). The transient test period has not given rise to separately detectable extra oxidation because the peak temperature was moderate. [Fig. 120](#), illustrating the 940 mm level, indicates the history of the outer and inner part of the scale: The outer part shows breakaway related degradation features which are more coarse than those in the previous figure due to the higher temperature during the pre-oxidation phase of the test. The innermost part of the scale indicates the presence of cubic oxide formed above 1800 K during the period near peak temperature. (This unstable cubic oxide modification re-transforms to the tetragonal form under precipitation of α -Zr(O) phase, decorating the elongated zirconia crystallites.) Finally [Fig. 121](#) describes the 1120 mm level for corner rod F. At this elevation above the upper end of the heated bundle zone the temperature level remained moderate enough to keep the rod within the breakaway regime. During the transient no temperature escalation took place and consequently cubic oxide is absent.

The presence of sound oxide grown at high temperature at the elevations 820 and 940 mm below defective post-transition oxide is again stressed. With this observation it is proved that the breakaway related degradation of the scale cannot be seen like a disease or contamination. Instead, the material can leave the breakaway regime (in the present case by a temperature increase beyond the upper temperature limit of ca. 1350 K) and this will terminate the growth of defective scale. A certain “recovery” growth period might be necessary to establish the “fresh skin” at the whole surface. Results on such details seem to be not available up to now.

For comparison [Fig. 122](#) illustrates the oxidation of corner rod B at the 700 mm level. At this elevation the oxidation during the transient phase including the test termination by quenching was too weak to be obvious in the final state, which is characterized by breakaway related scale growth and degradation with considerable local variation. [Fig. 123](#) depicts the 820 mm elevation, for which some breakaway related scale de-lamination is seen in the outer (older) part of the oxide at some positions (right), whereas sound oxide has grown everywhere else. Since the above described description of the removed corner rods did not reveal strange behavior compared to that of the bundle no additional elevations of corner rod B are described and documented.

[Fig. 124](#) gives an overview of investigated cross sections of the withdrawn corner rods.

6.5.4 Lateral and Axial Distribution of ZrO₂ Scale and α -Zr(O) Layer Thickness

Measurements of layer thicknesses formed at each elevation are made in four points of each simulator cladding with an azimuth interval of 90°. Results of measurements are summarized in [Table 20](#) (for lower bundle elevations) and [Table 21](#) (for upper bundle elevations).

Figures [Fig. 125](#) to [Fig. 131](#) illustrate the results of the oxide scale and α -Zr(O) layer thickness measurements for the respective bundle elevations and give the lateral distribution profiles. [Fig. 125](#) indicates a scatter in the data and some temperature related lateral profile

at the 550 mm level. Heated and unheated rods do not differ systematically. Breakaway related splitting of the scale into sub-layers has occurred mainly in the centre of the bundle at moderate oxidation extent. At the 650 mm level more than 50 μm oxide and more than 100 μm $\alpha\text{-Zr(O)}$ are measured according to [Fig. 126](#). At the increased oxidation level the relative scatter and the lateral profile are similar. Splitting into scale sub-layers and spalling of those took place on rods within the whole cross section. [Fig. 127](#) summarizes the effect of the higher temperature level at 750 mm elevation after the pre-oxidation test phase. The $\alpha\text{-Zr(O)}$ layer thickness values have increased less compared to the scale thickness values, which are close to the 100 μm order of magnitude. [Fig. 128](#) illustrates the strong bundle fragmentation at the 850 mm level by the partial or total loss of pellets or cladding of several rods. Question marks indicate the positions where the $\alpha\text{-Zr(O)}$ layer could not be distinguished from eventually remaining $\beta\text{-Zr}$ matrix, which has a quite similar microstructure in the given oxygen enriched condition. Due to the brittleness of the $\beta\text{-Zr}$ phase in the given state it was not reliable to use the presence of through-wall cracks or broken crystallites as indicators. According to [Fig. 129](#) the situation at 950 mm is again more simple, because no $\beta\text{-Zr}$ matrix remains from rod cladding, which is mostly converted to oxide and residual $\alpha\text{-Zr(O)}$. The schematic distribution of melt does not consider later melt losses and retention of ceramic residues of melt oxidation. No quantitative data on the oxidation of the melts are given, because such results would be hardly helpful: A kinetic evaluation would require melt residence period and temperature, oblique cuts through such small pools would lead to errors in scale thickness determination. [Fig. 130](#) shows intensive oxidation at elevation 1050 mm. The oxide layer thickness of corner rods could not be measured because intensive oxide scales spalling. [Fig. 131](#) illustrates the moderate extent of bundle oxidation at the 1150 mm level, and thus 126 mm above the heated zone. The large oxide scale thickness measured for corner rod C and most positions of E cannot be interpreted. Only an upward rod movement of those corner rods as artifact of the preparation of the cut could explain the deviation from the main bundle, otherwise an influence of the manufacturing procedure of those corner rods could eventually be the reason as well.

The determined axial oxidation profile, as given in [Fig. 132](#), is based on the separate results of oxide scale and $\alpha\text{-Zr(O)}$ layer thickness measurements for simulator rods, corner rods, and shroud inner side, and includes the deviation range for the simulator rods. Accordingly, the extent of oxidation is rising steeply from small to moderate values for the lower levels to complete cladding oxidation, reached for most of the rods at 950 mm, and is decreasing above. The profile of the residual $\beta\text{-Zr}$, given for comparison, shows the consistent inverted trend with a minimum at 950 mm.

Tabulated oxide layer thickness results for the corner rods B, D, and F are available in [Table 18](#). In addition, the results of the thickness measurement of the individual sub-layers of scales are also given in this table. Those data refer to the post-transition scale growth, so that available information on the breakaway mechanisms may be helpful for the interpretation and discussion.

The main body of information on the breakaway phenomenon has been gained for Zircaloy-4, and the simple application of this experience to Zr-1Nb is not possible. But it is also known that different alloy families and even pure zirconium have many similarities in their qualitative breakaway behavior. In morphological and kinetic studies on the oxidation of Zry-4 in steam at 600 °C and above [16] “breakaway oxidation” was distinguished from

“normal oxidation”. The breakaway related anomalies are initiated in a period of scale growth retardation, during which the α -Zr(O) layers are able to grow to anomalous thickness. At the phase transition point stress relief is gained for the compound by formation of a system of lateral cracks along the interface. A first scale sub-layer of critical thickness loses the contact to the substrate almost totally. During the post-transition period scale growth continues fast under periodic formation of new sub-layers [17]. With some scatter their thickness is usually comparable to or smaller than the critical layer thickness at the transition point. The sub-scales may keep loose contact, but even then the resulting oxygen permeability is higher than that of compact, sound oxide. This is why the α -Zr(O) layers are consumed to thin residual ones. In total, the thickness relation between oxide and α -Zr(O) can give a clear indication of the actual position within the breakaway regime, the pre-transition or the post-transition range.

The critical scale thickness reached at the transition point can give some indication of the oxidation temperature, because it is temperature dependent. For Zry-4 the critical scale thickness increases with increasing temperature from a few microns for reactor operating temperatures to the order of 100 μm for ca. 1350 K, the upper breakaway regime limit [16 - 19]. Whereas the scale is able to indicate much about the oxidation history like a document, the α -Zr(O) layer changes its character dynamically according to the temporal condition, because it is continuously consumed with the further oxide growth. This is why the thickness relation between oxide scale and α -Zr(O) layer cannot be evaluated in the case of temperature transient exposure history, and especially after leaving the breakaway regime during a respective experiment.

The determined thickness values of the oxide scale sub-layers in Table 18 give some hints on the temperature during the pre-oxidation phase of the QUENCH-12 test, during which post-transition oxidation proceeded. Based on the experience with Zry-4 a critical scale thickness of typically 10 μm should be seen at a temperature level of ca. 1100 K and its variation within a factor of 2 and 0.5, respectively would compare to a variation range of about ± 100 K. Accordingly, the results in the table within [Fig. 133](#) given for the elevations 550, 650, and 750 mm and for the first and the following sub-layers correspond reasonably to the temperature levels and variation ranges recorded for the pre-oxidation phase of the test. At 550 mm the bundle should have remained within the breakaway regime during the whole test, at 650 mm up to most of the transient period, in accordance with the measured data. At the 750 mm level the breakaway regime was left in the transient test phase, indeed critical scales up to the 100 μm order are registered, and the oxidation has continued in the normal manner. The static information from the oxide scale morphology has remained available, but the continued inward growth of the α -Zr(O) layer has shaded the previous post-transition period during which this layer had been thin. This is why the information from the α -Zr(O) layer thickness measurements has turned out to be less informative than expected.

Table 18 gives additional information on areas of the metal part of withdrawn rods. The values were obtained with help of computer image analyses. They allow to estimate the original oxide layer thicknesses before the decrease due to spalling and a subsequent removal of spalled oxide scales during rod withdrawal and handling. The results of this estimation together with estimated thicknesses of the spalled oxide scales are presented in [Table 19](#). This table also contains a comparison of the results of the opposite cross sections of the withdrawn corner rods gained by RIAR with the same method of image analysis (see

section 6.7.3). The deviations between both results could be explained by two facts: On the one hand the method has a limitation in resolution by choice of the phase boundary. On the other hand the breakaway oxidation is substantially of a stochastic nature, and neighboring axial regions can be significantly different.

6.5.5 Analysis of the Spalled Fraction of the Oxide Scales

As already mentioned, a large amount of oxide flakes was found on the spacer grid at middle bundle elevation. In order to take into account such losses of scale for the original elevations 550, 650, 750, and 850 mm, an evaluation of thickness measurement results for the simulator rods (Fig. 133) was performed. A calculated average oxide layer thickness for the respective elevations was gained as follows: Subtraction of the measured average remaining metal thickness value from the original tube wall thickness, nominally 700 μm , gives the consumed metal thickness. Multiplication of this by the Pilling-Bedworth factor 1.56 gives the corresponding calculated oxide layer thickness, used as basis for quantification of the lost partial scale thickness in addition to the measured remaining scale. The relative fractions of spalled plus relocated scale partial shells are presented in Fig. 133. The obtained fractions of spalled oxide are large and the increase with decreasing bundle elevation and thus temperature is pronounced. The corresponding comparison of the calculated initial oxide layer thickness with the thickness of the residual oxide layers is given in [Fig. 134](#).

This result is well confirmed: Reasonable assumptions on deviations from the nominal tube wall thickness have a small influence on the absolute values and do not change the trend for the different elevations. The results have not been corrected for the partial oxygen transfer from oxide to substrate, because this contribution is especially small within the post-transition regime. The temperature dependence of the spalling fraction seems to reflect the temperature dependence of the “critical” thickness of partial scale layers (for Zircaloy-4 a few microns at low temperatures, ca. 100 μm at the upper breakaway regime limit, ca. 1350 K). The large contribution of spalling was not anticipated. Considering this remarkable result means accepting the loss of the earliest formed part of the scales in the conventional post-test bundle evaluation.

6.6 Measurements of thicknesses of residual metal layers and comparison with QUENCH-06

The measurements of complete thicknesses of metal layers were performed by FZK and RIAR for all rod simulators for calculation of original oxide layer thicknesses. The measurements were performed at bundle elevations 550, 650, 750, 850, and 1150 mm. Corresponding results are presented on [Figs. 135-139](#) as bar diagrams. The elevation of 950 mm is not presented because the metal remnants were found here only in few positions (Fig. 129). Figs. 135-138 present comparison of the FZK results with the RIAR results on counterpart surfaces of four bundle cross-sections (the axial distance between these surfaces was 4 mm). One can see that the average metal layer thicknesses are in good agreement between the results evaluated at the two organizations. This holds also for the morphology of the radial thickness distribution.

On the basis of described measurements a calculation of original oxide layer thicknesses (using the Pilling-Bedworth factor – chapter 6.5.5) was performed. The calculated results

were compared with corresponding results for reference test QUENCH-06. Figs. 140-143 present this comparison for four elevations (550 mm, 750 mm, 850 mm and 1150 mm) together with corresponding temperature profiles for both bundle tests. Though the temperatures on almost each elevation were somewhat lower for QUENCH-12 in comparison to QUENCH-06, the oxide layers are significantly thicker for QUENCH-12 compared to QUENCH-06. This is due to the pronounced breakaway oxidation in QUENCH-12 (discussed in details in the chapter 6.5). The oxide layers are thinner for QUENCH-12 than for QUENCH-06 only at elevation 750 mm where the temperature during the transient was significantly higher for QUENCH-06 compared to QUENCH-12 (Fig. 30). At other elevations the oxide layers are significantly thicker for QUENCH-12 compared to QUENCH-06. This is due to a strongly pronounced breakaway oxidation in the QUENCH-12 bundle (discussed in section 6.5).

The comparison of the bar diagrams in Figs. 140-143 shows that the radial distribution of the oxide layer thicknesses was more inhomogeneous for the QUENCH-12 test bundle in comparison to QUENCH-06. This inhomogeneity can be seen even more clearly in Fig. 144 which presents the oxide layer thickness distribution across the QUENCH-12 bundle at three elevations. Fig. 145 gives the main reason for this phenomenon: the radial oxide layer profile correlates quite well with the temperature radial profile.

6.7 Results of Metallographic Posttest Examinations by RIAR

6.7.1 Introduction

Five samples (cross sections of the QUENCH-12 test bundle) were delivered to RIAR for posttest examinations to complement the posttest examinations of five samples that were investigated at FZK. The RIAR and FZK were selected in this way that the bottom ones were investigated at FZK, and the top ones at RIAR. The objective of the examination was to estimate the state of oxidation of the claddings, to reveal possible heterogeneity of the temperatures in the investigated bundle cross sections, and based on the obtained results to assess reliability of the on-line thermocouple readings and the measured integrated hydrogen release [20].

Oxidation of the claddings is estimated by the results of measured thickness of unoxidized claddings layer and the thickness of the formed zirconia and alpha zirconium layers, stabilized by oxygen, using a metallographic microscope.

The overall objective of this work is to present the results obtained on the samples investigated in RIAR and their comparison with the results obtained on similar FZK samples as well as revealing possible systematic discrepancies related to identification of the boundaries of the measured layers and differences in methodical approaches to the measurement techniques.

The samples examined (elevations 554 mm, 654 mm, 754 mm, 854 mm, and 954 mm) are pictured in Figs. 48 - 52.

6.7.2 Examination of the Cross Sections

Section 554 mm

In section 554 mm the bundle is not deformed. The outer surface of the simulator claddings is uniformly oxidized and obviously there is a spalling effect in the oxides formed on the cladding surface. This effect is typical of alloy E110 at temperatures of 950-1050 °C (temperatures during the test are measured by TCs attached to the cladding outer surface). In the space between the simulators the fragments of oxide scales and oxidized claddings from the upper sections are observed.

Measurements of thickness of the layers formed in this section are made in four points of each simulator cladding with an azimuth pitch of 90°. Results of measurements are summarized in [Table 22](#). It is necessary to note, that oxide spalling at the cladding surface affect the investigated sections essentially in reducing reliability of the claddings oxidation estimation by the results of measurements of the thickness of formed ZrO₂ layer. In this case the cladding oxidation can be estimated by the results of measurement of the cladding thickness after the test. The diagrams (Fig. 135) show relative changes of the averaged residual thickness of the cladding metal part and thickness of α-Zr (O) layers. [Fig. 146](#) demonstrates typical structures of the fuel rod simulator claddings.

Section 654 mm

In section 654 mm the bundle is deformed. (The cladding temperature during pre-oxidation measured by TC was 1050-1150 °C). The outer surfaces of the simulator claddings are uniformly oxidized. In this cross section there are no fragments of the claddings in the space (coolant channel) between the simulators. Results of measurements of the oxide layer thickness in this section are summarized in [Table 20](#). [Fig. 136](#) and [Fig. 147](#) show the diagrams of the averaged thickness of the measured layers and typical structures of the claddings, respectively.

Section 754 mm

This cross section is not essentially different to the section 654 mm described above. The cladding surface temperature measured by TC during pre-oxidation in section 754 mm was 1100-1200 °C with a result of less spalling of the formed oxides. Results of the measured oxide layer thickness in this section are summarized in [Table 20](#) and in the diagram ([Fig. 137](#)). Typical cladding structures are shown in [Fig. 148](#).

Section 854 mm

The given section differs from the sections described above by essentially stronger simulator cladding oxidation. The temperature measured by TC located on the claddings during pre-oxidation was about 1250-1350 °C. Melt drops are observed in the gap between the simulators. The maximum temperature measured in this section before quenching amounted to 1900 °C that is close to the melting temperature of the α-Zr (O) phase (1970 °C). However, no melt is observed in this section. The simulator claddings have through-wall cracks. Part of the claddings failed completely and crumbled. Two simulators without a tungsten rod in the

centre of the pellets (unheated rods) are destroyed in this section. It is necessary to note, that the surfaces of the cracks in the simulator claddings are not oxidized, which is proof that their damage occurred during the reflood phase. Absence of the crack surface oxidation also points at the fact that the process of their damage does not make an essential contribution to hydrogen production during the reflood. Results of examinations of this section are summarized in Table 20 and Fig. 138 and [Fig. 149](#).

Section 954 mm

In this section we observed melting and full oxidation of the simulator claddings ([Fig. 150](#)). The measured claddings temperature during pre-oxidation was 1300-1450 °C. The maximum temperature before quenching was about 2000 °C. The bundle shroud melted as well.

Due to complete oxidation of the claddings in this section, their essential deformation and complete loss of a number of simulators, quantitative measurements were not done. The structure of the formed melt is shown in [Fig. 151](#).

By the examination of five sections it is possible to conclude that the most reasonable way to assess the amount of cladding oxidation is the one based on the residual metal layer thickness. In the lower sections (554 and 654 mm) was observed a non-uniform oxidation which is apparently caused by a radial thermal gradient in the direction of 180°. The cladding oxidation is more uniform across the 754 mm section, a thermal gradient may also be observed in the direction of 180°. Section 854 mm exhibits essential non-uniformity of the cladding oxidation presumably owing to a strong radial thermal gradient in the direction of 315°. [Fig. 152](#) demonstrates for all the examined sections the thickness of the residual metal part of the cladding. [Fig. 153](#) shows a diagram of the α -Zr(O) layer thickness in the investigated sections that exhibits similar periodicity of thickness changes in the sections. However, it should be noted that the reliability of these data is small because it is difficult to identify the layer boundaries and thorough transformation of the cladding metal to α -Zr (O) in the top sections.

6.7.3 Measurement of Oxidation of the Corner Rods Withdrawn

As is found at the corner simulator claddings, the effect of oxide scale spalling is distinctly observed on the withdrawn rods. Therefore the results of ZrO₂ layer thickness measurements cannot be used to assess the amount of oxidation. To compare the oxidation of the withdrawn rods, residual metal parts of the rods were measured. The area of the metal part of the rods at the investigated elevations was measured with help of the pictures of the cross-sections made with a 12x magnification using a method of the quantitative image analysis. The diameter of an equi-dimensional circle was calculated by the results of measurements. Difference in the measured and initial (6 mm) rod diameters was taken as the extent of oxidation.

Photos of the sections examined are shown in [Fig. 154](#). [Table 23](#) contains the results of measurements and calculations.

6.7.4 Conclusions

1. Results of the posttest examination are in agreement with the results of the on-line temperature measurements.
2. The cross sections revealed essential non-uniform oxidation of the claddings that should be caused by significant radial thermal gradients during the test.
3. Observable cracks of the cladding are not oxidized testifying that the claddings are damaged at the stage of quenching and that this process has small influence on hydrogen generation at the end of the test.
4. Formation and essential oxidation of the cladding melt contributes to the observed increased generation of hydrogen.

6.8 Analysis of the Hydrogen Absorbed in the Corner Rods

Neutron radiography experiments provide the possibility of a fast, non-destructive and quantitative determination of the hydrogen content with a spatial resolution better than 50 μm . In [21] the experimental setup was optimized and the calibration of the dependence of macroscopic total neutron cross section on hydrogen content was given.

The method was applied to determine quantitatively the hydrogen absorbed in corner rods and cladding rod segments of the QUENCH-12 bundle. The measurements were performed at the cold neutron radiography facility ICON (SINQ, PSI, Switzerland) [22] with a camera length $L/d = 350$. L is the aperture to sample distance and d the aperture opening size.

The neutron radiographs were detected by a camera system, specially developed for neutron micro-tomography applications. It consists of an ultra-thin Gadox scintillator (thickness 10 μm), a lens without any optical distortions (diameter: 155 mm, height: 620 mm mass: 30 kg) and the high resolution 1:1 magnification CCD camera ANDOR DV436 (Peltier cooled, pixel size 13.5 μm , field of view: 28 mm x 28 mm, 2048 x 2048 pixels, 16 bit).

Additionally, the hydrogen content in corner rod and cladding segments of 10 and 20 mm length, respectively, were determined by hot extraction. The specimens were put in the "LAVA" furnace at room temperature. The furnace was evacuated and flushed by Ar. Then the specimens were heated up in flowing Ar until a temperature of 1773 K was reached. After annealing of 30 min at this temperature the specimens were cooled down to room temperature in the furnace. The hydrogen concentration in the off-gas was measured by the mass spectrometer "GAM300". The integration of the hydrogen flux over the annealing time gives the amount of hydrogen extracted from the specimen.

Fig. 155 compares the radiographs with the optical appearance of typical positions of corner rod D. Different grey levels in the neutron radiographs of the rod and different types of the macroscopic oxide appearance are visible.

The radiography data were analyzed with the "ImageJ" software package. The measurements were normalized with an open beam frame and corrected for dark current.

With an axial step size of 20 mm the intensity distribution of the position perpendicular to the rod axis was determined by integration over an axial width of 1 mm.

The normalized intensity distributions perpendicular to the rod axis are given for five axial positions in [Fig. 156](#). At the two edges of the regions behind the rod small increases of the intensities are visible. This increase is caused by Fraunhofer diffraction. In the region attenuated by the rods the intensity distribution can be described by the Eqs. (3) and (4). It is a hint that no radial gradients in the hydrogen distribution exist. The transmission T of the neutron beam behind the specimen is given by:

$$T = \frac{I - I_B}{I_o - I_B} = \exp(-\Sigma_{total} \cdot s) \quad (3)$$

I is the intensity behind the specimen, I_o the primary beam intensity, I_B the background intensity measured behind a Cd specimen with comparable dimension and s the path through the specimen. As hydrogen is added to the Zry-4, $\Sigma_{total, sample}$ can be given as:

$$\Sigma_{total, sample} = N_H \sigma_{total, H} + \Sigma_{total, Zry-4} \quad (4)$$

$\Sigma_{total, Zry-4}$ is the total macroscopic neutron cross section of the dehydrated Zry-4 specimen N_H the hydrogen atom number density and $\sigma_{total, H}$ the total microscopic cross section of hydrogen. For an illumination in radial direction the path length s through a rod shaped specimen is given by the complex equation:

$$s = \Re\left(\sqrt{d^2 - (x - x_0)^2}\right) \quad (5)$$

\Re is the real part of the complex term, x the actual radial position, x_0 the radial middle position of the specimen and d the rod diameter. For the analysis of the measurements in radial direction the intensity was averaged in z direction over a height of 10 mm. Due to this height the intensity fit at the sample edges is very sensitive for the sample alignment, whereas the middle ranges are not influenced strongly. Therefore for the analysis only the middle positions were used where:

$$s \approx d = 6 \text{ mm} \quad (6)$$

Since the total cross section of hydrogen-free E110 alloy is very close to the cross section of hydrogen-free Zry-4, the hydrogen atomic concentration c_H^m in at.% is given according to [21] by:

$$c_H^m = \frac{\frac{\Sigma_{total} - 0.21 \text{ cm}^{-1}}{2.90 \text{ cm}^{-1}}}{\frac{\Sigma_{total} - 0.21 \text{ cm}^{-1}}{2.90 \text{ cm}^{-1}} + 1} \quad (7)$$

[Fig. 157](#) gives the axial distribution of the hydrogen content in the three investigated corner rods determined by neutron radiography (NR) according to eq. (7) and by hot extraction

(HE). The values determined by HE are lower than the values determined by NR but show the same distribution in principle. [Fig. 158](#) gives the ratio of the values determined by hot extraction and the values determined by neutron radiography in dependence on the test number after inert annealing of the empty “LAVA” furnace. It shows that the hot-extraction data converge against the neutron radiography data. The reason of this effect is hydrogen adsorption at the furnace and pipe walls. The furnace walls were made from high-porosity ceramics with a very large free surface. A part of the hydrogen released from the specimens is adsorbed at these surfaces until adsorption reaches saturation. As a consequence, the hydrogen content is determined as too low by hot extraction until saturation of hydrogen adsorption is reached. Due to these experimental uncertainties only the neutron radiography data are used for further analysis and discussion.

From the NR results it can be estimated that about 25 % of the free hydrogen produced in the pre-oxidation phase is absorbed in the zirconium alloy. An unexpected high hydrogen release during the reflooding process additional to the free hydrogen production by the strong oxidation can be explained by this finding. A large amount of the thin cladding rods were oxidized. Due to the very low hydrogen solubility in ZrO_2 , H is desorbed from the claddings to the gas environment. For rod D two local maxima at $z \approx 850$ and 1080 mm and a local minimum at $z \approx 970$ mm was found. The axial positions of these extrema are the same for rod F but the maximum at 1080 mm is here significantly higher than for rod D. The second maximum in rod B is very flat. The minimum would be in the region lost by melting.

The analysis of the axial hydrogen distributions has to be focused to the discussion of the results for corner rod D. This rod is withdrawn after 53 min isothermal annealing at 1473 K (central rod, $z = 950$ mm). Due to the large time and the relative high temperatures a quasi-equilibrium state can be assumed. At temperatures above 1273 K zirconium oxidation follows parabolic kinetics. The changes in the free hydrogen production rate is low after long times. Due to the breakaway effect at temperatures between 1073 and 1273 K the steam oxidation kinetics is linear. For the axial regions having this temperature range the free hydrogen production rate is constant. It means that according to the Sieverts' law an equilibrium between the hydrogen in the gas phase and in the metal has to be established, independently on the oxide layer between these two phases:

$$c_H^m = k_s \cdot \sqrt{p_H} \quad (8)$$

k_s is the Sieverts constant and p_H the hydrogen partial pressure in the gas. In [23] the temperature dependence of k_s is determined also for the E110 alloy. The axial temperature distribution at the moment of withdrawal of corner rod D can be fitted by two lines given in [Fig. 159](#). From the axial temperature and hydrogen concentration distributions the axial hydrogen partial pressure distribution can be estimated according to equation (8).

As [Fig. 159](#) shows, a maximum in p_H can be found at $z \approx 870$ mm. The estimated maximal values of $p_H \approx 36$ kPa are two orders of magnitude higher than the hydrogen partial pressure in the off-gas at the time of withdrawing of rod D determined by mass spectrometry. Such a high hydrogen partial pressure in the bulk of the gas phase can be excluded because the oxidation behavior gives no hints for such strong reaction needed to produce such high partial pressure. However, for the equilibrium not the gas bulk hydrogen concentration but the gas hydrogen partial pressure at the rod surface is determining. A comparison of the

neutron radiographs and the optical appearance of rod D shows that the highest hydrogen content can be found at positions with a thick oxide scale containing large open cracks. Fig. 160 shows the micrographs of the cross section at the axial positions $z = 700$ mm (beginning of the first hydrogen peak), $z = 940$ mm (location of the local minimum of the hydrogen concentration) and $z = 1120$ mm (position in the range of the second peak). Steam can penetrate into these cracks. The remaining oxide barrier between the crack front and the metal is small or the crack grows directly into the metal. Therefore a relative strong oxidation occurs at crack positions. The release of the gases out of the crack is small. Consequently, hydrogen is here strongly enriched.

The same situation can be found for the upper part of the shroud (above the melting zone). Fig. 161 compares the axial hydrogen distribution with the macroscopic appearance of the shroud segment investigated. Whereas the hydrogen concentrations are low (< 2 at.%) at axial positions higher than $z = 1150$ mm, it reaches 10 at.% at positions with breakaway oxides ($z < 1100$ mm). The hydrogen concentration in the shroud is about 30 % lower than the concentration in corner rod B at comparable axial positions. Differences in the oxidation rate caused by differences in the niobium content, in the maximum temperature during the reflooding and in the material thicknesses can be the reason.

The quasi-equilibrium model can not be applied to discuss the hydrogen content and distribution in the rods F and B, withdrawn during and after the transient phase, respectively. For instance, the equilibrium hydrogen partial pressure at $z = 1080$ mm in rod F would be about 450 kPa. Such a high pressure would destroy the oxide layer. Obviously, the hydrogen has not enough time to diffuse out of the corner rod bulk during the transient phase to reach equilibrium.

In Fig. 162 the hydrogen concentration of the remaining rod cladding is compared with the concentration in corner rod B. As the cladding segments were prepared from bundle cross sections (discs) used for the metallographic investigations, the epoxy had to be removed from the specimens. As the radiography images have shown the removal was not successful for each specimen. Parts of remaining epoxy films are visible. Such regions were excluded from the analysis. However, a homogeneous epoxy film would not be detectable and would result in too high a hydrogen value. The hydrogen concentrations of the cladding tube segments show large scatter not only caused by uncertainties in hydrogen determination. Also radial differences mainly at $z = 725$ mm were found. Here cladding rods of the innermost ring show a concentration more than two times higher than that in the outer cladding rods. Except for $z = 1127$ mm the concentration in corner rod B is higher than the mean values of the cladding tubes. In the solid corner rod B the time during quenching is too low that all hydrogen can diffuse out of the sample from each radial position, whereas the diffusion paths in the cladding tubes are short enough to extract more hydrogen.

Fig. 163 shows the neutron radiograph of the upper end of the lower part of rod B. It is comparable to the lower end of the upper part of this rod. The deep hole is clearly visible. At the hole surface the dark grey color indicates a high hydrogen content. The formation of these holes can be explained by the α - β phase composition. At the high temperatures that occurred at the beginning of the reflood the bcc β phase is thermodynamic stable. However, dissolved hydrogen stabilizes this phase, but absorbed oxygen stabilizes the hexagonal α phase. During reflood hydrogen diffuses from the rod surface into the gas environment

whereas oxygen diffuses into the metal. An α -phase at the outer regions and a β -phase in the bulk of the rod is established. Due to the lower melting temperature of the β -phase (2128 K) than of the oxygen stabilized α -phase (2248 K) a partial melting of the bulk occurs whereas the outer regions stay solid. After solidification stresses and micro-cracks can be formed at the interface and the rod breaks along this interface.

Fig. 164 shows a comparison of hydrogen absorption in claddings of bundles QUENCH-12 and QUENCH-06. Breakaway oxidation at mid-section and at high elevations of the QUENCH-12 bundle makes possible the intensive uptake of hydrogen by the Zr through cracks in the oxide scale. The long-term cladding hydriding during breakaway oxidation causes strong embrittlement of the cladding material, which may lead to bundle degradation during quenching. Such sequence of events was observed during the Paks accident with a cleaning tank [25].

In summary, the results of the analysis of the hydrogen concentration and distribution in the QUENCH-12 corner rods show that hydrogen is accumulated in the remaining metallic Zr alloys during the pre-oxidation phase. The hydrogen concentrations in the corner rods are much higher than it was found for QUENCH-6 experiments (one broad maximum in the axial distribution, maximal hydrogen content about 10 at.%). During temperature escalation at the beginning of reflooding phase additionally to the hydrogen produced by the strong oxidation a large amount of hydrogen absorbed in the metal is assumed to be released at once. A short but very high hydrogen peak is the consequence. The hydrogen uptake of the zirconium alloy E110 is mainly determined by very local gas conditions at the metal or oxide surface. These conditions are strongly influenced by the macroscopic oxide appearance. This fact is not yet taken into account in computer codes simulating severe accidents. Models considering hydrogen absorption behavior have to be included in SFD computer codes to describe the severe accident behavior of VVER-type reactors well.

7 Summary

The QUENCH-12 experiment was carried out to investigate the effects of VVER materials (Zr1%Nb for rod simulators) and bundle geometry on core reflood, in comparison with the test QUENCH-06 (ISP-45) with western materials and geometry (Zircaloy-4, PWR). The electrical power history during the test corresponded completely to the pre-calculated values up to reflood phase. The temperatures at all bundle elevations during preoxidation are about 30-40 K lower than during corresponding phase of QUENCH-06.

Two corner rods were withdrawn at the end of preoxidation and transient phases correspondingly. The third corner rod was withdrawn after the test. The surfaces of the rods show intensive breakaway oxidation as do the surfaces of the rod simulators and shroud. However, the breakaway is more pronounced at the surfaces of the corner rods. Possible reasons could be different mechanical properties of tube and massive rod and other surface preparation of cladding and corner rods.

Following reflood initiation, a moderate temperature excursion of ca. 50 K was observed, over a longer period than in QUENCH-06. The temperatures at elevations between 850 mm and 1050 mm exceeded the melting temperature of β -Zr. At the peak temperature elevation

of 950 mm, melt pool formation, non-coherent melt relocation, dissolution of embedded scale and melt oxidation were observed.

Posttest bundle examinations performed at RIAR and FZK showed a higher degree of oxidation of cladding surfaces in comparison to QUENCH-06. Also, the radial inhomogeneity of the oxidation is much higher for QUENCH-12 bundle.

The content of hydrogen absorbed in the corner rods of the QUENCH-12 bundle reached a value of more than 30 at% at the bundle elevations of 850 and 1100 mm. The hydrogen content in claddings of the QUENCH-12 bundle was also significantly higher in comparison to corresponding elevations of the QUENCH-06 bundle.

The total hydrogen production was 58 g (for QUENCH-06: 36 g), during the reflood 24 g of hydrogen was released (for QUENCH-06: 4 g). The reasons for the increased hydrogen production may be enhanced breakaway oxidation, local melt formation with subsequent melt oxidation, and the release of hydrogen previously absorbed by the metal.

Acknowledgments

Test QUENCH-12 was co-financed in the frame of the ISTC Project 1648.2. In general, the broad support needed for preparation, execution, and evaluation of the experiment is gratefully acknowledged. In particular, the authors would like to thank Mr. J. Moch for the assembly of the entire test section, Mr. S. Horn, FZK/IK, for the preparation of the hydrogen measurement with the "Caldos" analyzer and the various support, Mrs. J. Laier for processing the test data, and Dr. L. Steinbock for the posttest videoscope inspection of the bundle.

The determination of the test protocol was based on numerous calculations with the SCDAP/RELAP5, SCDAPSIM and MELCOR codes performed by Drs. J. Birchley and T. Haste of the Paul-Scherrer-Institut (PSI) and ICARE/CATHARE V1 code by Drs. A. Volchek and Yu. Zvonarev of the Kurchatov Institute Moscow. The final calculations, which took advantage of the pre-experiment data, were performed by PSI using the SCDAP-based codes. This work is gratefully acknowledged.

References

- [1] J.M. Broughton, P. Kuan, and D.A. Petti, "A Scenario of the Three Mile Island Unit 2 Accident," *Nuclear Technology*, 87, 34, 1989.
- [2] P. Hofmann, S. Hagen, V. Noack, G. Schanz, L. Sepold, "Chemical-Physical Behavior of Light Water Reactor Core Components Tested under Severe Reactor Accident Conditions in the CORA Facility," *Nuclear Technology*, vol. 118, 1997, p. 200.
- [3] S. Hagen, P. Hofmann, V. Noack, L. Sepold, G. Schanz, G. Schumacher, "Comparison of the Quench Experiments CORA-12, CORA-13, CORA-17," FZKA 5679, Forschungszentrum Karlsruhe, 1996.
- [4] S.M. Modro and M.L. Carboneau, "The LP-FP-2 Severe Fuel Damage Scenario; Discussion of the Relative Influence of the Transient and Reflood Phase in Affecting the Final Condition of the Bundle," OECD/LOFT Final Event, ISBN 92-64-03339-4, 1991, p. 388.
- [5] B. Clement, N. Hanniet/Girault, G. Repetto, D. Jacquemain, A.V. Jones, M.P. Kissane, P. von der Hardt, "LWR Severe Accident Simulation: Synthesis of the Results and Interpretation of the First Phebus FP Experiment FPT0," *Nuclear Engineering and Design*, 2003.
- [6] L. Sepold, A. Miassoedov, G. Schanz, U. Stegmaier, M. Steinbrück, J. Stuckert, C. Homann, "Hydrogen Generation in Reflooding Experiments with LWR-type Rod Bundles (QUENCH Program)," *Journal Nuclear Technology*, Vol. 147, Aug. 2004, pp. 202-214.
- [7] P. Hofmann, V. Noack, M.S. Veshchunov, A.V. Berdyshev, A.V. Boldyrev, L.V. Matweev, A.V. Palagin, V.E. Shestak, "Physico-Chemical Behavior of Zircaloy Fuel Rod Cladding Tubes During LWR Severe Accident Reflood," FZKA 5846, Forschungszentrum Karlsruhe, 1997.
- [8] P. Hofmann, A. Miassoedov, L. Steinbock, M. Steinbrück, A.V. Berdyshev, A.V. Boldyrev, A.V. Palagin, V.E. Shestak, M. Veshchunov, "Quench Behavior of Zircaloy Fuel Rod Cladding Tubes. Small-Scale Experiments and Modeling of the Quench Phenomena," FZKA 6208, Forschungszentrum Karlsruhe, 1999
- [9] J. Stuckert, M. Steinbrück, U. Stegmaier, "Single Rod Quench Tests with Zr-1Nb. Comparison with Zircaloy-4 Cladding Tests and Modelling," FZKA 6604, Forschungszentrum Karlsruhe, 2001
- [10] L. Sepold, W. Hering, C. Homann, A. Miassoedov, G. Schanz, U. Stegmaier, M. Steinbrück, H. Steiner, J. Stuckert, "Experimental and Computational Results of the QUENCH-06 Test (OECD ISP-45)," FZKA 6664, Forschungszentrum Karlsruhe, February 2004.
- [11] W. Hering, C. Homann, J.S. Lamy, A. Miassoedov, G. Schanz, L. Sepold, M. Steinbrück, "Comparison and Interpretation Report of the OECD International Standard Problem No. 45 Exercise (QUENCH-06)," FZKA 6722, Forschungszentrum Karlsruhe, July 2002.
- [12] J. Birchley, T. Haste, B. Jäckel, "Pre-Test Analytical Support for Experiments QUENCH-11 and -12," 12th International QUENCH Workshop, Forschungszentrum Karlsruhe, October 2006, CD-ROM (ISBN 978-3-923704-57-6).

- [13] A. Volchek, Yu. Zvonarev, "ICARE/CATHARE V1 Code Application to QUENCH-12 Test," 12th International QUENCH Workshop, Forschungszentrum Karlsruhe, October 2006, CD-ROM (ISBN 978-3-923704-57-6).
- [14] A.V. Palagin, J. Stuckert, "Application of the SVECHA/QUENCH Code to the Simulation of the Bundle Tests QUENCH-06 and QUENCH-12," FZKA 7353, Forschungszentrum Karlsruhe, 2007.
- [15] M. Steinbrück, A. Miassoedov, G. Schanz, L. Sepold, U. Stegmaier, H. Steiner, J. Stuckert, „Results of the QUENCH-09 Experiment with a B₄C Control Rod”, FZKA 6829, Forschungszentrum Karlsruhe, December 2004.
- [16] S. Leistikow, G. Schanz, H. v. Berg, A.E. Aly, "Comprehensive Presentation of Extended Zircaloy-4/Steam Oxidation Results (600-1600 °C)", OECD-NEA-CSNI/IAEA Specialists' Meeting on Water Reactor Safety and Fission Product Release in Off-Normal and Accident Conditions; Risø Nat. Lab., Denmark, May 16-20, 1983, Proc. IAEA IWGFPT/16, 188-199.
- [17] G. Schanz, S. Leistikow, "Microstructural Reasons for Mechanical Oxide Degradation (Breakaway Effect) and Resulting Kinetic Anomalies of Zircaloy 4/Steam High-Temperature Oxidation", 8th Int. Congress on Metallic Corrosion, Mainz, Germany, Sept. 6-11, 1981, Proc. DECHEMA, Vol. II, 1981) 1712-1717.
- [18] G. Schanz, "Semi-mechanistic Approach for Evaluation of Zr Oxidation Experiments", ANS Annual Meeting, Reno (NV), June 4-8 2006; American Nuclear Society Transactions Vol. 94.
- [19] G. Schanz, "Semi-Mechanistic Approach for the Kinetic Evaluation of Experiments on the Oxidation of Zirconium Alloys", FZKA 7329, Forschungszentrum Karlsruhe, 2007.
- [20] A. Goryachev, I. Ivanova, „Results of the QUENCH-12 bundle post-test examinations", 13th International QUENCH Workshop, Forschungszentrum Karlsruhe, November 20-22, 2007; CD-ROM (ISBN 978-3-923704-63-7).
- [21] M. Grosse, E. Lehmann, P. Vontobel, and M. Steinbrueck, "Quantitative determination of absorbed hydrogen in oxidised zircaloy by means of neutron radiography," *Nucl. Inst. Meth. In Phys. Res. A* **566** 739, 2006.
- [22] G. Kühne, G. Frei, E. Lehmann, and P. Vontobel, "Quantitative determination of absorbed hydrogen in oxidised zircaloy by means of neutron radiography," *Nucl. Instr. & Meth. A* **542 (1-3)** 264, 2005.
- [23] M. Steinbrück, "Hydrogen absorption by zirconium alloys at high temperatures," *J. Nucl. Mater.* **334** 58, 2004.
- [24] L. Sepold, M. Steinbrück, J. Stuckert, Internal report (Quick Look), 2006.
- [25] Final Report of the OECD-IAEA Paks Fuel Project (in press as NEA/CSNI/R(2008)2 report).

Table 1: QUENCH test matrix

Test	Quench medium	Injection rate	Temp. at onset of flooding ¹⁾	Max. ZrO ₂ before flooding ²⁾	Max. ZrO ₂ layer thickness ³⁾	H ₂ production before / during cooldown	Remarks, objectives
QUENCH-00 Oct. 9 - 16, 97	Water	80 g/s	≈ 1800 K		≈ 500 μm		COBE Project; commissioning tests.
QUENCH-01 February 26, 98	Water	52 g/s	≈ 1830 K	312 μm	≈ 580 μm	36 / 3	COBE Project; partial fragmentation of pre-oxidized cladding.
QUENCH-02 July 7, 98	Water	47 g/s	≈ 2400 K		completely oxidized	20 / 140	COBE Project; no additional pre-oxidation; quenching from high temperatures.
QUENCH-03 January 20, 99	Water	40 g/s	≈ 2350 K		completely oxidized	18 / 120	No additional pre-oxidation, quenching from high temperatures.
QUENCH-04 June 30, 99	Steam	50 g/s	≈ 2160 K	82 μm	≈ 360 μm	10 / 2	Cool-down behavior of slightly pre-oxidized cladding by cold steam injection.
QUENCH-05 March 29, 2000	Steam	48 g/s	≈ 2020 K	160 μm	≈ 520 μm	25 / 2	Cool-down behavior of pre-oxidized cladding by cold steam injection.
QUENCH-06 Dec. 13 2000	Water	42 g/s	≈ 2060 K	207 μm	≈ 850 μm	32 / 4	OECD-ISP 45; prediction of H ₂ source term by different code systems.
QUENCH-07 July 25, 2001	Steam	15 g/s	≈ 2100 K	230 μm	completely oxidized	66 / 120	COLOSS Project; impact of B ₄ C absorber rod failure on H ₂ , CO, CO ₂ , and CH ₄ generation.

Test	Quench medium	Injection rate	Temp. at onset of flooding ¹⁾	Max. ZrO ₂ before flooding ²⁾	Max. ZrO ₂ layer thickness ³⁾	H ₂ production before / during cooldown	Remarks, objectives
QUENCH-09 July 3, 2002	Steam	49 g/s	≈ 2100 K		completely oxidized	60 / 400	As QUENCH-07, steam-starved conditions prior to cooldown.
QUENCH-08 July 24, 2003	Steam	15 g/s	≈ 2090 K	274 μm	completely oxidized	46 / 38	As QUENCH-07, no absorber rod
QUENCH-10 July 21, 2004	Water	50 g/s	≈ 2200 K	514 μm	completely oxidized	48 / 5	LACOMERA Project; Air ingress.
QUENCH-11 Dec 08, 2005	Water	18 g/s	≈ 2040 K	170 μm	completely oxidized	9 / 132	LACOMERA Project; Boil-off.
QUENCH-12 Sept 27, 2006	Water	48 g/s	≈ 2100 K	213 μm	completely oxidized	34 / 24	ISTC Project; VVER

1) Maximum measured bundle temperature at 950 mm.

2) Measured at a withdrawn corner rod.

3) Measured posttest at the bundle elevation of maximum temperature.

Revised: November 2007

Table 2: Design characteristics of the QUENCH-VVER test bundle

Bundle type		VVER
Bundle size		31 rods
Pitch		12.75 mm
Coolant channel area		32.8 cm ²
Hydraulic diameter		10.4 mm
Number of heated rods		18
Number of unheated rods		13
Rod cladding material		Zr1%Nb (E 110), etched and anodized*
Rod cladding diameter		9.11 / 7.75 mm **
Rod length	heated rod (levels) unheated rod (levels) unheated central rod (levels)	2480 mm (-690 mm to 1790 mm) 2350 mm (-425 mm to 1925 mm) 2842 mm (-827 mm to 2015 mm), (incl. extension piece for unheated)
Rod fill gas (0.22 MPa)	heated rod unheated rod	Ar5%Kr He
Heater material		tungsten (W)
Heater length		1024 mm
Heater diameter		4 mm
Annular pellet	material heated rod unheated rod	ZrO ₂ ;Y ₂ O ₃ -stabilized Ø 7.57/4.15 mm; L=11 mm Ø 7.57/2.5 mm; L=11 mm
Pellet stack length	heated rod unheated rod	0 mm to 1024 mm 0 mm to 1557 mm
Corner rod (6)	material instrumented not instrumented (solid)	Zr1%Nb tube Ø 5.8x0.525 (from -1140 mm) rod Ø 6 mm (top: +1300 mm) rod Ø 6 mm (-1350 to +1155 mm)
Grid spacer (7)	material length plate thickness mass location of lower edge	Zr1%Nb 20 mm 0.25 mm 46.5 g -200, 50, 300, 550, 800, 1050, 1300 mm
Shroud	material inside diameter outside diameter length (levels)	Zr2.5%Nb (E 125) 83.5 mm 88.0 mm 1600 mm (-300 mm to 1300 mm)
Shroud insulation	material insulation thickness elevation	ZrO ₂ fiber ~ 37 mm -300 mm to ~1000 mm
Molybdenum-copper electrodes	length of upper electrodes length of lower electrodes diameter of electrodes: - prior to coating - after coating with ZrO ₂	766 mm (576 Mo, 190 mm Cu) 690 mm (300 Mo, 390 mm Cu) 7.0 mm 7.4 mm
Cooling jacket	material: inner/outer tube inner tube outer tube	Inconel 600 (2.4816)/SS (1.4571) Ø 158.3 / 168.3 mm Ø 181.7 / 193.7 mm

*initial oxide thickness ~0.3 µm

01/2008

** measured at FZK; manufacturer nominal values before etching: $9.13^{+0.06}_{-0.05}$ / $7.72^{+0.07}$ mm

Table 3. Comparison of some physical/chemical properties of different zirconium alloys.

Chemical analysis results of E110 and Zircaloy-4 cladding materials (wt%)

Element	E110	Zircaloy-4
Nb	0.971 ± 0.004	-
Sn	< 0.004	1.525 ± 0.011
Hf	0.0252 ± 0.0001	< 0.005
Fe	0.0079 ± 0.0002	0.221 ± 0.001
Cr	0.0022 ± 0.00005	0.105 ± 0.001
Ni	0.0023 ± 0.0001	-
Cu	< 0.0003	-
O	0.046 ± 0.002	0.135 ± 0.015
N	0.004 ± 0.001	0.007 ± 0.005

Basis: FZKA 6604

Thermal conductivity

T, K	373	573	773	973	1173	1373	1573	1773	1973
Zr*	18,8	17,2	18,0	20,6	24,0	27,4	30,1	31,2	
E110*	20,6	17,6	18,4	21,4	25,2	28,5	33,1		
Zry-4**	13,7	16,2	18,5	21,2	24,5	28,7	34,4	41,7	51,2

* Vladislav E Peletsky. "High-temperature thermal conductivity of zirconium based alloys". High Temperatures - High Pressures, 1999, volume 31, pages 627 – 632

** MATPRO. NUREG/CR-5273

Specific heat

T, K	873	1023	1073	1123	1167	1223	1273	1973
Zr*	344,2	359,2	364,1	371,0	298,3	299,6	300,8	320,5
E110**	345,5	363,6	392,7	545,5	963,6	447,3	349,1	400,0
Zry-4***	380,5	401,1	408,0	546,7	977,7	656,1	402,6	
	α-phase	α+β-phases	β-phase					

* Alan Dinsdale, SGTE Data for Pure Elements, Calphad Vol 15(1991) pp. 317-425

** I. Petrova, V. E. Peletsky and B. N. Samsonov. "Thermophysical Properties of the Zr-O.01Nb Alloy at Various Heating Rates and Repeated Cycles of Heating-Cooling". International Journal of Thermophysics, Vol. 20. No. 4. 1999

*** FZKA 6739

Table 4: Properties of zirconia fiber insulating boards of type ZYFB3

Chemical composition

oxide	ZrO ₂	Y ₂ O ₃	HfO ₂	TiO ₂	SiO ₂	CaO	MgO	Fe ₂ O ₃	Al ₂ O ₃	Na ₂ O
typical wt%	88	10	2	0.14	0.12	0.09	0.03	0.04	0.01	0.01

Physical properties

bulk density	porosity	shrinkage		thermal expansion coefficient @298K-1453K	melting point	max service temperature	flexural strength	compressive strength @10% compression
		(1 hour @1925 K)	(24 hours @1925 K)					
g/cm ³	%	%		1/K	K	K	MPa	MPa
0.48	92	1.2	2.8	10.7*10 ⁻⁶	2866	2500	0.59	0.29

Thermal conductivity

temperature, K	673	1073	1373	1673	1923
conductivity, W/(m*K)	0.08	0.11	0.14	0.19	0.24

Specific heat capacity

temperature, K	366	2644
specific heat capacity, J/(kg*K)	544	754

Table 5: Diameters of the materials used for the QUENCH high-temperature thermocouples [mm]

Material	As-received	Final
W/Re wires	0.254	
HfO ₂ insulation OD (see drawing below)	1.1	
Ta tube OD / ID	2.15 / 1.65	1.4 / 0.94
Zr tube OD / ID	2.35 / 1.65 ± 0.013	2.1 / 1.4

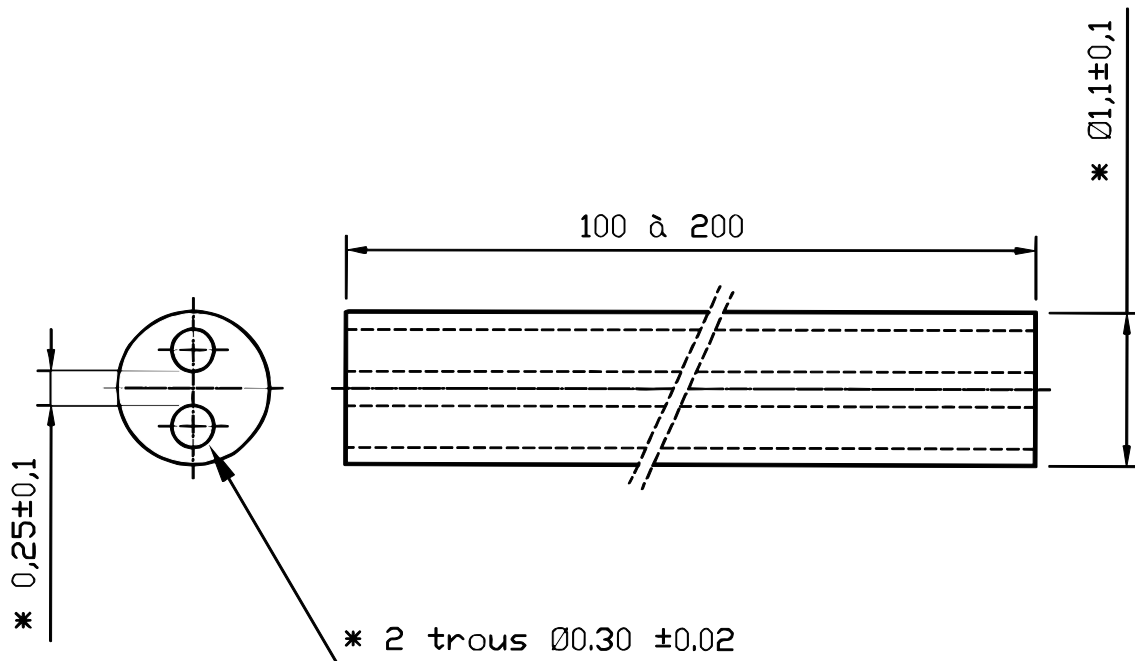


Table 6: Main characteristics of the HfO₂ thermocouple insulator

Property	Data
Composition of basic material	99 % HfO ₂
Melting temperature	2840 °C
Max. use temperature	2500 °C
Density	8.4 g/cm ³
Thermal conductivity at 20-1000 °C	1.14 W/m K
Linear expansion	5.8 x 10 ⁻⁶ /K

According to Saint-Gobain ceramics, 1997

Table 7: Main characteristics of the ZrO₂ pellet material, yttria-stabilized, type FZY

Property	Data	
Density	5.5-5.8 g/cm ³	
Open porosity	0	
Mean grain size	50 μm	
Hardness (Knoop, 100 g)	17000 N/mm ²	
Yield strength under compression	2000 N/mm ²	
Bending strength	350 N/mm ²	
Elastic modulus	165 GPa	
Specific heat at 20 °C	400 J/kg K	
Thermal conductivity at 100 °C	2.5 W/m K	
Linear expansion, 20-1000 °C	10.5 x 10 ⁻⁶ /K	
Specific electric resistance	at 20 °C	10 ¹⁰ Ω cm
	at 500 °C	5000 Ω cm
	at 1000 °C	50 Ω cm

According to FRIATEC, Mannheim

Table 8: List of Instrumentation of the QUENCH-12 Test Bundle

Chan	Designation	Instrument, location	Unit
0	TFSH 31/5/17	TC (W/Re), surface of fuel rod simulator 31, group 5, 1350 mm	K
1	TFC 18/4/17	TC (W/Re), <i>center line</i> of fuel rod simulator 18, group 4, 1350 mm	K
2	TFSU 11/3/17	TC (W/Re), surface of fuel rod simulator 11, group 3, 1350 mm	K
3	TFSH 30/5/16	TC (W/Re), surface of fuel rod simulator 30, group 5, 1250 mm	K
4	TFSU 15/3/16	TC (W/Re), surface of fuel rod simulator 15, group 3, 1250 mm	K
5	TFC 13/3/16	TC (W/Re), <i>center line</i> of fuel rod simulator 13, group 3, 1250 mm	K
6	TFSH 21/5/15	TC (W/Re), surface of fuel rod simulator 21, group 5, 1150 mm	K
7	TFC 16/4/15	TC (W/Re), <i>center line</i> of fuel rod simulator 16, group 4, 1150 mm	K
8	TFC 10/4/15	TC (W/Re), <i>center line</i> of fuel rod simulator 10, group 4, 1150 mm	K
9	TFSU 9/3/15	TC (W/Re), surface of fuel rod simulator 9, group 3, 1150 mm	K
10	TFSH 5/2/15	TC (W/Re), surface of fuel rod simulator 5, group 2, 1150 mm	K
11	TFSH 27/5/14	TC (W/Re), surface of fuel rod simulator 27, group 5, 1050 mm	K
12	TFSU 19/3/14	TC (W/Re), surface of fuel rod simulator 19, group 3, 1050 mm	K
13	TFC 19/3/14	TC (W/Re), <i>center line</i> of fuel rod simulator 19, group 3, 1050 mm	K
14	TFC 15/3/14	TC (W/Re), <i>center line</i> of fuel rod simulator 15, group 3, 1050 mm	K
15	TFSU 12/4/14	TC (W/Re), surface of fuel rod simulator 12, group 4, 1050 mm	K
16	TFC 12/4/14	TC (W/Re), <i>center line</i> of fuel rod simulator 12, group 4, 1050 mm	K
17	TFC 9/3/14	TC (W/Re), <i>center line</i> of fuel rod simulator 9, group 3, 1050 mm	K
18	TFSH 6/2/14	TC (W/Re), surface of fuel rod simulator 6, group 2, 1050 mm	K
19	TFSH 29/5/13	TC (W/Re), surface of fuel rod simulator 29, group 5, 950 mm	K
20	TFSU 17/3/13	TC (W/Re), surface of fuel rod simulator 17, group 3, 950 mm	K
21	TFC 17/3/13	TC (W/Re), <i>center line</i> of fuel rod simulator 17, group 3, 950 mm	K
22	TFSH 30/5/9	TC (NiCr/Ni), surface of fuel rod simulator 30, group 5, 550 mm	K
23	TFSH 25/5/9	TC (NiCr/Ni), surface of fuel rod simulator 25, group 5, 550 mm	K
24	F 902	Off-gas flow rate upstream Caldos (H ₂), (20 mA)	Nm ³ /h
25	FM 401	Argon gas mass flow rate, (20 mA)	g/s
26	TFC 14/4/13	TC (W/Re), <i>center line</i> of fuel rod simulator 14, group 4, 950 mm	K
27	TFC 11/3/13	TC (W/Re), <i>center line</i> of fuel rod simulator 11, group 3, 950 mm	K
28	TFSU 10/4/13	TC (W/Re), surface of fuel rod simulator 10, group 4, 950 mm	K
29	TFC 8/4/13	TC (W/Re), <i>center line</i> of fuel rod simulator 8, group 4, 950 mm	K

Chan	Designation	Instrument, location	Unit
30	TFSH 2/2/13	TC (W/Re), surface of fuel rod simulator 2, group 2, 950 mm	K
31	TFSU 1/13	TC (W/Re), surface of fuel rod simulator 1, 950 mm	K
32	TFC 1/13	TC (W/Re), <i>center line</i> of fuel rod simulator 1, 950 mm	K
33	TFSH 26/5/12	TC (W/Re), surface of fuel rod simulator 26, group 5, 850 mm	K
34	TFSU 18/4/12	TC (W/Re), surface of fuel rod simulator 18, group 4, 850 mm	K
35	TFSU 17/3/9	TC (NiCr/Ni), surface of fuel rod simulator 17, group 3, 550 mm	K
36	TFSU 9/3/9	TC (NiCr/Ni), surface of fuel rod simulator 9, group 3, 550 mm	K
37	TFSH 3/2/12	TC (W/Re), surface of fuel rod simulator 3, group 2, 850 mm	K
38	TFSH 4/2/9	TC (NiCr/Ni), surface of fuel rod simulator 4, group 2, 550 mm	K
39	TFSU 1/7	TC (NiCr/Ni), surface of fuel rod simulator 1, 350 mm	K
40	TFSH 23/5/11	TC (W/Re), surface of fuel rod simulator 23, group 5, 750 mm	K
41	TFSH 7/2/11	TC (W/Re), surface of fuel rod simulator 7, group 2, 750 mm	K
42	TFSU 1/9	TC (NiCr/Ni), surface of fuel rod simulator 1, 550 mm	K
43	TFSU 19/3/8	TC (NiCr/Ni), surface of fuel rod simulator 19, group 3, 450 mm	K
44	TFSU 12/4/8	TC (NiCr/Ni), surface of fuel rod simulator 12, group 4, 450 mm	K
45	TFSH 28/5/7	TC (NiCr/Ni), surface of fuel rod simulator 28, group 5, 350 mm	K
46	TFSH 5/2/7	TC (NiCr/Ni), surface of fuel rod simulator 5, group 2, 350 mm	K
47	TFSH 20/5/10	TC (W/Re), surface of fuel rod simulator 20, group 5, 650 mm	K
48	TFSU 16/4/10	TC (W/Re), surface of fuel rod simulator 16, group 4, 650 mm	K
49	TIT A/13	TC (W/Re), <i>center line</i> of corner rod A, 950 mm	K
50	TIT C/12	TC (W/Re), <i>center line</i> of corner rod C, 850 mm	K
51	TFC 1/12	TC (W/Re), <i>center line</i> of fuel rod simulator 1, group 1, 850 mm	K
52	TIT E/11	TC (W/Re), <i>center line</i> of corner rod E, 750 mm	K
53	TSH 16/180	TC (W/Re) shroud outer surface, 1250 mm, 191°, behind shroud insulation	K
54	TSH 16/0	TC (W/Re) shroud outer surface, 1250 mm, 11°, behind shroud insulation	K
55	TSH 15/180	TC (W/Re) shroud outer surface, 1150 mm, 191°, behind shroud insulation	K
56	TSH 15/0	TC (W/Re) shroud outer surface, 1150 mm, 11°, behind shroud insulation	K
57	TSH 14/270	TC (W/Re) shroud outer surface, 1050 mm, 289°, behind shroud insulation	K
58		Reserve	

Chan	Designation	Instrument, location	Unit
59	TSH 14/90	TC (W/Re) shroud outer surface, 1050 mm, 109°, behind shroud insulation	K
60	TSH 13/270	TC (W/Re) shroud outer surface, 950 mm, 289°, behind shroud insulation	K
61	T 206	Temperature upstream steam flow instrument location 1 g/s	K
62	P 206	Pressure at steam flow instrument location 1 g/s, (20 mA)	bar
63	F 206	Flow rate steam 1 g/s, (20 mA)	g/s
64	T 402 b	TC (NiCr/Ni), Ar super heater	K
65	TSH 13/90	TC (W/Re) shroud outer surface, 950 mm, 109°, behind shroud insulation	K
66	TSH 12/180	TC (W/Re) shroud outer surface, 850 mm, 191°, behind shroud insulation	K
67	TSH 12/0	TC (W/Re) shroud outer surface, 850 mm, 11°, behind shroud insulation	K
68	T 512	TC (NiCr/Ni), gas temperature bundle outlet	K
69	TSH 11/180	TC (W/Re) shroud outer surface, 750 mm, 191°, behind shroud insulation	K
70	TSH 11/0	TC (W/Re) shroud outer surface, 750 mm, 11°, behind shroud insulation	K
71	<i>Ref. T01</i>	<i>Temperature of measuring crate 1 (reference temperature)</i>	K
72	TFSU 15/3/6	TC (NiCr/Ni), surface of fuel rod simulator 15, group 3, 250 mm	K
73	TFSU 11/3/6	TC (NiCr/Ni), surface of fuel rod simulator 11, group 3, 250 mm	K
74	TFSU 13/3/5	TC (NiCr/Ni), surface of fuel rod simulator 13, group 3, 150 mm	K
75	TFSH 2/2/5	TC (NiCr/Ni), surface of fuel rod simulator 2, group 2, 150 mm	K
76	TFSH 30/5/4	TC (NiCr/Ni), surface of fuel rod simulator 30, group 5, 50 mm	K
77	TFSH 24/5/4	TC (NiCr/Ni), surface of fuel rod simulator 24, group 5, 50 mm	K
78	TSH 10/90	TC (NiCr/Ni) shroud outer surface, 650 mm, 109°	K
79	TSH 10/270	TC (NiCr/Ni) shroud outer surface, 650 mm, 289°	K
80	TSH 9/0	TC (NiCr/Ni) shroud outer surface, 550 mm, 11°	K
81	TSH 9/180	TC (NiCr/Ni) shroud outer surface, 550 mm, 191°	K
82	TSH 8/90	TC (NiCr/Ni) shroud outer surface, 450 mm, 109°	K
83	TSH 8/270	TC (NiCr/Ni) shroud outer surface, 450 mm, 289°	K
84	TSH 7/0	TC (NiCr/Ni) shroud outer surface, 350 mm, 11°	K
85	TSH 7/180	TC (NiCr/Ni) shroud outer surface, 350 mm, 191°	K
86	TSH 6/0	TC (NiCr/Ni) shroud outer surface, 250 mm, 11°	K

Chan	Designation	Instrument, location	Unit
87	TSH 5/180	TC (NiCr/Ni) shroud outer surface, 150 mm, 191°	K
88	TSH 4/90	TC (NiCr/Ni) shroud outer surface, 50 mm, 109°	K
89	TSH 3/270	TC (NiCr/Ni) shroud outer surface, -50 mm, 289°	K
90	TSH 1/0	TC (NiCr/Ni) shroud outer surface, -250 mm, 11°	K
91	TCI 9/270	TC (NiCr/Ni) cooling jacket inner tube wall, 550 mm, 270°	K
92	TCI 10/270	TC (NiCr/Ni) cooling jacket inner tube wall, 650 mm, 270°	K
93	TCI 11/270	TC (NiCr/Ni) cooling jacket inner tube wall, 750 mm, 270°	K
94	TCI 13/270	TC (NiCr/Ni) cooling jacket inner tube wall, 950 mm, 270°	K
95	TFSU 8/4/3	TC (NiCr/Ni), surface of fuel rod simulator 8, group 4, -50 mm	K
96	TCI 1/180	TC (NiCr/Ni) cooling jacket inner tube wall, -250 mm, 180°	K
97	TCI 4/180	TC (NiCr/Ni) cooling jacket inner tube wall, 50 mm, 180°	K
98	TCI 7/180	TC (NiCr/Ni) cooling jacket inner tube wall, 350 mm, 180°	K
99	TCI 11/180	TC (NiCr/Ni) cooling jacket inner tube wall, 750 mm, 180°	K
100	TCI 12/180	TC (NiCr/Ni) cooling jacket inner tube wall, 850 mm, 180°	K
101	TCI 13/180	TC (NiCr/Ni) cooling jacket inner tube wall, 950 mm, 180°	K
102	TCI 15/180	TC (NiCr/Ni) cooling jacket inner tube wall, 1150 mm, 180°	K
103	T 002	TC (NiCr/Ni) cooling water, inlet of off-gas tube	K
104	TCI 9/90	TC (NiCr/Ni) cooling jacket inner tube wall, 550 mm, 90°	K
105	TCI 10/90	TC (NiCr/Ni) cooling jacket inner tube wall, 650 mm, 90°	K
106	TCI 11/90	TC (NiCr/Ni) cooling jacket inner tube wall, 750 mm, 90°	K
107	TCI 13/90	TC (NiCr/Ni) cooling jacket inner tube wall, 950 mm, 90°	K
108	TFSH 6/2/2	TC (NiCr/Ni), surface of fuel rod simulator 6, group 2, -150 mm	K
109	TCI 1/0	TC (NiCr/Ni) cooling jacket inner tube wall, -250 mm, 0°	K
110	TCI 4/0	TC (NiCr/Ni) cooling jacket inner tube wall, 50 mm, 0°	K
111	TCI 7/0	TC (NiCr/Ni) cooling jacket inner tube wall, 350 mm, 0°	K
112	TCI 11/0	TC (NiCr/Ni) cooling jacket inner tube wall, 750 mm, 0°	K
113	TCI 12/0	TC (NiCr/Ni) cooling jacket inner tube wall, 850 mm, 0°	K
114	TCI 13/0	TC (NiCr/Ni) cooling jacket inner tube wall, 950 mm, 0°	K
115	TCI 15/0	TC (NiCr/Ni) cooling jacket inner tube wall, 1150 mm, 0°	K
116	T 003	TC (NiCr/Ni) cooling water, outlet of off-gas tube	K
117	T 309	TC (NiCr/Ni) Ar bundle top	K
118	T 306	TC (NiCr/Ni) bundle foot outer surface	K

Chan	Designation	Instrument, location	Unit
119	TFSH 4/2/1	TC (NiCr/Ni), surface of fuel rod simulator 4, group 2, -250 mm	K
120	TCO 1/0	TC (NiCr/Ni) cooling jacket outer tube surface, -250 mm, 0°	K
121	TCO 7/0	TC (NiCr/Ni) cooling jacket outer tube surface, 350 mm, 0°	K
122	TCO 13/0	TC (NiCr/Ni) cooling jacket outer tube surface, 950 mm, 0°	K
123	T 601	Temperature off-gas, 2660 mm from test section outlet (flange)	K
124	T 513	Temperature bundle head top (wall)	K
125	T 514	Temperature bundle head, cooling water inlet	K
126	T 307	TC (NiCr/Ni) inner surface of inlet of off-gas pipe	K
127	T 305	TC (NiCr/Ni) bundle inlet flange	K
128	T 104	Temperature quench water	K
129	T 201	Temperature steam generator heating pipe	K
130	T 204	Temperature upstream steam flow instrument location 50 g/s	K
131	T 205	Temperature upstream steam flow instrument location 10 g/s	K
132	T 301A	Temperature downstream superheater	K
133	T 302	Temperature superheater heating pipe	K
134	T 303	Temperature upstream total flow instrument location	K
135	T 401	Temperature upstream Ar flow instrument (orifice) location	K
136	T 403	Temperature of Ar at inlet cooling jacket	K
137	T 404	Temperature of Ar at outlet cooling jacket	K
138	T 501	Temperature in containment (near from bundle head)	K
139	T 502	Temperature at outer surface of containment, 0°, 2.4 m	K
140	T 503	Temperature at outer surface of containment, 270°, 2.2 m	K
141	T 504	Temperature at outer surface of containment, 270°, 3.2 m	K
142	T 505	Temperature at outer surface of containment, 90°, 3.2 m	K
143	T 506	Temperature at outer surface of containment, 270°, 3.6 m	K
144	T 507	Temperature at outer surface of containment, 90°, 3.6 m	K
145	T 508	Temperature at outer surface of containment, 180°, 4.0 m	K
146		Reserve TC (NiCr/Ni)	
147	T 510	Temperature at outer surface of containment, 270°, 4.4 m	K
148	T 511	Gas temperature at bundle inlet	K
149	T 901	Temperature upstream off-gas flow instrument F 901	K
150	T 304	Temperature of pipe surface at valve V 302	K

Chan	Designation	Instrument, location	Unit
151	Ref. T02	Temperature of measuring crate 2 (reference temperature)	K
152	P 201	Pressure steam generator	bar
153	P 204	Pressure at steam flow instrument location 50 g/s	bar
154	P 205	Pressure at steam flow instrument location 10 g/s	bar
155	P 303	Pressure upstream total flow instrument (orifice) location	bar
156	P 401	Pressure upstream gas flow instrument location	bar
157	P 511	Pressure at bundle inlet	bar
158	P 512	Pressure at bundle outlet	bar
159	P 601	Pressure upstream off-gas flow instrument (orifice) F 601	bar
160	P 901	Pressure He supply for unheated rods	bar
161	L 201	Liquid level steam generator	mm
162	L 501	Liquid level quench water	mm
163	L 701	Liquid level condensation vessel	mm
164	Q 901	H ₂ concentration, off-gas (Caldos)	%H ₂
165	P 411	Pressure Ar + 5% Kr supply for heated rods	bar
166	P 403	Pressure Ar cooling of cooling jacket	bar
167	P 406	Pressure insulation shroud/cooling jacket	bar
168	F 104	Flow rate quench water	l/h
169	F 204	Flow rate steam 50 g/s	m ³ /h
170	F 205	Flow rate steam 10 g/s	m ³ /h
171	F 303	Flow rate at bundle inlet (steam + Argon), orifice	mbar
172	F 401	Argon gas flow rate	Nm ³ /h
173	F 403	Flow rate cooling gas	Nm ³ /h
174	F 601	Flow rate off-gas (orifice), 2000 mm from test section outlet (flange)	mbar
175	F 406	Flow rate argon into annulus between shroud and cooling jacket	g/s
176	E 201	Electric current steam generator	A
177	E 301	Electric current superheater	A
178	E 501	Electric current inner ring of fuel rod simulators	A
179	E 502	Electric current outer ring of fuel rod simulators	A
180	E 503	Electric voltage inner ring of fuel rod simulators	V
181	E 504	Electric voltage outer ring of fuel rod simulators	V

Chan	Designation	Instrument, location	Unit
182	Hub_V302	Gas supply valve lift	%
183	Ref. T03	Temperature of buffer amplifier (reference temperature)	K
184..... 199		Binary inputs	
200..... 215		Analog outputs	
250	E 505	Electric power inner ring of fuel rod simulators (<u>calculated</u>)	W
251	E 506	Electric power outer ring of fuel rod simulators (<u>calculated</u>)	W

Designations:

TFSH: TC at the surface of heated rod,

TFSU: TC at the surface of unheated rod;

(e.g. TFSH x/y/z with x = rod number, y = group number, z = axial level.)

TFC: centerline TC in the center of annular pellets (high temperature or standard);

TFS: standard TC at the rod surface;

TSH: TC at outer surface of shroud (high temperature or standard);

TIT: centerline TC inside the Zircaloy corner rods;

TCO: TC cooling jacket outer tube surface;

TCI: TC cooling jacket inner tube wall.

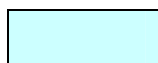
 gage outside of containment.

Table 9: QUENCH-12; Bundle thermocouples positions

Elevation, mm SRod/Elevation	-250	-150	-50	50	150	250	350	450	550	650	750	850	950	1050	1150	1250	1350
	1	2	3	4	5	6	7	8	9	10	11	12	13	14	15	16	17
1							N		N			W	W, W				
2					N							W	W				
3																	
4	N						N										
5															W		
6		N									W						
7																	
8			N										W				
9									N					W			
10														W			
11						N		N					W				W
12													W	W, W			
13					N											W	
14														W			
15						N								W			W
16										W							
17									N				W, W				
18								N				W		W, W			W
19																	
20										W					W		
21																	
22																	
23											W						
24				N													
25									N								
26												W					
27														W			
28							N										
29																	
30									N				W				W
31																	W

Number per elevation	1	1	1	2	2	2	3	2	2	6	2	4	10	8	5	3	3	
	Heated rods (18)			Unheated rods (13)														
	NiCr/Ni (20 TCs)																	
	W/Re (37 TCs = 23+14)																	
							W internal TCs											
													ICs to bundle bottom (7 W/Re+20 NiCr/Ni + 1 W/Re internal)					
																ICs to bundle top (16 W/Re surface + 13 W/Re internal)		

Table 10: QUENCH-12; Failure of thermocouples

Thermocouple	Elevation [mm]	Time at failure [s]	Failure temperature [K]
TFC 19/3/14	1050	Prior to test	
TFSU 15/3/16	1250	Prior to test	
TSH 11/180	750	Prior to test	
TSH 14/90	1050	7276	2438
TFSU 12/4/14	1050	7290	1466
TSH 14/270	1050	7489	358*)
TFSH 2/2/13	950	7492	345
TFSU 10/4/13	950	7554	371
TFC 14/4/13	950	7589	410
TFC 17/3/13	950	7638	299
TFSH 21/5/15	1150	7647	274
TFSH 31/5/17	1350	7656	275

*) Temperature readings of high-temperature thermocouples unreliable under ~500 K.

Table 11: QUENCH-12; Electrical resistances of circuits, contacts, and cables [mΩ]

Electrical resistance of separate rods at T = 20 °C.

Rod number	2	3	4	5	6	7	20	21	22	23	24	25	26	27	28	29	30	31
R before test, mΩ	7.3	8.8	8.6	8.0	7.6	6.9	7.5	7.0	7.6	8.0	8.3	6.8	8.2	7.8	7.1	9.0	7.3	8.1

Note: Measured values include the resistance of slide contacts $R_s=1.7$ mΩ.

The resistance of the cable between rod group and generator was measured as $R_c=1.3$ mΩ. The inner rod group of six rods is connected to the generator with three cables. There are six outer rod groups of two rods. Each outer group is connected to the generator with one cable. Therefore, the external (outside) resistance corresponding to each heated rod (indicated by SCDAP/RELAP as fxwid) is $R_{oe}=R_s+R_c=3.0$ mΩ for the outer rod circuit and $R_{ie}=R_s+R_c/3=2.1$ mΩ for the inner rod group.

Comparison of electrical resistance of rod groups at T = 20 °C before and after test QUENCH-12.

Rod group	Rod number	R before test, mΩ	R after test, mΩ	Change, %
Inner group (6 rods)	2, 3, 4, 5, 6, 7	1.24	1.12	-10
Outer group, 2 rods at 0°	22, 23	3.76	3.56	-6
Outer group, 2 rods 60°	24, 25	3.55	3.27	-9
Outer group, 2 rods 120°	26, 27	3.75	3.16	-19
Outer group, 2 rods 180°	28, 29	3.99	3.38	-18
Outer group, 2 rods 240°	30, 31	3.62	3.33	-9
Outer group, 2 rods 300°	20, 21	3.30	3.15	-5

Note: Measured values include the resistance of slide contacts $R_s=1.7$ mΩ.

Table 12: QUENCH-12; Sequence of events

Time [s]	Event
0 (12:21:52 h)	Start data recording, bundle at 906 K (TFC 1/13), electrical power at 3.5 kW.
1995	Plateau of electrical power of 9.9 kW reached. TFC 1/13: 1430 K.
2930	Temperature plateau at 950 mm reached. TFC 1/13: 1485 K; TSH 13/270: 1360 K.
5972	Corner rod D removed from bundle (reaction of TFSU 16/4/10).
6035	Transient start with electrical power rate of 5.1 W/s.
7158	Corner rod F removed from bundle (reaction of TFC 8/4/13, TFSU 8/4/3, TSH 3/270). TFC 1/13: 1809 K; TSH 13/90: 1800 K.
7241	First unheated rod failure (P 901 and He indication). TFC 1/13: 1943 K; TFC 14/4/13: 1992 K; TSH 13/90: 2136 K.
7249	First heated rod failure (P 411 and Kr indication); TSH 13/90: 2169 K.
7268	Shroud failure (P 406). TFC 1/13: 1960 K; TFC 14/4/13: 2054 K; TSH 13/90: 2204 K.
7270	Initiation of fast water injection. First indication of cooling (T 511). Start of moderate temperature escalation at elevations from 850 mm to 1350 mm.
7272	Start of quench water flow (F 104), water at -250 mm (TFSH 4/2/1).
7279	Temperature maximum. TFSU 10/4/13: 2164 K; TSH 14/90: 2445 K.
7280 - 7310	Temporary decrease of cladding surface temperatures due to fast water injection.
7299	Electrical power reduction from 16.6 kW. TFC 14/4/13: 1973 K; TSH 14/90: 2187 K.
7316	Electrical power at 3.9 kW (simulation of decay power). TFC 14/4/13: 1915 K; TSH 14/90: 2136 K.
7496	Water level (L 501) at elevation 900 mm (approximate position of shroud breach)
7649	Quench pump shut off. Maximum of water level reached: L 501= 1250 mm. Electrical power shut off. TFC 1/13: 380 K; TSH 15/0: 371 K.
7692	End of quench water flow (F 104).
7825	Water level decreased to the shroud breach position of ~900 mm. No further change in water level.
12172	End of data recording.
	Corner rod B removed from bundle after test termination.

Table 13: QUENCH-12; Maximum measured test bundle and shroud temperatures evaluated for upper elevations

Elevation [mm]	Thermocouple	Time [s]	Maximum temperature [K]
650	TFSU 16/4/10	7270	1438
650	TSH 10/90	7271	1409
750	TSFH 23/5/11	7271	1633
750	TSH 11/0	7275	1583
850	TSFH 3/2/12	7274	1958
850	TSH 12/0	7275	1919
950	TFSU 10/4/13	7279	2164
950	TSH 13/90	7275	2319
1050	TFC 9/3/14	7288	2123
1150	TFSH 5/2/15	7279	1668
1150	TSH 15/0	7282	1345
1250	TFSH 30/5/16	7279	1318
1250	TSH 16/0	7282	1255

Table 14: QUENCH-12; Water/steam balance

Accumulated mass of water [g]	
Total steam injected (F 205)	24067
Total quench water injected (F 104)	18321
Quench water from fast injection system	4000
Total used water	46388
Condensed water collected (L 701)*: 2174.979 mm	31102
Water/steam consumed by Zr oxidation (58 g H ₂)	522
Water found posttest in the test bundle	8900
Water found posttest retained in the ZrO ₂ fiber insulation**	5013
Water found posttest in the annulus of the upper plenum	400
Total water collected posttest as condensate	45937

*) water column of 1 mm corresponds to 14.3 g

**) posttest insulation weight (between -300 mm and 1000 mm): 14013 g; weight of the dry insulation (10 annuli): 10 x 900 g = 9000 g

Table 15: QUENCH-12; Quench front progression

Elevation [mm]	Thermocouple	Time *) [s]
50	TFSH 24/5/4	7278
150	TFSH 2/2/5	7357
250	TFSU 15/3/6	7366
350	TFSU 1/7	7386
450	TFSU 12/4/8	7401
550 (center)	TFSH 4/2/9	7373
550 (periphery)	TFSH 30/5/9	7406
650	TFSU 16/4/10	7419
750	TFSH 23/5/11	7443
850	TFSH 26/5/12	7451
950	TFSU 17/3/13	7466
1050	TFSH 27/5/14	7543
1150	TFSU 9/3/15	7557
1250	TFSH 30/5/16	7567

*) First time at boiling point (~395 K).

Table 16: QUENCH-12; Results of bundle filling with epoxy resin

Elevation, mm	Epoxy mass, g/10 mm
260	0
270	100
280	115
290	95
300	100
310	105
320	100
330	95
340	95
350	85
360	85
370	100
380	85
390	95
400	90
410	100
420	80
430	105
440	100
450	75
460	85
470	90
480	85
490	105
500	100
510	100
520	90
530	90
540	85
550	95
560	100
570	95
580	90
590	85
600	100
610	90
620	70
630	105
640	85
650	85
660	75
670	85
680	95
690	70
700	85

Elevation, mm	Epoxy mass, g/10 mm
710	85
720	95
730	85
740	90
750	85
760	95
770	90
780	80
790	95
800	100
810	85
820	95
830	85
840	100
850	95
860	95
870	95
880	90
890	100
900	70
910	60
920	75
930	70
940	100
950	50
960	50
970	85
980	115
990	95
1000	90
1010	115
1020	95
1030	105
1040	80
1050	100
1060	100
1070	135
1080	90
1090	90
1100	95
1110	105
1120	95
1130	140
1160	160

Table 17: QUENCH-12; Cross sections for the metallographic examination

Sample	Sample length (mm)	Axial position (mm)		Remarks
		bottom	top	
QUE-12-a	540	-10	530	Lower remnant
Cut	4	530	534	
QUE-12-1	16	534	550	Spacer 4, 550 mm polished
Cut	4	550	554	
QUE-12-2	16	554	570	554 mm polished (RIAR)
Cut	4	570	574	
QUE-12-b	44	574	618	
Cut	2	618	620	
QUE-12-13	10	620	630	For hydrogen analysis
Cut	4	630	634	
QUE-12-3	16	634	650	TC elevation 10, 650 mm polished
Cut	4	650	654	
QUE-12-4	16	654	670	654 mm polished (RIAR)
Cut	4	670	674	
QUE-12-c	43	674	717	
Cut	2	717	719	
QUE-12-14	11	719	730	For hydrogen analysis
Cut	4	730	734	
QUE-12-5	16	734	750	TC elevation 11, 750 mm polished
Cut	4	750	754	
QUE-12-6	16	754	770	754 mm polished (RIAR)
Cut	4	770	774	
QUE-12-d	42	774	816	
Cut	2	816	818	
QUE-12-15	12	818	830	For hydrogen analysis
Cut	4	830	834	

Sample	Sample length (mm)	Axial position (mm)		Remarks
		bottom	top	
QUE-12-7	16	834	850	TC elevation 12, 850 mm polished
Cut	4	850	854	
QUE-12-8	16	854	870	854 mm polished (RIAR)
Cut	4	870	874	
QUE-12-e	56	874	930	
Cut	4	930	934	
QUE-12-9	16	934	950	TC elevation 13, 950 mm polished
Cut	4	950	954	
QUE-12-10	16	954	970	954 mm polished (RIAR)
Cut	4	970	974	
QUE-12-f1	58	974	1032	
Cut	2	1032	1034	
QUE-12-12	16	1034	1050	TC elevation 14, 1050 mm polished
Cut	4	1050	1054	
QUE-12-16	11	1054	1065	For hydrogen analysis
Cut	2	1065	1067	
QUE-12-f2	54	1067	1121	
Cut	2	1121	1123	
QUE-12-17	9	1123	1132	For hydrogen analysis
Cut	2	1132	1134	
QUE-12-11	16	1134	1150	TC elevation 15, 1150 mm polished
Cut	2	1150	1152	
QUE-12-g	198	1152	1350	Upper remnant
Cut	4	1350	1354	
		1354		Disposal

11.01.2008

Table 18: QUENCH-12; Oxide layers, α -layers and residual metal of withdrawn corner rods D, F, B

	ZrO ₂ layer at 8 points on circumference (total thickness incl. gaps), μm	ZrO ₂ average, μm	Typical thicknesses of separate ZrO ₂ scales, μm	ZrO ₂ deviation, μm	ZrO ₂ thinnest scale, μm	ZrO ₂ thickest scale, μm	α -layer at 4 points on circumference μm	α -layer average, μm	Remained metal ($\alpha+\beta$), mm^2
Corner rod D 700 mm	86; 62; 64; 48; 76; 56; 24; 62	60	7 - 12 and very small scales with 1 μm and smaller	19	10	108	20; 25; 15; 20	20	28.16
Corner rod D 940 mm	160; 112; 120; 120; 160; 100; 90; 120	123	3 - 4 and 10 - 12; only few regions with breakaway	25	90 (no break-away)	180 (break-away)	90; 100; 100; 110	100	26.47
Corner rod D 1120 mm	60; 216; 62; 48; 72; 92; 100; 96	93	8; 10 and 12	53	26	228	20; 20; 15; 25	20	27.63
Corner rod F 700 mm	32; 12; 15; 88; 108; 14; 44; 20	42	2 - 4 and 12	37	8	110	15; 10; 15; 20	15	26.48
Corner rod F 940mm	140; 216; 220; 204; 260; 230; 160; 270	213	10; 25; 70 - 80	45	130	335	160; 200; 200; 180	185	25.15
Corner rod F 1120 mm	25; 70; 35; 45; 0; 22; 44; 25	33	2 - 3; 5 - 20	21	0	100	25; 15; 30; 15	21	25.93
Corner rod B 700 mm	10; 28; 8; 10; 10; 32; 12; 6	15	not determinable	10	2	35	40; 40; 50; 30	40	27.40
Corner rod B 820 mm	120; 126; 130; 100; 122; 126; 104; 94	115	3 - 5, only few regions with breakaway, otherwise stable layer	14	55	130	150; 130; 150; 150	145	25.97

Table 19: Estimation of complete oxide layer thicknesses on corner rods withdrawn from the QUENCH-12 test bundle

Corner Rod	Elevation mm	Area of residual metal mm ²	Diameter of residual metal D_r mm	Calculated* oxide layer δ_{ox} μm	Measured residual oxide average of 8 points δ_r μm	Spalled oxide** δ_s μm	Metallic area meas. by
<i>D</i>	698	28.1	5.98	17	60		RIAR
D	702	28.16	5.99	9	60		FZK
<i>F</i>	698	27.1	5.88	92	42	50	RIAR
F	702	26.48	5.81	151	42	109	FZK
<i>B</i>	698	27.9	5.96	28	15	13	RIAR
B	702	27.4	5.91	73	15	58	FZK
<i>B</i>	818	25.9	5.74	203	115	88	RIAR
B	822	25.97	5.75	195	115	80	FZK
<i>D</i>	938	26.6	5.82	139	123	16	RIAR
D	942	26.47	5.81	152	123	29	FZK
<i>F</i>	938	24.5	5.58	326	213	113	RIAR
F	942	25.15	5.66	266	213	53	FZK
<i>D</i>	1118	28.2	5.99	6	93		RIAR
D	1122	27.63	5.93	54	76		FZK
<i>F</i>	1118	26.4	5.8	159	33	126	RIAR
F	1122	25.93	5.75	198	33	165	FZK

* $\delta_{ox} = 1.56 \cdot (6 - D_r) / 2$

** $\delta_s = \delta_{ox} - \delta_r$

D – withdrawn before transient initiation

F – withdrawn before quench initiation

B – withdrawn on end of test

Table 20: Average layer thicknesses measured by FZK at lower cross sections of the QUENCH-12 test bundle

Elevation, mm	1		2		3		4		5		6		7								
	ZrO ₂	α-layer	β-layer	ZrO ₂	α-layer	β-layer	ZrO ₂	α-layer	β-layer	ZrO ₂	α-layer	β-layer	ZrO ₂	α-layer	β-layer						
Rod																					
550	34	50	573	27	44	596	30	39	604	20	41	594	28	47	596	28	49	591	24	48	593
650	63	113	503	41	91	541	33	81	551	40	87	546	42	99	529	48	100	530	49	98	527
750	85	113	493	78	100	525	73	85	545	82	100	525	81	95	528	71	100	533	86	105	523
850				334		463										295		476	321		458
Rod																					
		8			9			10		11			12		13					14	
550	14	20	643	8	19	631	5	13	640	15	16	642	12	15	659	10	24	637	10	25	635
650	23	60	575	33	53	575	27	36	616	27	60	568	29	55	575	29	39	626	30	63	567
750	55	99	536	59	83	548	54	70	560	63	95	535	63	100	523	63	83	545	54	103	528
850	233	234	259	273	255	240	315	445		343	440								258		505
Rod																					
		15			16			17		18			19		20					21	
550	12	25	628	10	23	625	22	27	621	18	35	613	13	27	631	13	25	628	8	20	628
650	32	65	578	31	63	585	39	77	553	28	70	575	29	64	571	30	69	571	30	59	574
750	50	90	550	51	76	564	60	100	518	51	88	555	57	106	527	66	90	553	65	78	550
850	203	200	350	139	154	440	248	500		286	220	270	259	175	325	239	263	288			
Rod																					
		22			23			24		25			26		27					28	
550	7	16	641	10	20	640	11	26	647	24	36	609	20	37	606	24	37	610	25	33	620
650	30	62	573	31	60	583	34	58	580	27	66	564	32	78	558	31	78	565	30	72	568
750	76	87	546	77	91	542	75	95	533	73	100	523	65	110	528	59	80	550	66	80	565
850										250	275	300	228	226	308	173	208	340	223	257	273
Rod																					
		29			30			31													
550	24	41	609	23	40	625	16	38	619												
650	31	71	569	25	68	580	32	65	568												
750	65	83	555	71	85	543	61	98	525												
850	290		479	255	260	250	220	535													

Table 21: Average layer thicknesses measured by FZK at upper cross sections of the QUENCH-12 test bundle

Elevation, mm	1		2		3		4		5		6		7		
	ZrO ₂	α-layer	β-layer	ZrO ₂	α-layer	β-layer	ZrO ₂	α-layer	β-layer	ZrO ₂	α-layer	β-layer	ZrO ₂	α-layer	β-layer
Rod															
950	905			980			875			957			925		
1050	695	15		608	450		595	200		710	240		735	320	
1150	98	116	485	84	106	508	99	129	483	86	113	500	85	109	506
Rod		8						10						12	
950	735	250		975	300		1000			1000			1000		
1050	340	420		300	460		433	430		568	250		528	338	
1150	41	72	573	51	75	556	40	64	573	55	74	555	59	81	545
Rod		15						17						19	
950	1100			870	400		967	200		930			910	350	
1050	485	383		293	483		405	380		383	403		243	508	
1150	58	79	558	42	63	590	51	73	566	41	78	564	31	56	596
Rod		22						24						26	
950	967			950			1000			913			975		
1050	318	560		310	465	68	368	405		410	353		310	438	
1150	27	46	596	23	43	604	36	46	594	33	48	590	29	48	599
Rod		29						31						27	
950	1000			917			833	100							
1050	218	268	243	223	510		223	515							
1150	24	43	610	20	46	605	27	49	594						

Table 22: Average layer thicknesses measured by RIAR at different cross sections of the QUENCH-12 test bundle

Elevation, mm	1		2		3		4		5		6		7							
	ZrO ₂	α-layer	β-layer	ZrO ₂	α-layer	β-layer	ZrO ₂	α-layer	β-layer	ZrO ₂	α-layer	β-layer	ZrO ₂	α-layer	β-layer					
Rod																				
554	57	623	55	633	16	56	638	17	58	637	21	61	639	20	58	634				
654	60	617	71	637	34	57	643	39	62	631	46	66	636	49	72	634				
754	89	605	81	628	74	97	622	84	110	624	83	99	623	74	108	630				
854			354	439										314		410				
Rod																				
554	41	664	36	660		37	662		40	660		40	667		38	659				
654	58	631	27	633	22	43	638	25	66	630	26	65	639	26	53	660				
754	53	639	54	635	47	78	633	62	90	629	61	94	626	62	96	626				
854	243	499	299	480																
Rod																				
554	12	37	654	11	32	653	41	646		41	640		40	648		40	653			
654	29	80	640	28	81	644	89	633	26	75	632	29	65	630	35	68	644			
754	47	110	636	46	102	638	51	624	51	107	636	62	84	629	71	106	632			
854	251	198	510	167	165	574	276	471	306	434										
Rod																				
554	47	651	39	632	18	45	639	38	652	12	43	655		43	641		43	647		
654	28	67	644	28	79	644	84	642	30	76	635	27	77	649	31	94	642	32	84	649
754	71	97	630	69	126	621	65	623	61	125	627	66	92	634	59	118	633	62	96	643
854			240		515	253	484	283	492	259	197			452	197			248		505
Rod																				
554	43	640	41	639		52	624													
654	31	83	637	27	84	638	28	80	634											
754	65	95	640	68	93	629	61	104	626											
854	314		455	284	248	489														

Table 23: Detailed results of metallographic measurement performed by RIAR at withdrawn corner rods

Rod designation	Holder designation	Thickness of α -layer, μm		$S_{\text{rod section}}$, mm^2	D_{measured} , mm	$\delta_{\text{oxide film}}$, μm
D	D1 ~700-680 mm		39	28,1	5,98	11
			37			
			37			
		Average	38			
		RMSD	1			
	D3 ~940-920 mm		109	26,6	5,82	89
			151			
			163			
			164			
		Average	147			
	D2 ~1120-1100 mm		50	28,2	5,99	4
			52			
Average		51				
RMSD		2				
F	F2 ~700-680 mm		74	27,1	5,88	61
			65			
			37			
		Average	59			
		RMSD	19			
	F1 ~940-920 mm		205	24,5	5,58	209
			201			
		Average	203			
		RMSD	3			
	F3 ~1120-1100 mm		66	26,4	5,80	102
			70			
		Average	68			
RMSD		2				
B	B2 ~700-680 mm		31	27,9	5,96	18
			26			
			32			
			35			
		Average	31			
		RMSD	4			
	B1 ~820-800 mm		120	25,9	5,74	130
			126			
			118			
		Average	121			
		RMSD	5			

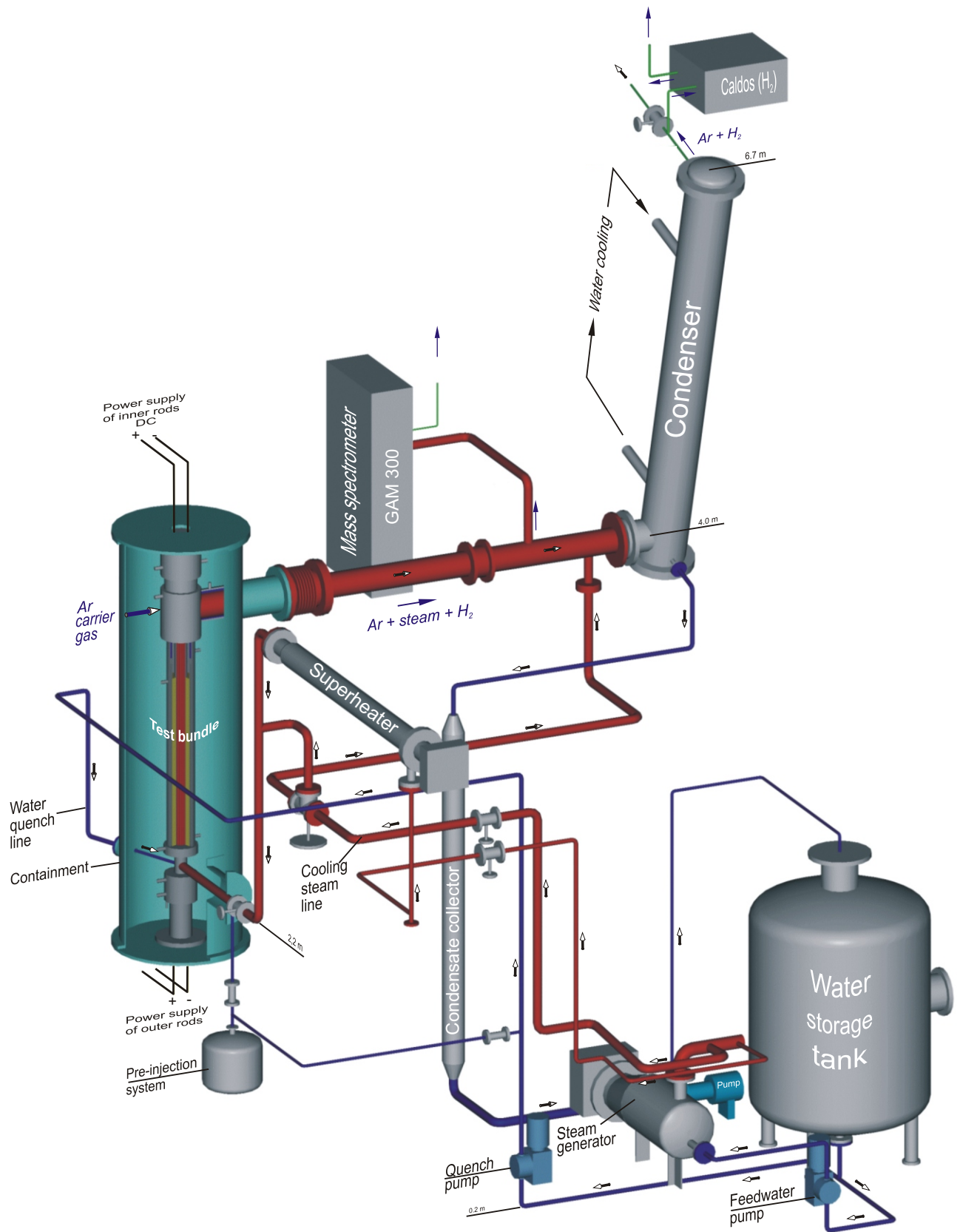


Fig.1-QUE12-Gesamtanlage.cdr
30.08.07 - IMF

Fig. 1: QUENCH Facility - Main components.

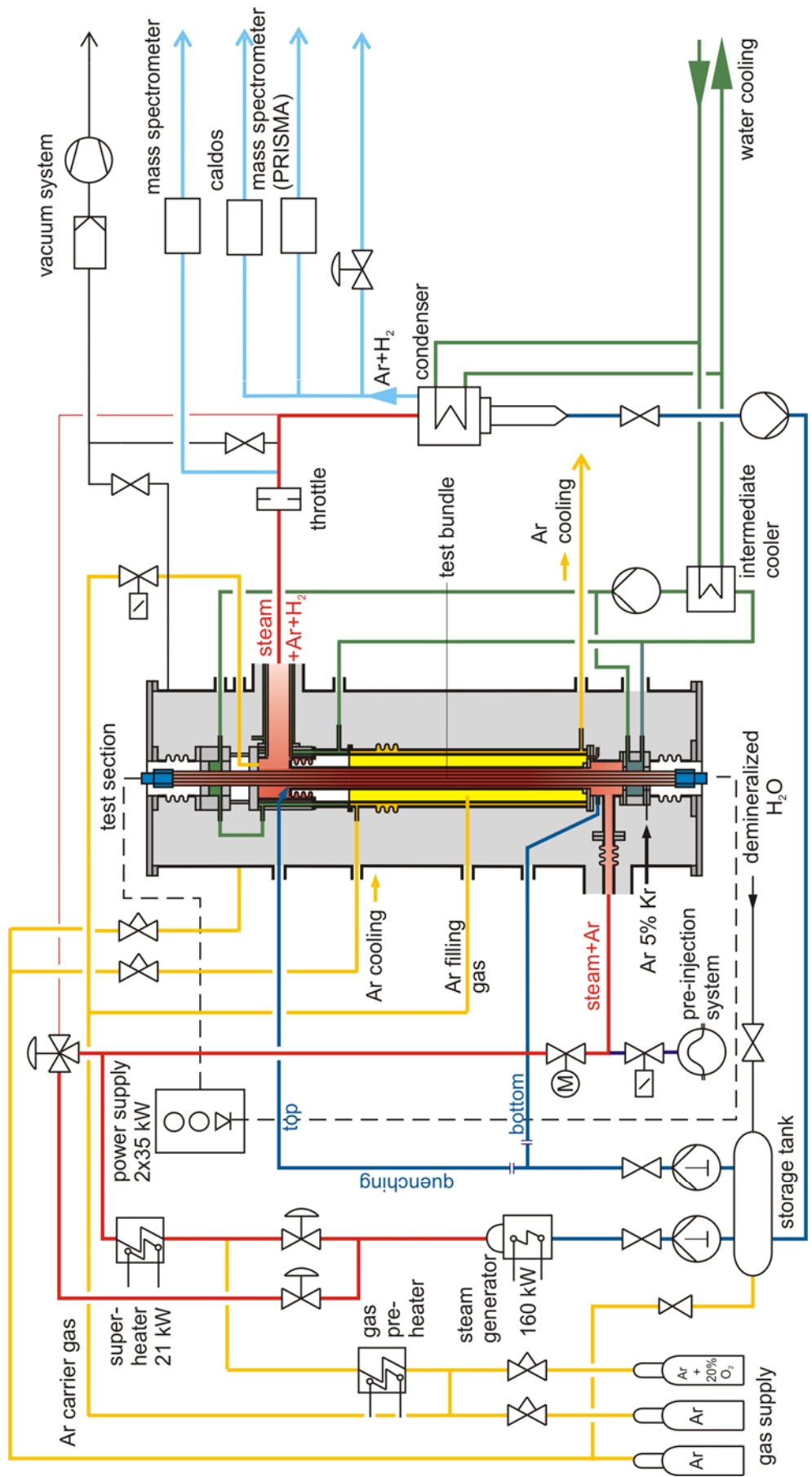


Fig.2-QUE 12-Flow diagram.doc
30.08.07 - IMF

Fig. 2: Flow diagram of the QUENCH test facility

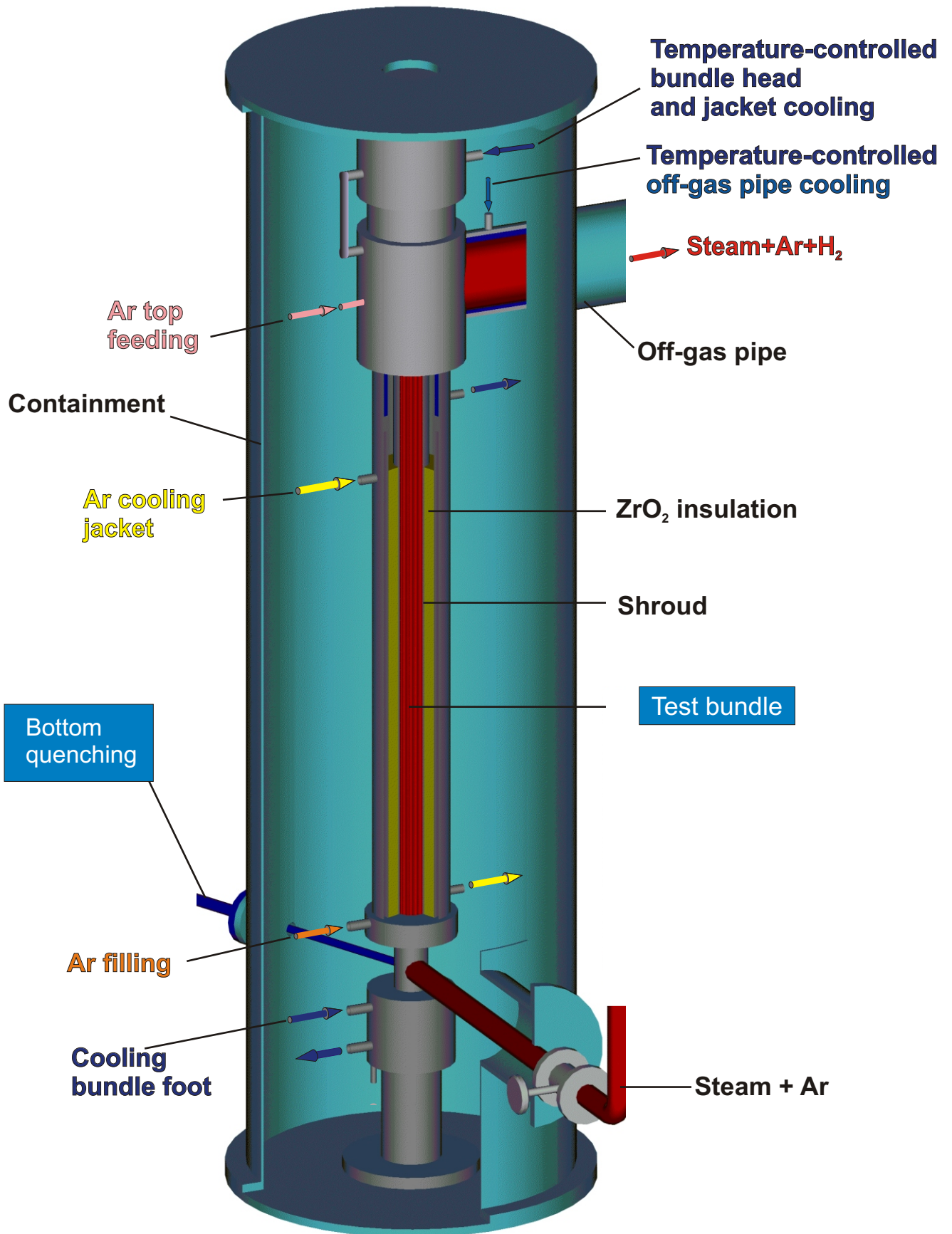


Fig.3-QUE12 Containment 3D.cdr
18.09.06 - IMF

Fig. 3: QUENCH Facility; Containment and test section.

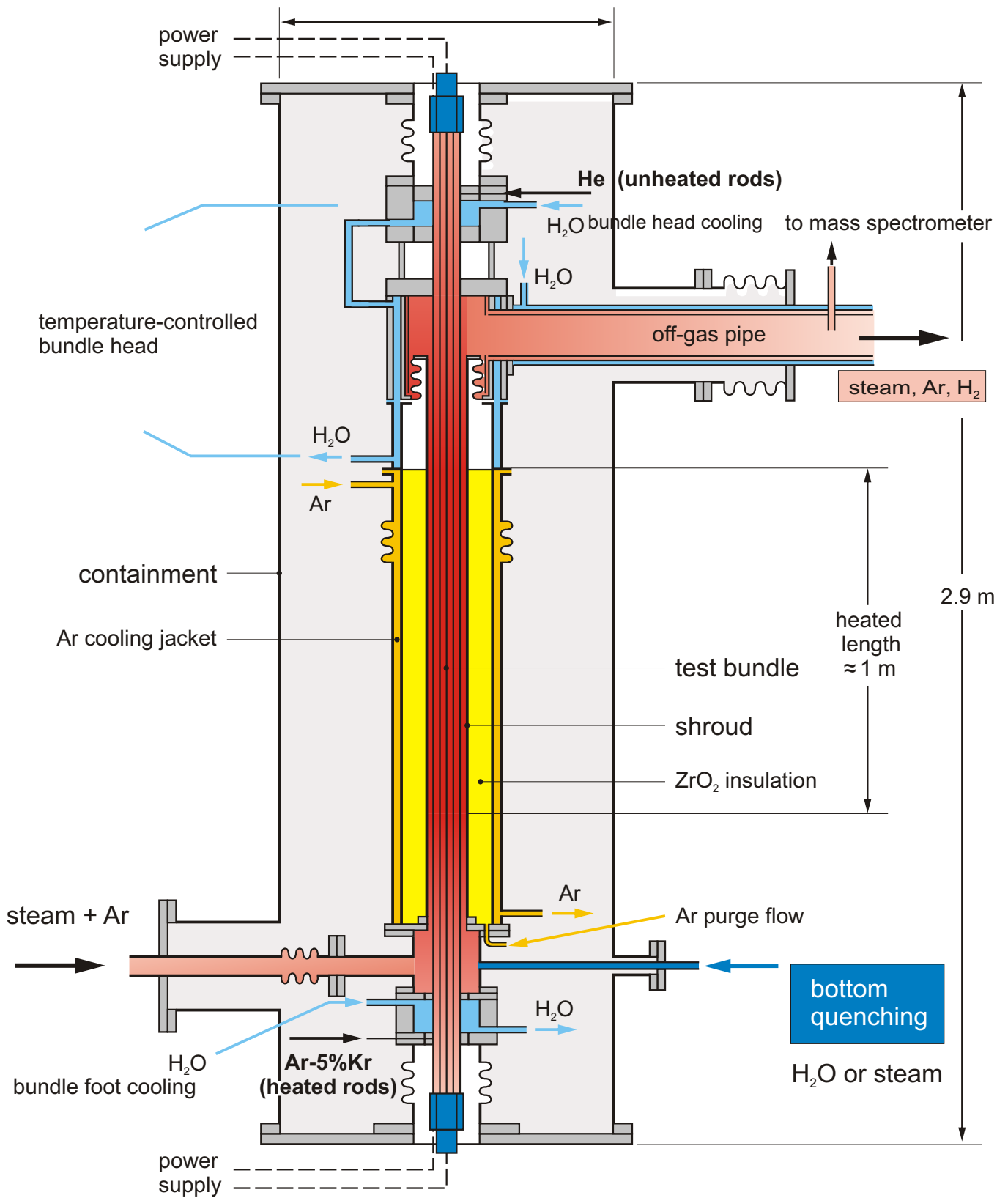


Fig 4-QUE12-Flow lines.cdr
08.01.08 - IMF

Fig. 4: QUENCH-12; Test section with flow lines.

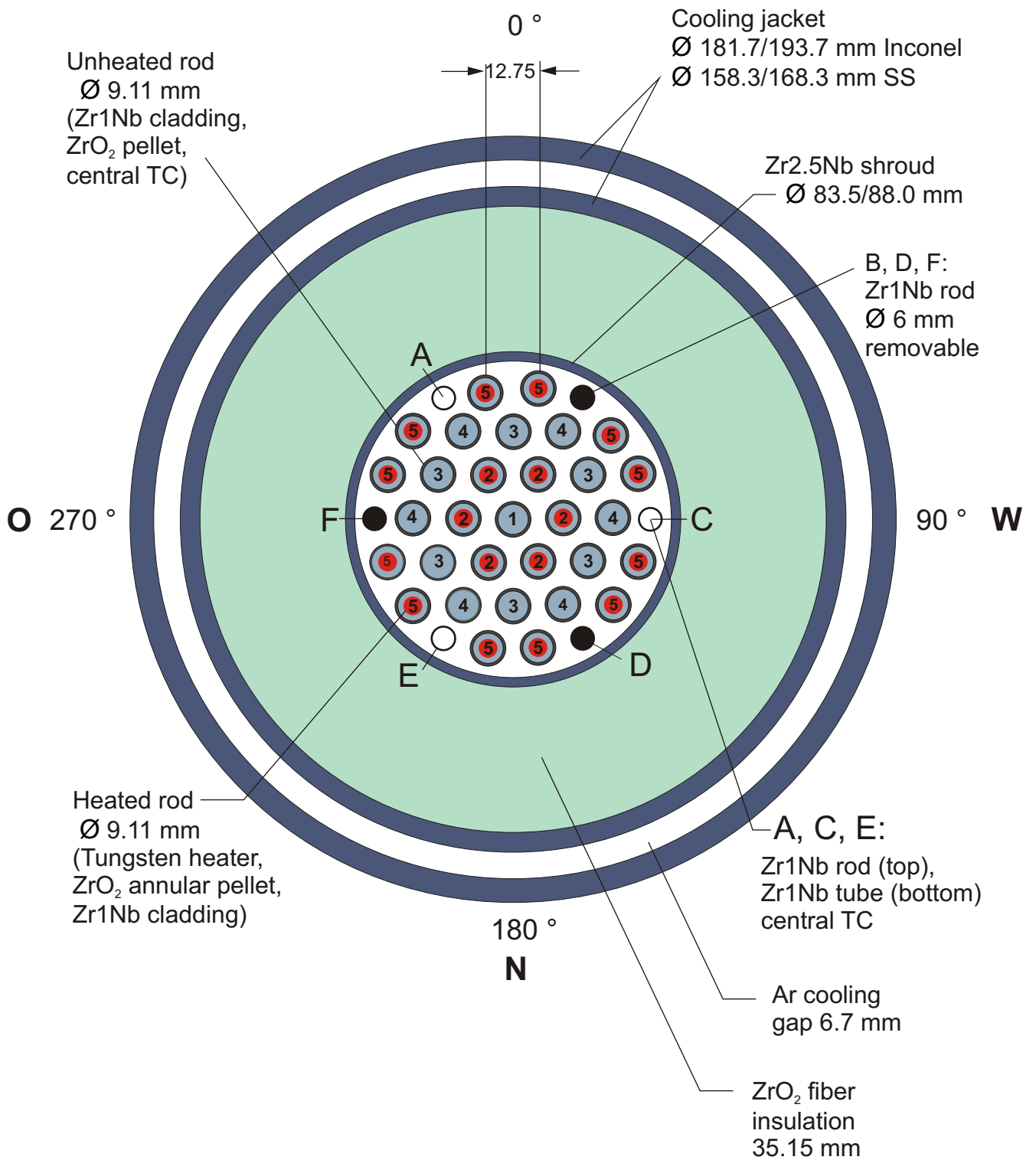


Fig.5-QUE12 Cross section.cdr
 27.03.08 - IMF

Fig. 5: QUENCH-12; VVER fuel rod simulator bundle (cross section, top view) including rod group numbers.

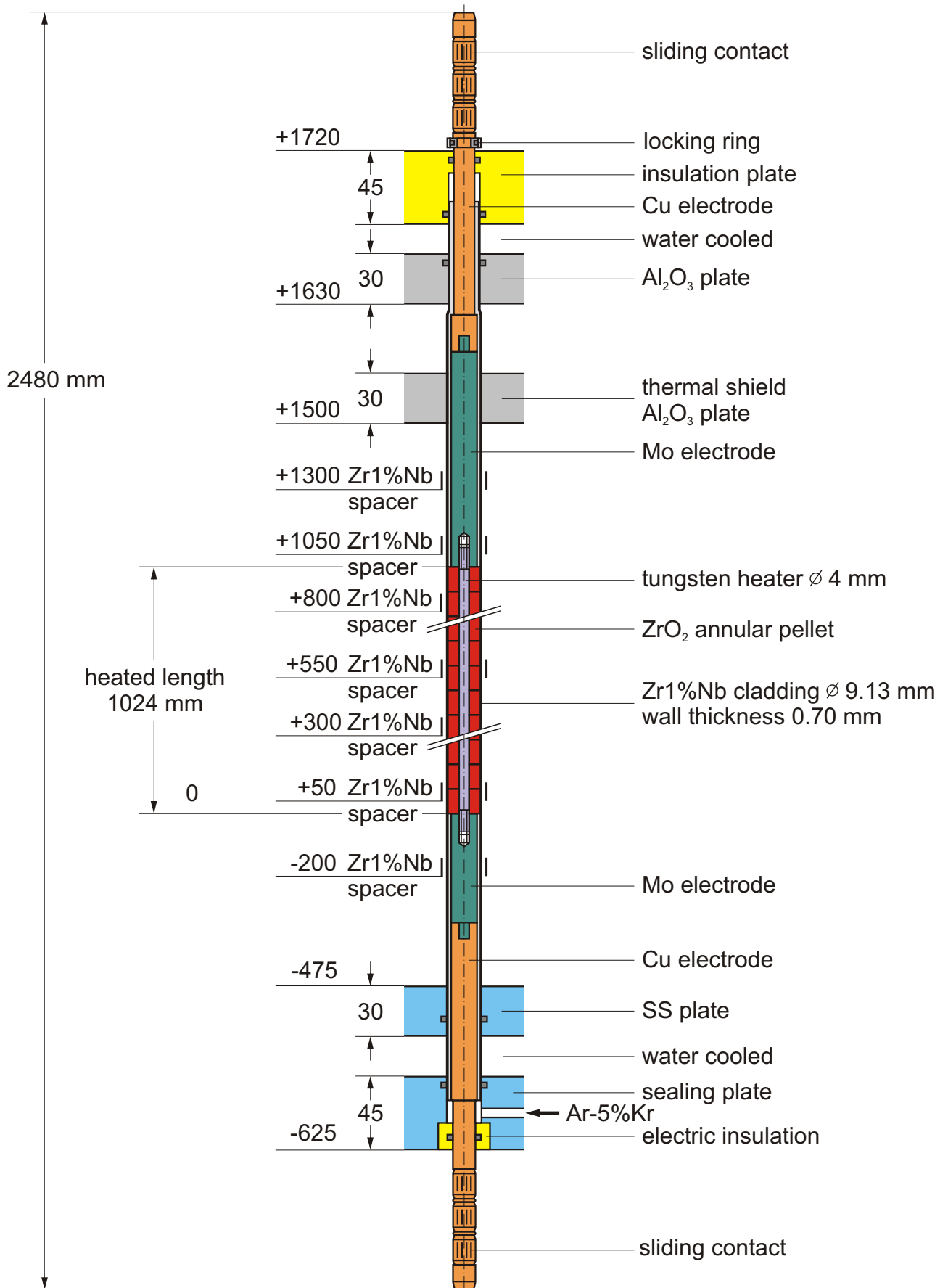


Fig.6-QUE12 heated rod.cdr
14.01.08 - IMF

Fig. 6: QUENCH-12; Heated VVER fuel rod simulator.

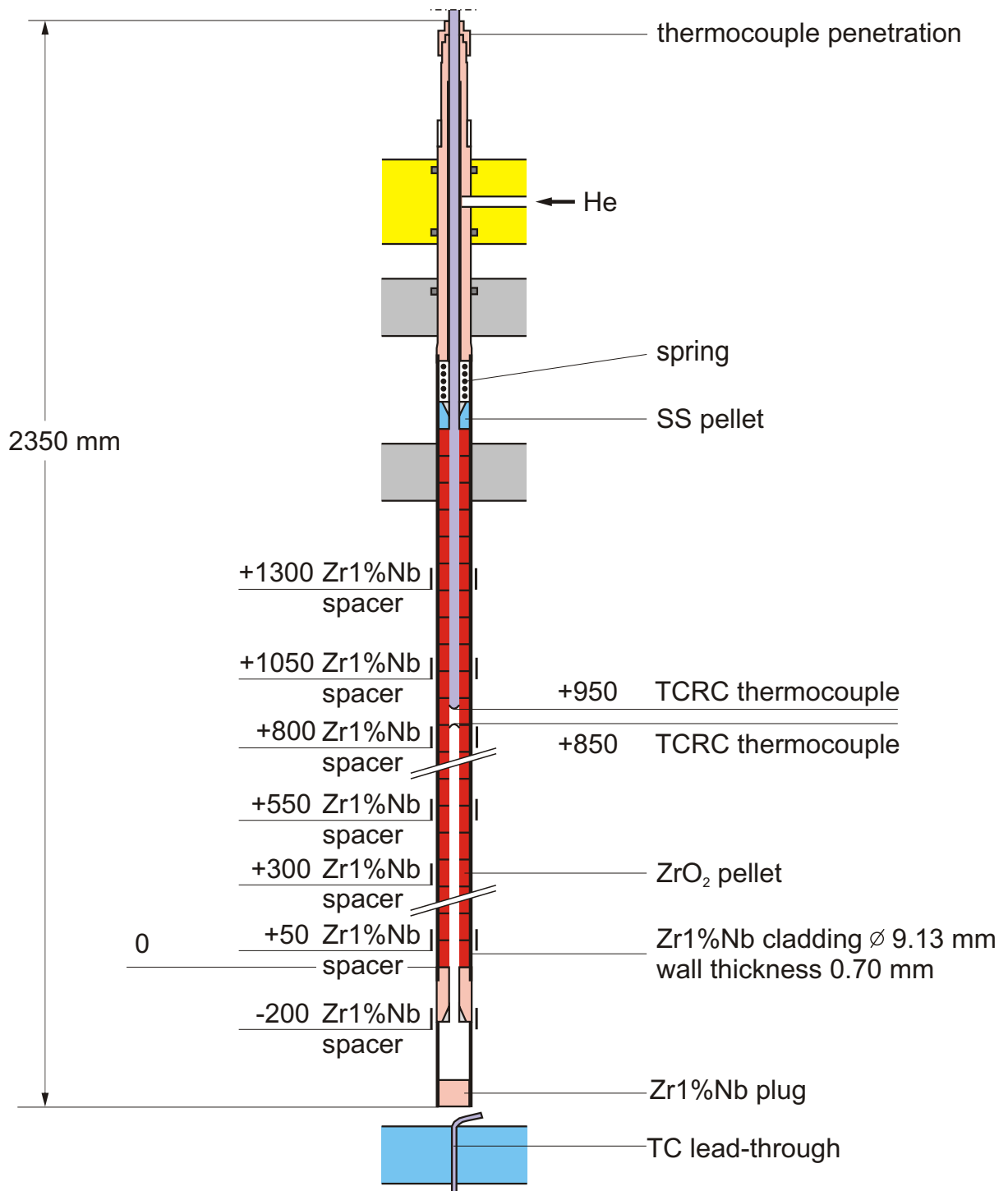


Fig. 7-QUE12 unheated rod.cdr
14.01.08 - IMF

Fig. 7 : QUENCH-12; Unheated VVER fuel rod simulator.

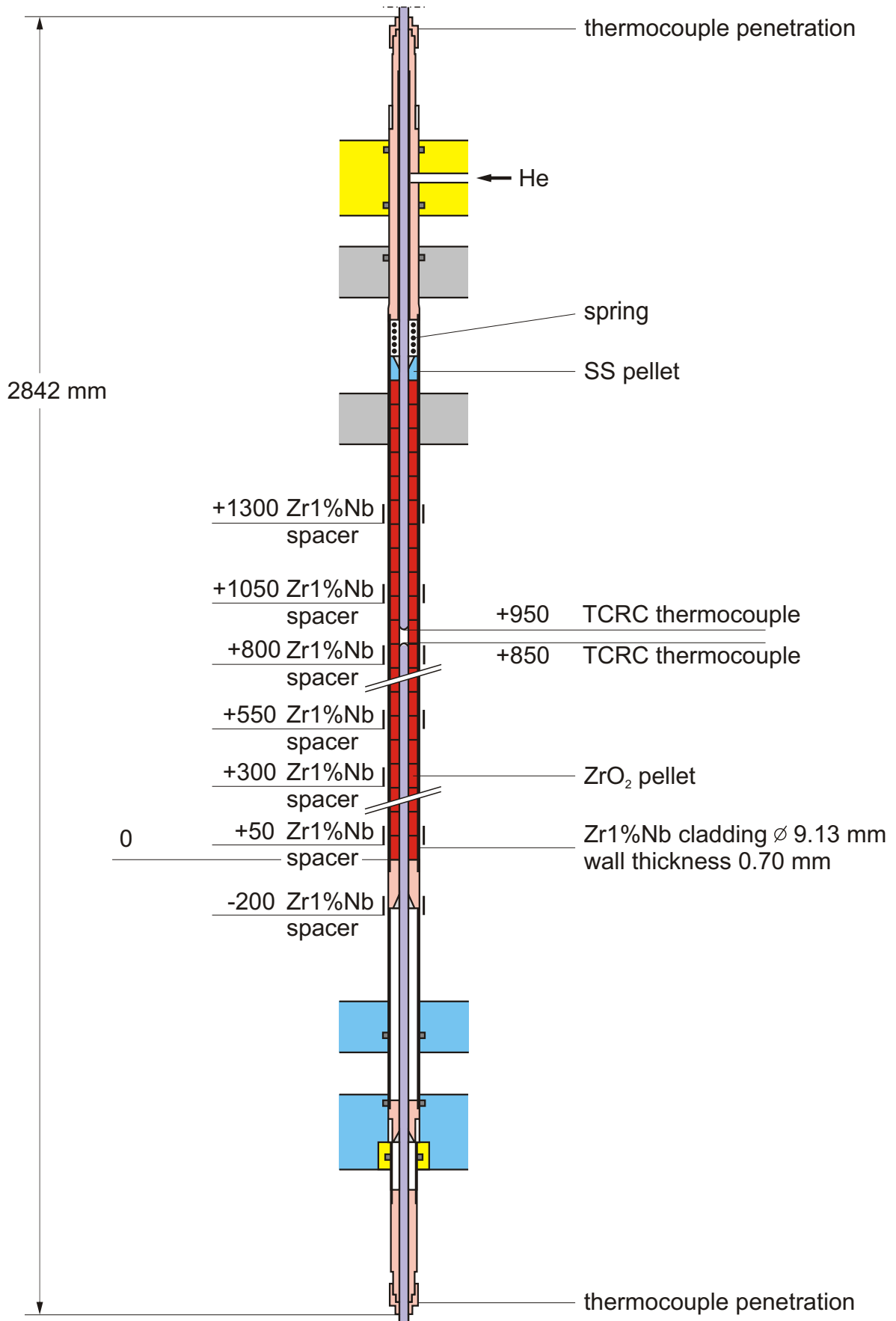


Fig.8-QUE12 unheated central rod.cdr
14.01.08 - IMF

Fig. 8: QUENCH-12; Unheated VVER-type central rod.

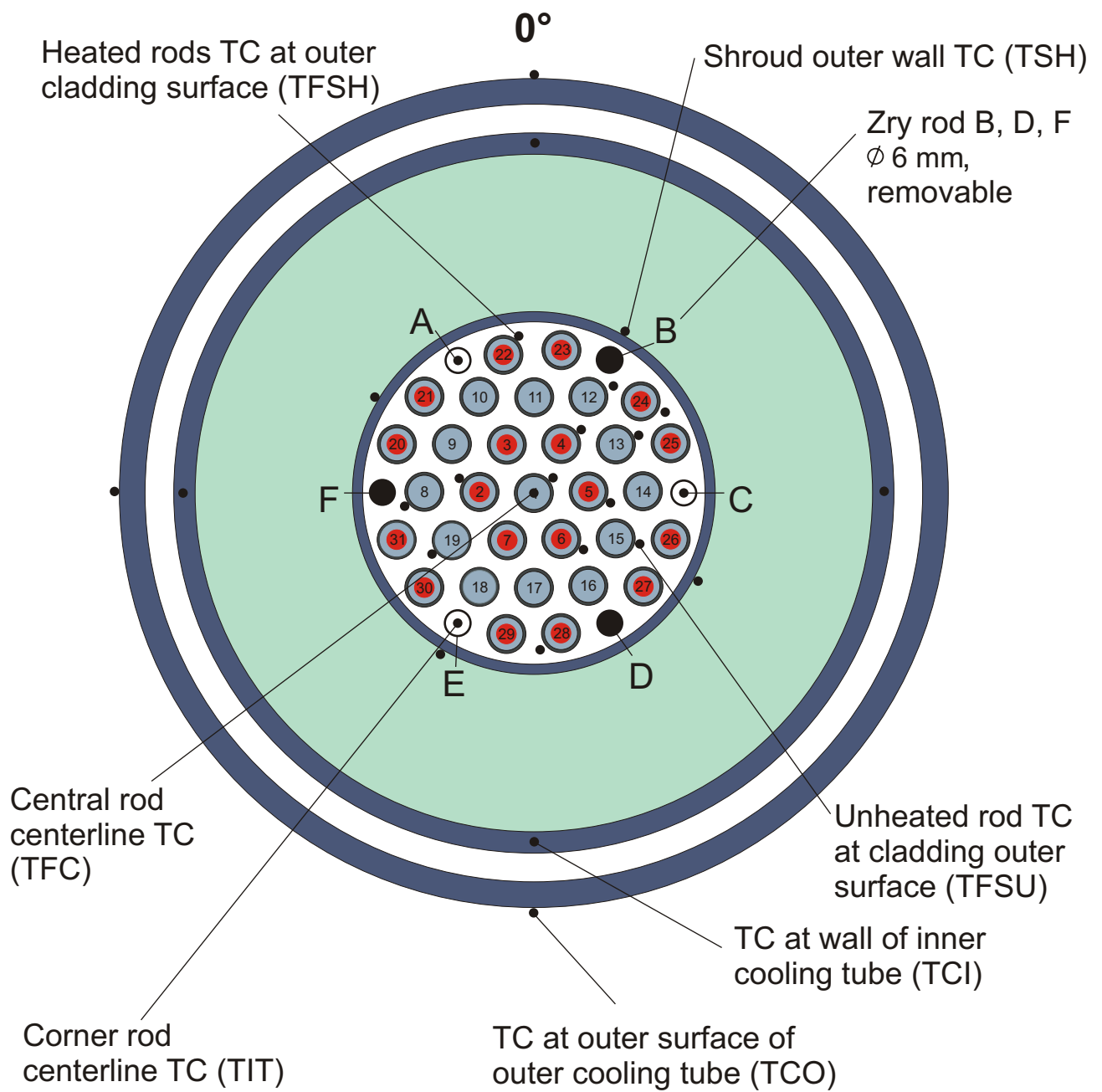


Fig. 9-QUE12 TC instr.cdr
18.01.08 - IMF

Fig. 9: Principal locations of the different types of thermocouples used in the QUENCH-12 test bundle (top view) together with rod designations.

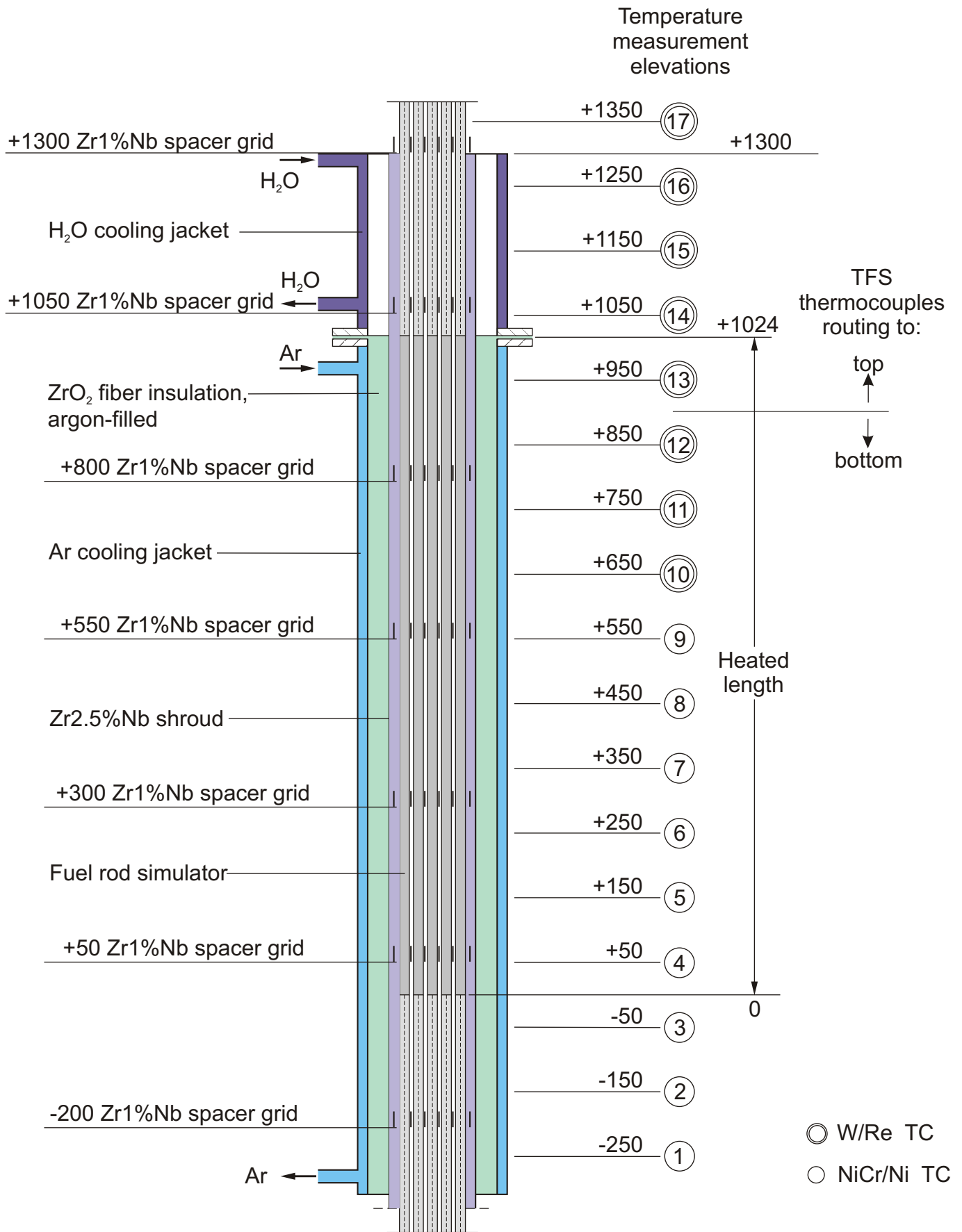
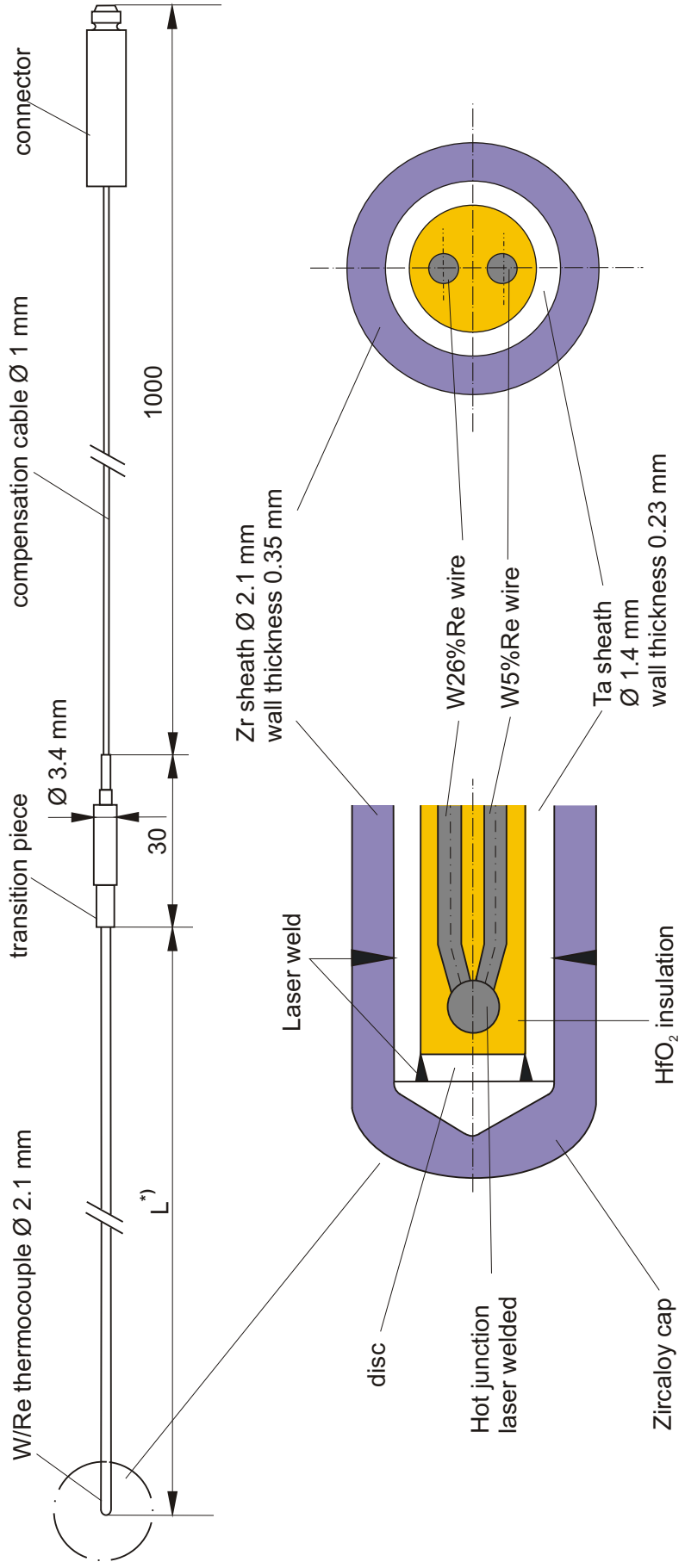


Fig.10-QUE12-TC elevations.cdr
18.01.08 - IMF

Fig. 10: QUENCH-12; Axial temperature measurement locations in the test section.



*) L: high-temperature section length dependent on the TC position in the test bundle 500 mm - 1700 mm

Fig.11-QUE12-High-temp thermocouple.cdr
17.01.08 - IMF

Fig. 11: QUENCH; High-temperature thermocouple.

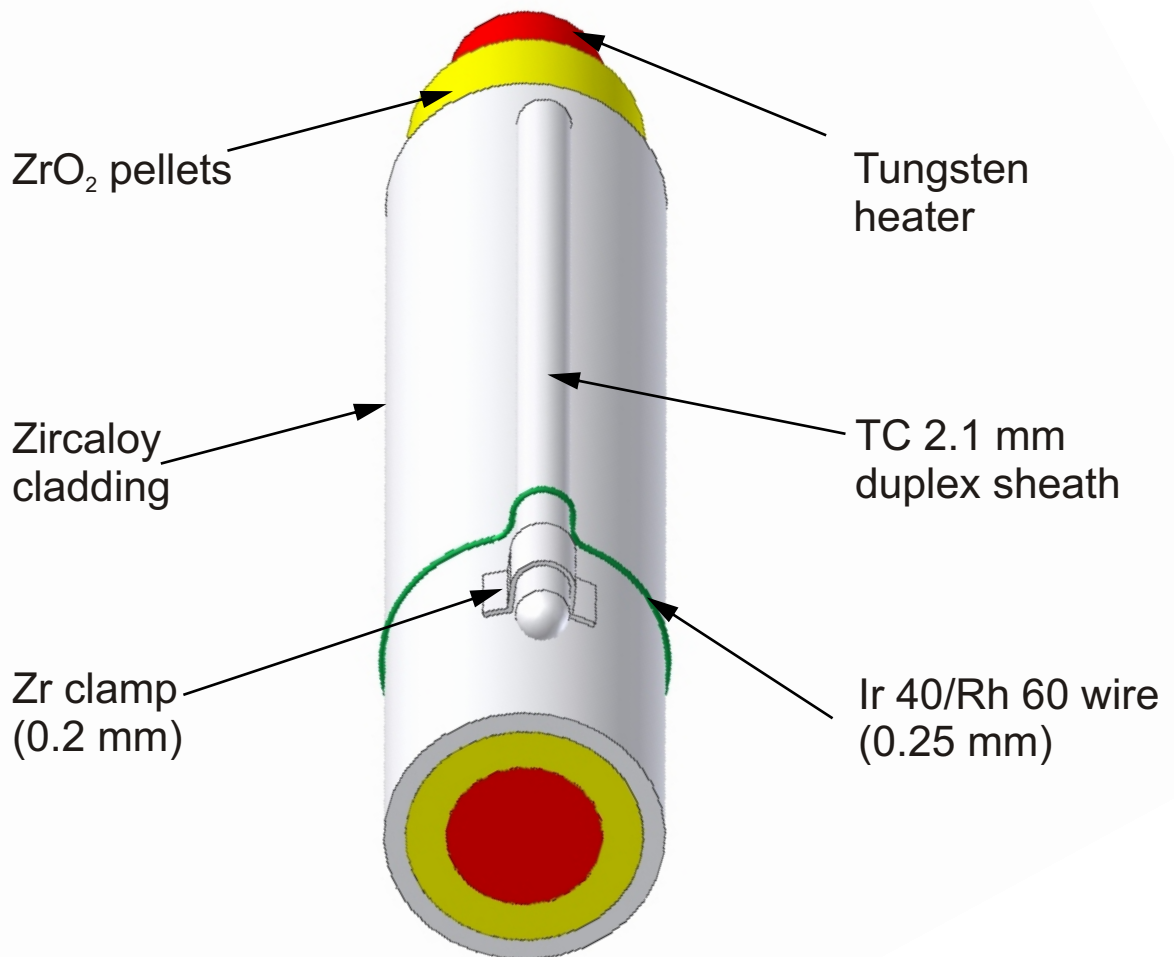
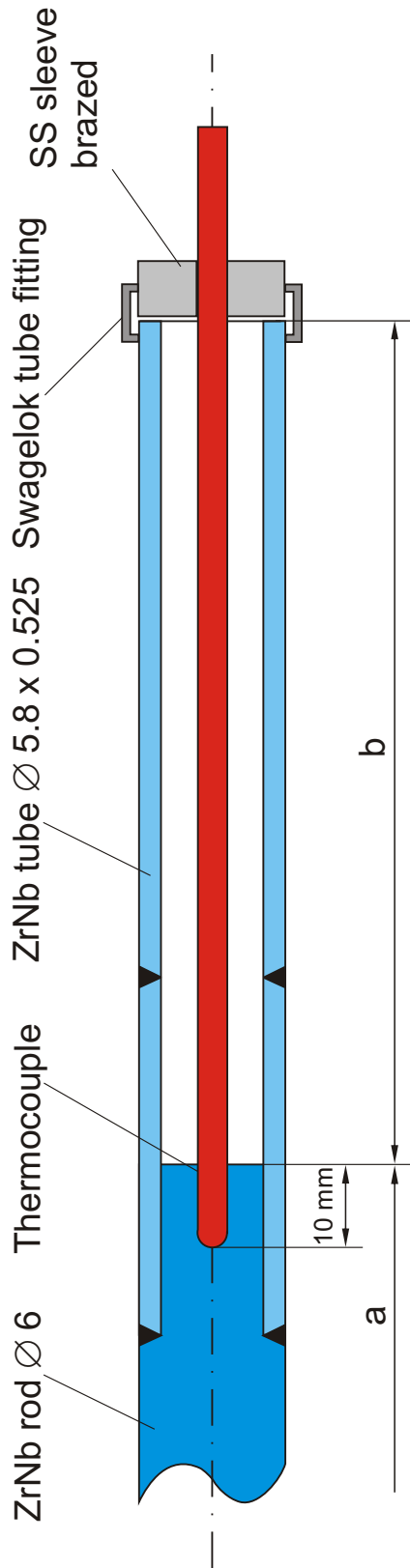


Fig 12-QUE12-TC Fastening3.cdr
17.01.08 - IMF

Fig. 12: QUENCH-12; Concept for fastening of cladding outer surface thermocouples.

(TIT A13, TIT C12, TIT E11)



- Rod A: TIT A/13 (950 mm), W/Re, $\varnothing 2.1$ mm, a = 360 mm, b = 2080 mm
 Rod C: TIT C/12 (850 mm), W/Re, $\varnothing 2.1$ mm, a = 460 mm, b = 1980 mm
 Rod E: TIT E/11 (750 mm), W/Re, $\varnothing 2.1$ mm, a = 560 mm, b = 1880 mm
 (Rod B, D, F: ZrNb rod, $\varnothing 6$ mm, removable)

Fig 12-QUE12-TC in Zry-rod.cdr
 17.01.08 - IMF

Fig. 13: QUENCH-12; Arrangement of the thermocouples inside the corner rods.

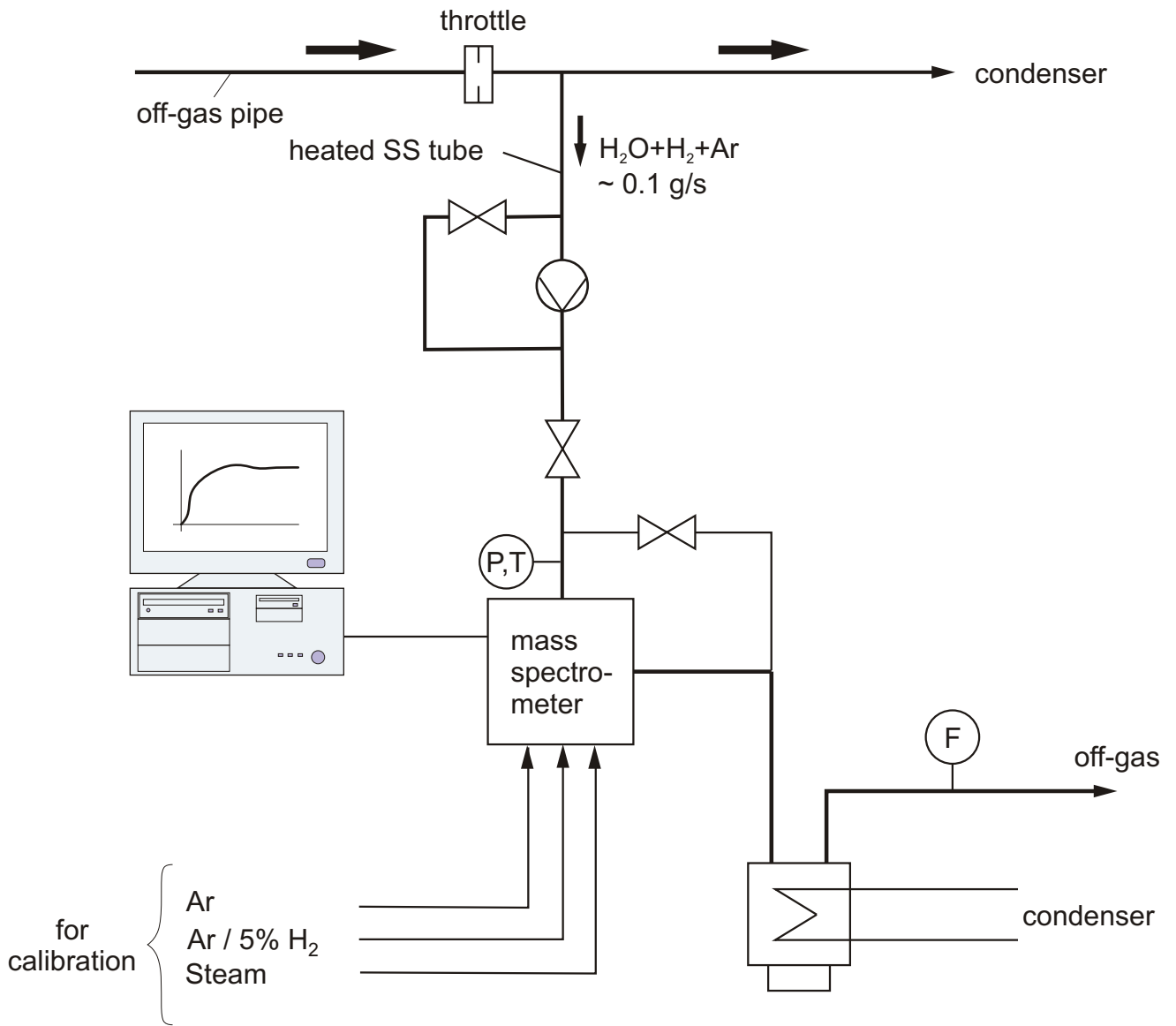


Fig.14-QUE12-MS Quench facility.cdr
17.01.08 - IMF

Fig. 14: QUENCH Facility; H_2 measurement with the GAM 300 mass spectrometer.

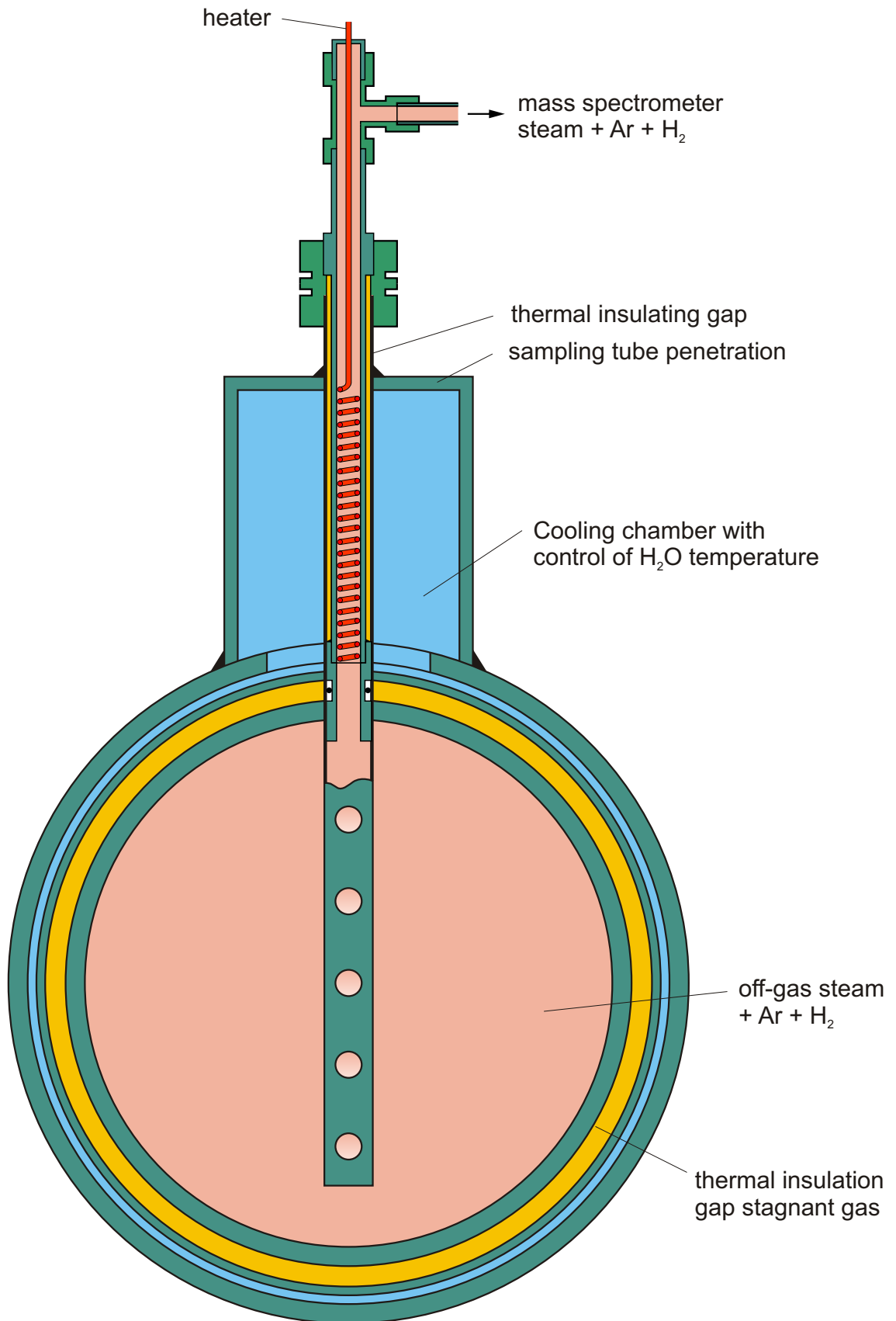


Fig 15-QUE12 MS sampling position new.cdr
21.01.08 - IMF

Fig.15: Mass spectrometer sampling position at the off-gas pipe of the QUENCH test facility.

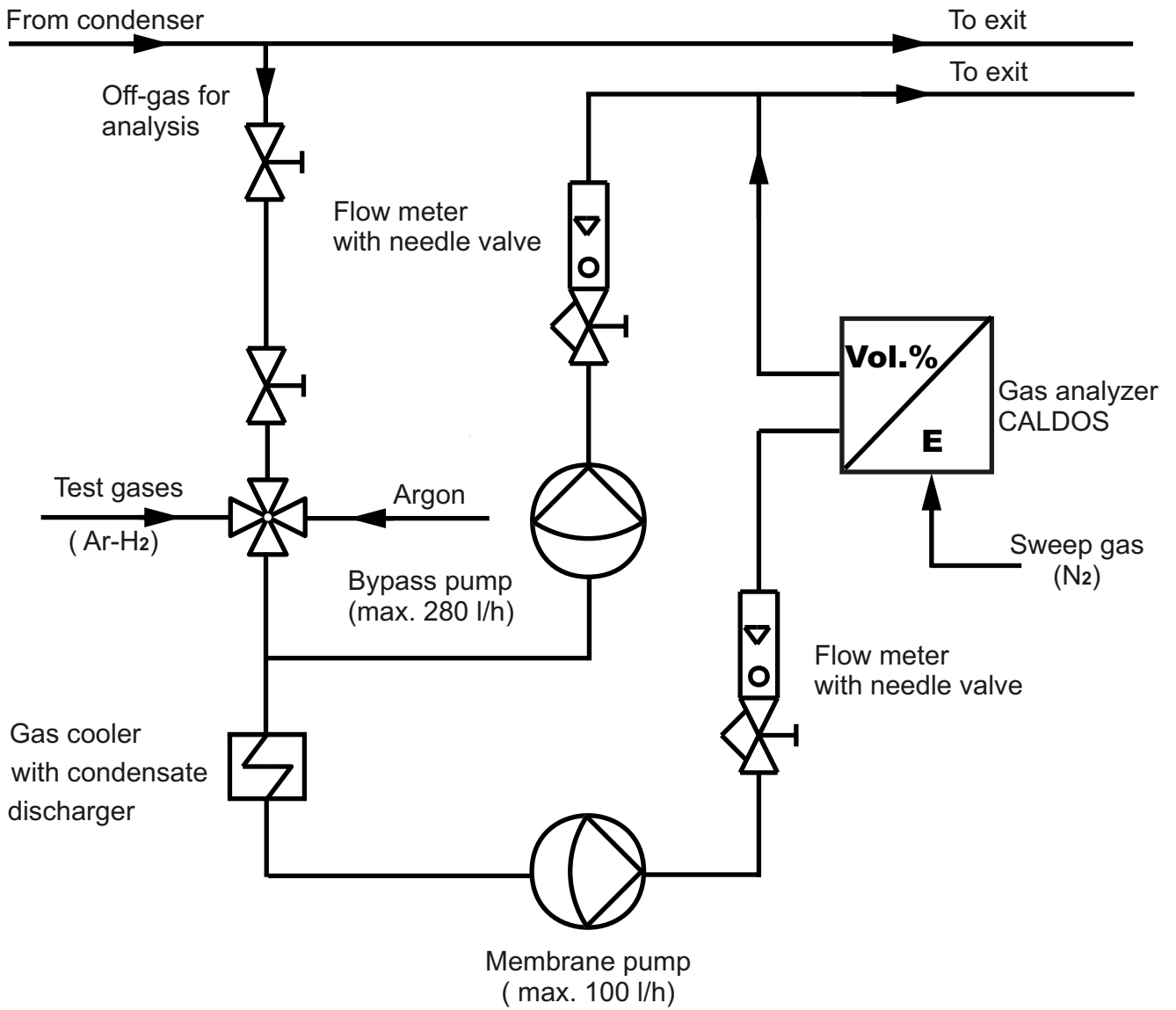
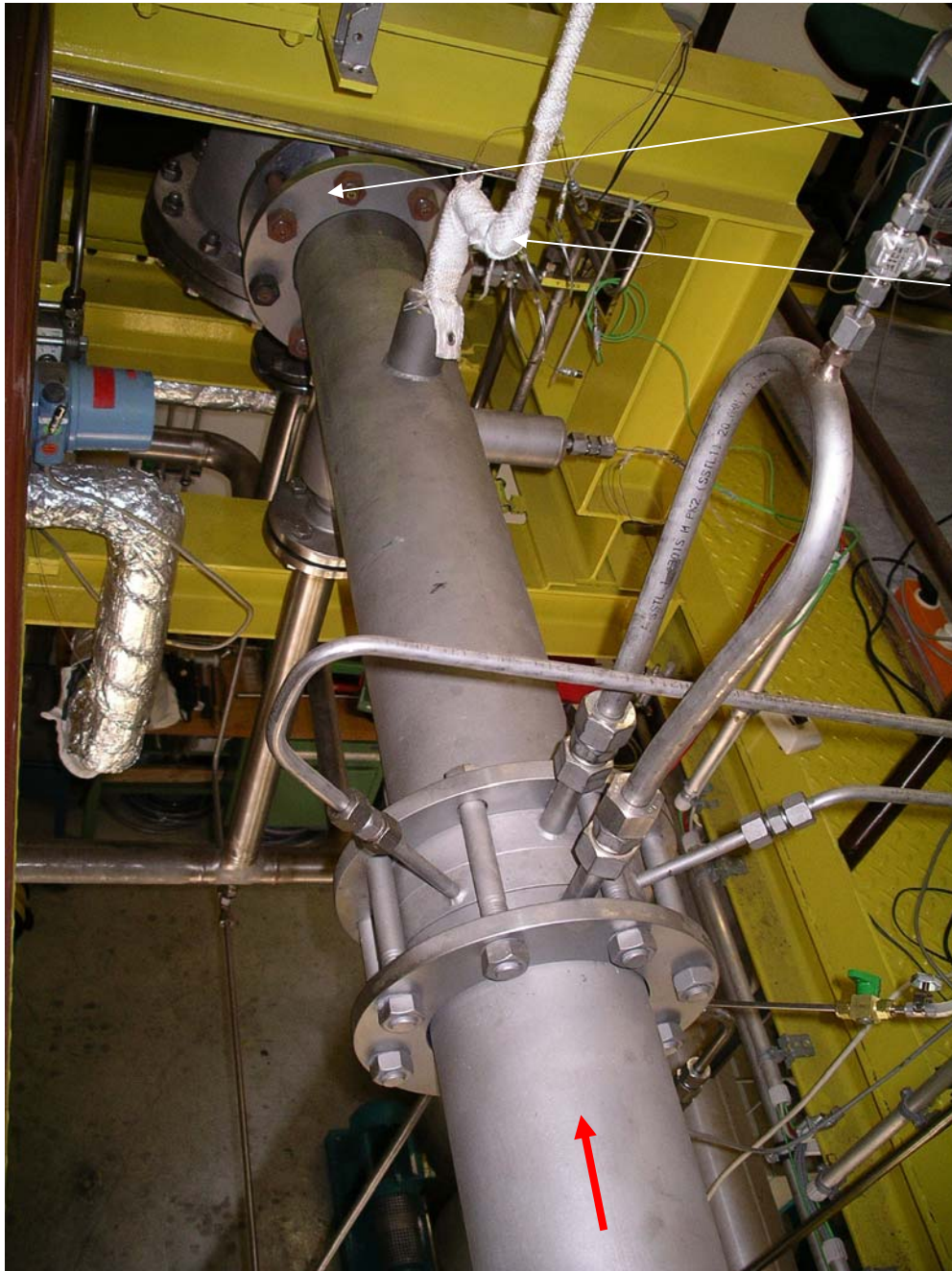


Fig 16 QUE12 Caldos Schema (ab QUE04).cdr
21.01.08 - IMF

Fig.16: Hydrogen measurement with the CALDOS analyzer connected to the exhaust gas pipe of the QUENCH facility.



**Baffle plate
(3053 mm)**

**Sampling line
to mass
spectrometer
(2700 mm)**

**F 601 differential
pressure (orifice,
2 lines, 2000 mm)**

Fig. 17: QUENCH-12; Top view of the off-gas pipe with the sampling line of the mass spectrometer and the standard orifice (F 601) between the two flanges (in the center of the photograph). Distances given refer to the flange at the entrance of the off-gas pipe.

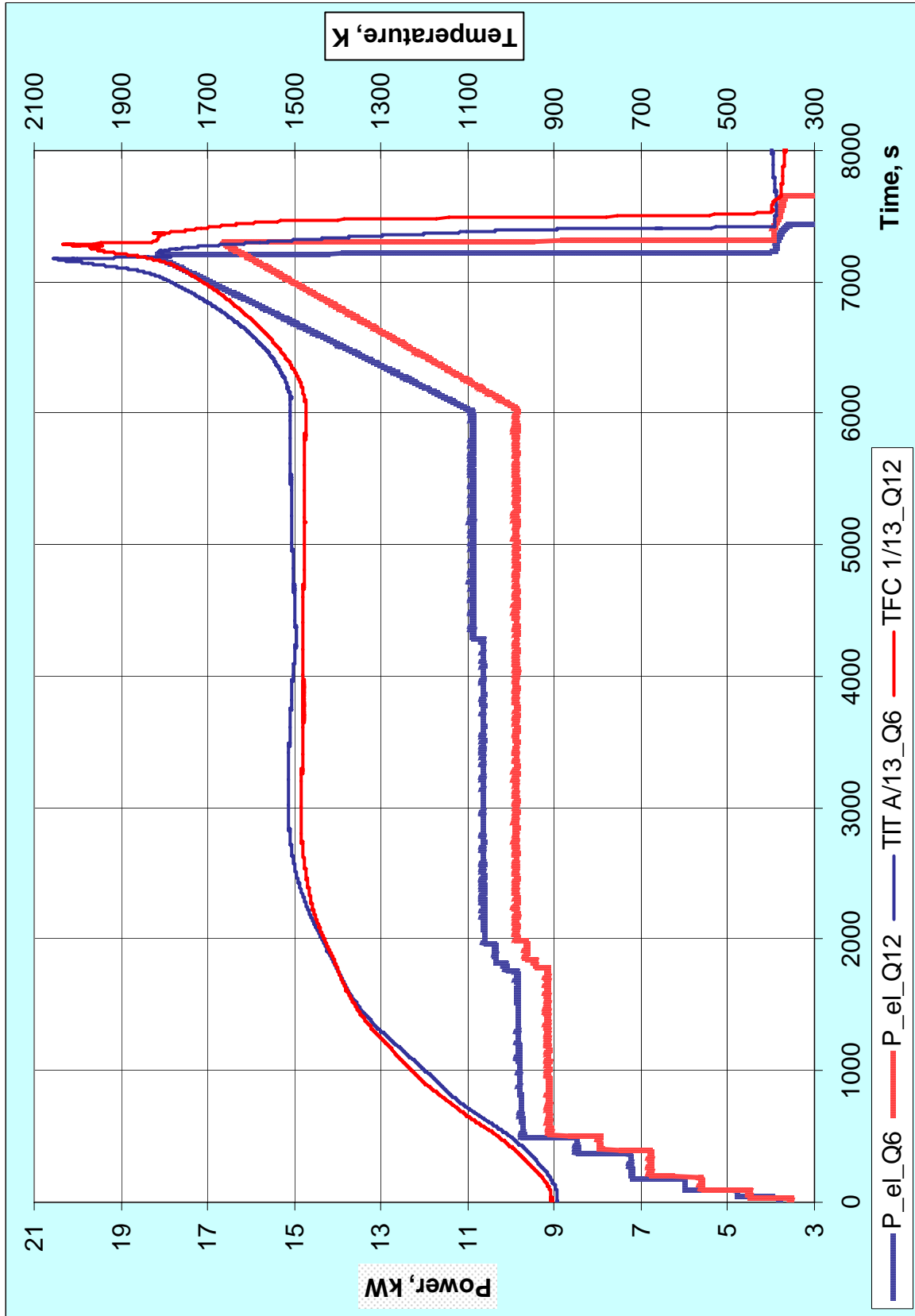


Fig. 18: QUENCH-12; Comparison of power and temperature profiles for QUENCH-12 and QUENCH-06.

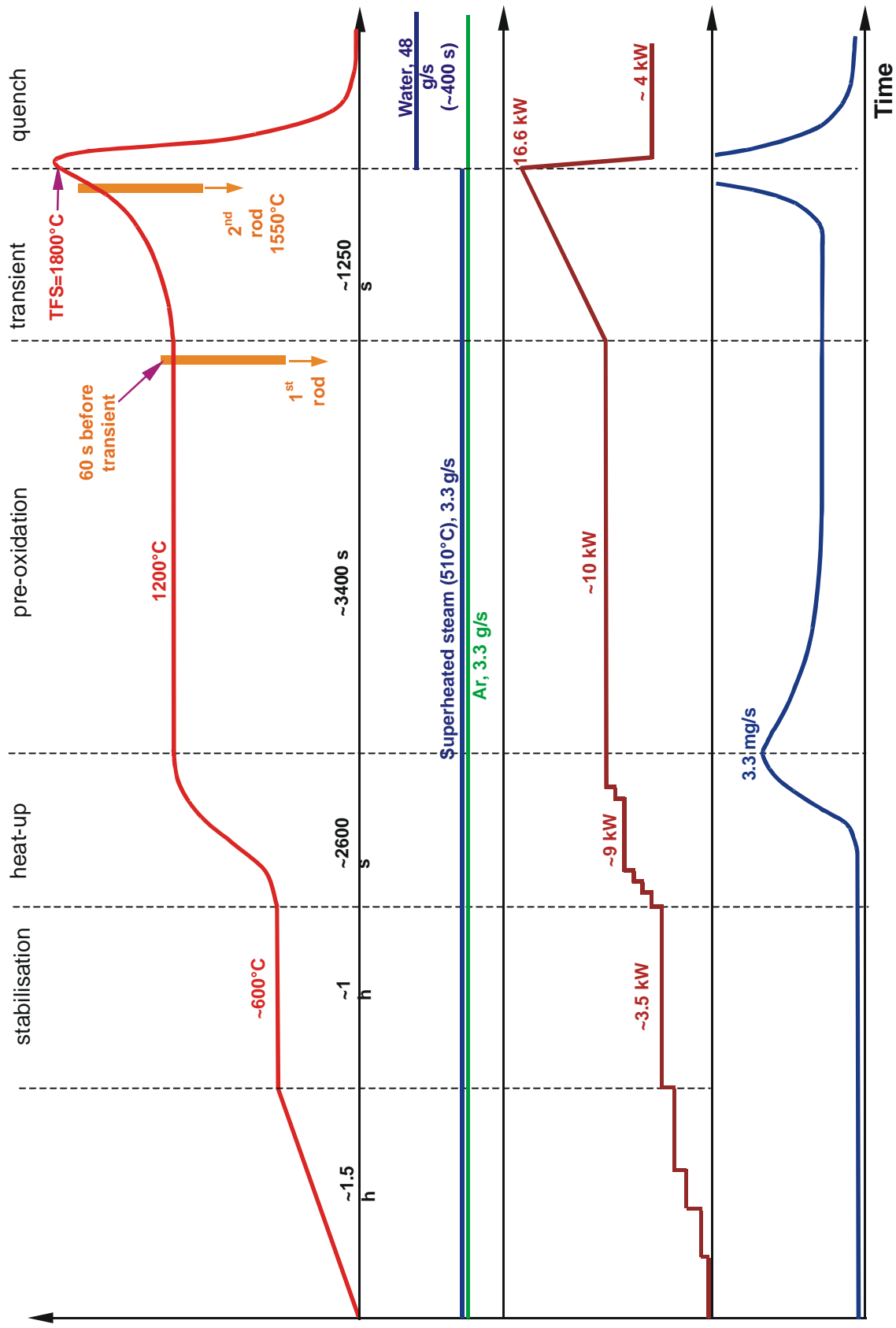


Fig. 19: QUENCH-12; test conduct (schematics of histories of bundle temperature, power, argon and steam flow rate and hydrogen production rate).

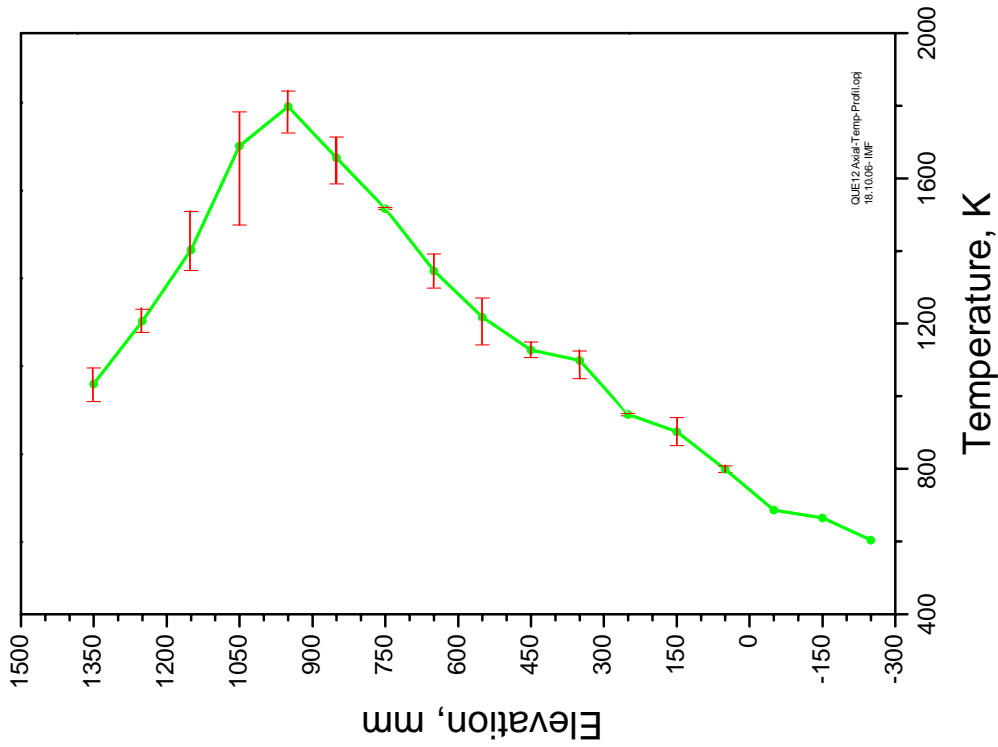
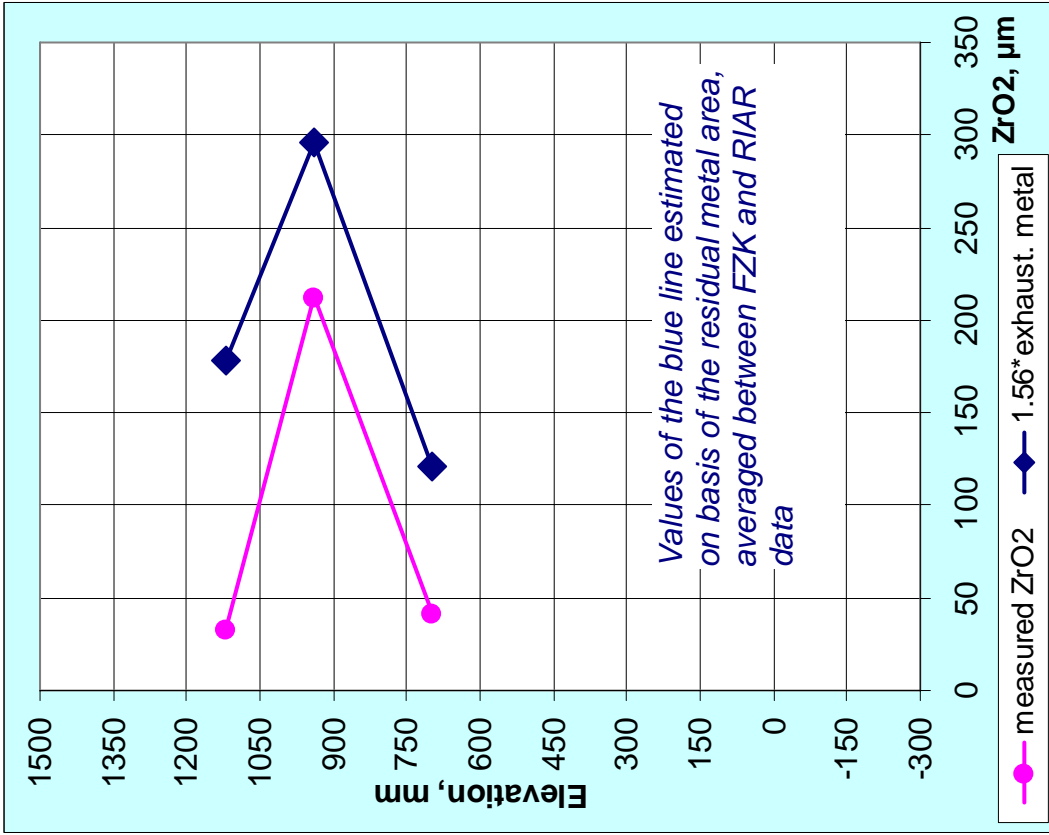


Fig. 20: QUENCH-12; Averaged axial temperature profile of all TFS thermocouples, left, and axial oxide layer profile of corner rod F for elevations 700-1120 mm, right, at time of rod pulling, i.e. 7175 s (transient phase).

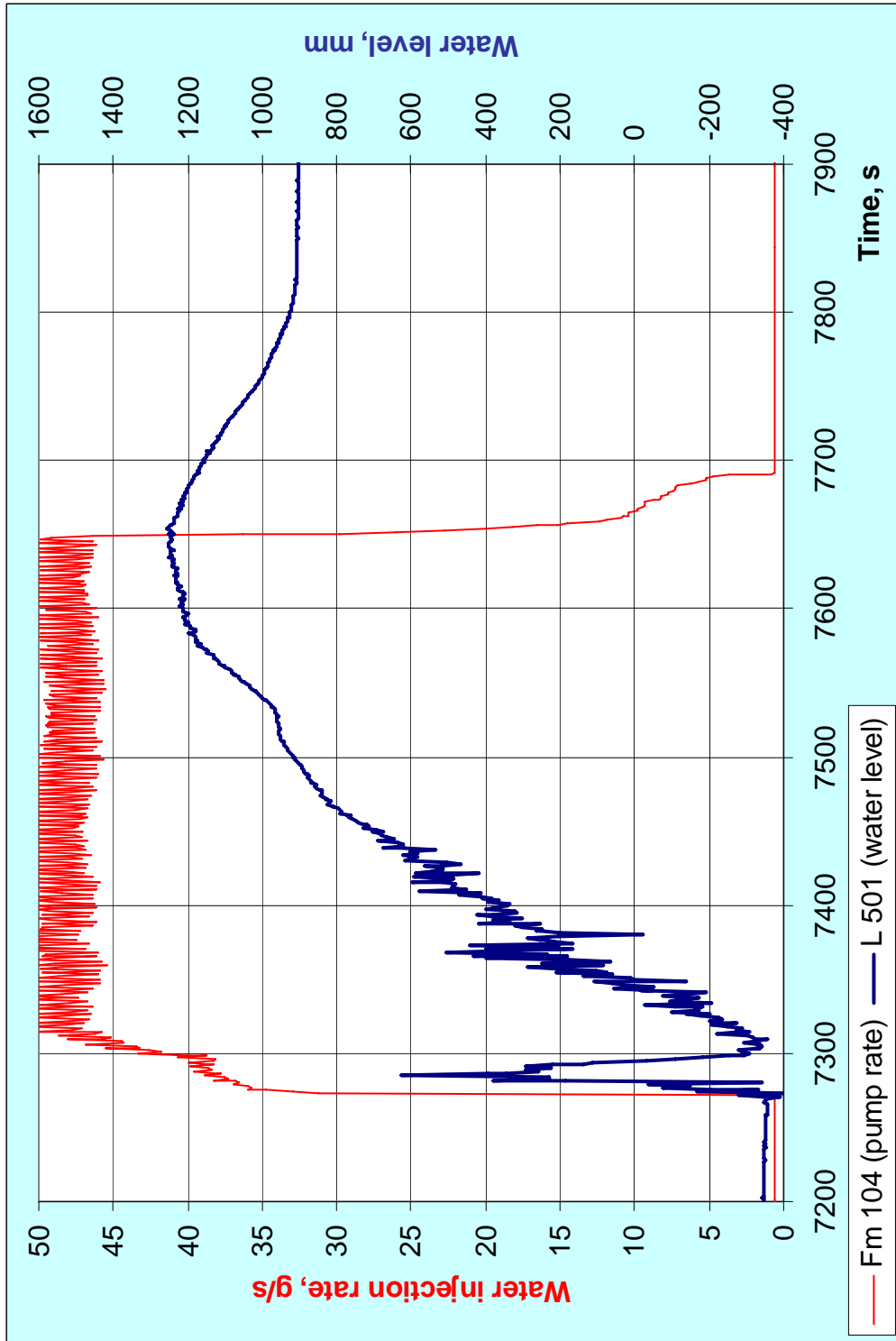


Fig. 21: QUENCH-12; Quench water injection rate and rise of water level in the test bundle.

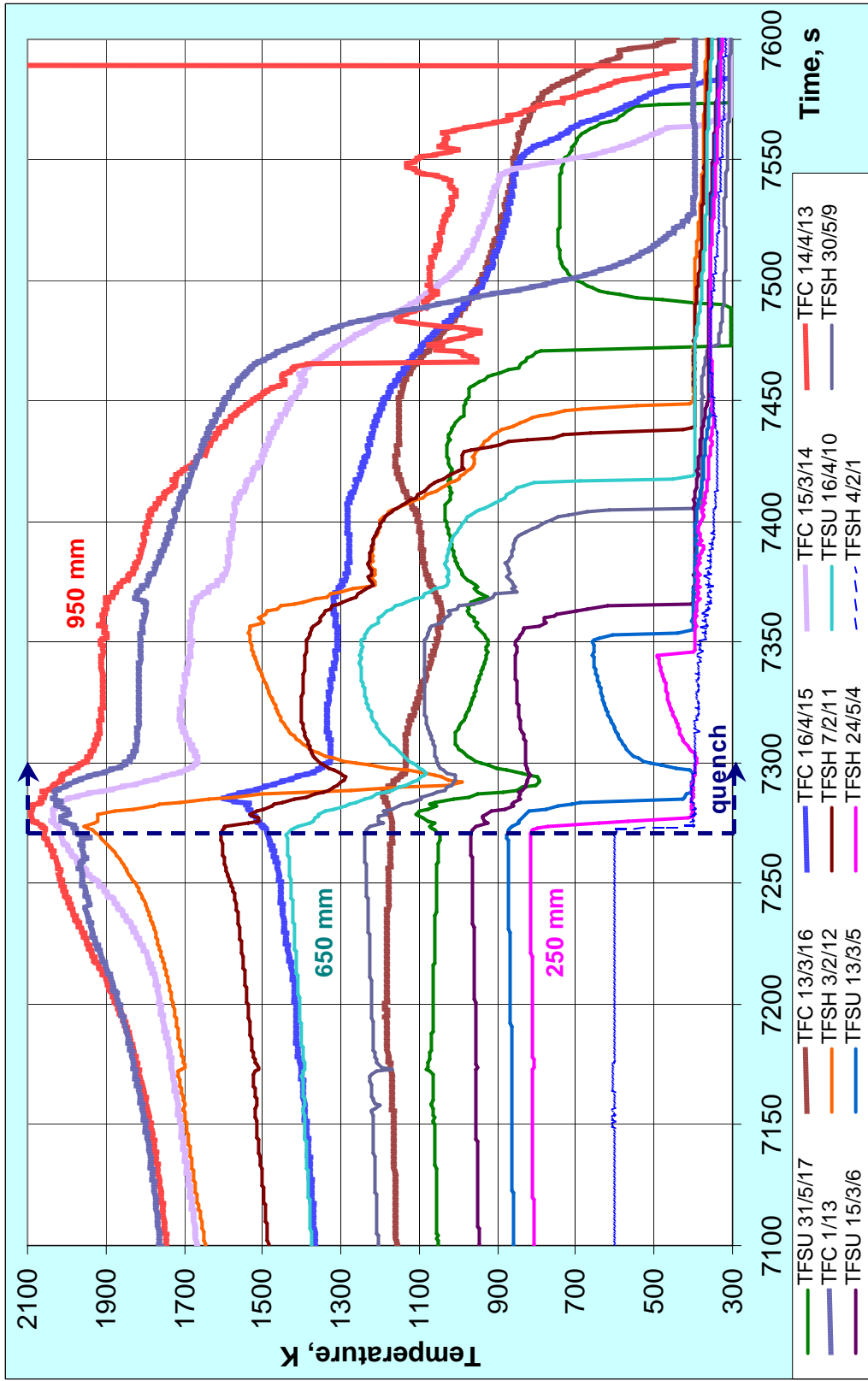


Fig. 22: QUENCH-12; Selected readings of the bundle thermocouples demonstrate the quench front propagation during the quench phase.



corner rod B after pre-test
 (800 °C, oxide layer thickness < 5 µm, measured with eddy-current technique)



Corner rods withdrawn during the main test:
D – after pre-oxidation,
F – before reflow,
B – after test.

Fig. 23: QUENCH-12; Spalling of outer scales of oxide layers at corner rods D, F, and B.

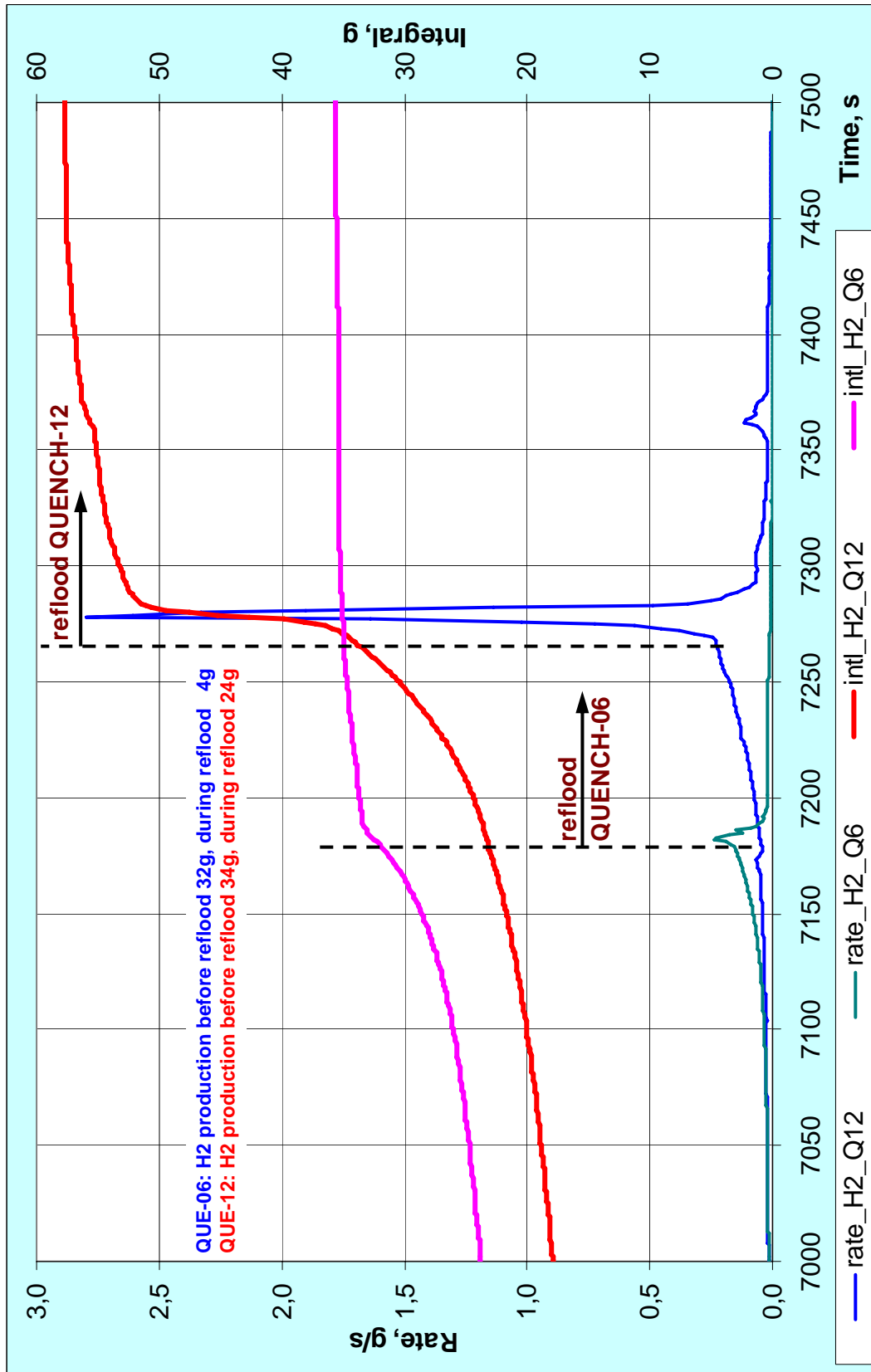
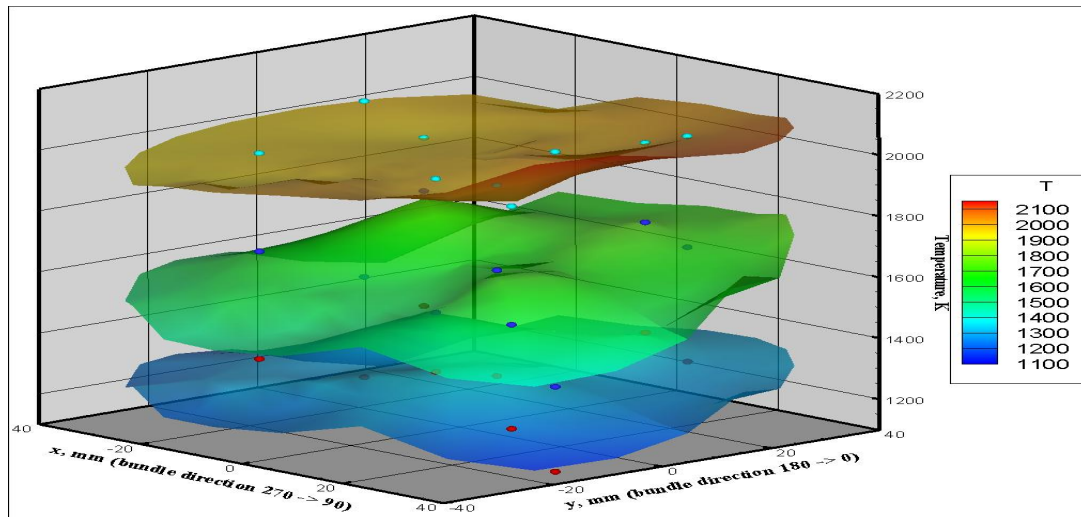
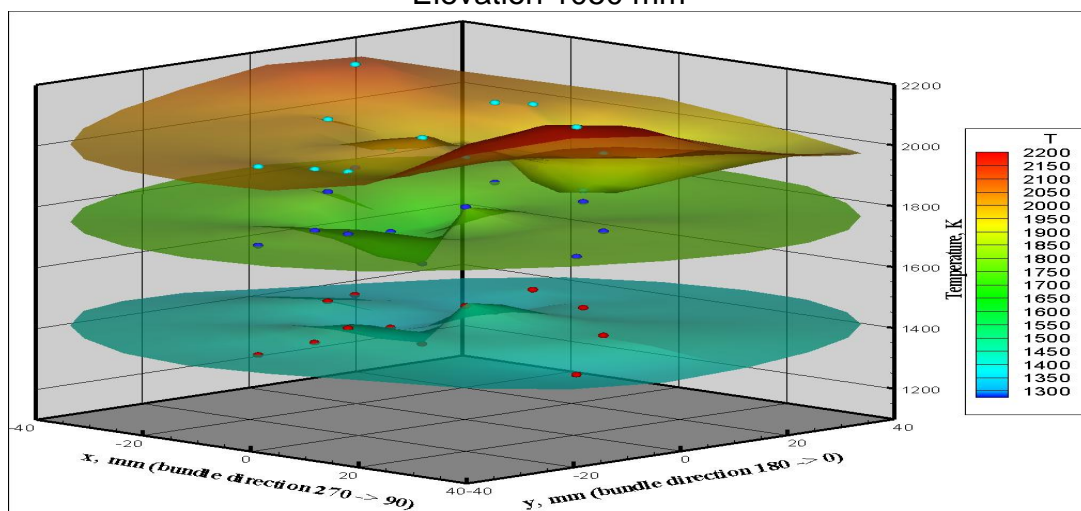


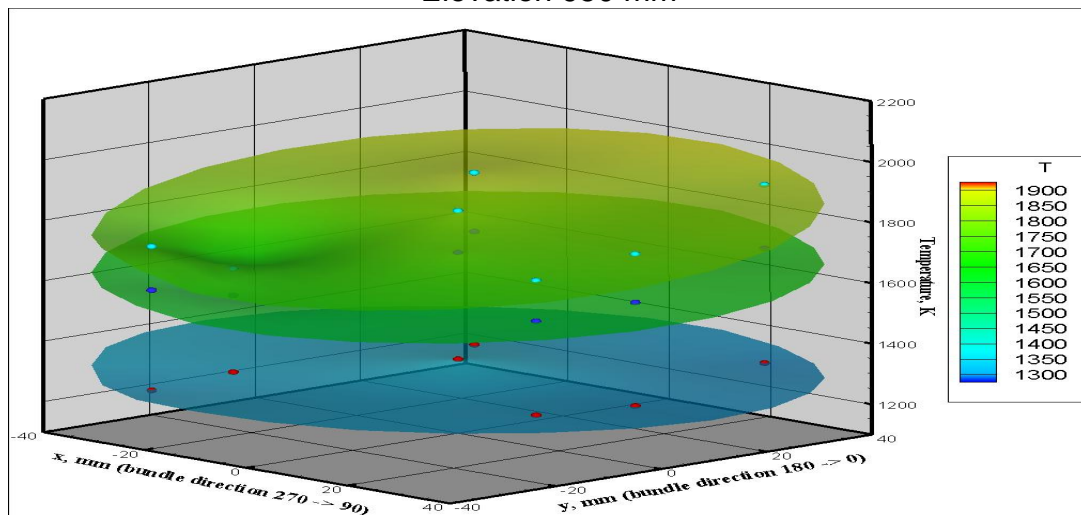
Fig. 24: QUEENCH-12; Comparison of hydrogen release during QUEENCH-12 and QUEENCH-06.



Elevation 1050 mm

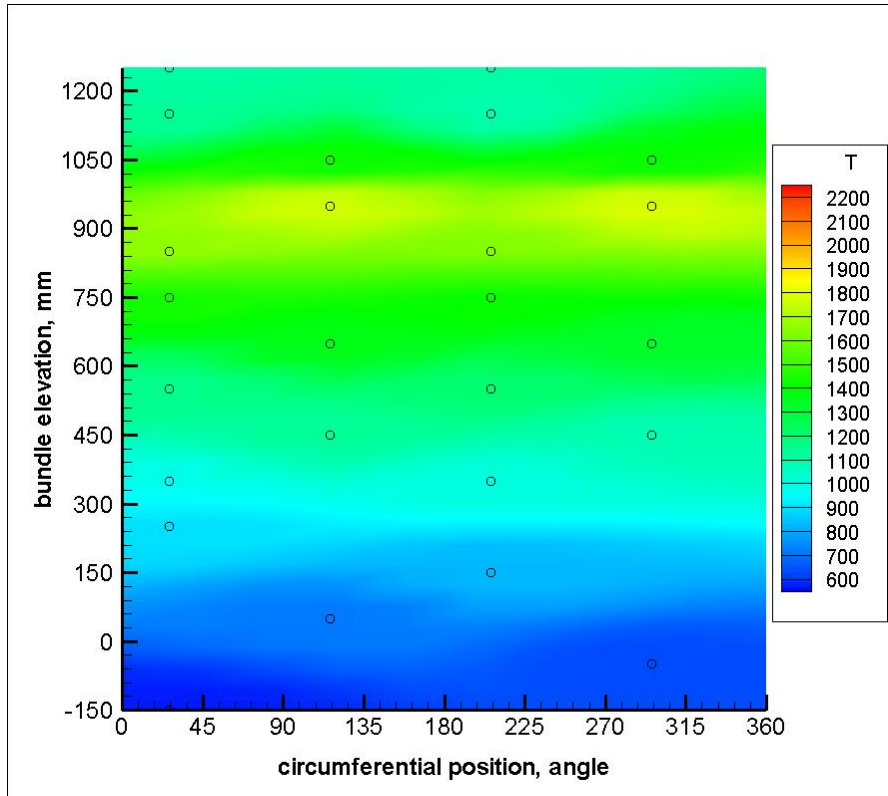


Elevation 950 mm

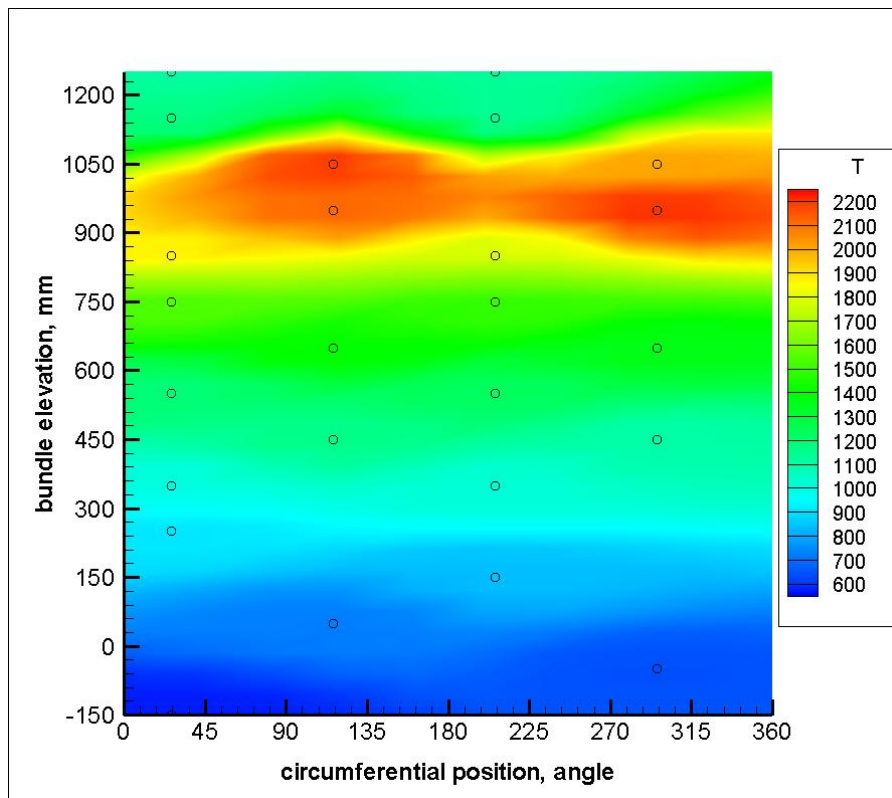


Elevation 850 mm

Fig. 25: QUENCH-12; Radial temperature distributions (bundle and shroud) for three time points: 1) 5960 s (1st corner rod removed), 2) 7150 s (2nd corner rod removed), 3) 7265 s (before reflood), and at three levels, i.e. 850 mm, bottom, 950 mm, center, and 1050 mm, top.



temperature field on 7150 s (115 s after onset of transient)



temperature field on 7265 s (5 s before reflow initiation)

Fig. 26: QUENCH-12; Comparison of axial temperature distribution versus the unwound shroud for two time points: a) before withdrawal of 2nd corner rod, top, b) before reflow, bottom.

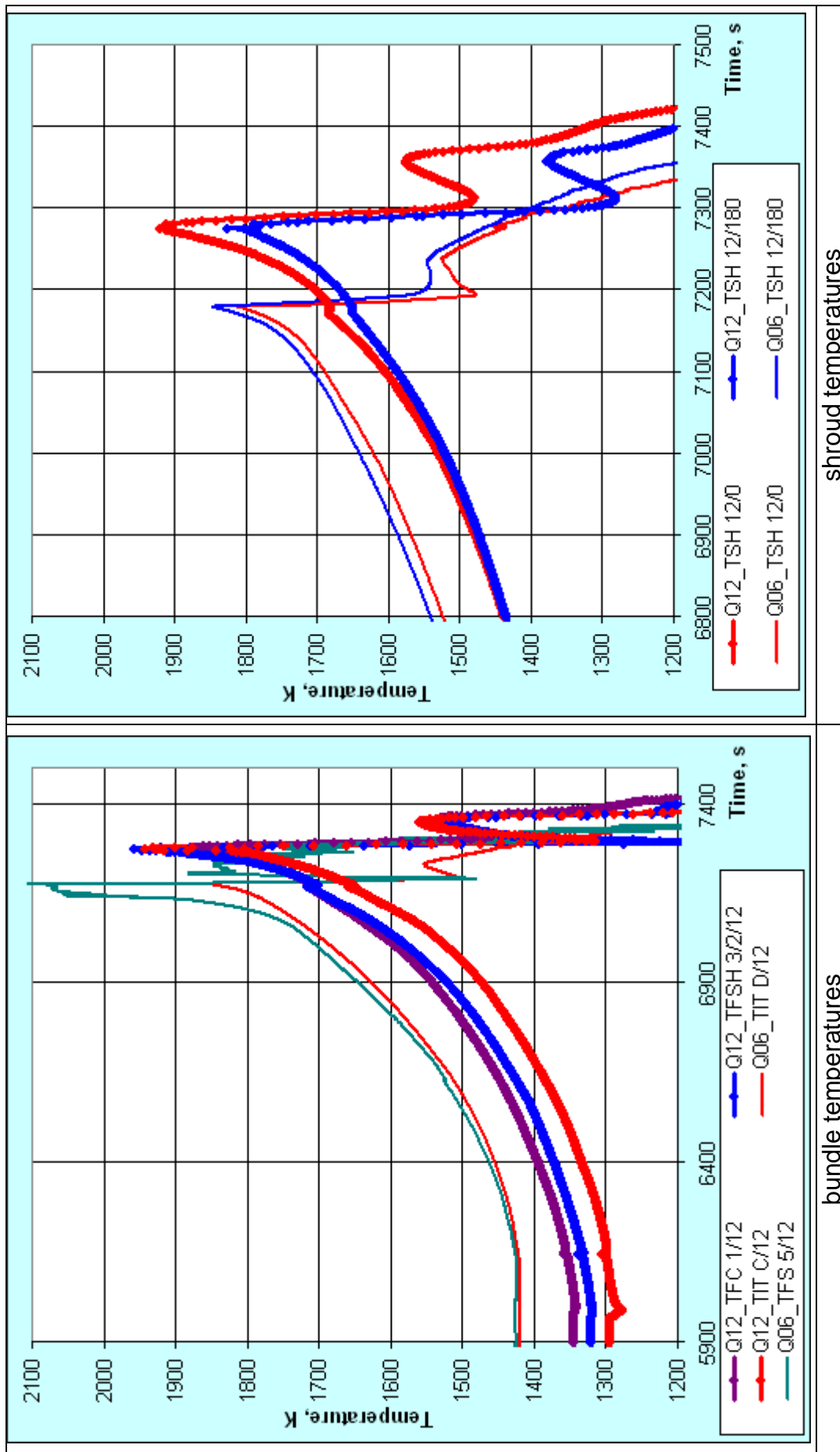


Fig. 27: Temperatures at elevation 850 mm of bundles QUENCH-06 and QUENCH-12 during transient and quench phases.

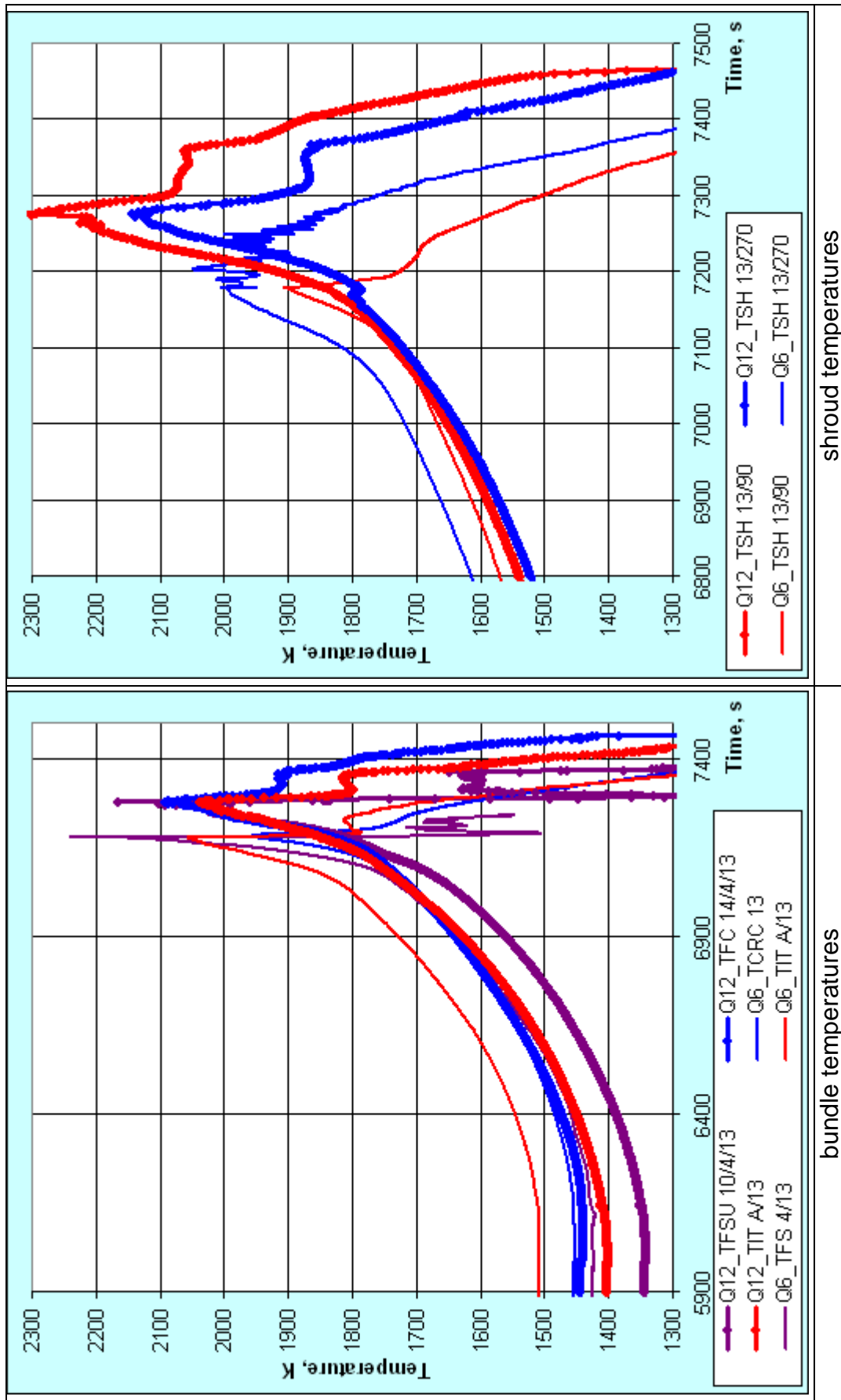


Fig. 28: Temperatures at elevation 950 mm of bundles QUENCH-06 and QUENCH-12 during transient and quench phases.

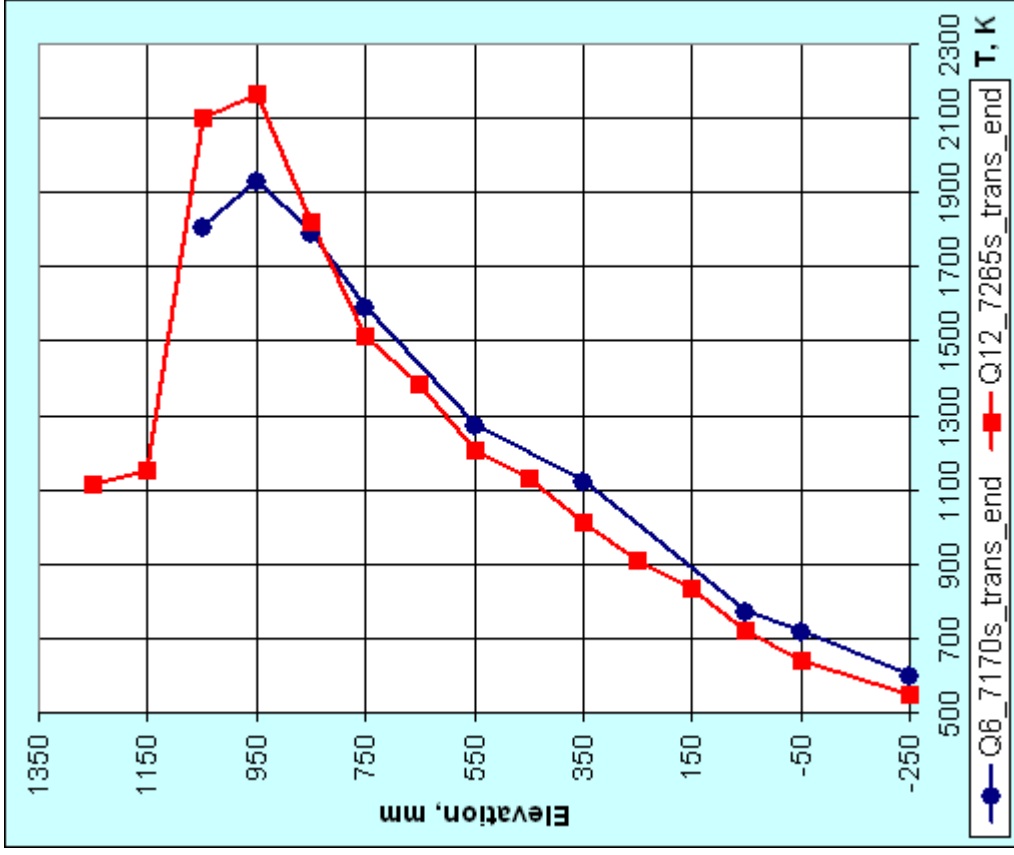
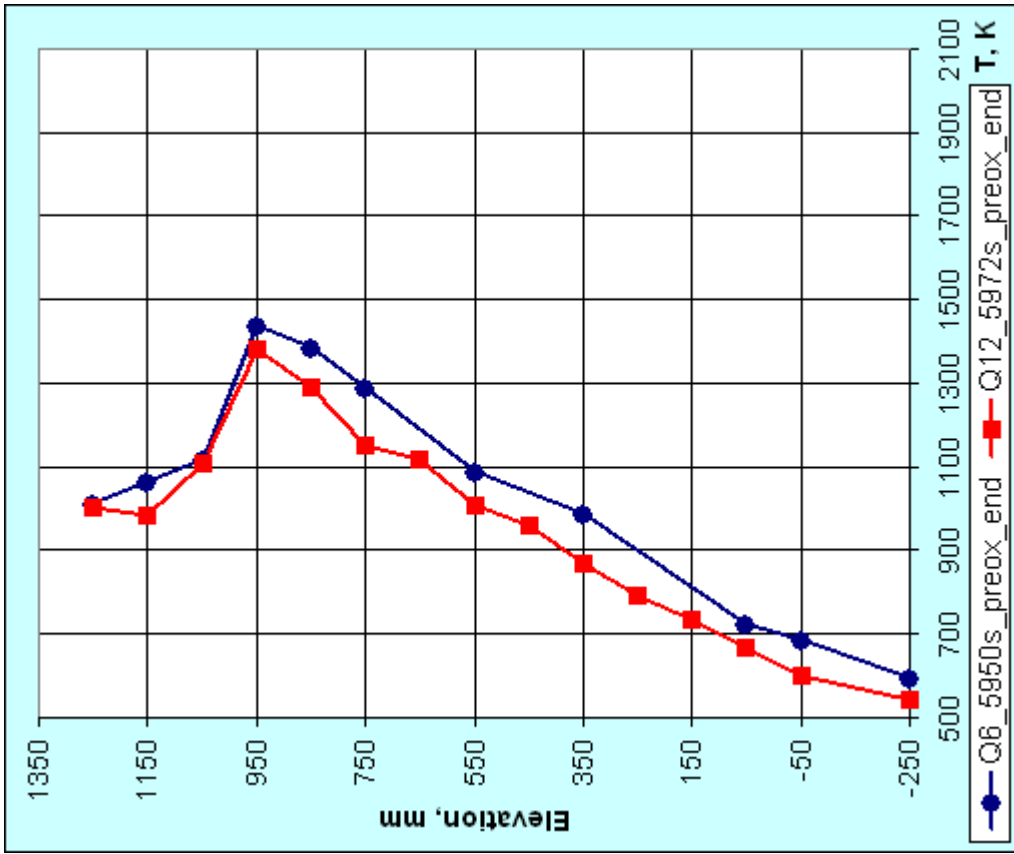
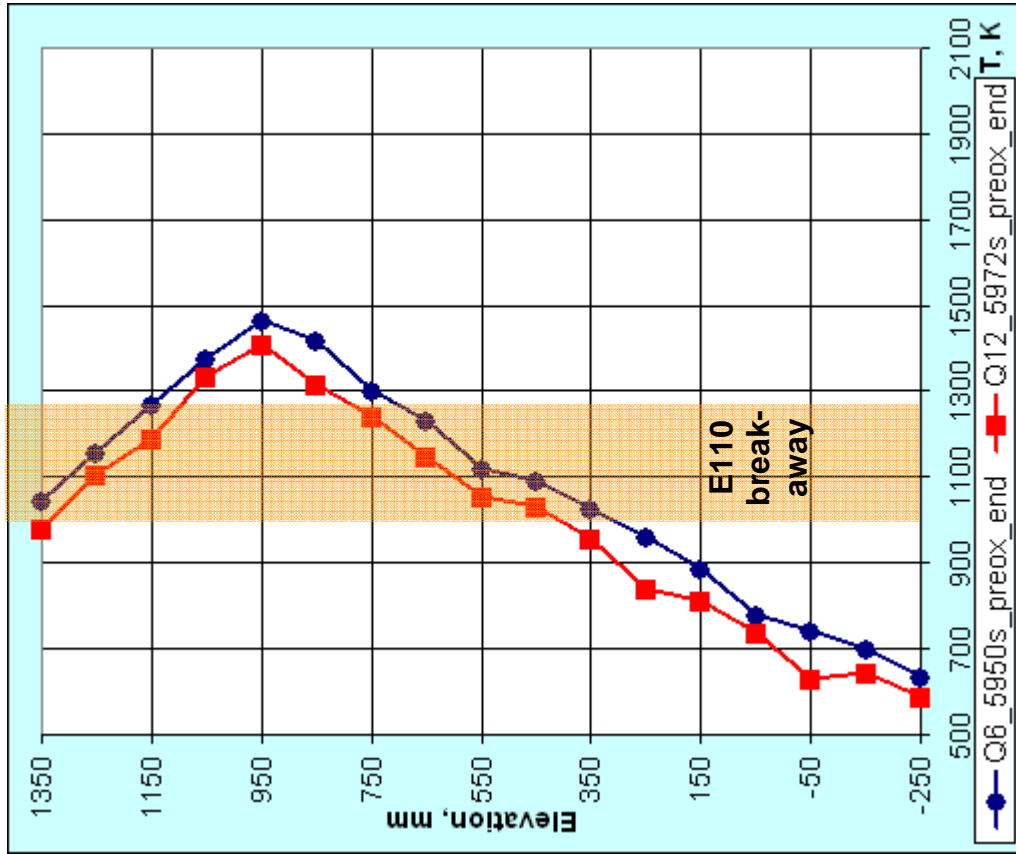
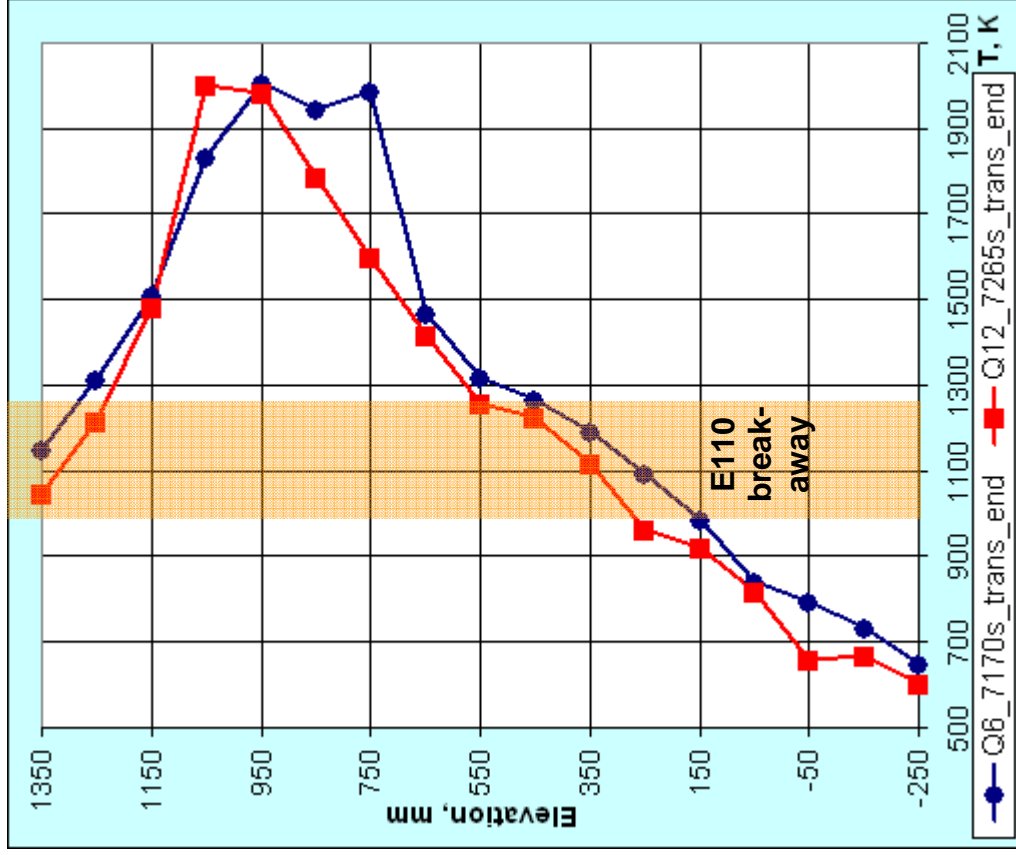


Fig. 29: Axial shroud temperature profiles for QUENCH-06 and QUENCH-12 at beginning and end of transient phase.



beginning of transient



end of transient

Fig. 30: Axial bundle temperature profiles for QUENCH-06 and QUENCH-12 at beginning and end of transient phase.



Fig. 31: QUENCH-12; Posttest appearance of the hot zone of shroud and test bundle (~750-1150 mm) at orientations 0, 90, 180, and 270 degrees (from left).



Fig. 32: QUENCH-12; Piece of upper shroud that broke off during dismantling.



Fig. 33: Debris transported to the inlet section of the off-gas tube during the QUENCH-12 test.



debris inside corner rod guide tube



top of corner rod guide tube



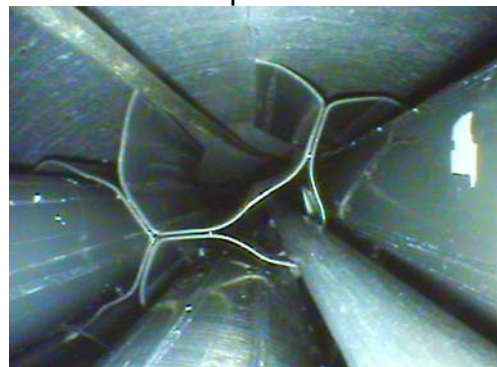
bottom of unheated rods, -425 mm



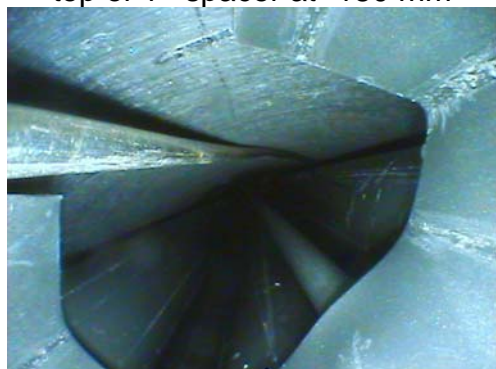
bottom of 1st spacer at -200 mm



top of 1st spacer at -180 mm



bottom of 2nd spacer at 50 mm

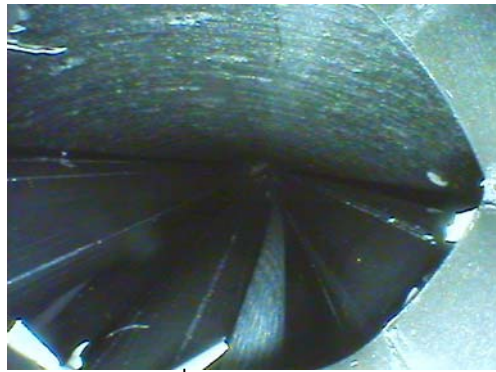


top of 2nd spacer at 70 mm



bottom of 3rd spacer at 300 mm

Fig. 34: QUENCH-12; Videoscope monitoring at the empty position of the withdrawn corner rod D, viewed from bottom to top.



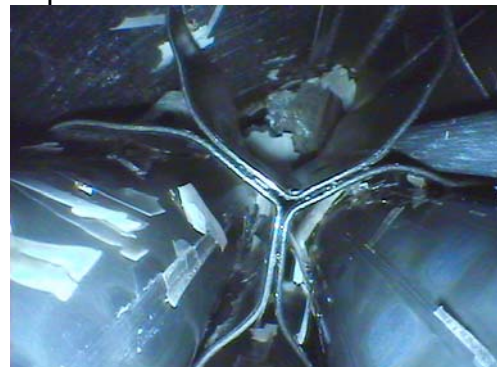
top of 3rd spacer at 320mm



spallations at rod 27 at 450 mm



spallations at rod 16 at 500 mm



bottom of 4th spacer at 550 mm



cladding piece on top of 4th spacer



spallations at 650 mm



bottom of 5th spacer at 800 mm

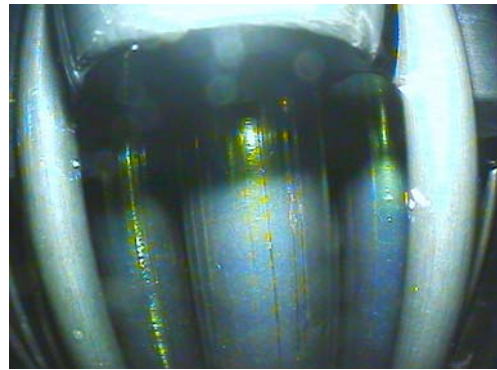


rod 16 break and rod 27 cracks at 900 mm

Fig. 35: QUENCH-12; Videoscope monitoring at empty position of the withdrawn corner rod D, viewed from bottom to top; cont'd.



debris on bottom of separator



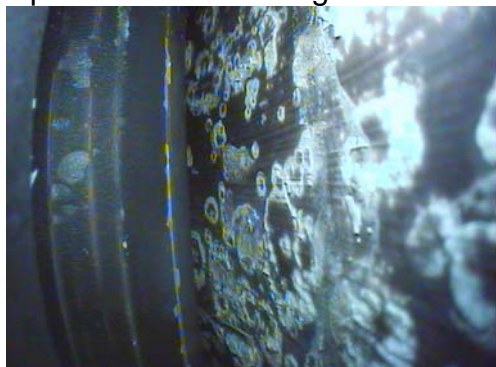
bottom of unheated rod



spallations at cladding at 400 mm



spallations at shroud at 400 mm

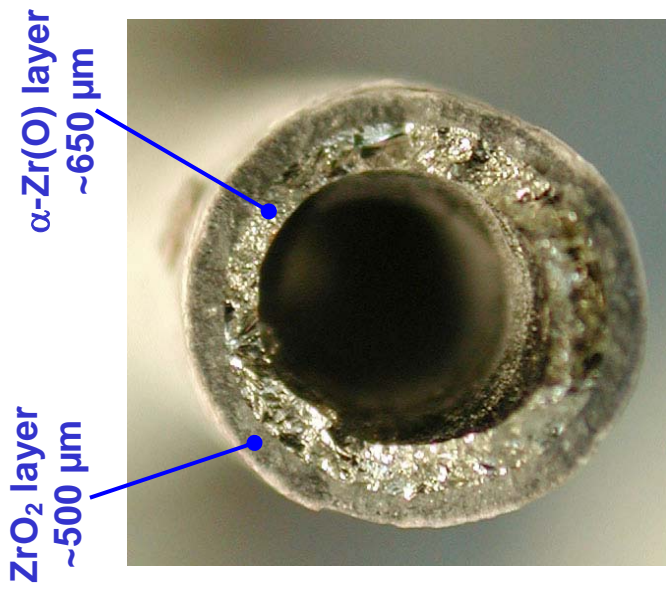


spallations at shroud at 850 mm

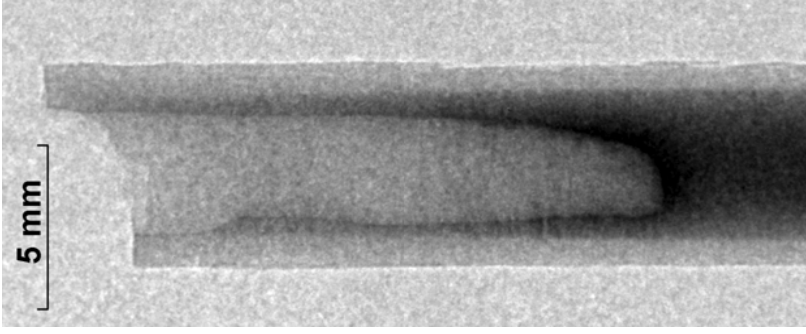


rod16 break at 900 mm

Fig. 36: QUENCH-12; Videoscope monitoring (side view) at the empty position of the withdrawn corner rod D.



Upper part of the broken rod with central part lost due to melting of β-Zr at T>2130 K



Neutron radiography shows deep hole with irregular diameter



Melt formation in bundle at the break position of the corner rod

Fig. 37: QUENCH-12; Local melt formation at 850 mm and the position of corner rod B withdrawn after the test.

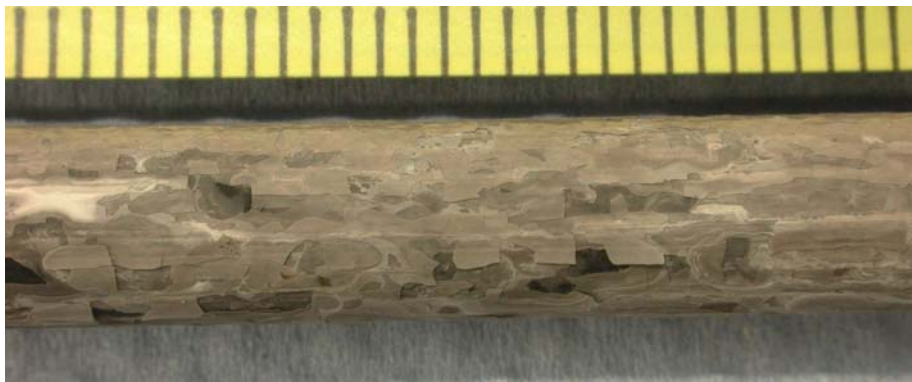
622-649 mm



645-672 mm



697-724 mm



724-751 mm

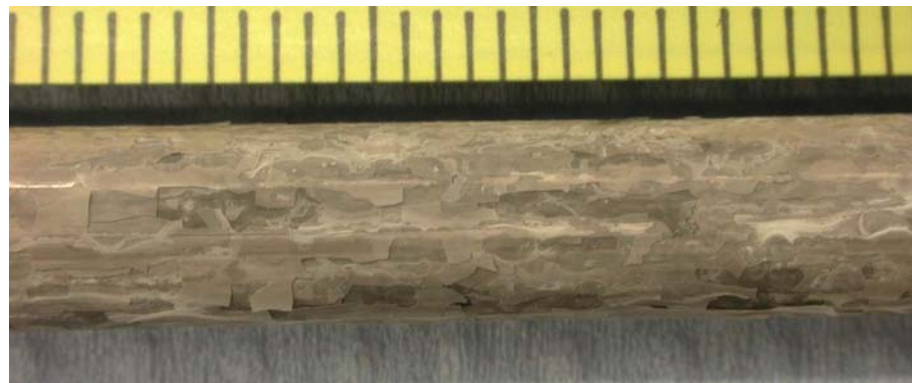
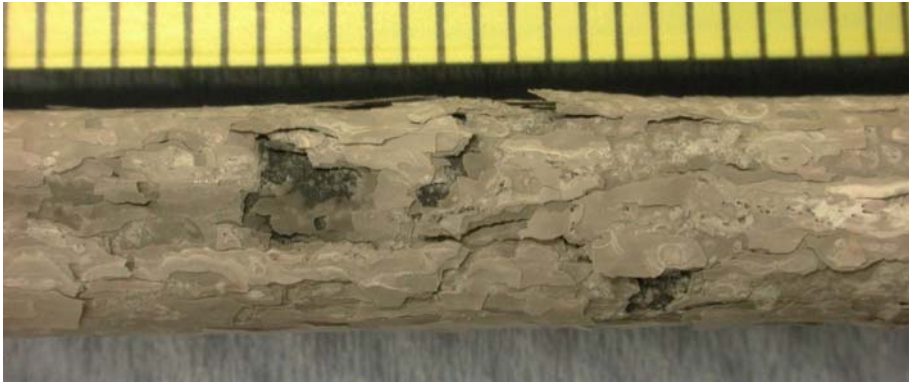
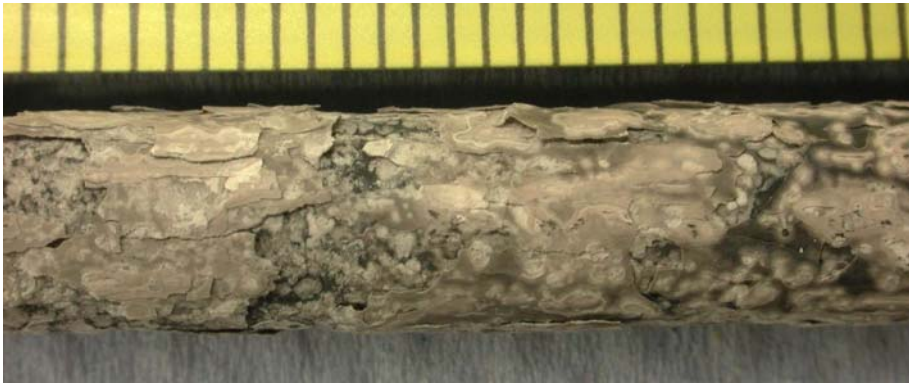


Fig. 38: QUENCH-12; Photographs of corner rod D, 622-751 mm.

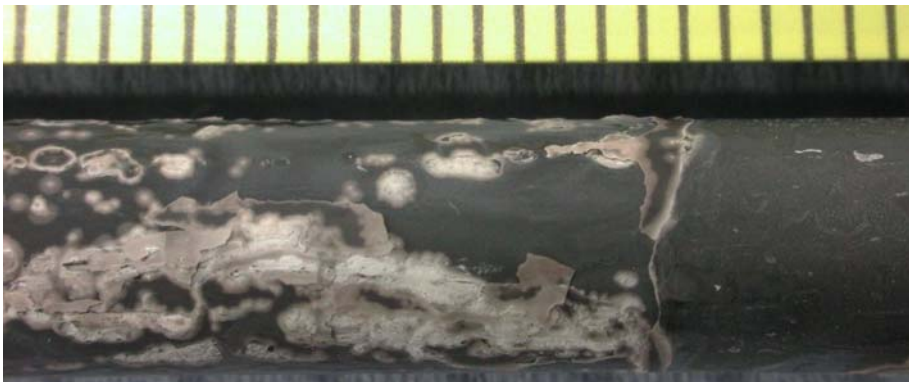
821-846 mm



860-885 mm



905-926 mm



982-1003 mm

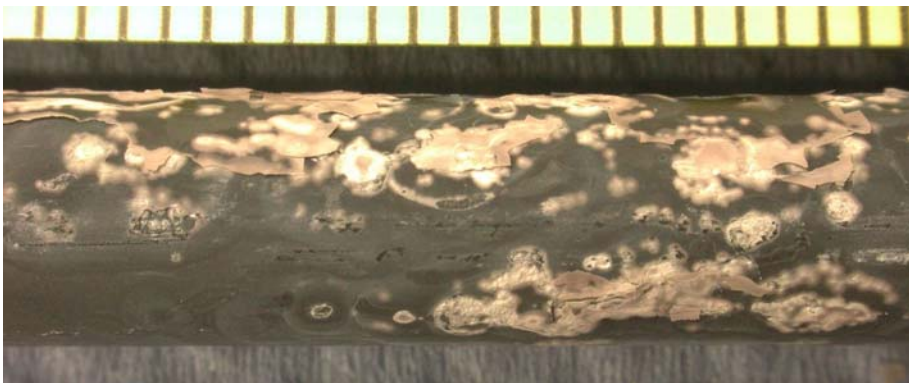
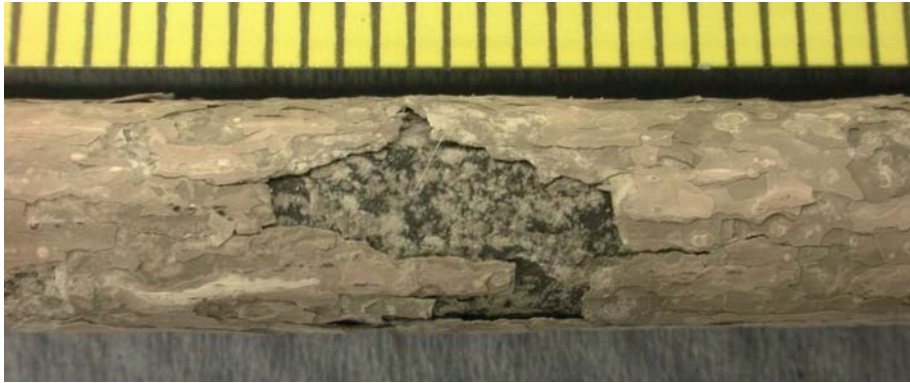


Fig. 39: QUENCH-12; Photographs of corner rod D 821-1003 mm.

1038-1063 mm



1131-1159 mm

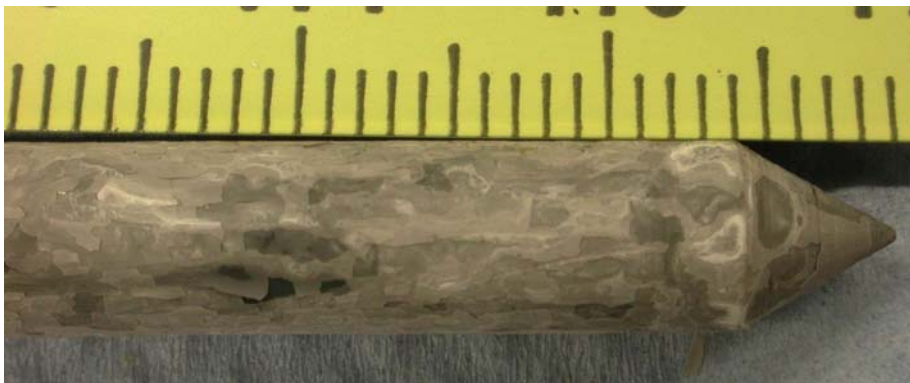


Fig. 40: QUENCH-12; Photographs of corner rod D 1038-1159 mm.

609-634 mm



650-676 mm



725-741 mm



741-766 mm

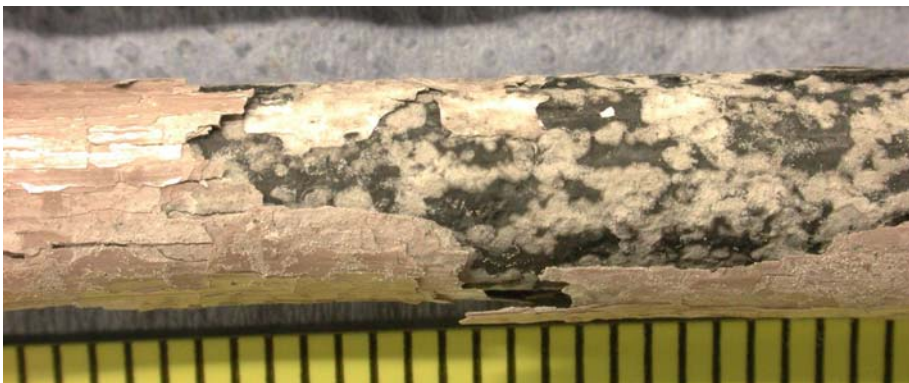


Fig. 41: QUENCH-12; Photographs of corner rod F 609-766 mm.

847-872 mm



935-961 mm



988-1014 mm



1012-1038 mm

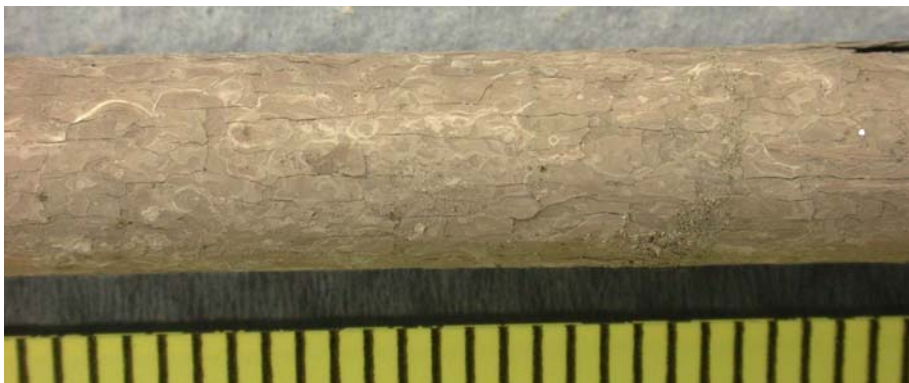


Fig. 42: QUENCH-12; Photographs of corner rod F, 847-1038 mm.

1062-1089 mm



1107-1133 mm



1133-1159 mm

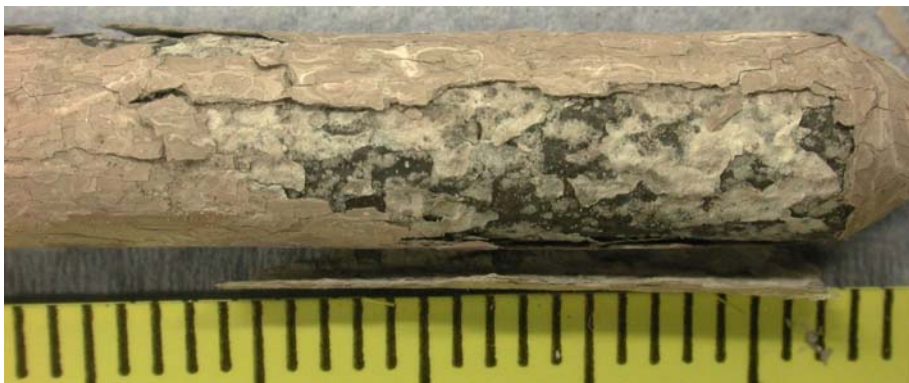
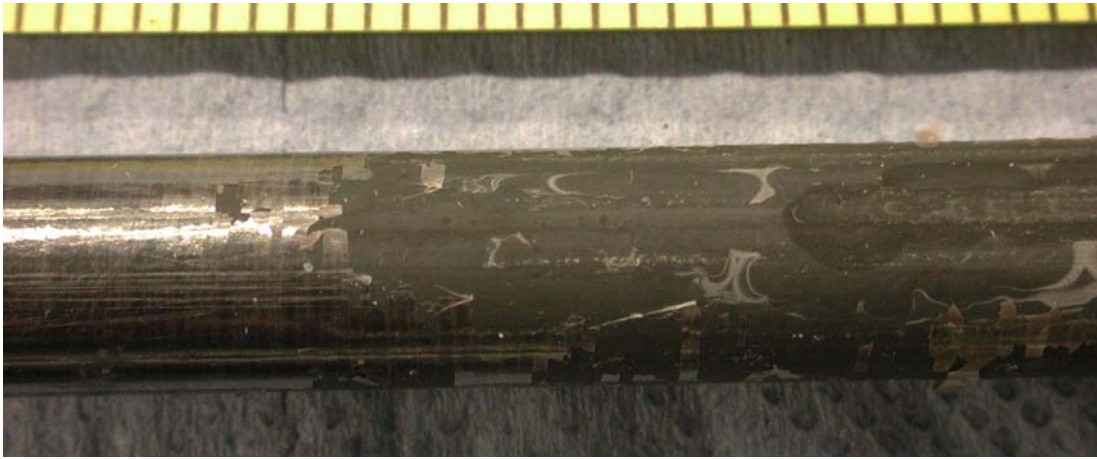


Fig. 43: QUENCH-12; Photographs of corner rod F, 1062-1159 mm.

552-580 mm



623-652 mm



673-701 mm

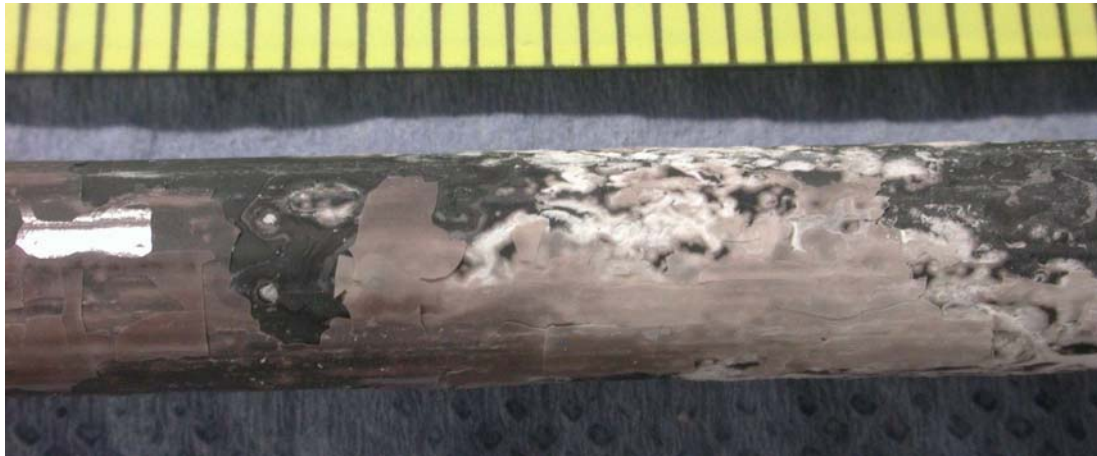
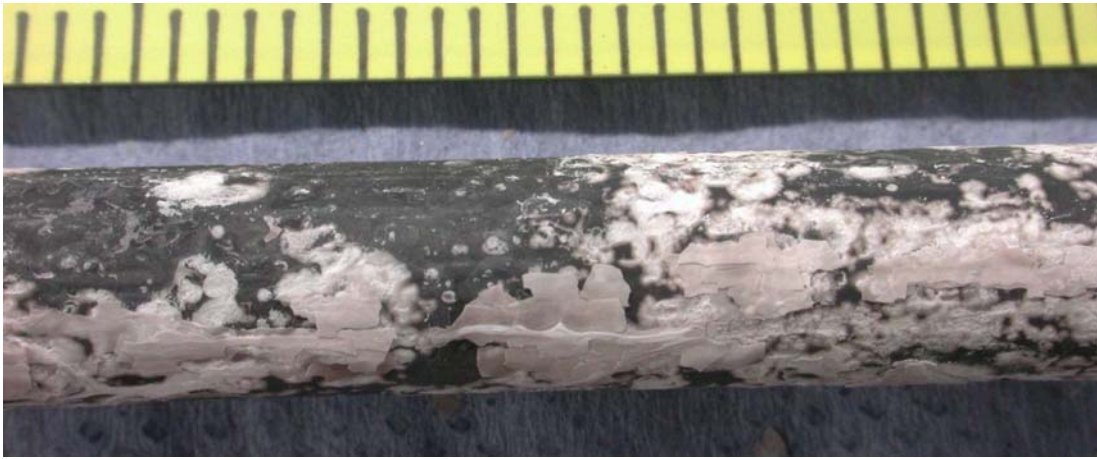
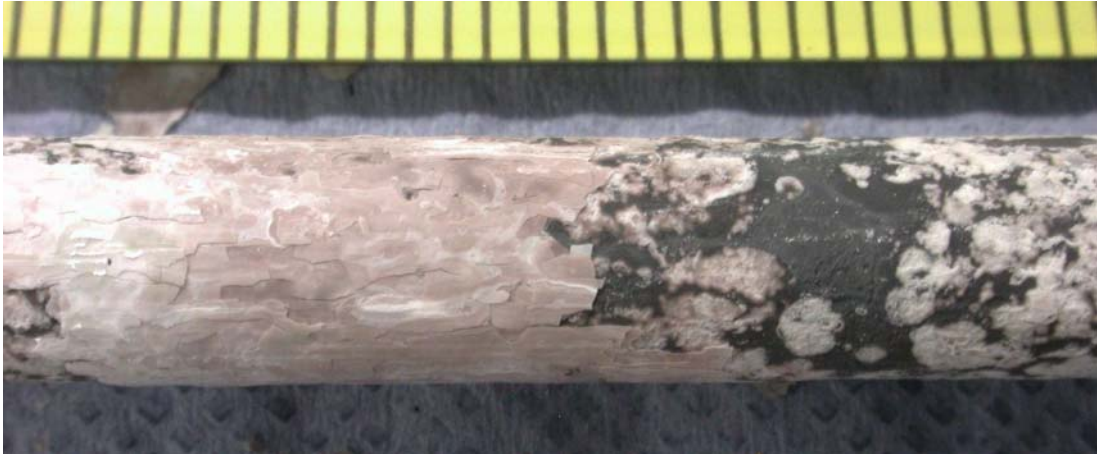


Fig. 44: QUENCH-12; Photographs of corner rod B, 552-701 mm.

697-725 mm



769-796 mm



855-884 mm

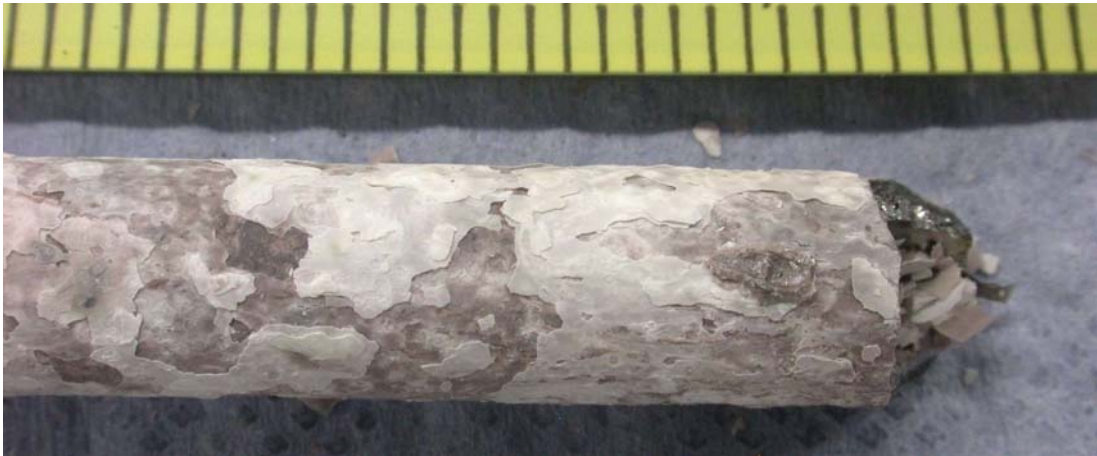


Fig. 45: QUENCH-12; Photographs of corner rod B, 697-884 mm.

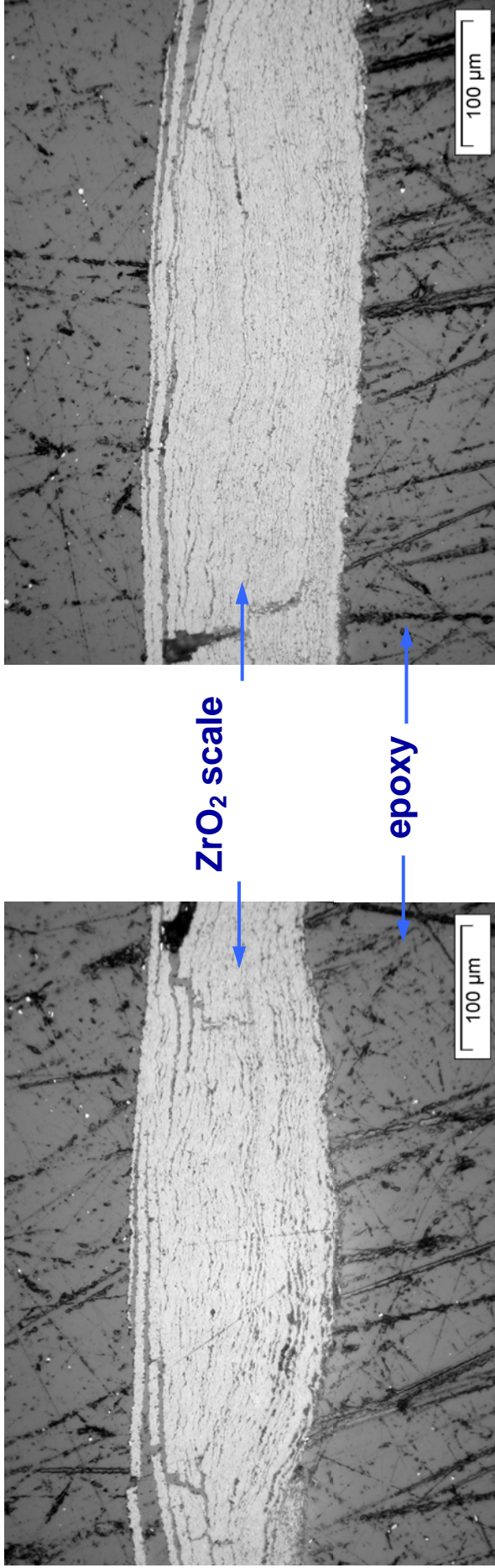


Fig. 46: QUENCH-12; Typical morphology of spalled oxide scale of corner rod (laminated structure).

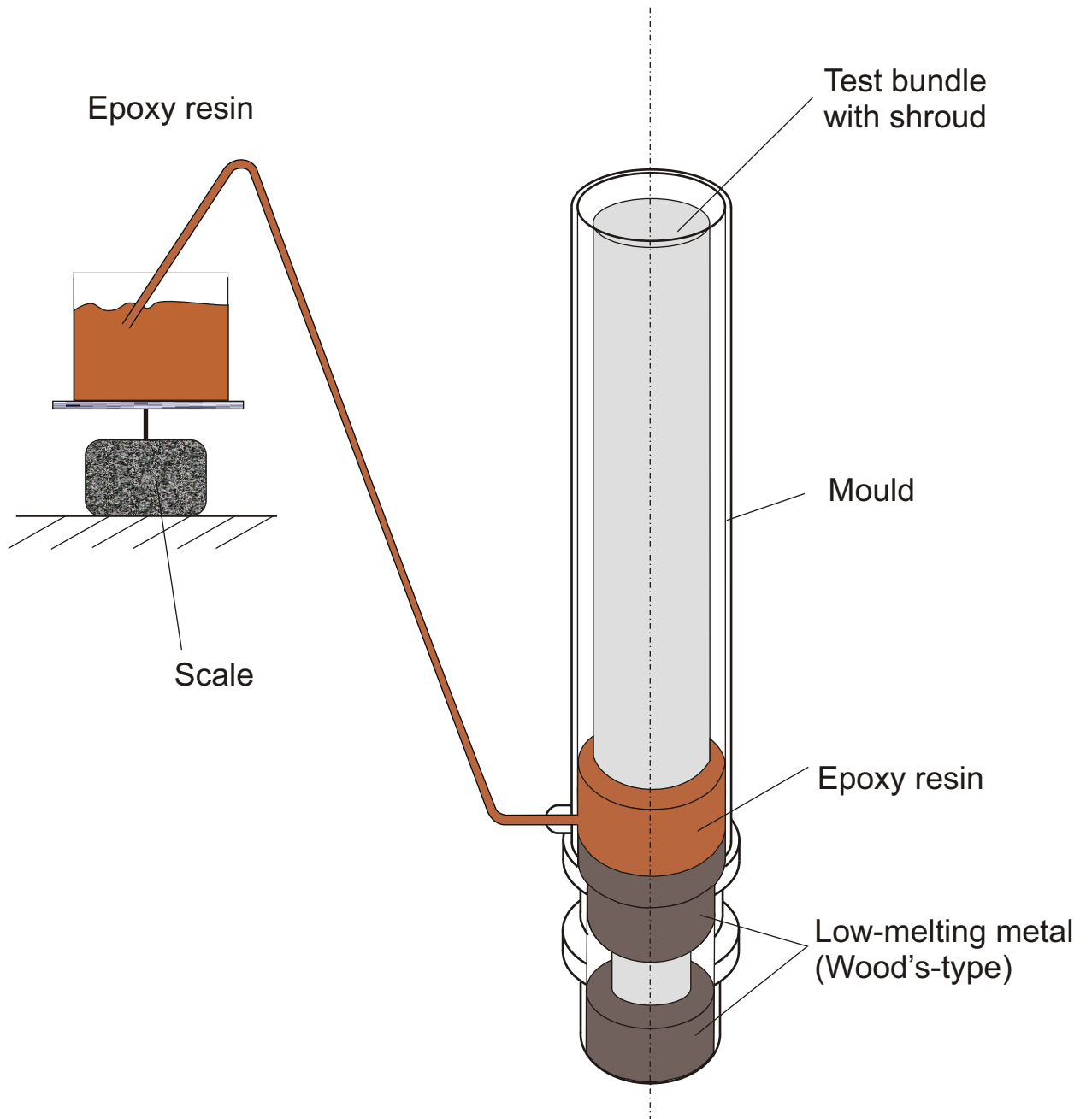


Fig. 47: QUENCH-12; Epoxying process of the tested bundle.



QUE-12-1 (534 mm, bottom)



QUE-12-1 (550 mm, top)



QUE-12-2 (554 mm, bottom)

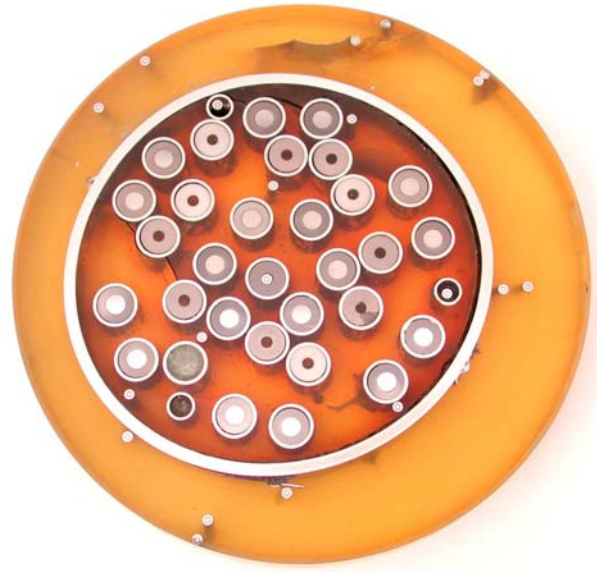


QUE-121-2 (570 mm, top)

Fig. 48: QUENCH-12; Cross sections at 534 mm, 550 mm, 554 mm and 570 mm.



QUE-12-3 (634 mm, bottom)



QUE-12-3 (650 mm, top)



QUE-12-4 (654 mm, bottom)



QUE-121-4 (670 mm, top)

Fig. 49: QUENCH-12; Cross sections at 634 mm, 650 mm, 654 mm and 670 mm.



QUE-12-5 (734 mm, bottom)



QUE-12-5 (750 mm, top)



QUE-12-6 (754 mm, bottom)



QUE-121-6 (770 mm, top)

Fig. 50: QUENCH-12; Cross sections at 734 mm, 750 mm, 754 mm, and 770 mm.



QUE-12-7 (834 mm, bottom)



QUE-12-7 (850 mm, top)



QUE-12-8 (854 mm, bottom)



QUE-121-8 (870 mm, top)

Fig. 51: QUENCH-12; Cross sections at 834 mm, 850 mm, 854 mm, and 870 mm.



QUE-12-9 (934 mm, bottom)



QUE-12-9 (950 mm, top)



QUE-12-10 (954 mm, bottom)



QUE-12-10 (970 mm, top)

Fig. 52: QUENCH-12; Cross sections at 934 mm, 950 mm, 954 mm, and 970 mm.



QUE-12-12 (1034 mm, bottom)



QUE-12-12 (1050 mm, top)

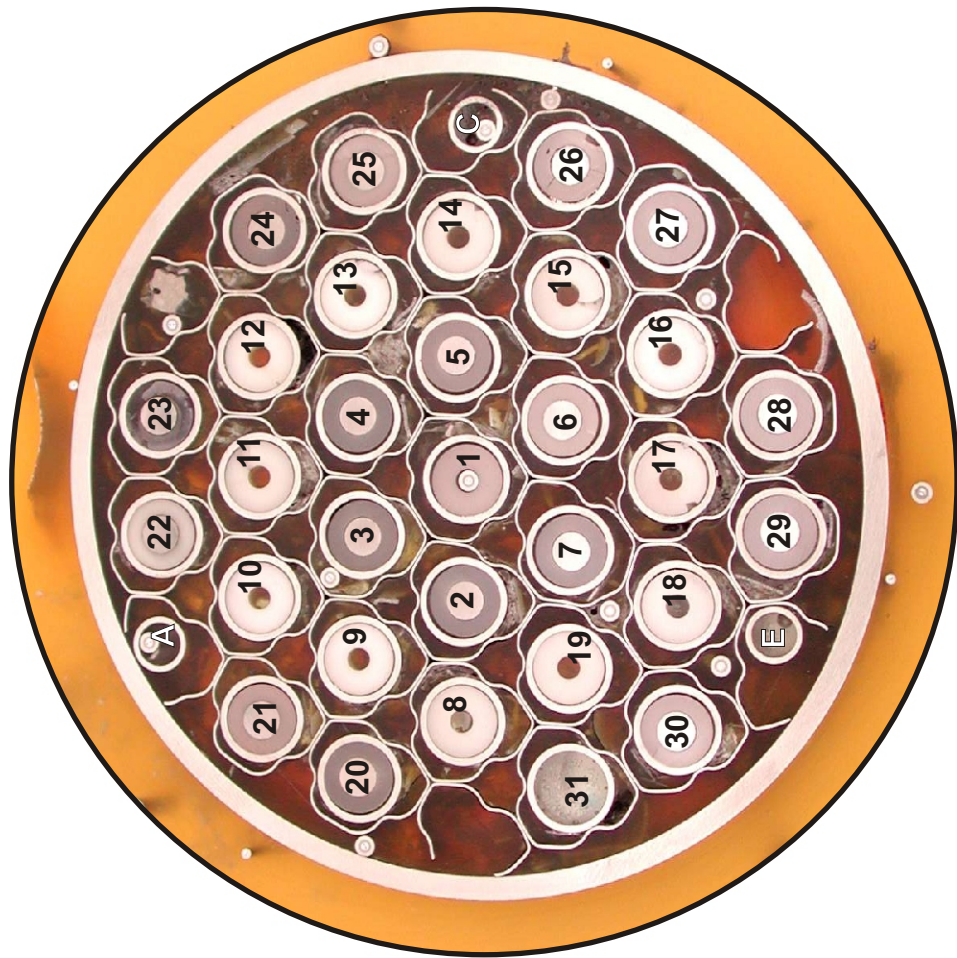


QUE-12-11 (1134 mm, bottom)

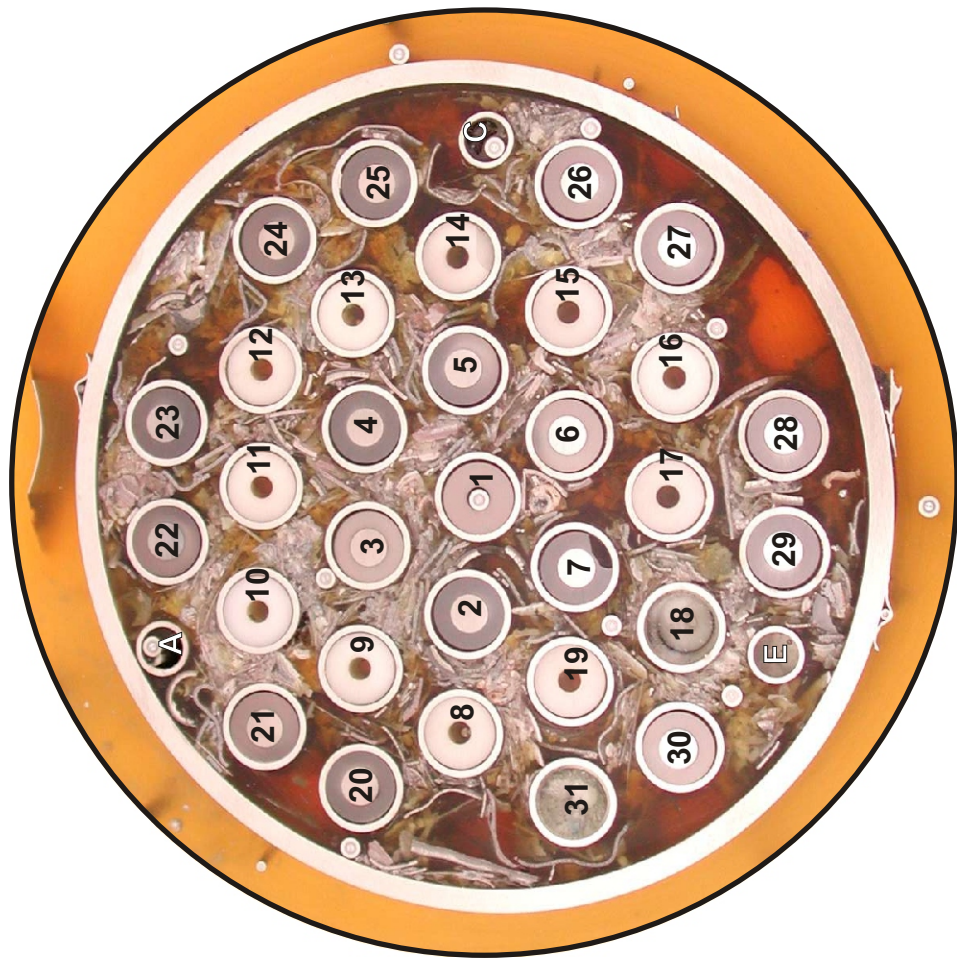


QUE-12-11 (1150 mm, top)

Fig. 53: QUENCH-12; Cross sections at 1034 mm, 1050 mm, 1134 mm and 1150 mm.



Elevation 534 mm, inverted to top view



Elevation 550mm, top view

Fig. 54: QUE-12-1, level 550 mm; cross section overview.

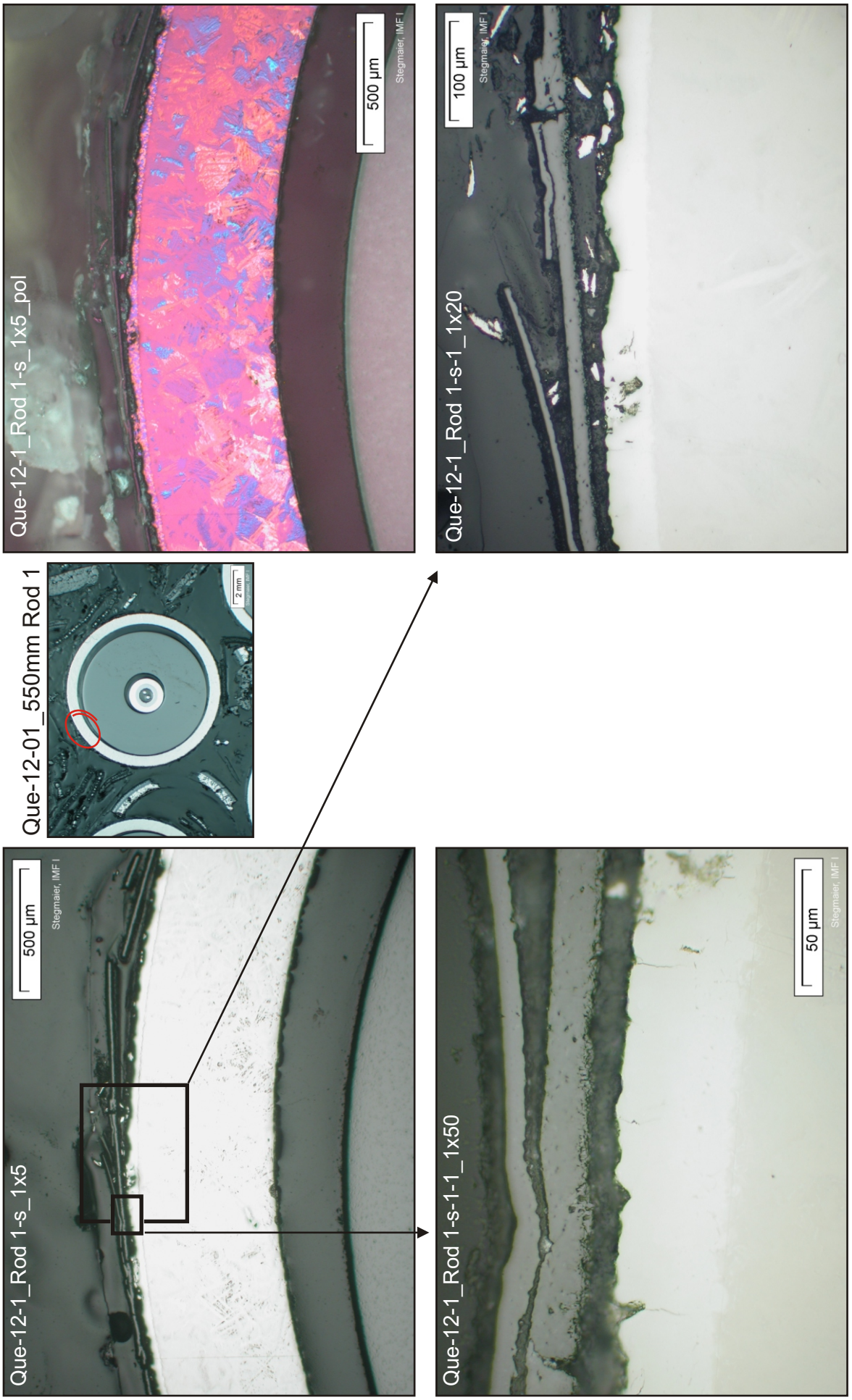


Fig. 55: QUE-12-1, level 550 mm; cladding oxidation of the central rod.

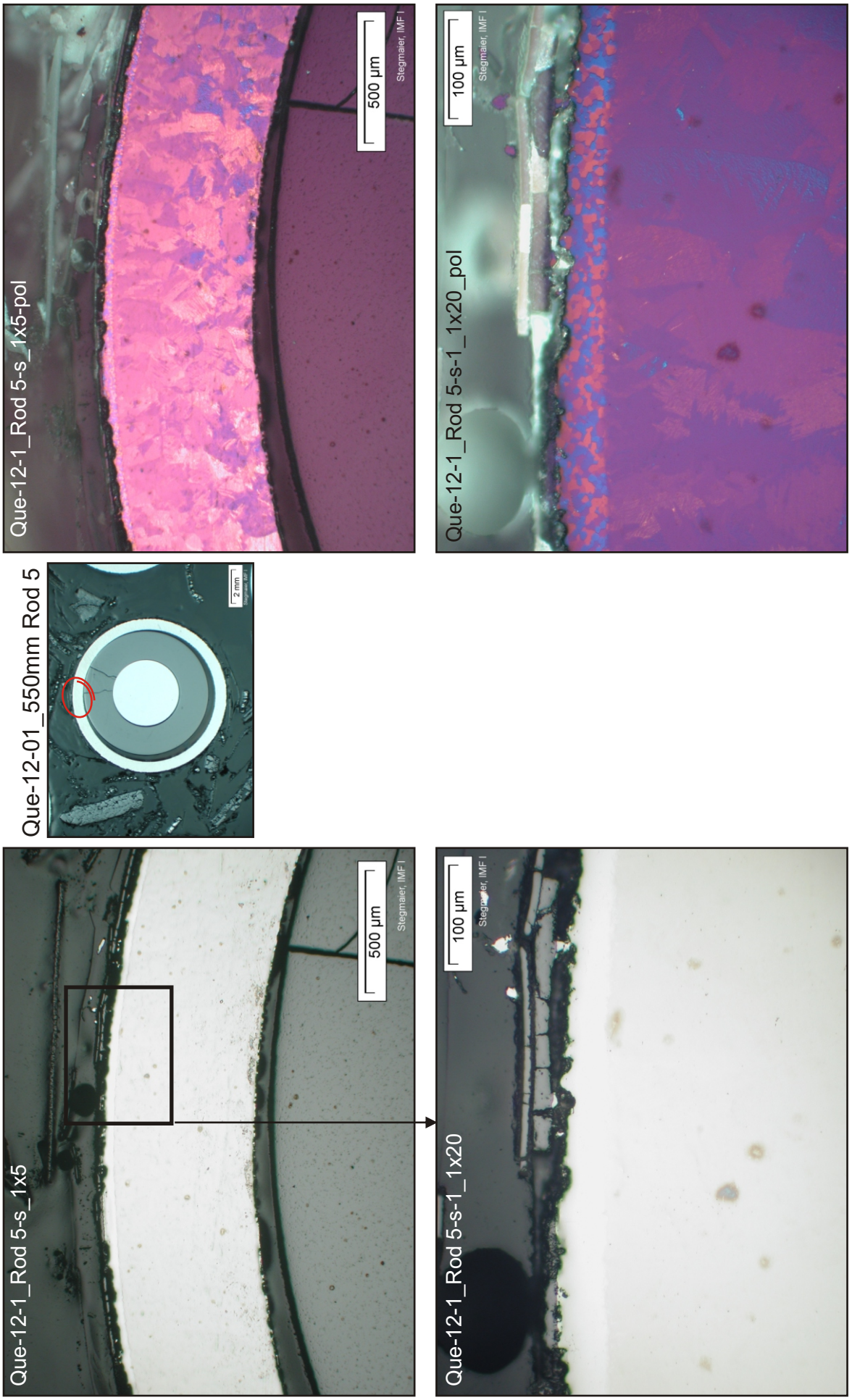


Fig. 56: QUE-12-1, level 550 mm; cladding oxidation of rod 5 (inner ring, heated).

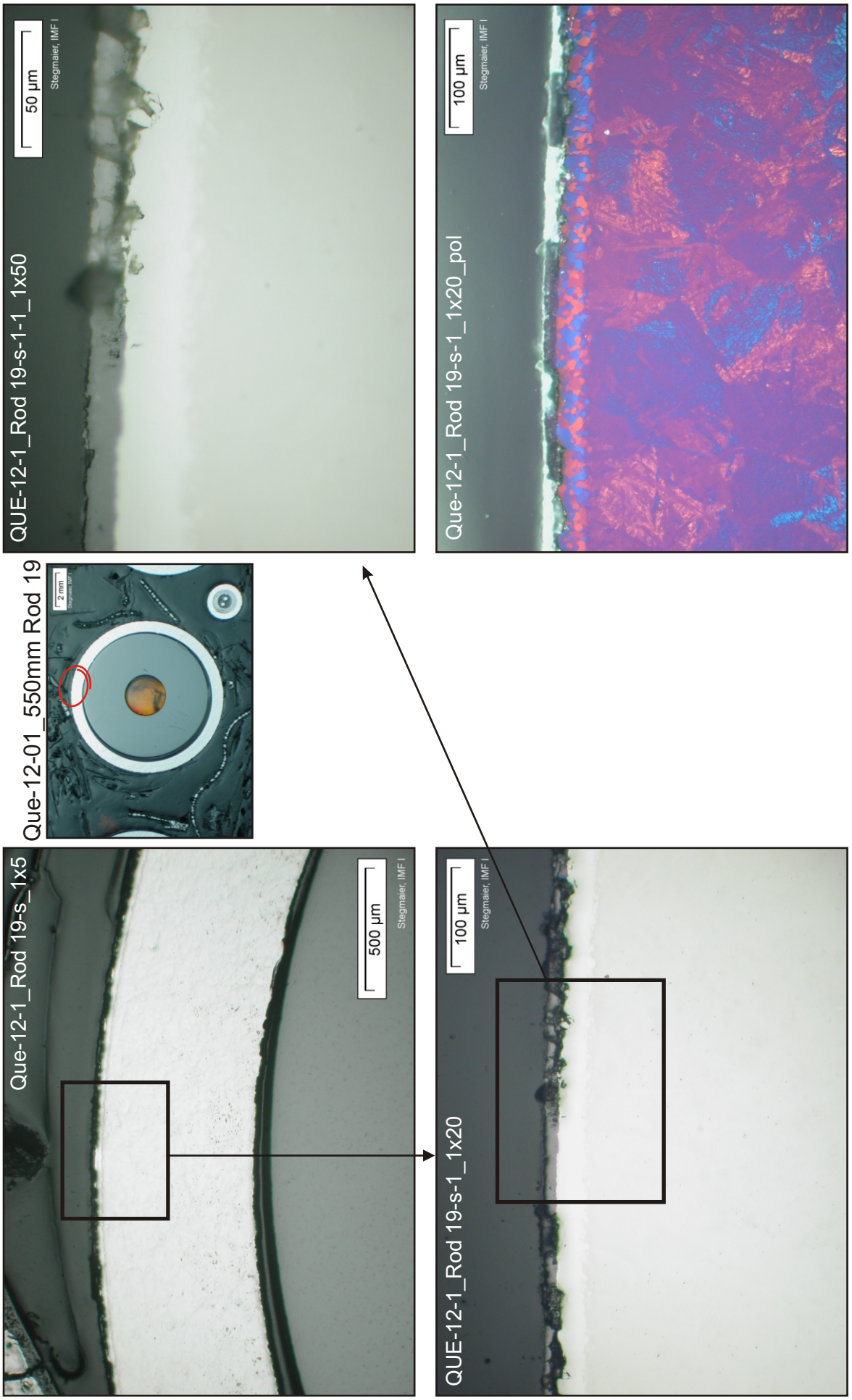


Fig. 57: QUE-12-1, level 550 mm; cladding oxidation of rod 19 (second ring, unheated).

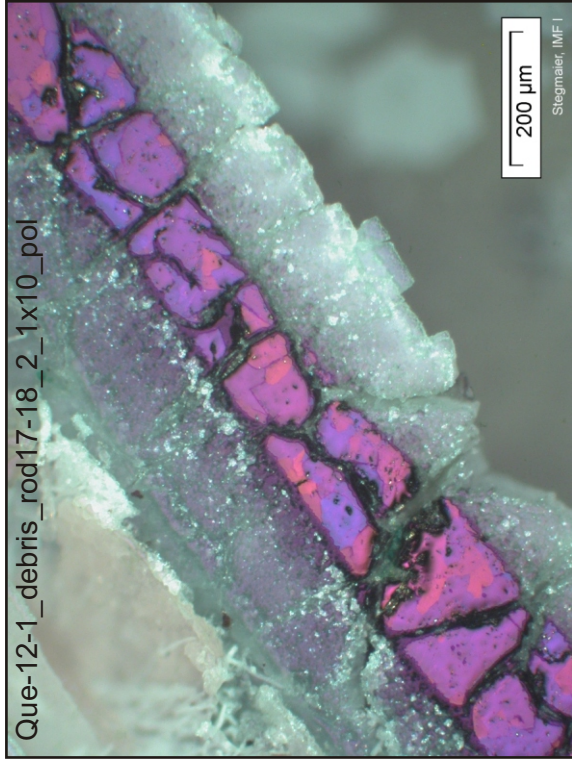
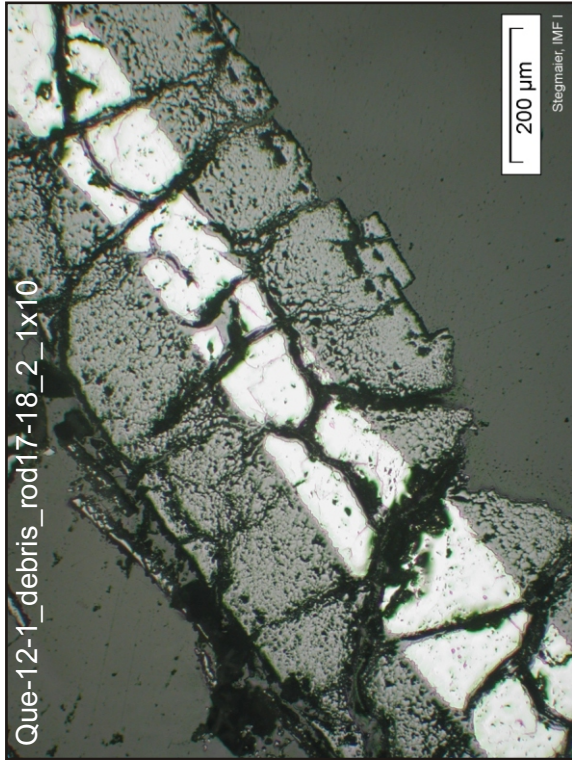
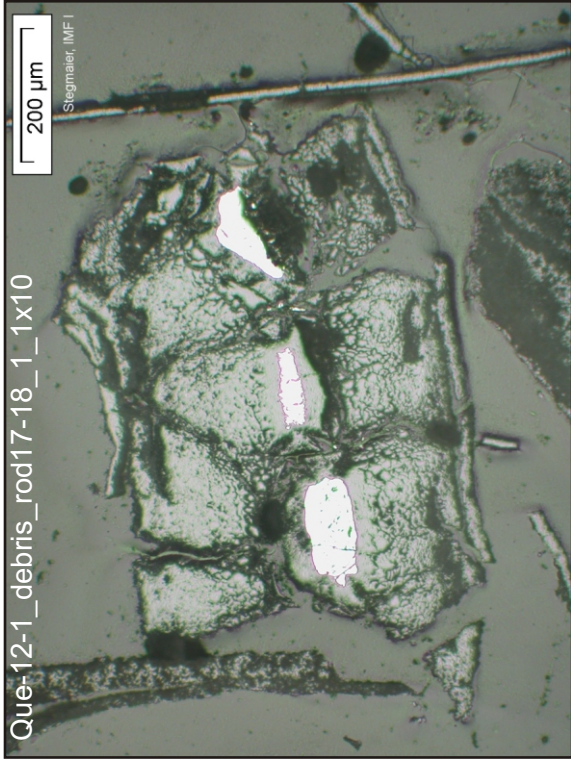
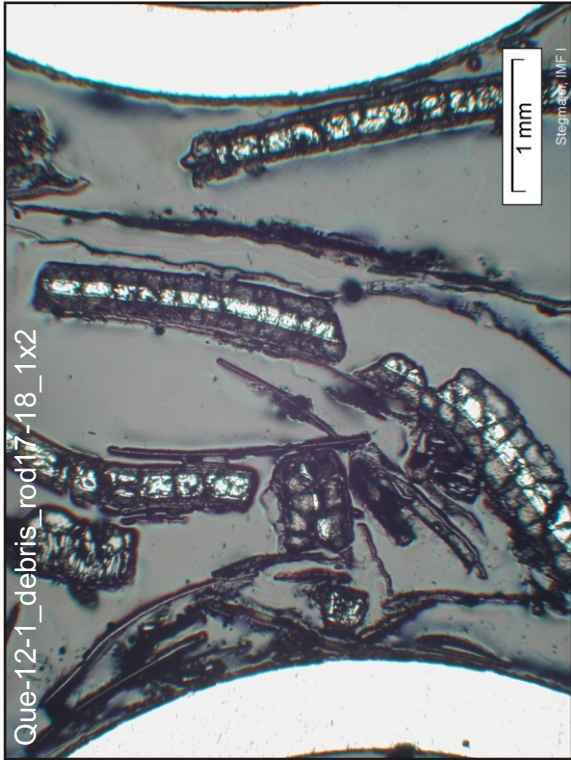


Fig. 58: QUE-12-1, level 550 mm; relocated cladding debris, showing both-sided oxidation.

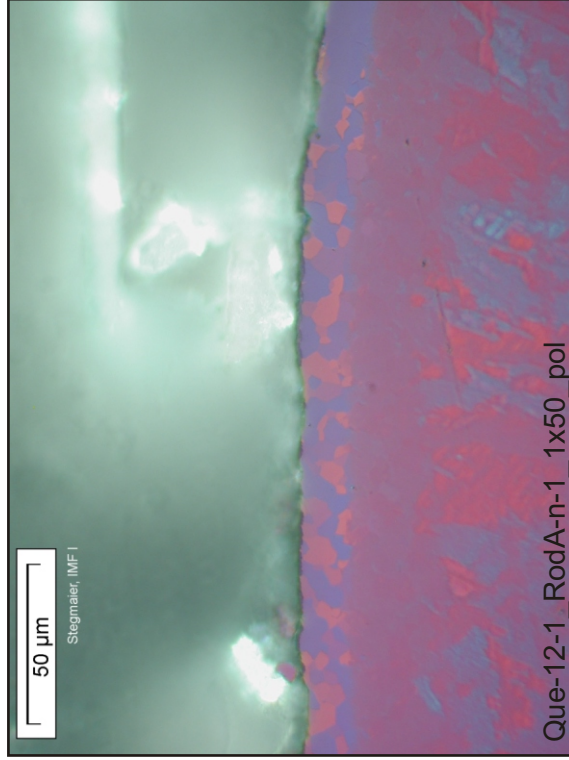
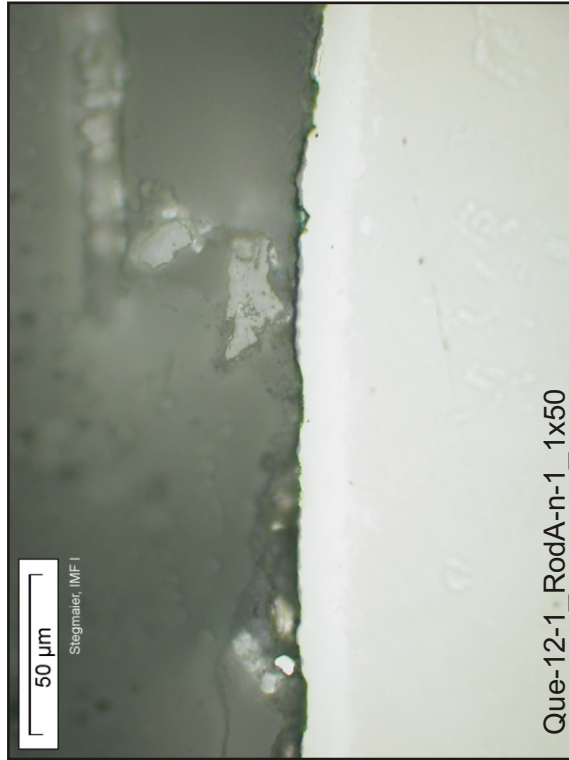
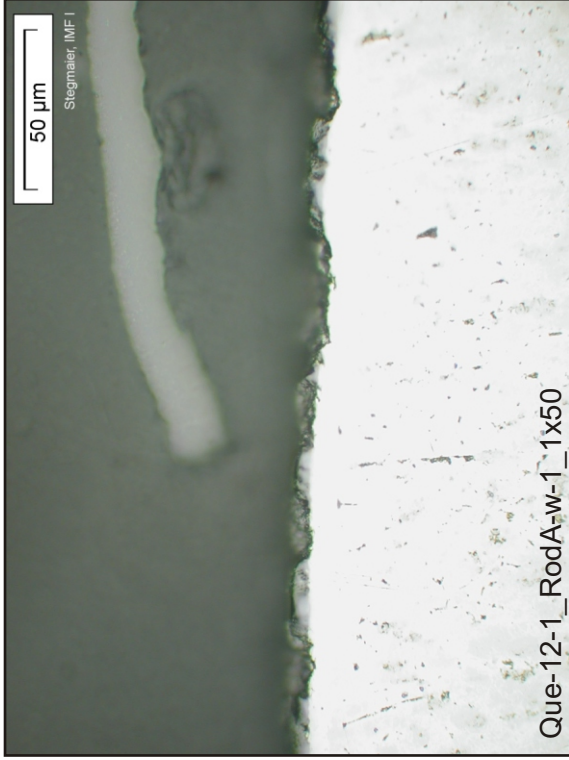
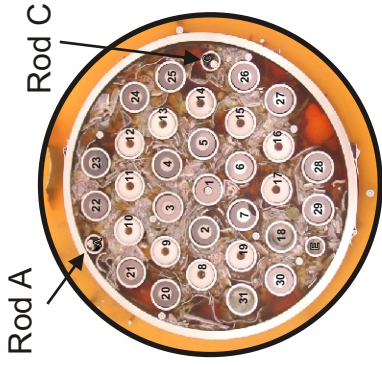
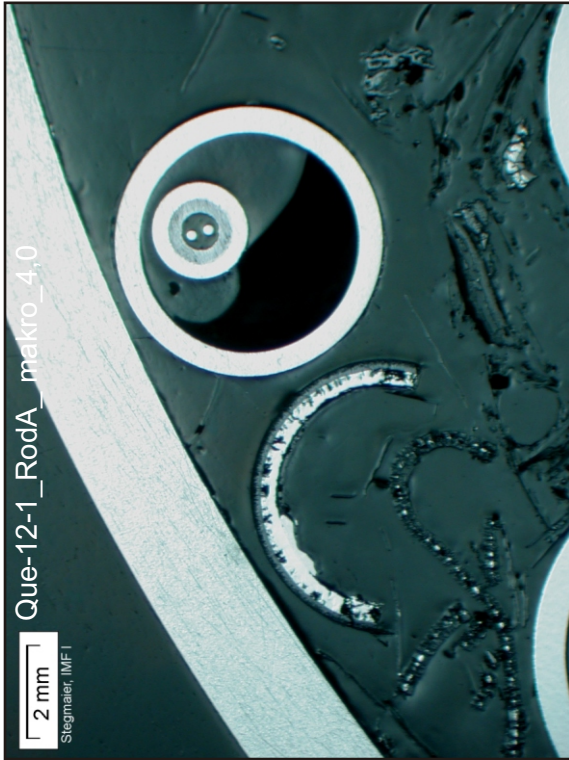


Fig. 59: QUE-12-1, level 550 mm; oxidation state of corner rod A.

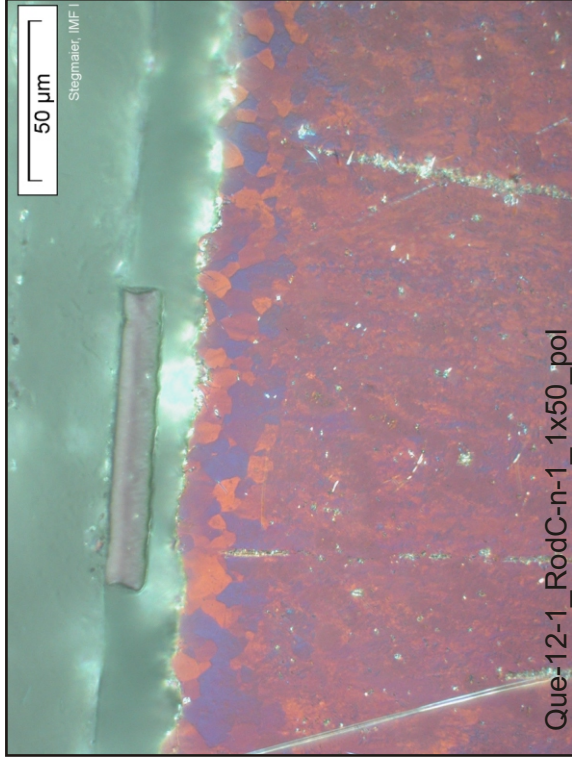
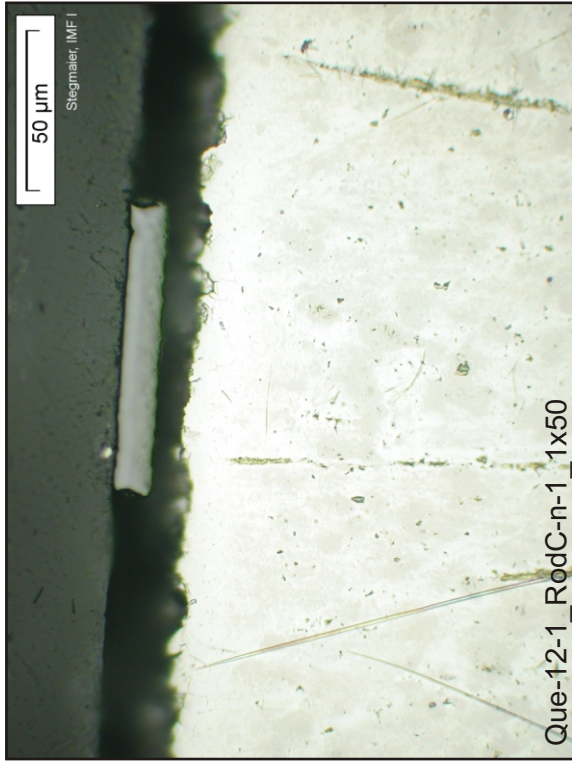
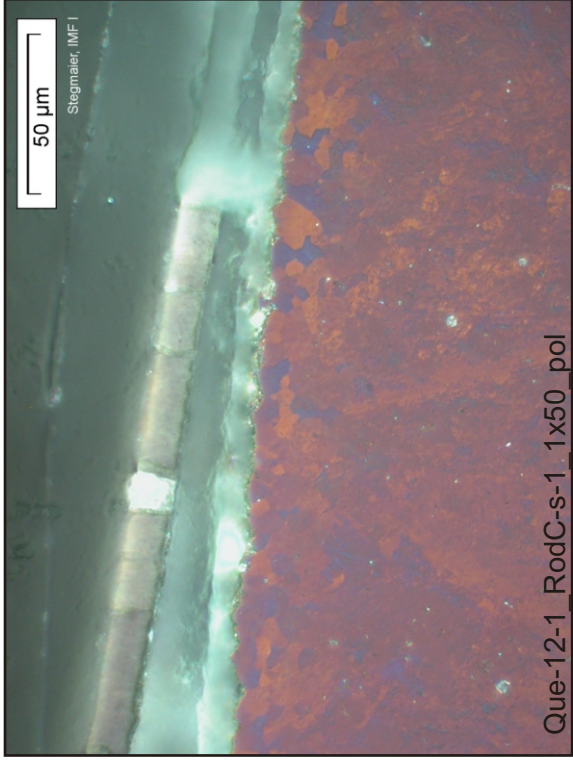
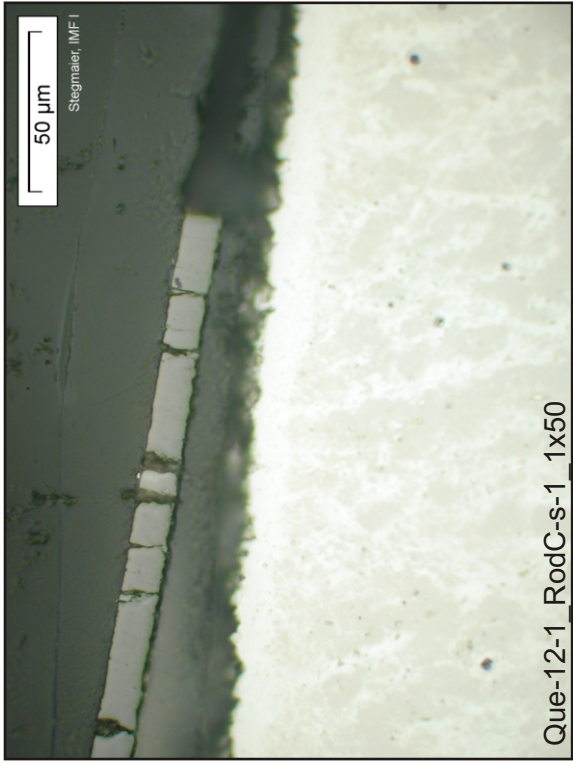
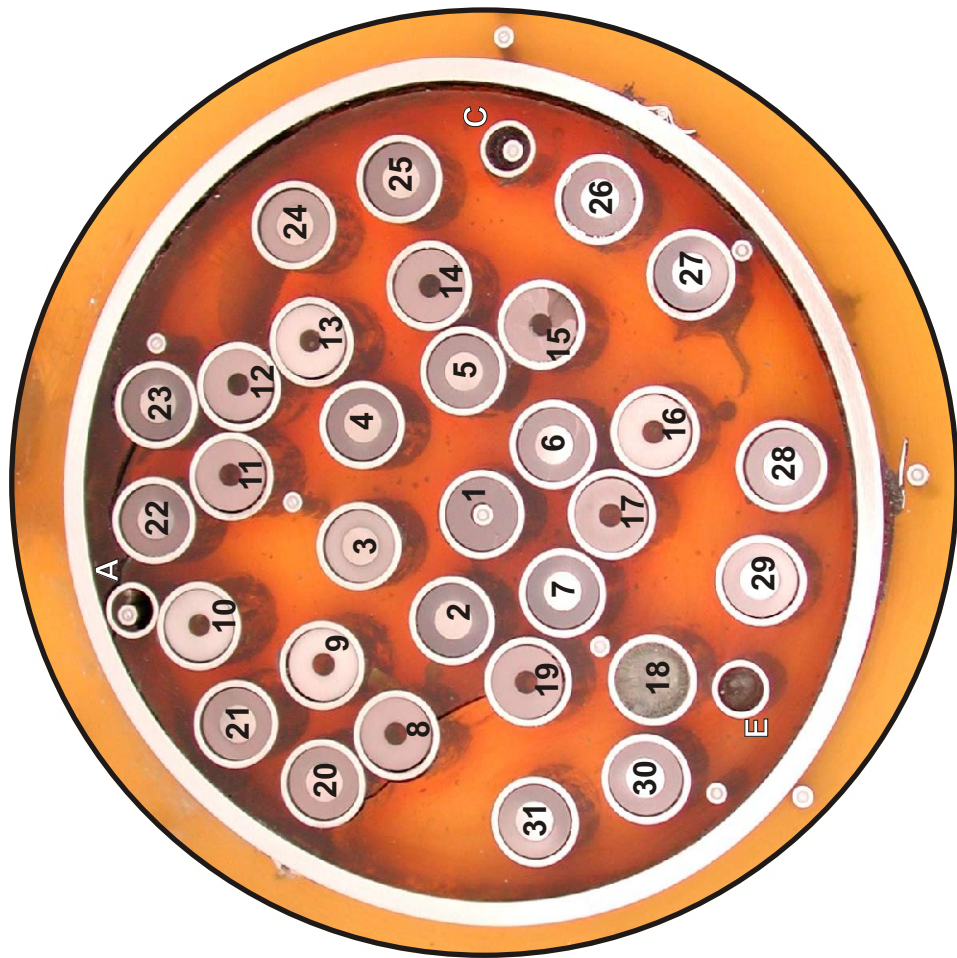


Fig. 60: QUE-12-1, level 550 mm; oxidation state of corner rod C.



Elevation 634 mm, inverted to top view



Elevation 650mm, top view

Fig. 61: QUE-12-3, level 650 mm; cross section overview.

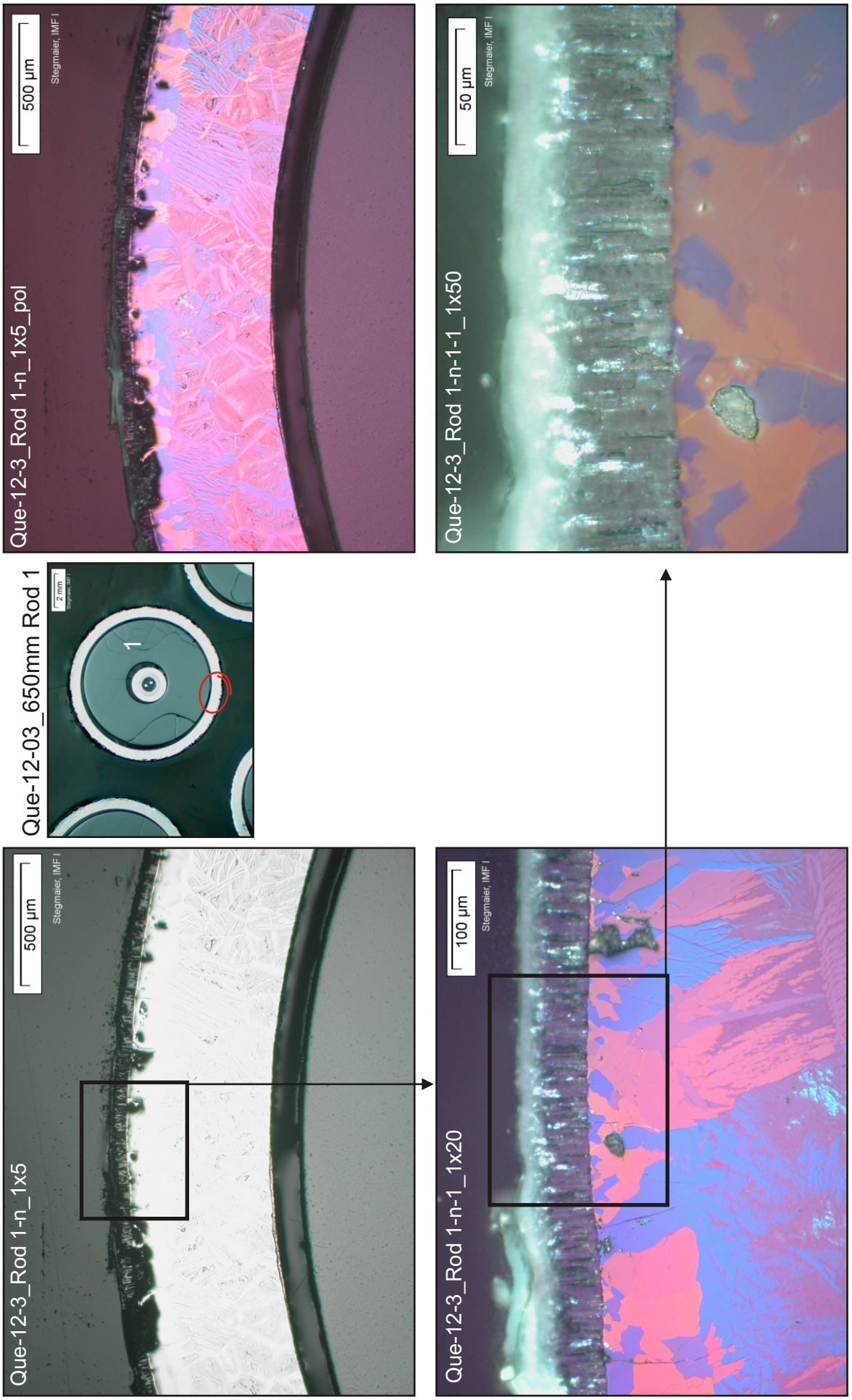


Fig. 62: QUE-12-3, level 650 mm; cladding oxidation of the central rod.

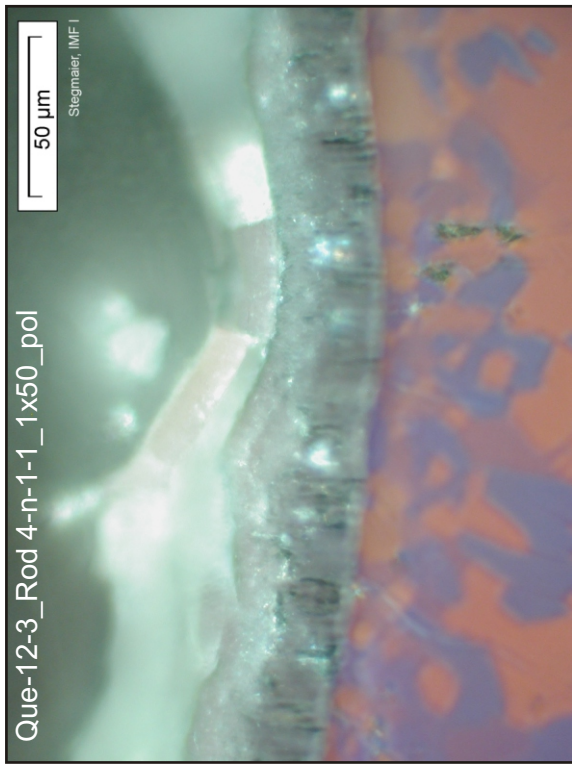
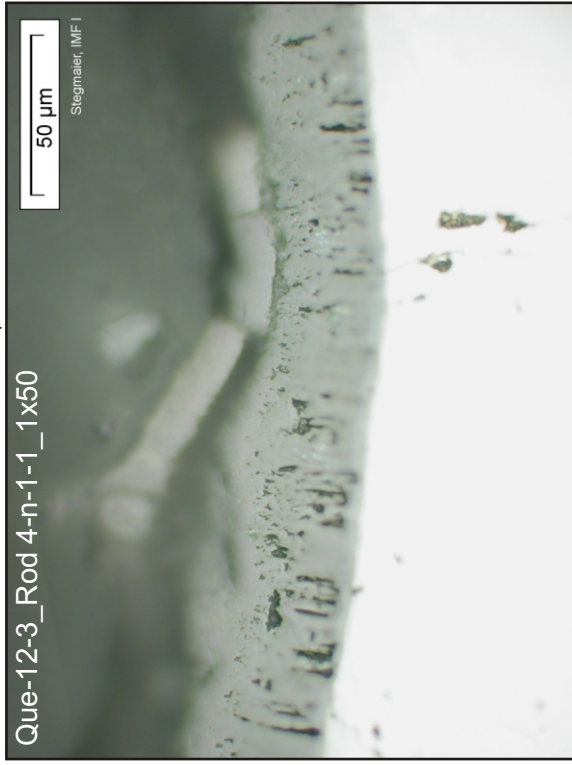
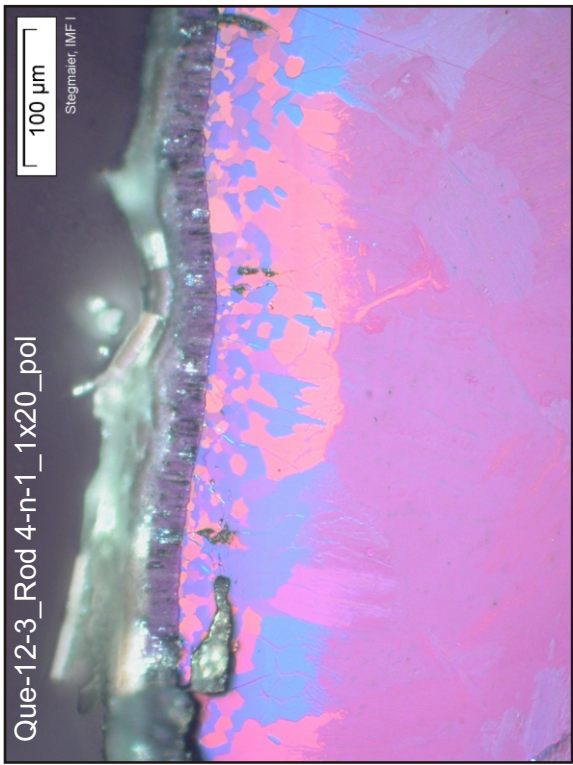
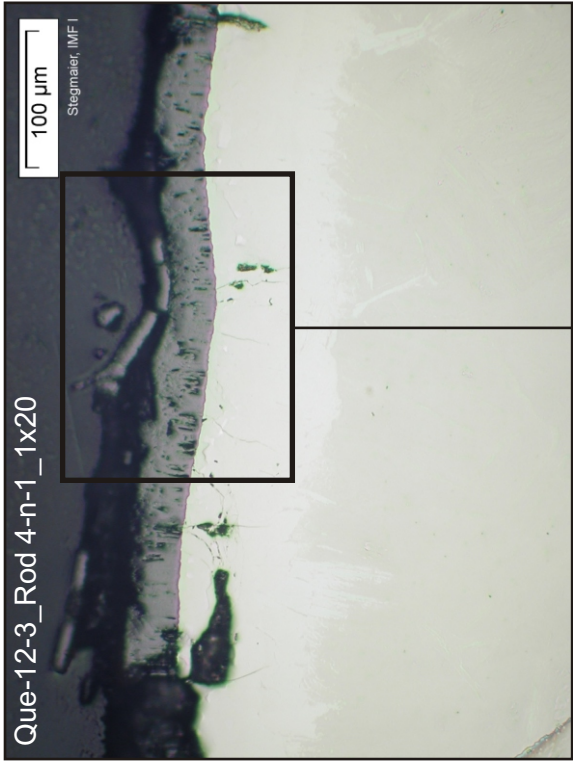


Fig. 63: QUE-12-3, level 650 mm; cladding oxidation of rod 4 (inner ring, heated).

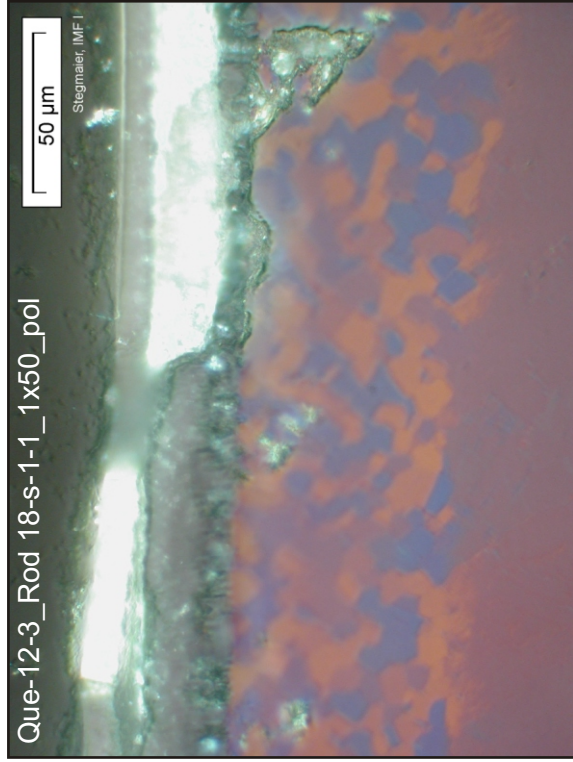
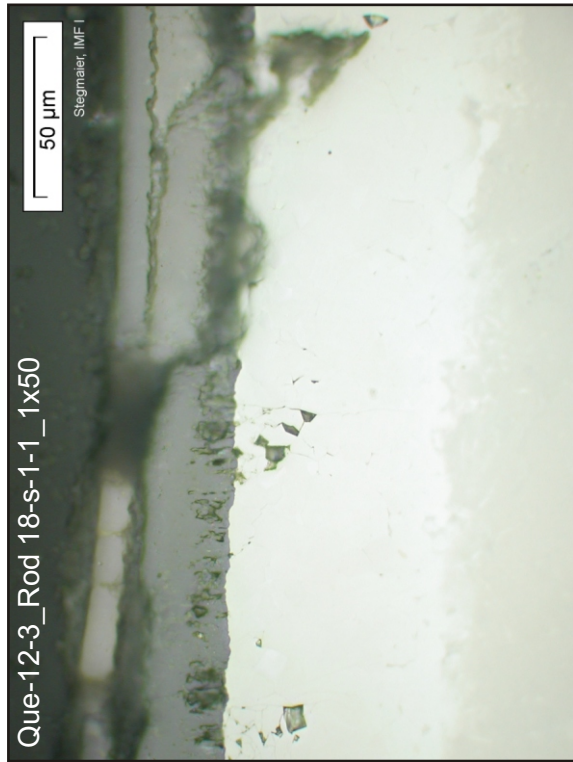
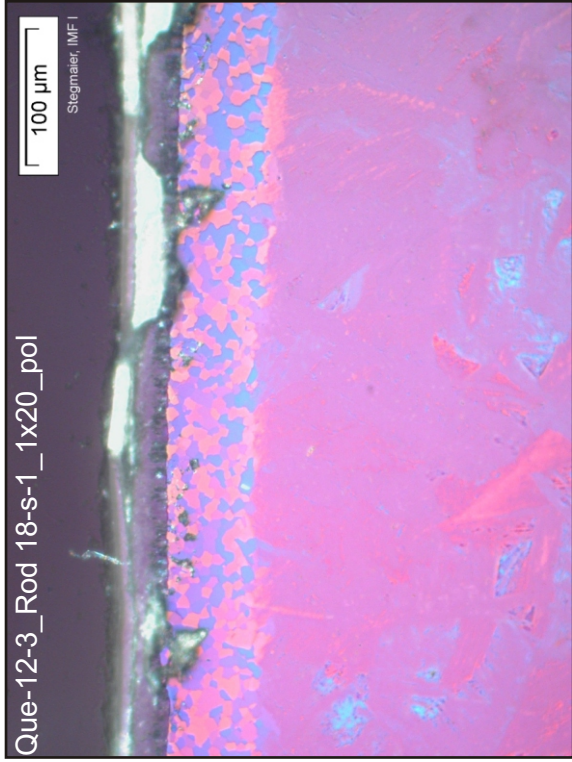
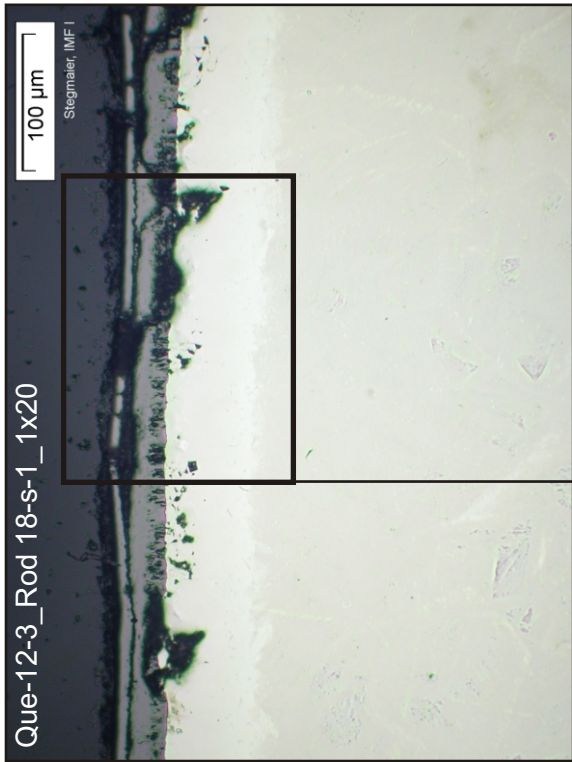


Fig. 64: QUE-12-3, level 650 mm; cladding oxidation of rod 18 (second ring, unheated).

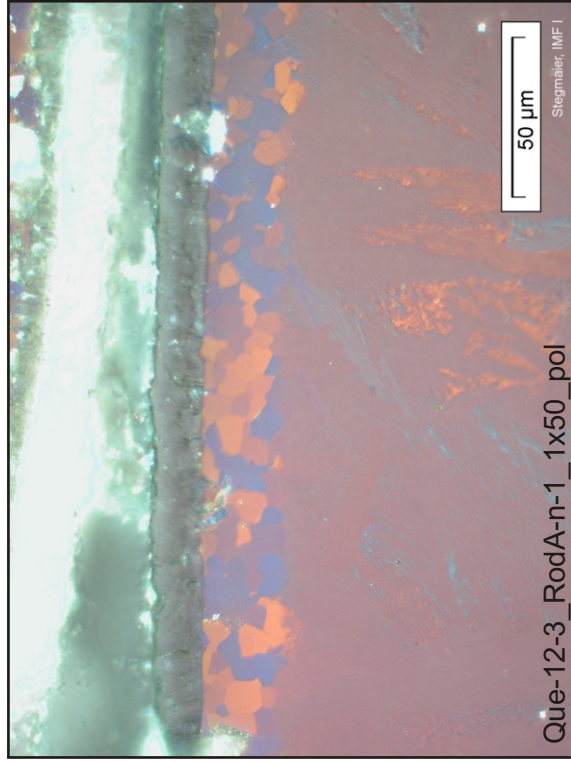
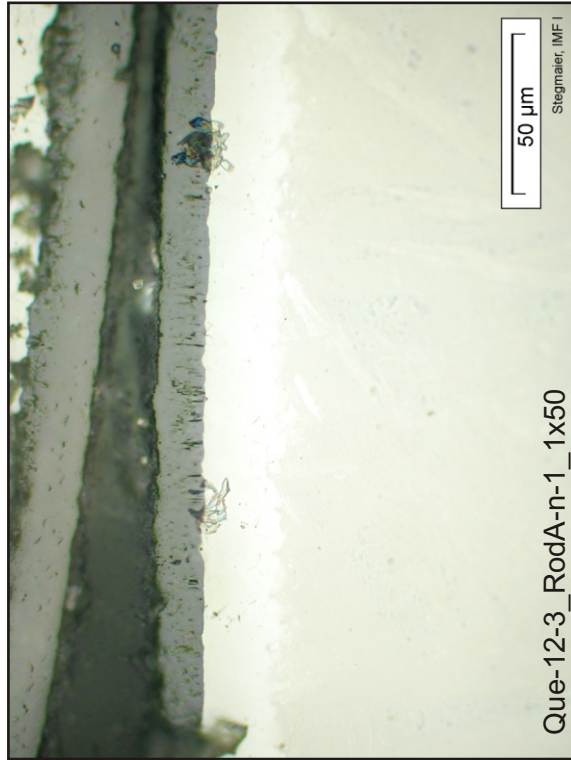
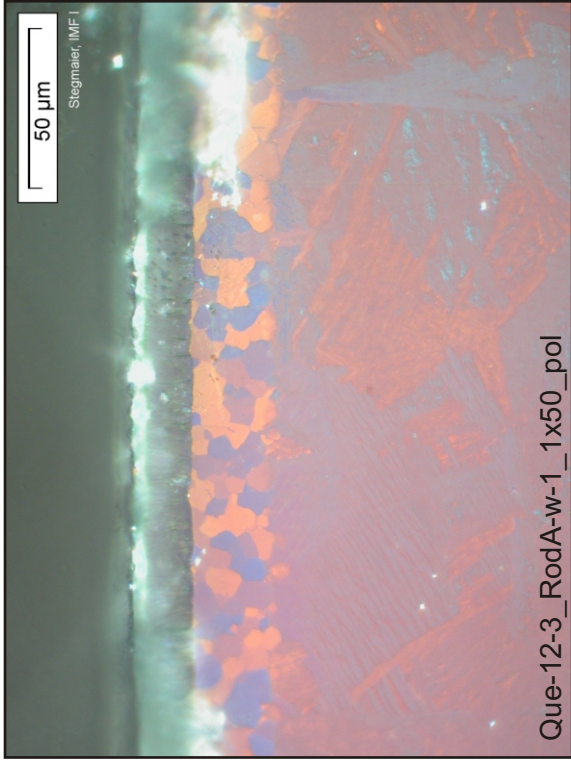
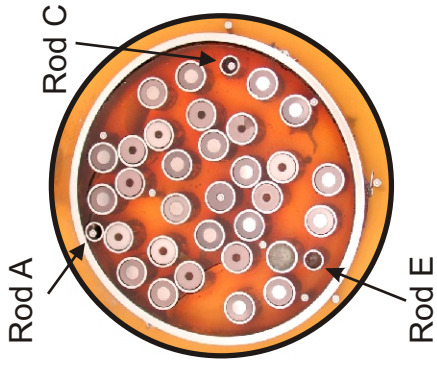


Fig. 65: QUE-12-3, level 650 mm; oxidation state of corner rod A.

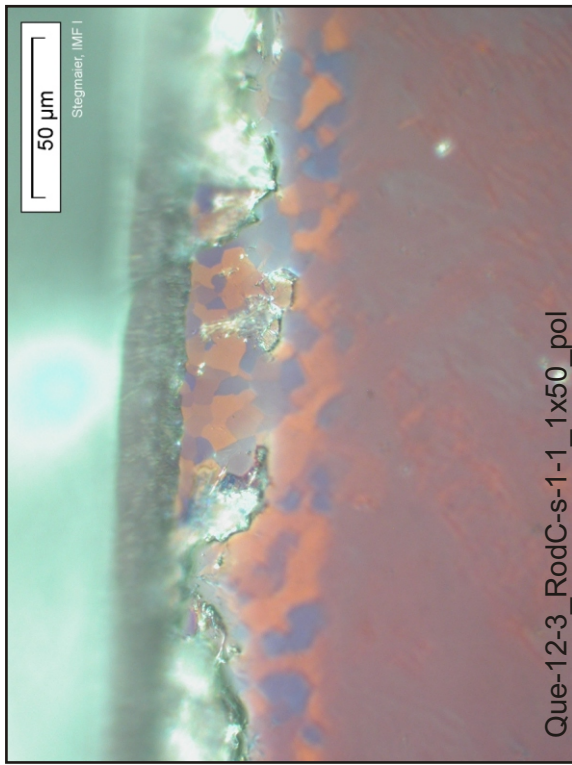
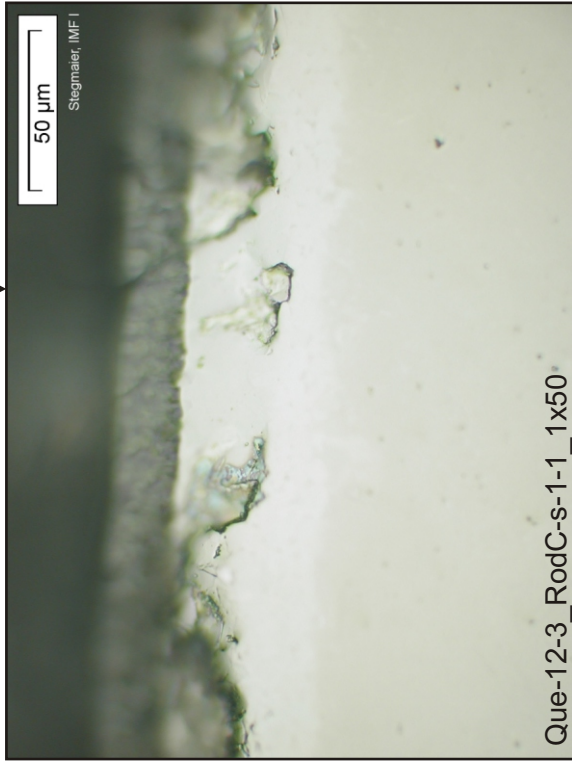
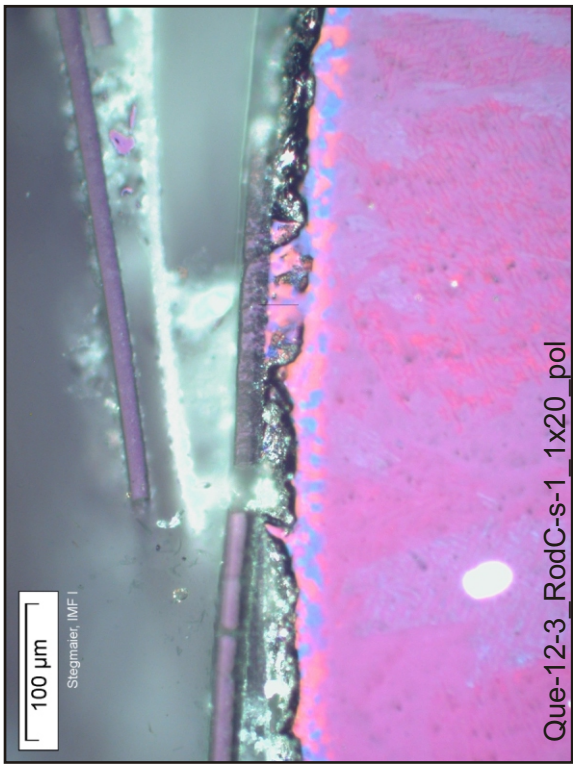
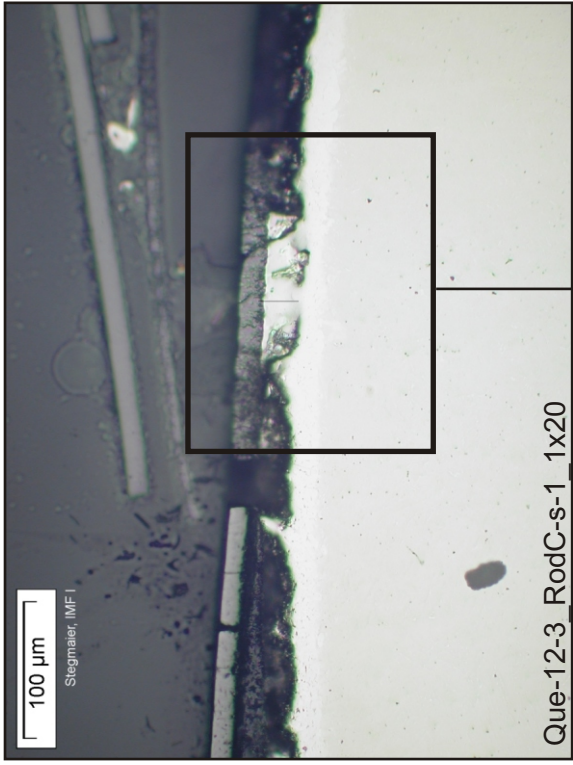


Fig. 66: QUE-12-3, level 650 mm; oxidation state of corner rod C.

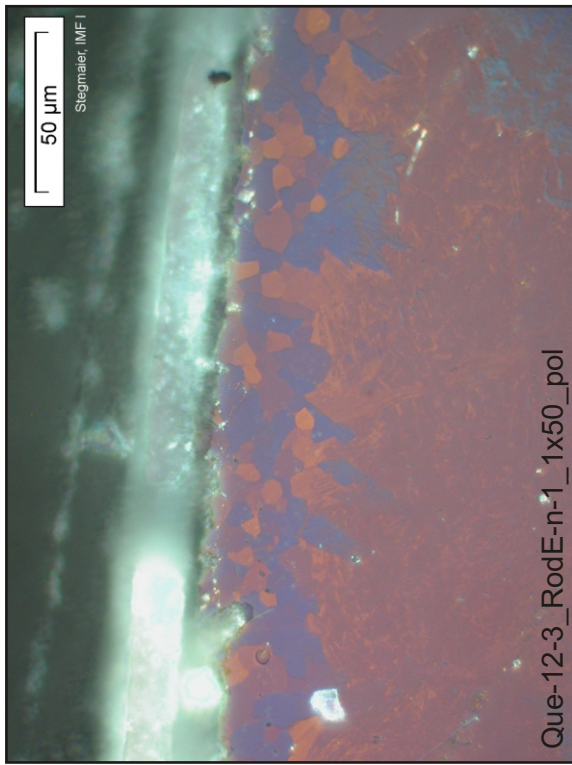
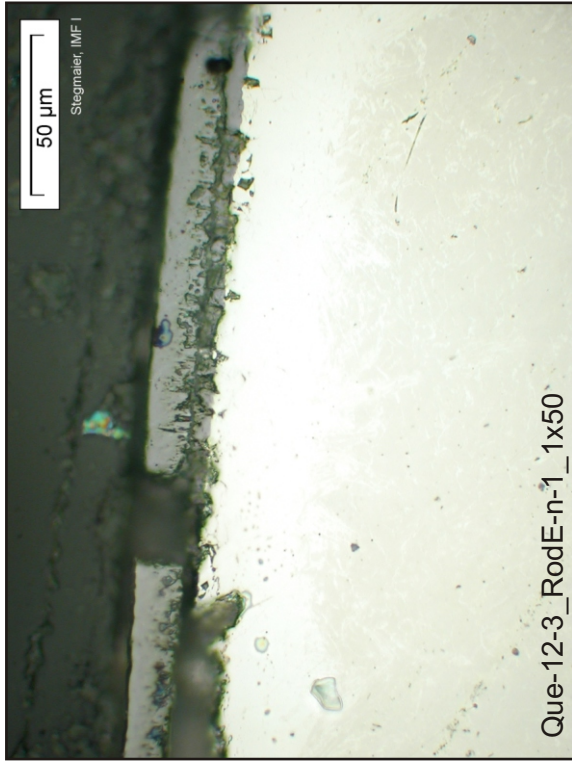
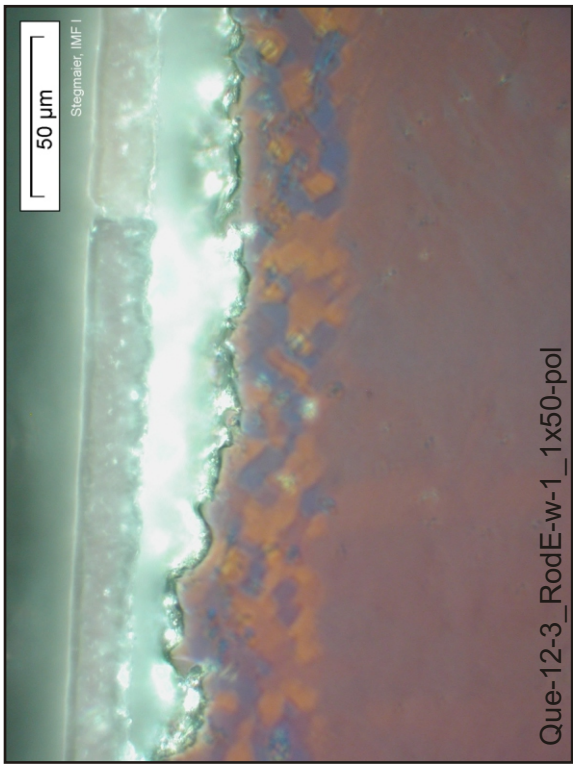
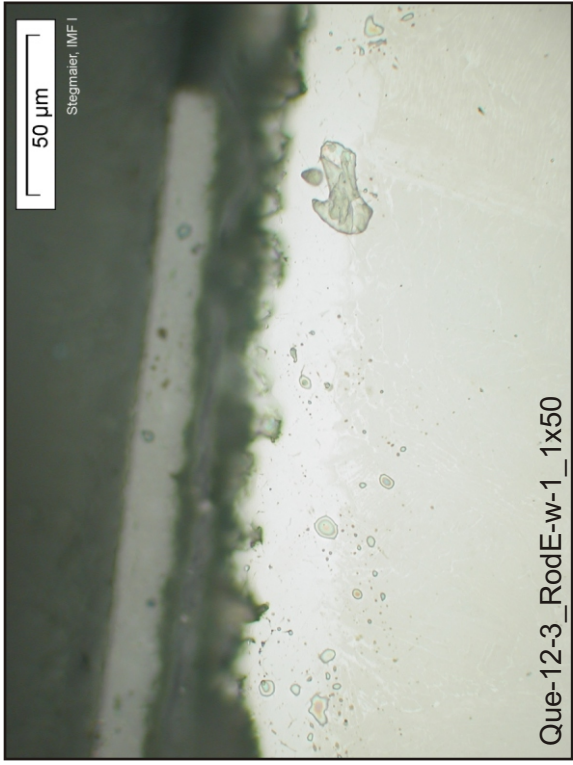
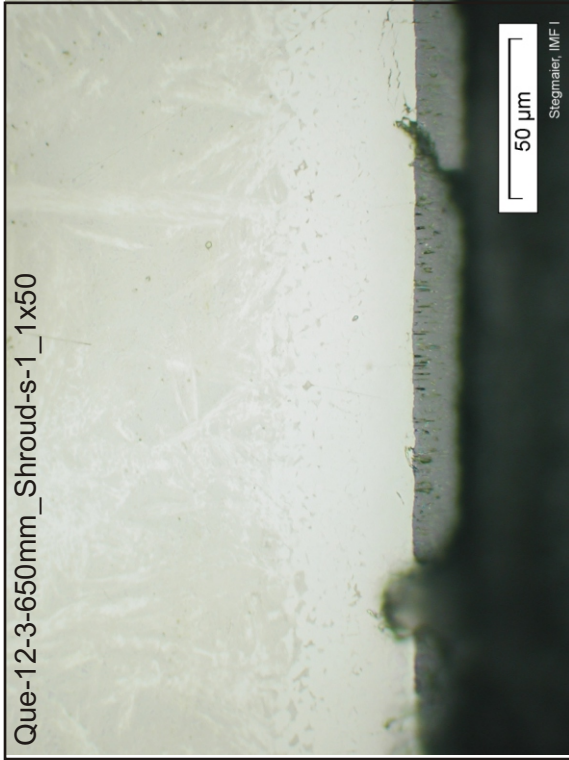
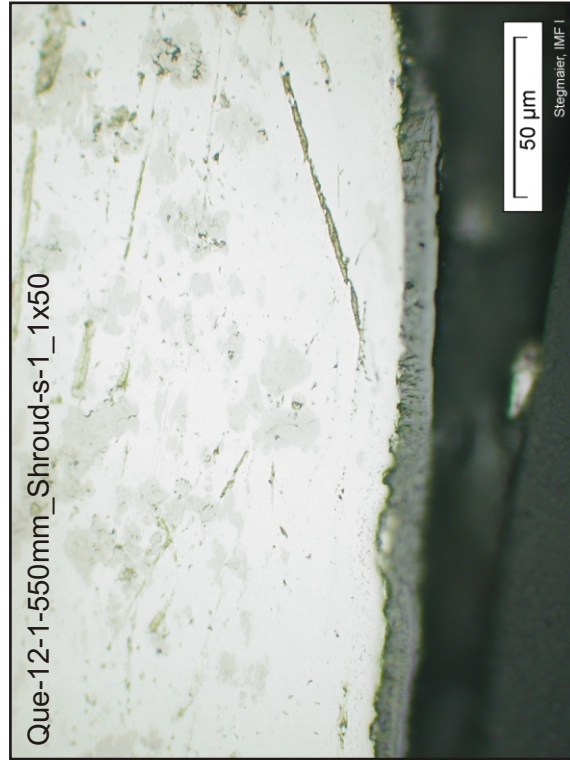
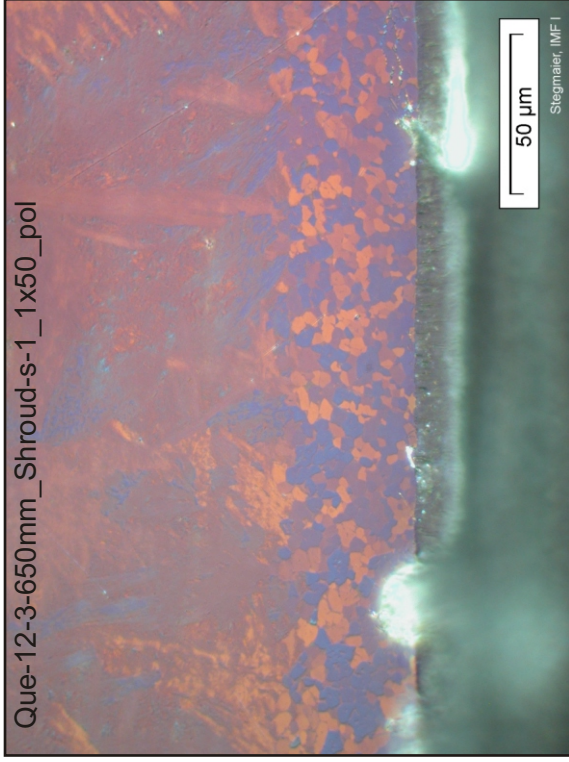


Fig. 67: QUE-12-3, level 650 mm; oxidation state of corner rod E.



Elevation 650 mm



Elevation 550 mm

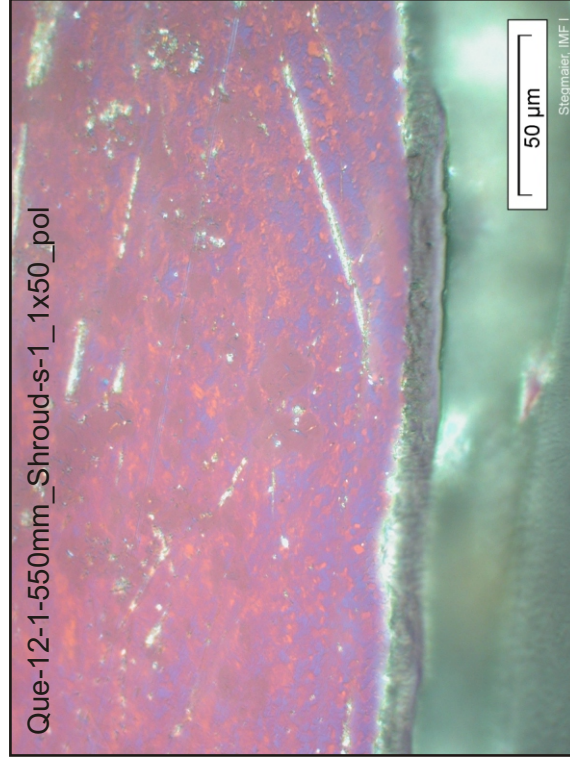
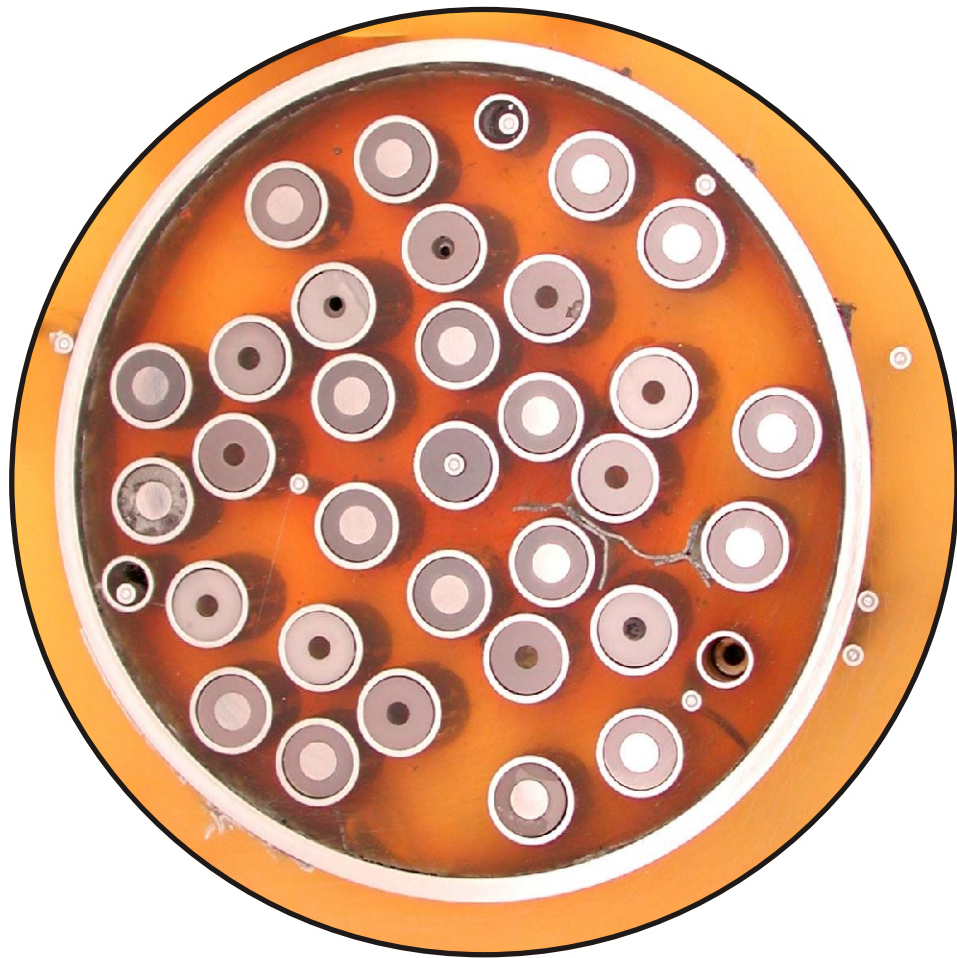
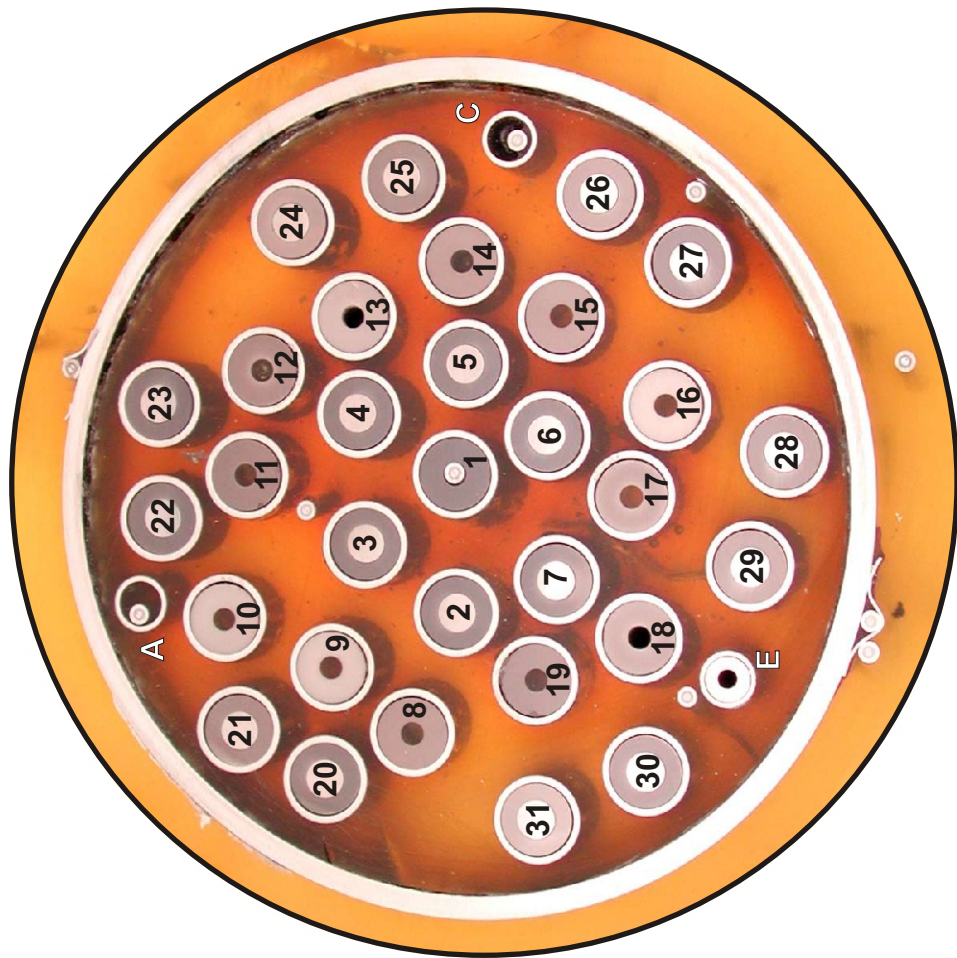


Fig. 68: QUE-12-1 and -3, levels 550 and 650 mm; oxidation of the shroud (inner side).



Elevation 734 mm, inverted to top view



Elevation 750mm, top view

Fig. 69: QUE-12-5, level 750 mm; cross section overview.

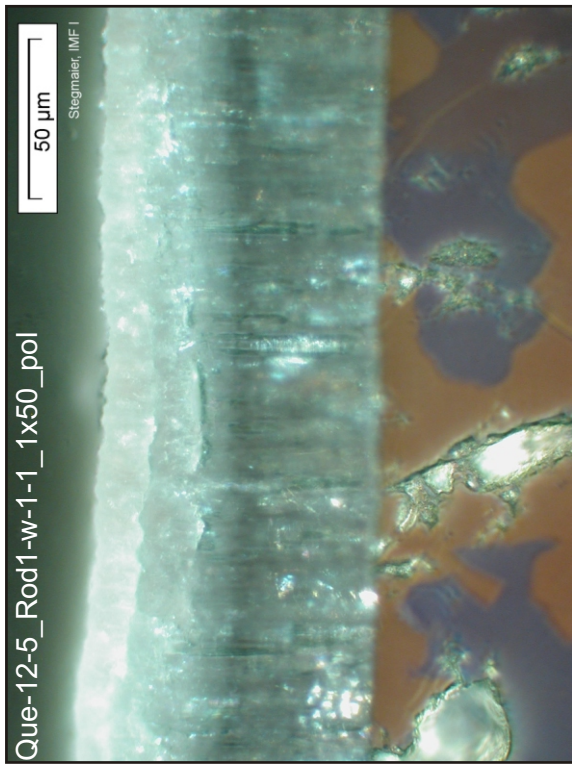
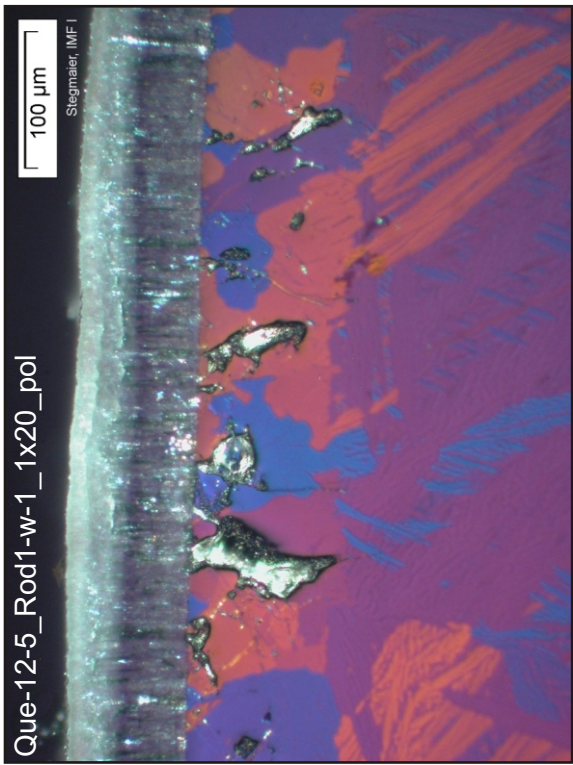
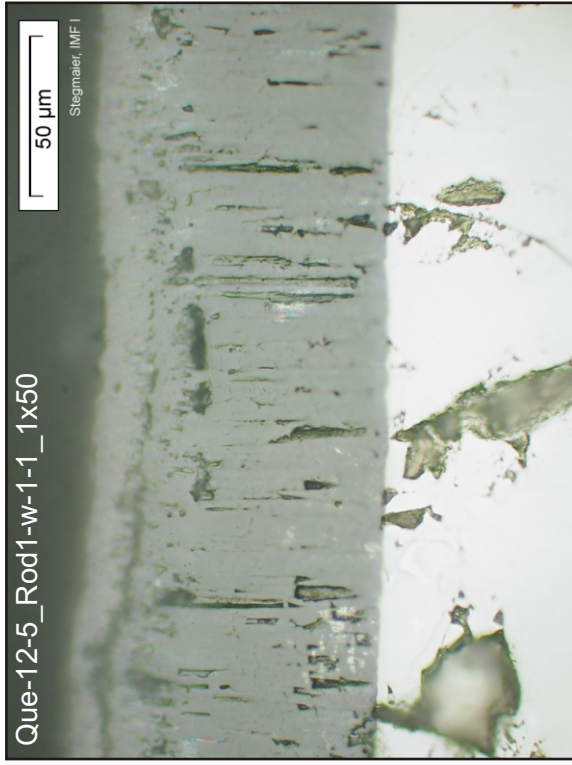
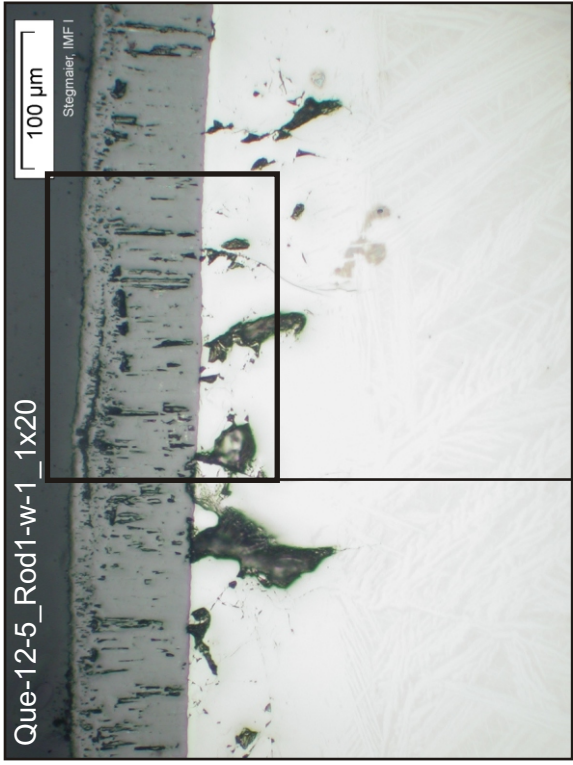


Fig. 70: QUE-12-5, level 750 mm; cladding oxidation of the central rod.

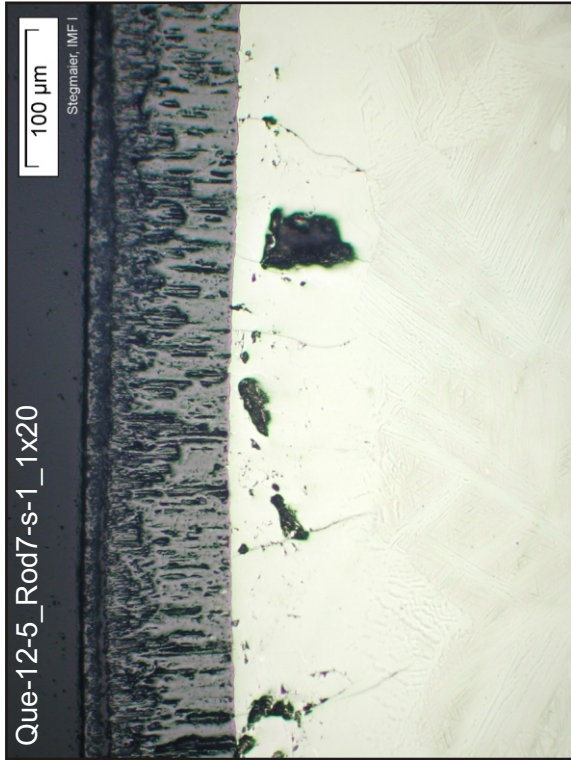


Fig. 71: QUE-12-5, level 750 mm; cladding oxidation of rods 2 and 7 (inner ring, heated).

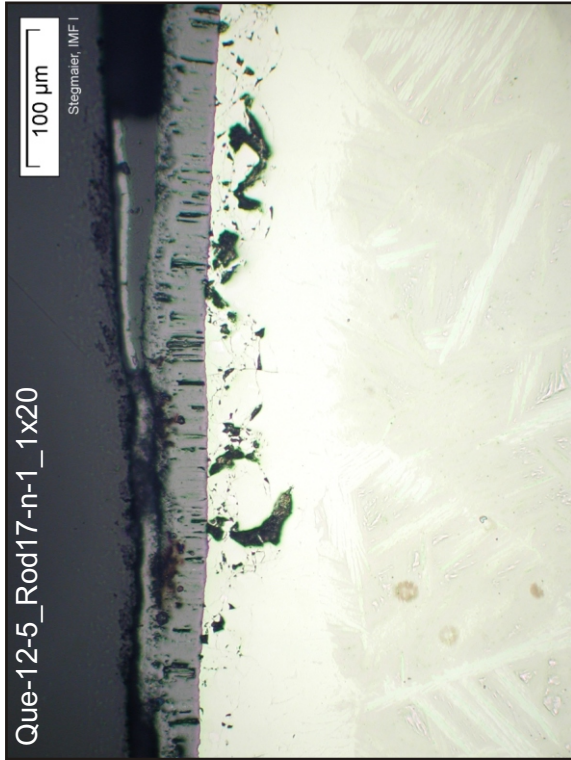
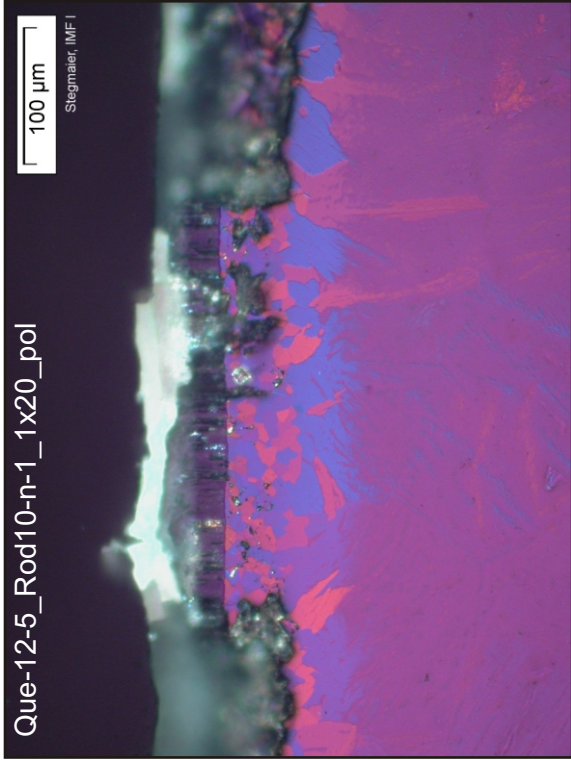
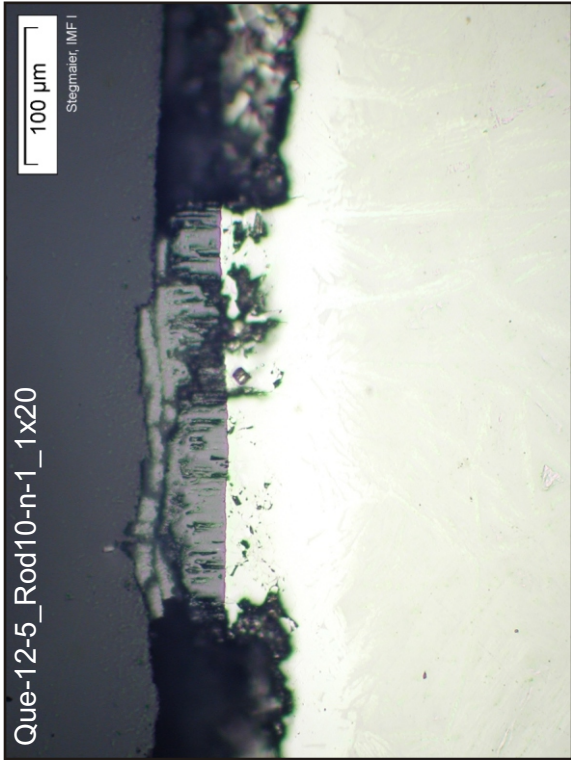


Fig. 72: QUE-12-5, level 750 mm; cladding oxidation of rods 10 and 17 (second ring, unheated).

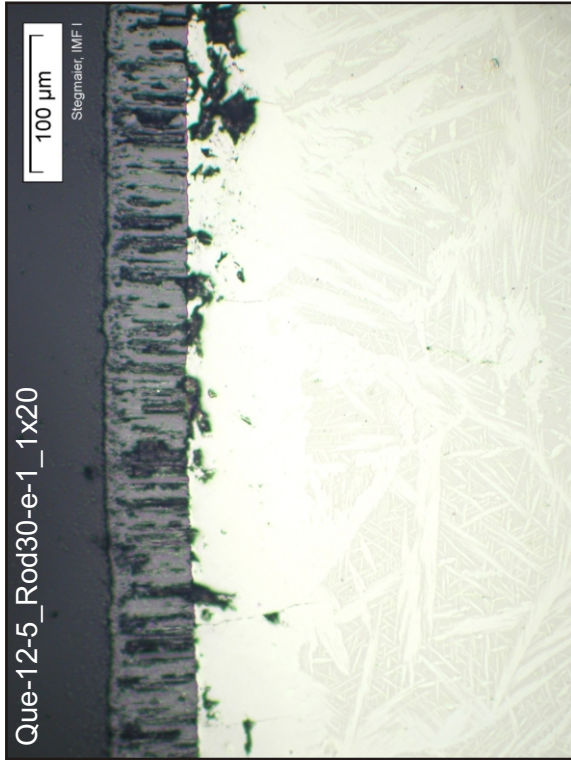
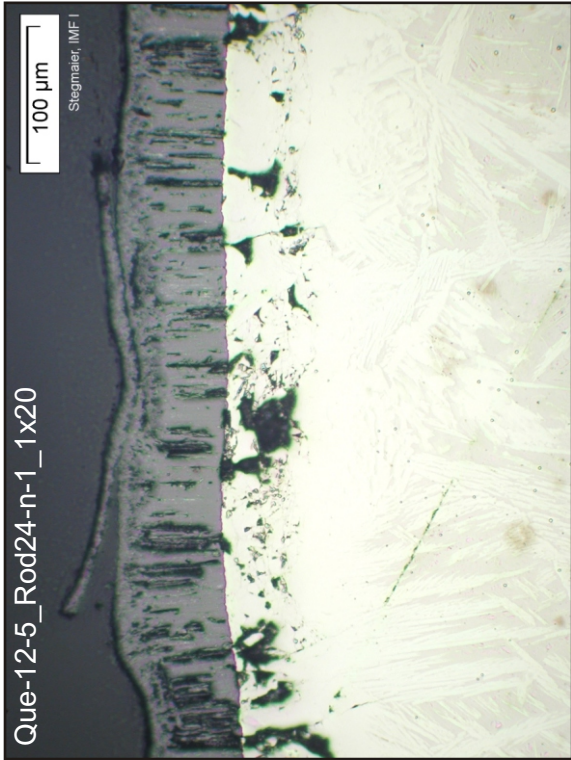


Fig. 73: QUE-12-5, level 750 mm; cladding oxidation of rods 24 and 30 (outer ring, heated).

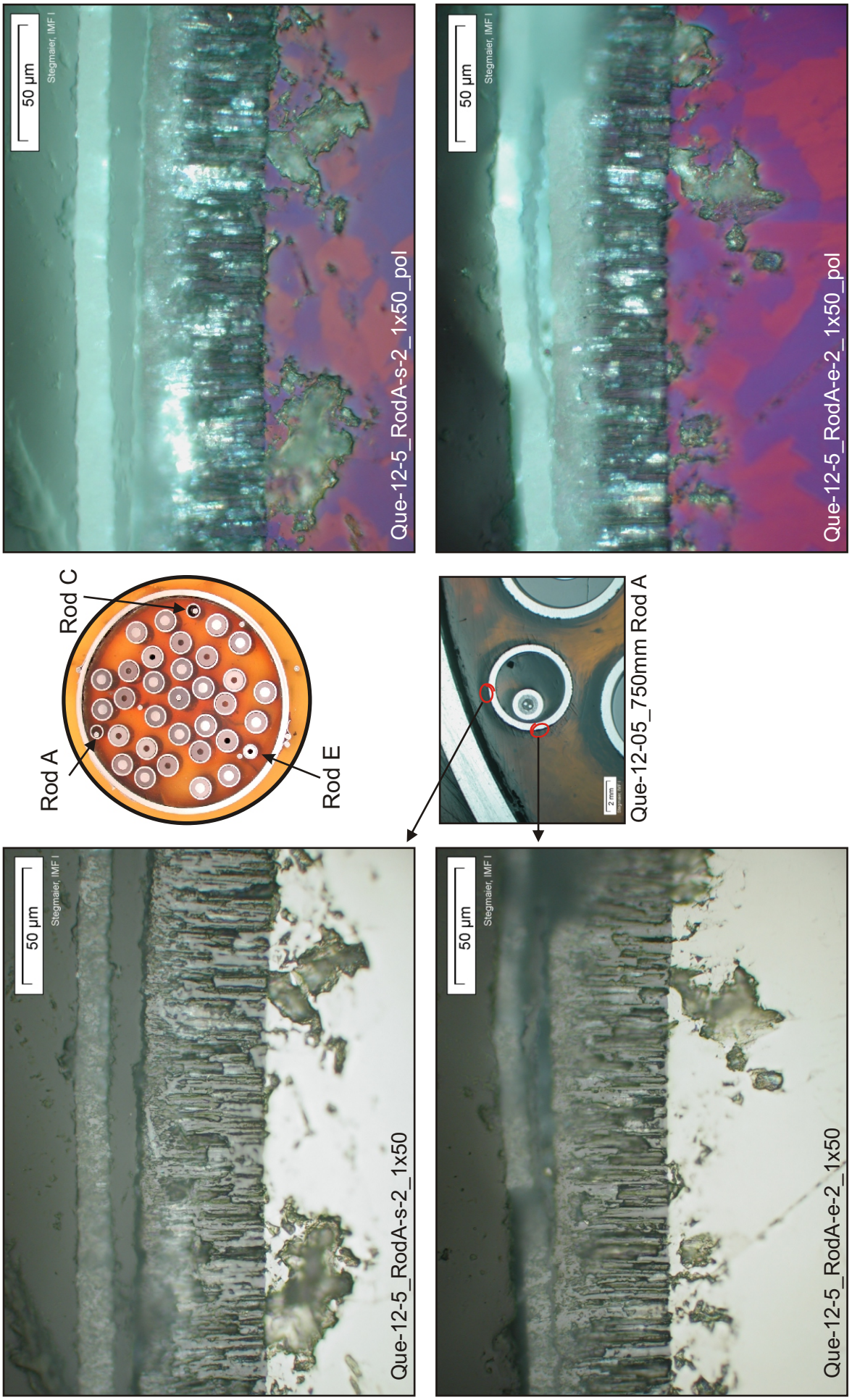


Fig. 74: QUE-12-5, level 750 mm; oxidation state of corner rod A.

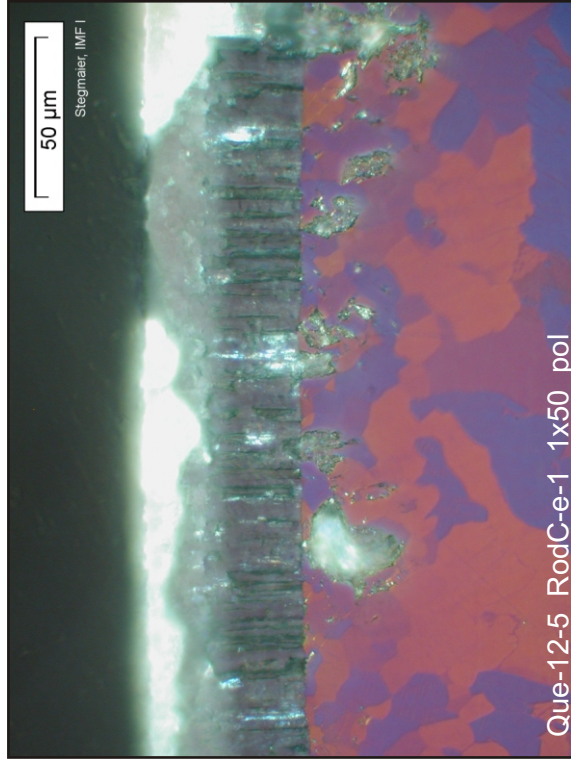
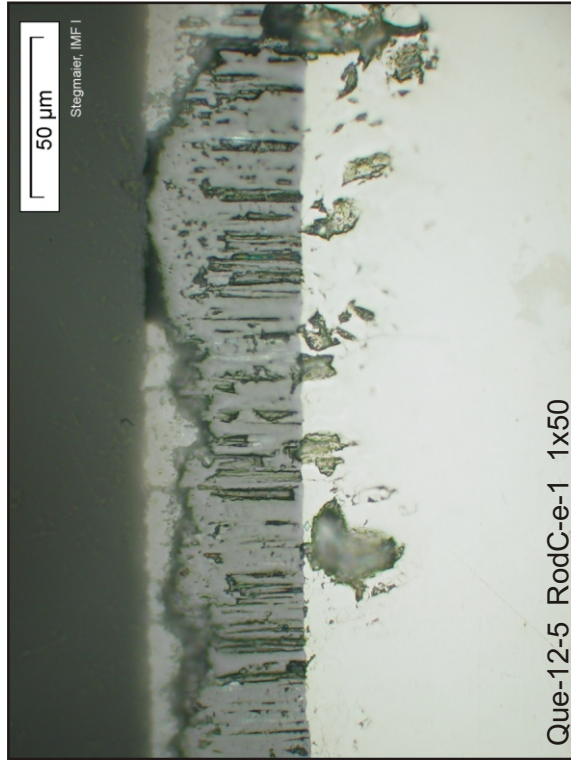
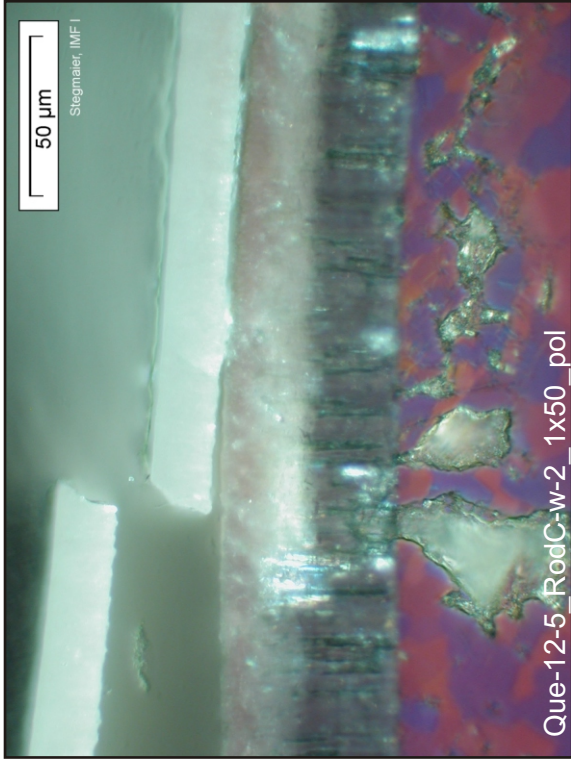
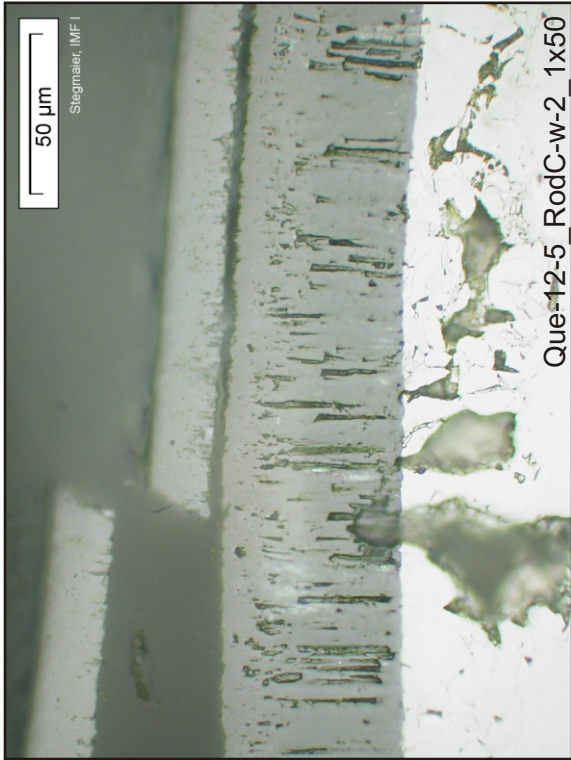
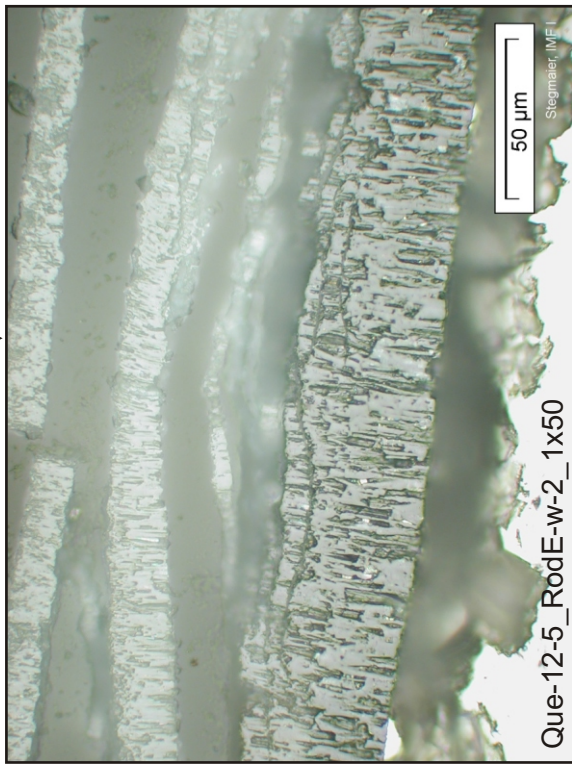
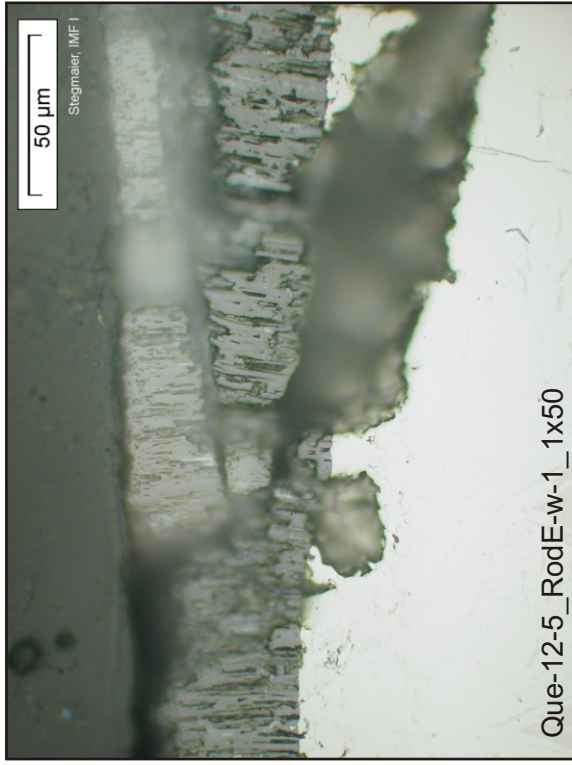
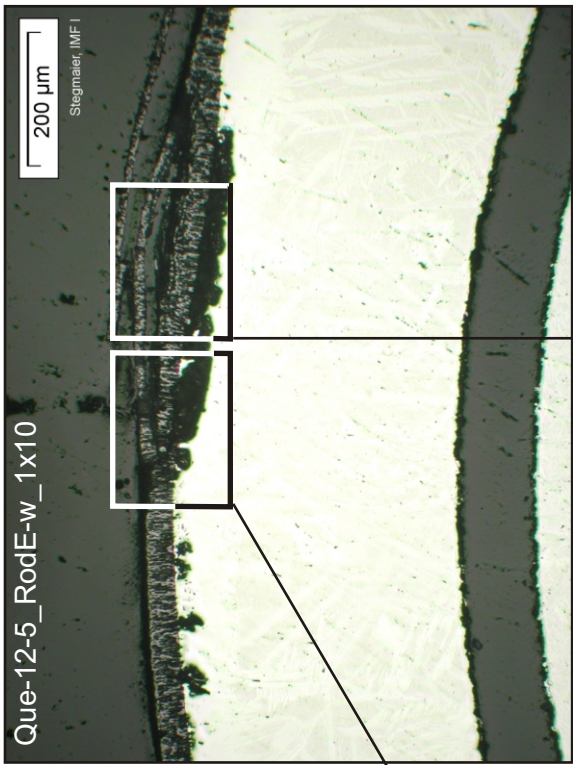
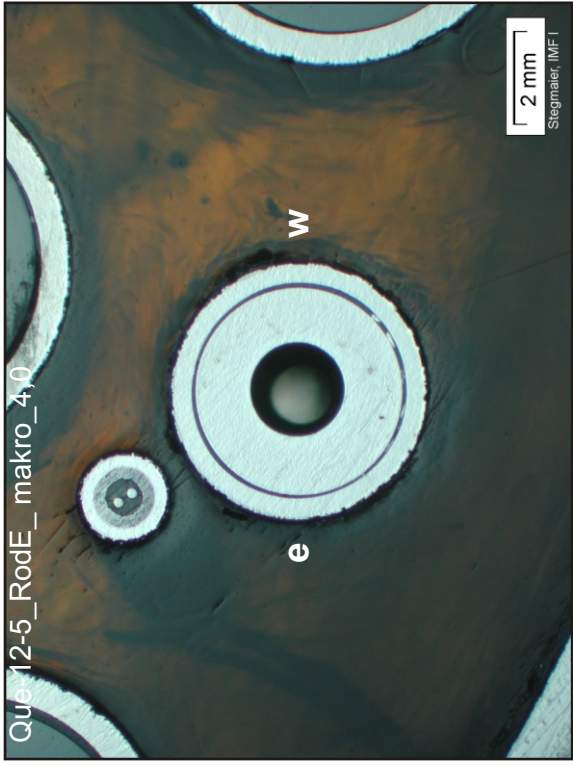
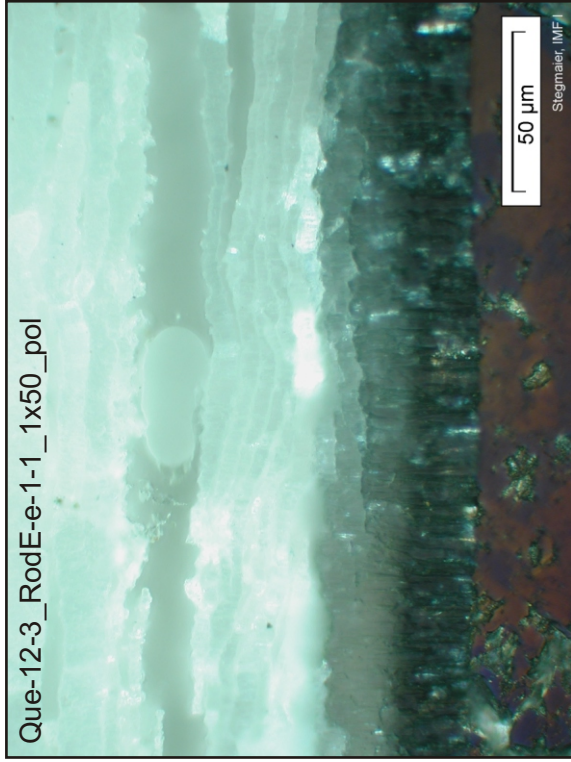
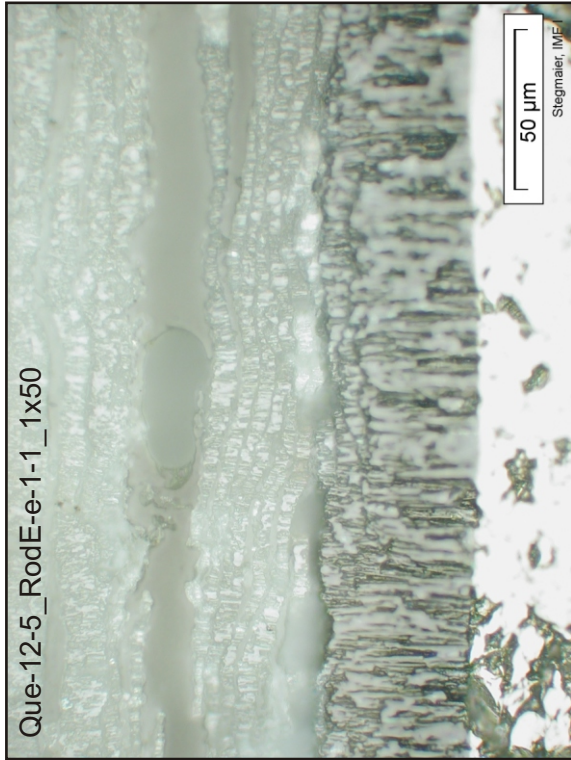
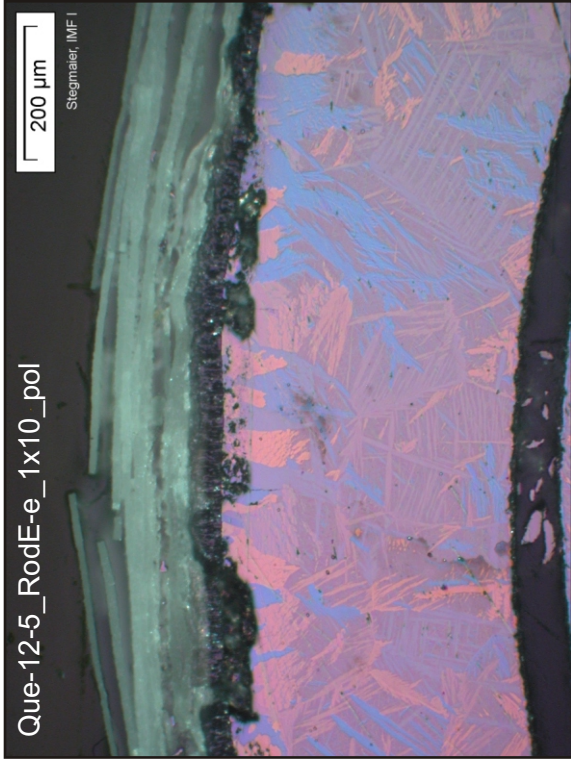
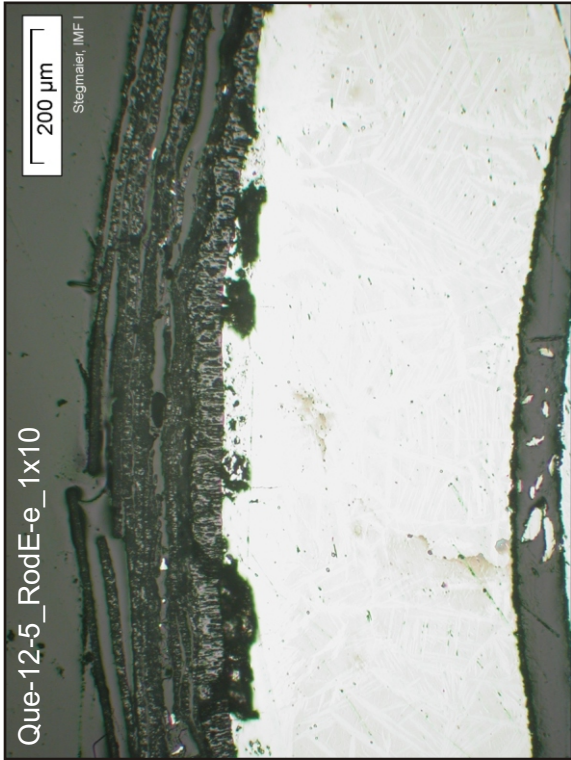


Fig. 75: QUE-12-5, level 750 mm; oxidation state of corner rod C.



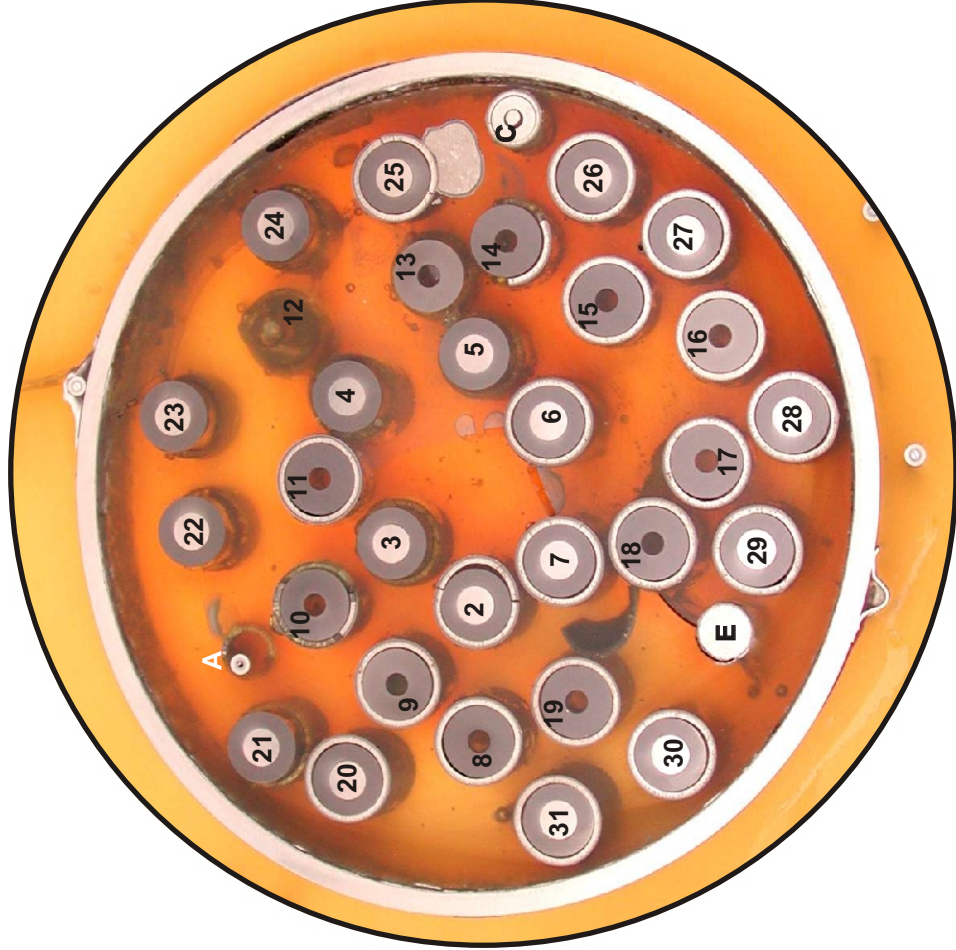
**Intact scale and regions
with sublayer spalling**

Fig. 76: QUE-12-5, level 750 mm; oxidation state of corner rod E towards west.

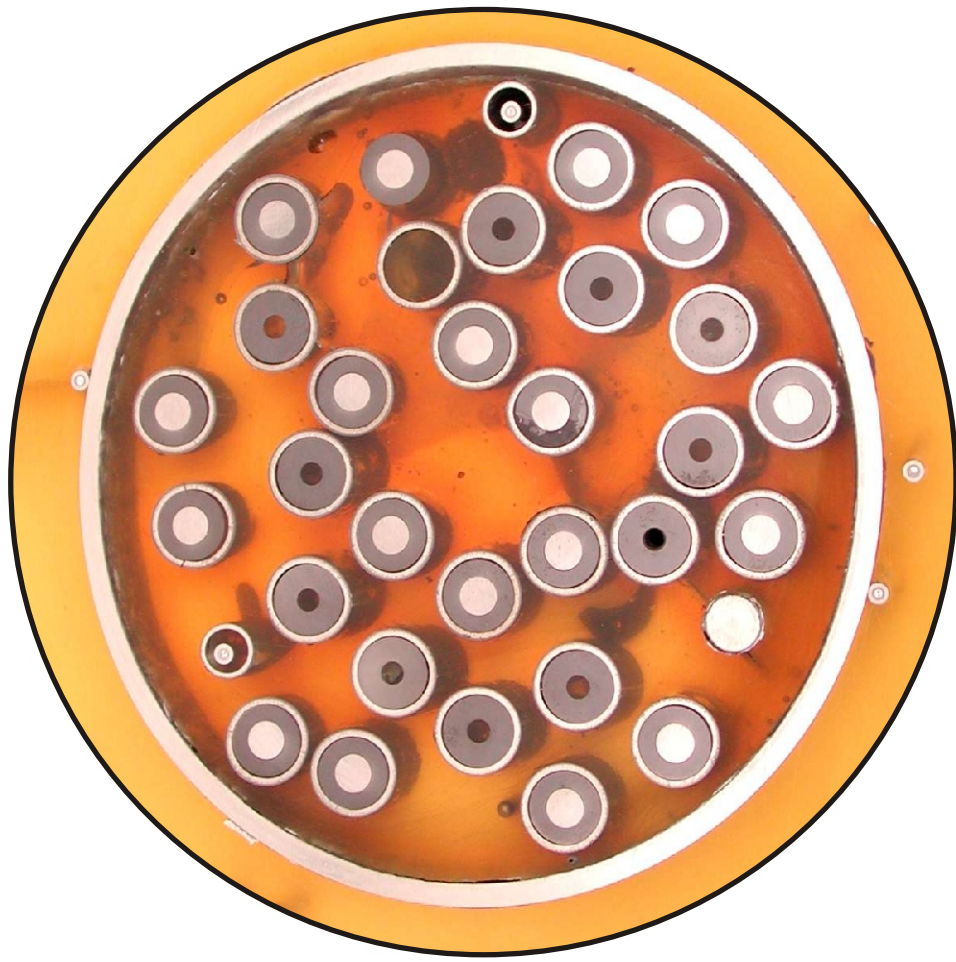


Spalling of many sub-layers from the compact inner part of the scale

Fig. 77: QUE-12-5, level 750 mm; oxidation state of corner rod E towards east.



Elevation 850mm, top view



Elevation 834 mm, inverted to top view

Fig. 78: QUE-12-7, level 850 mm; cross section overview.

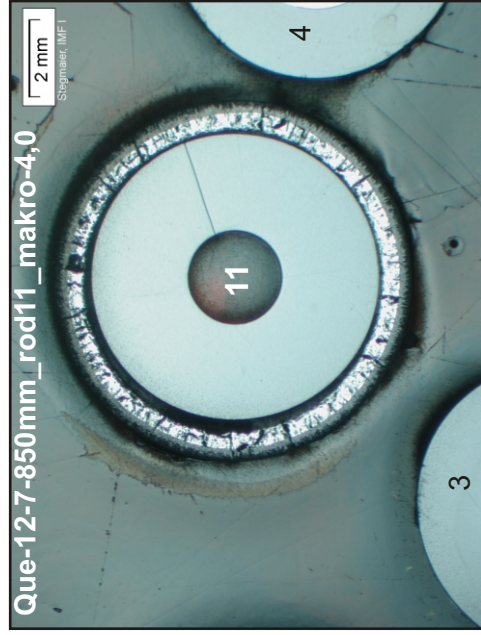
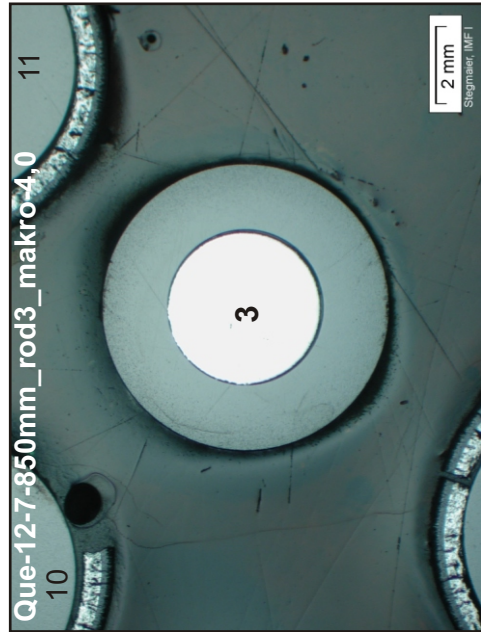
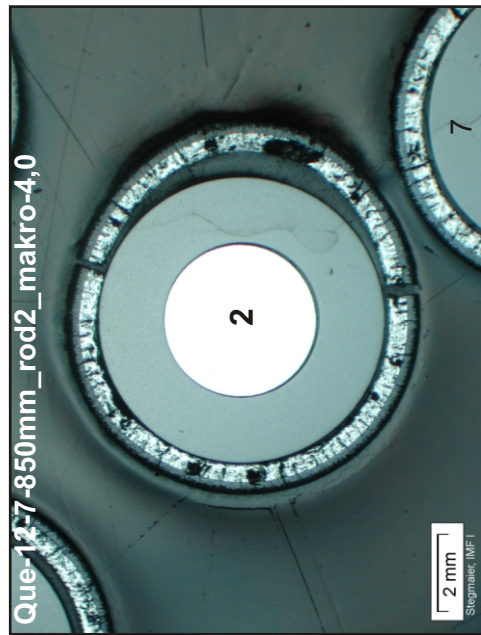
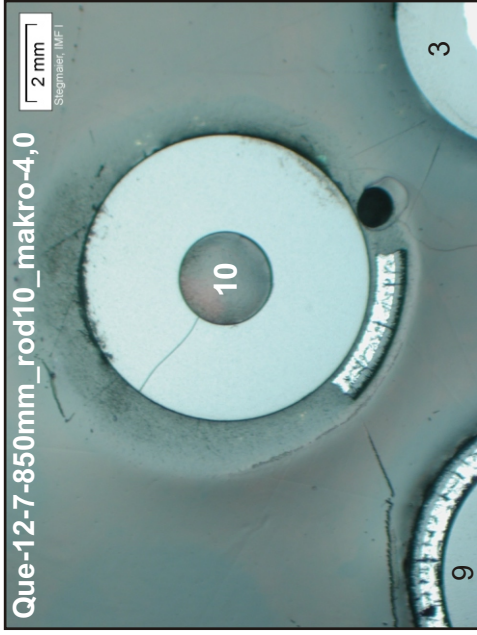
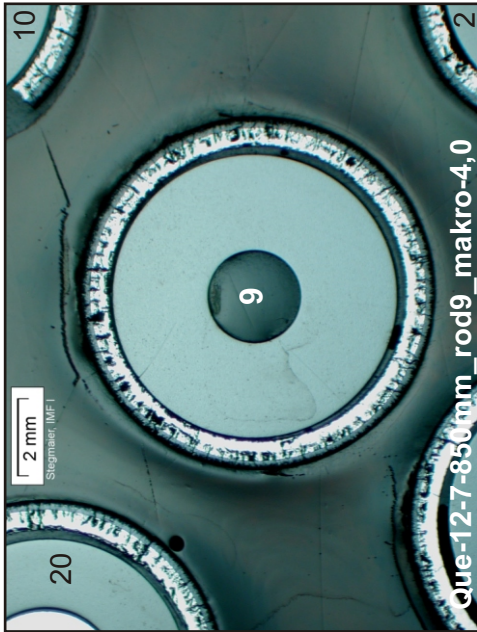
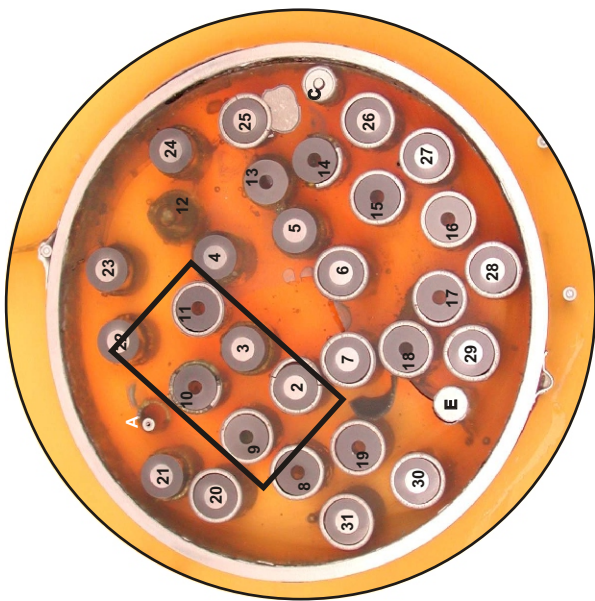


Fig. 79: QUE-12-7, level 850 mm; macrographs of rods towards SE, illustrating advanced oxidation and losses of cladding due to fracture.

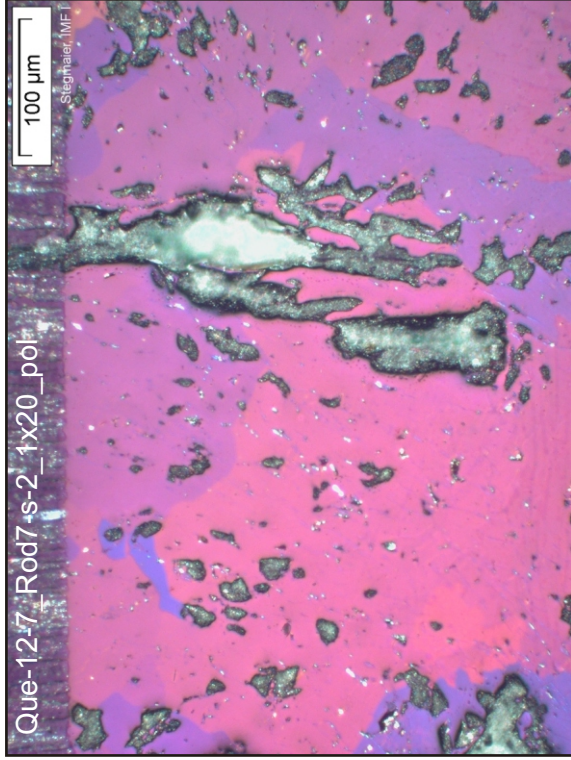
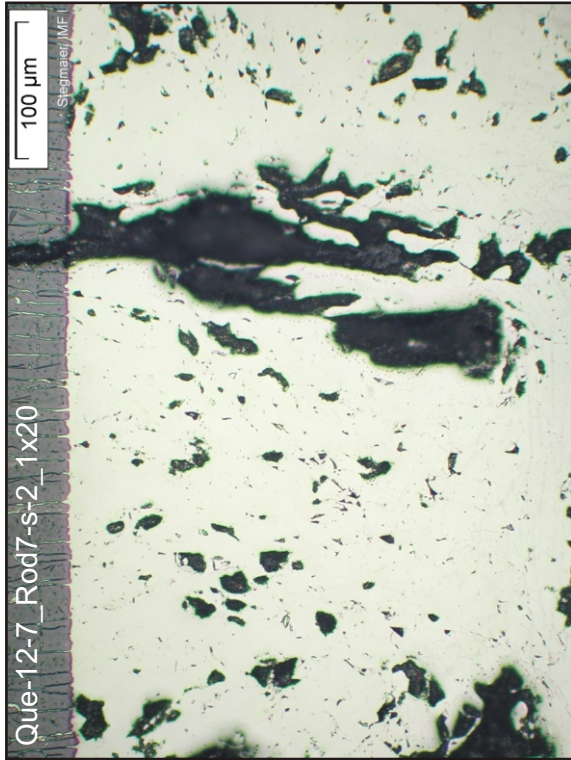
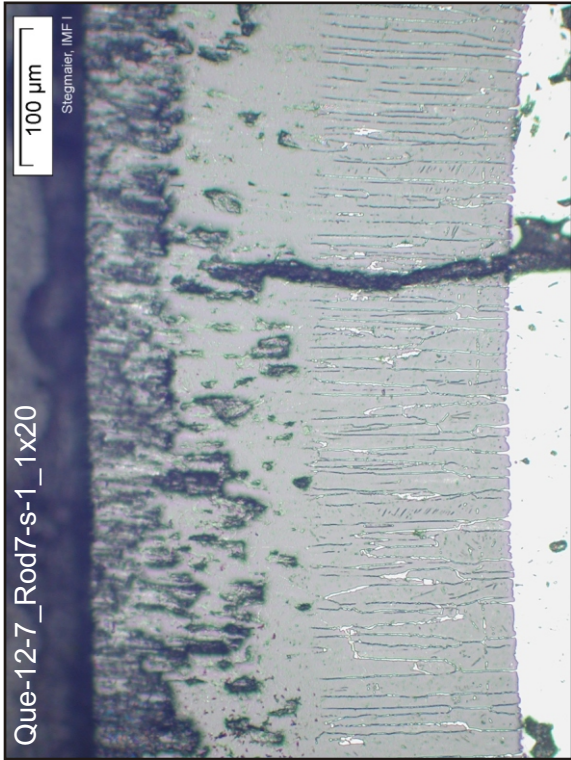
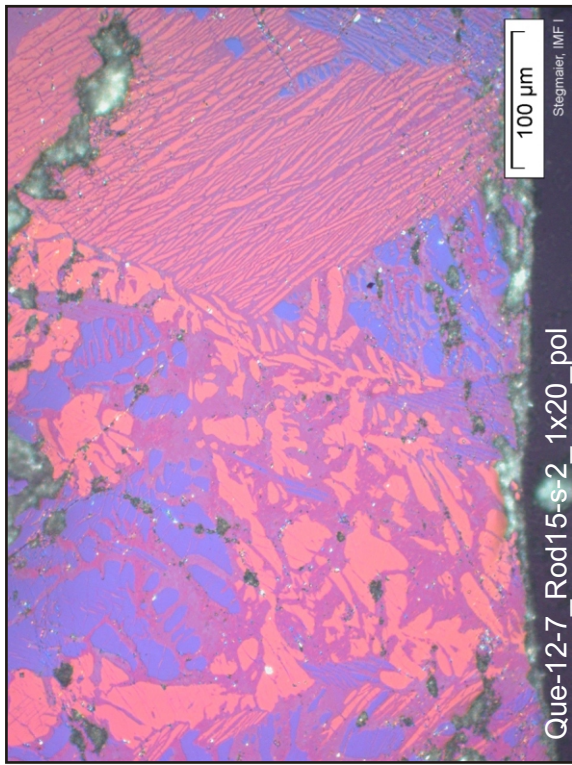
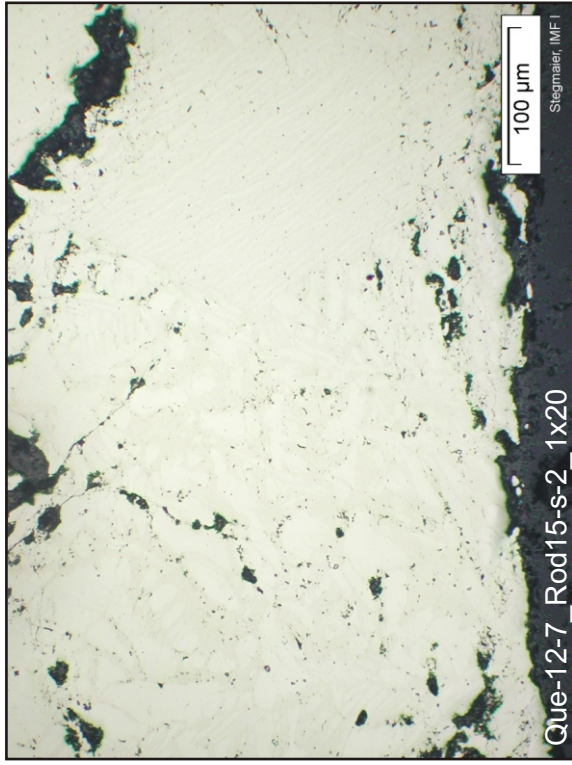
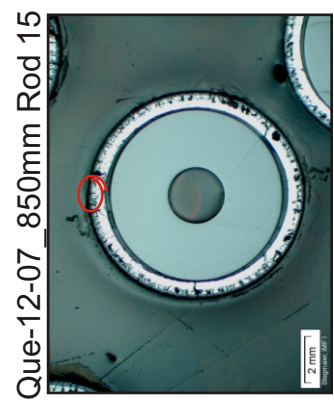
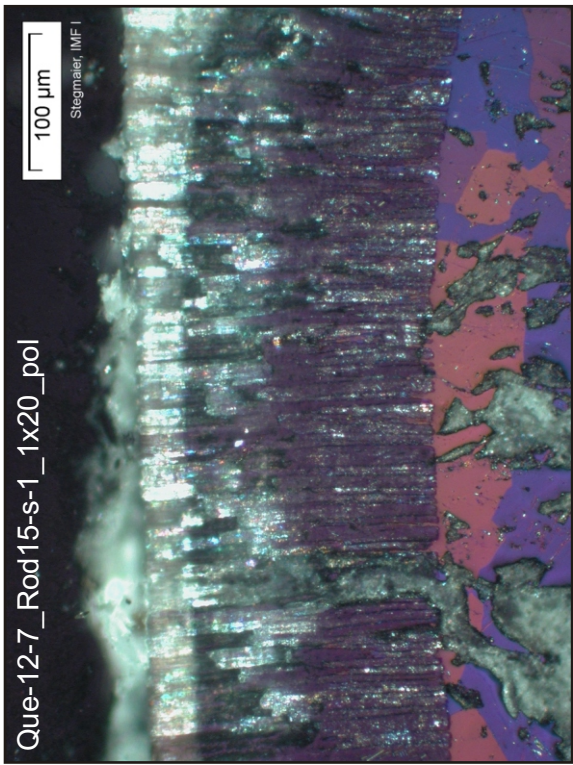
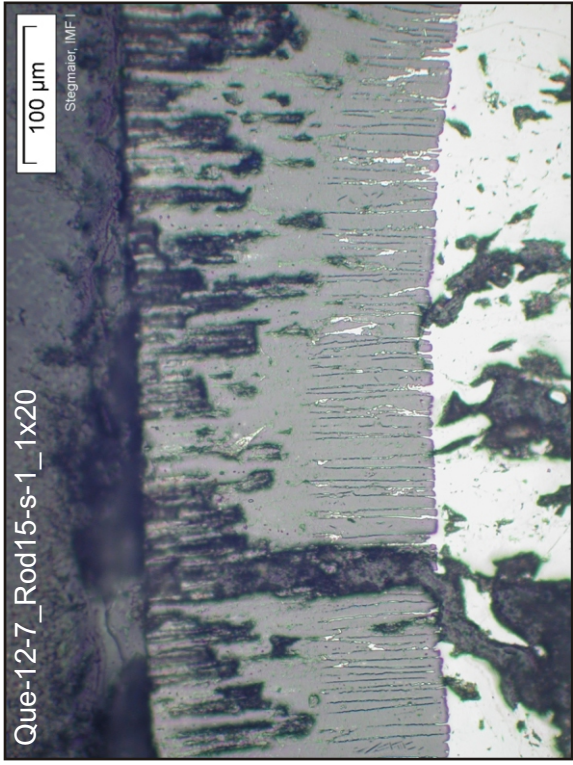


Fig. 80: QUE-12-7, level 850 mm; cladding oxidation of rod 7 (inner ring, heated).



β -Zr matrix
at inner rim

Fig. 81: QUE-12-7, level 850 mm; cladding oxidation of rod 15 (second ring, unheated).

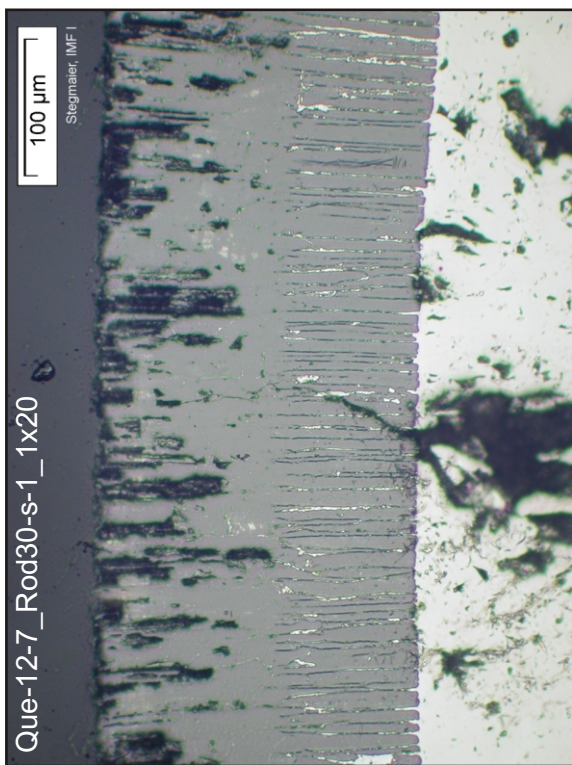
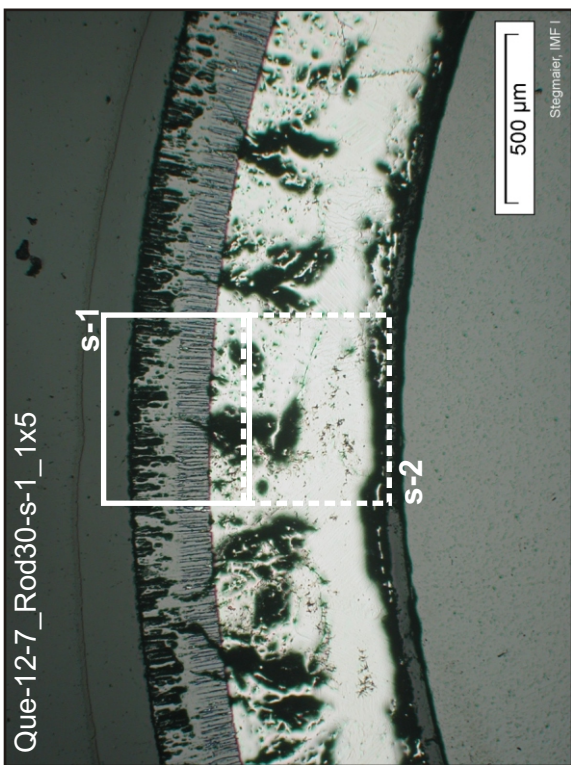
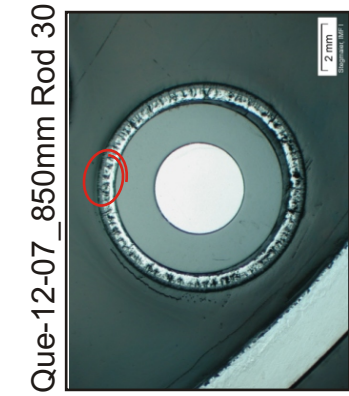
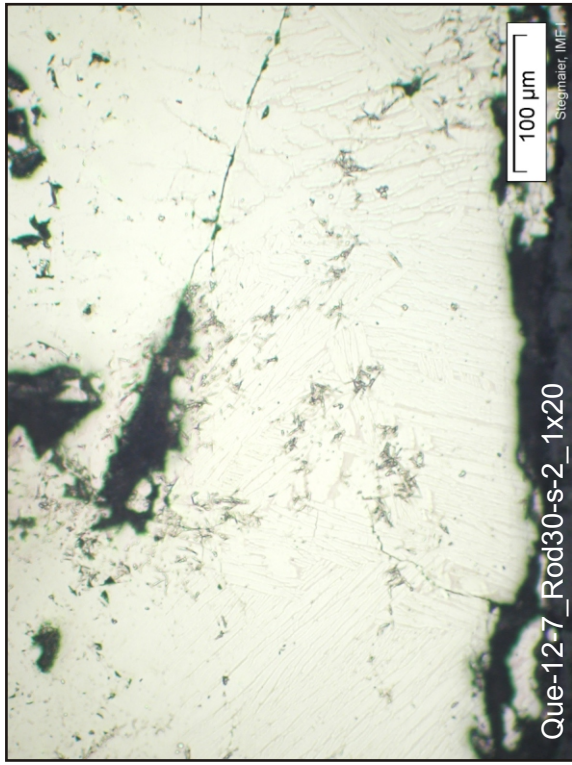
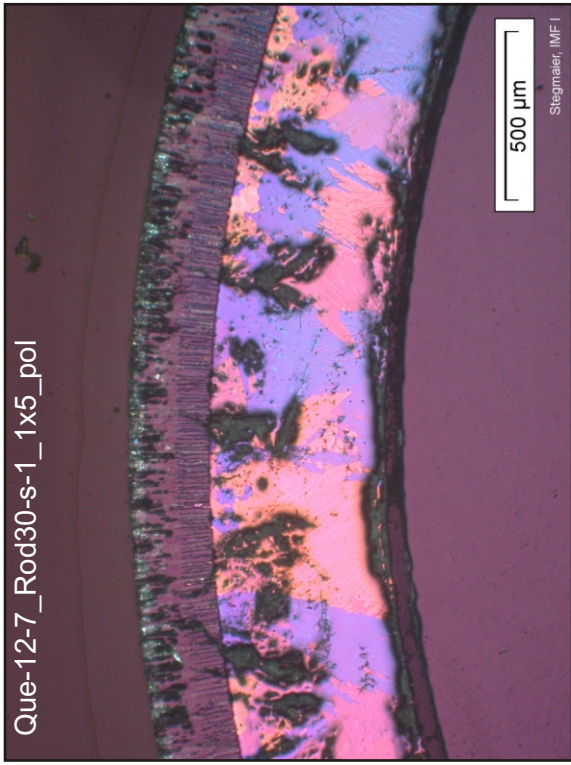
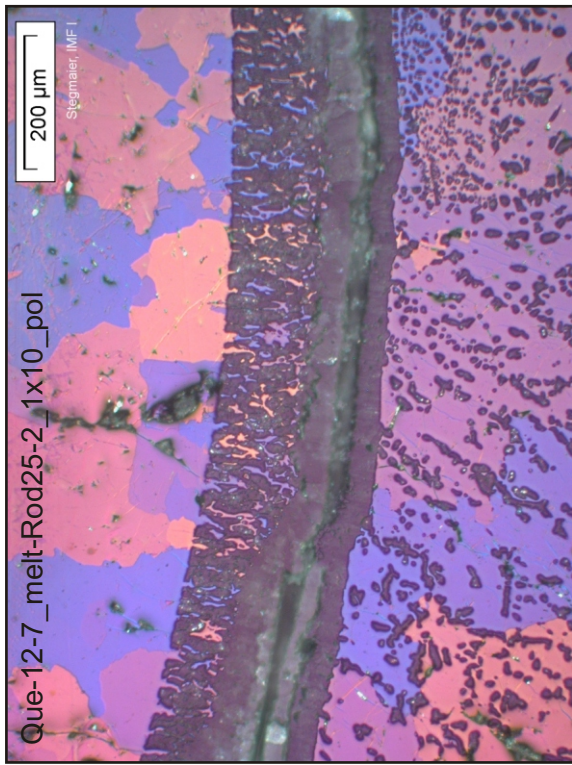
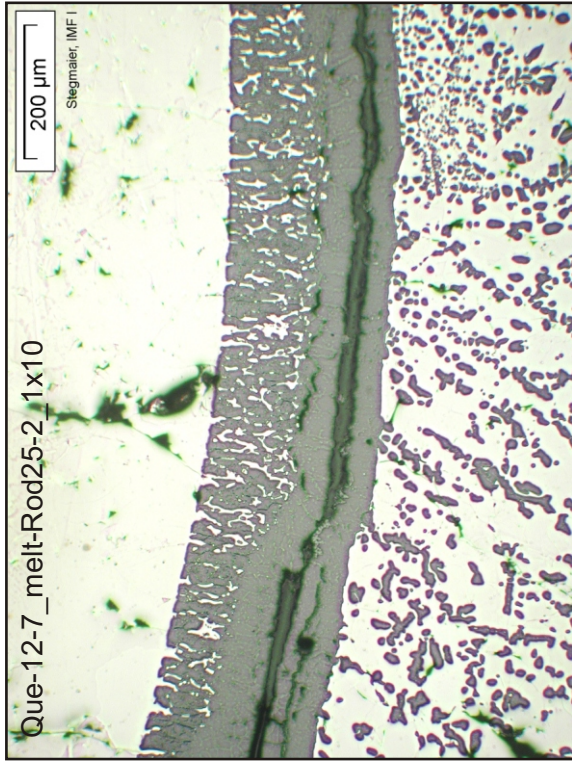
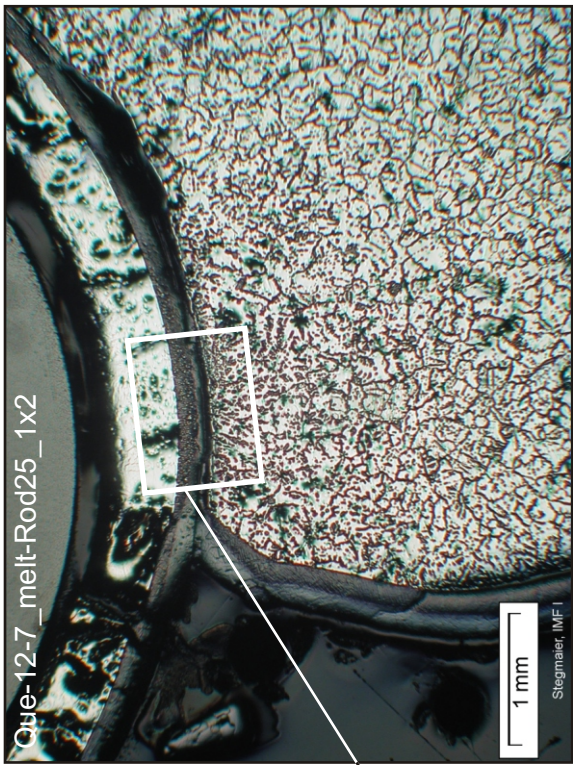
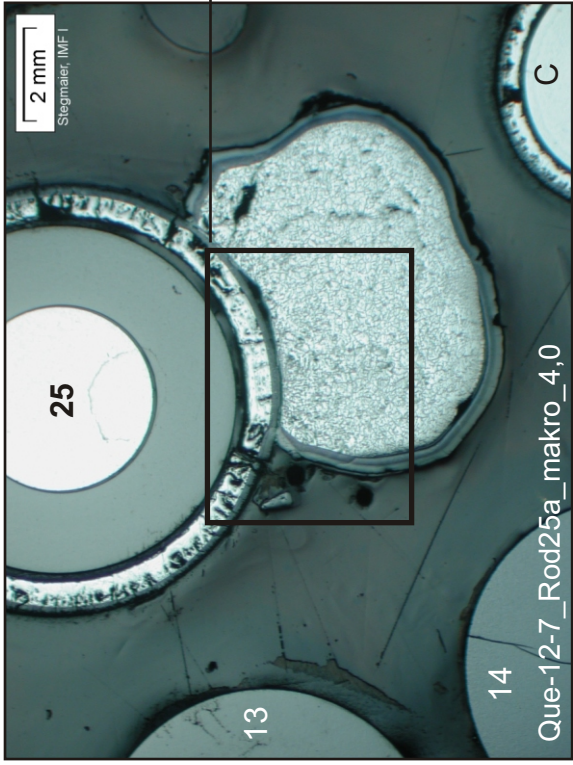
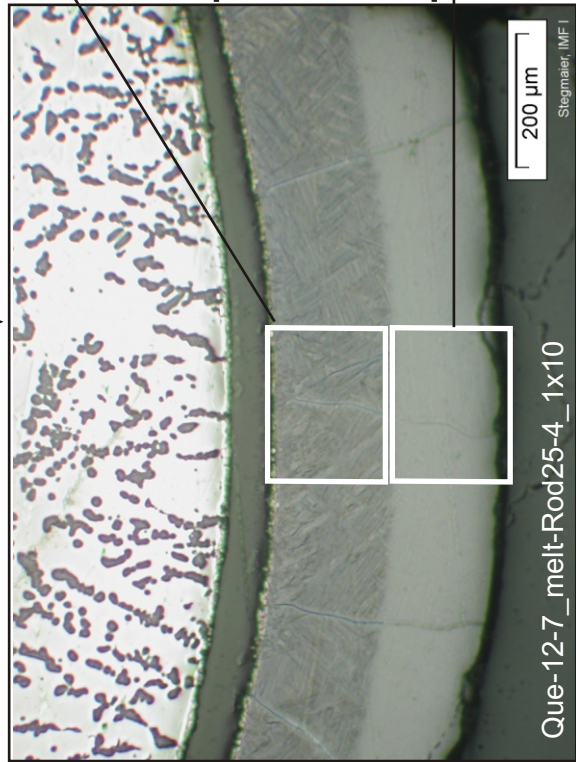
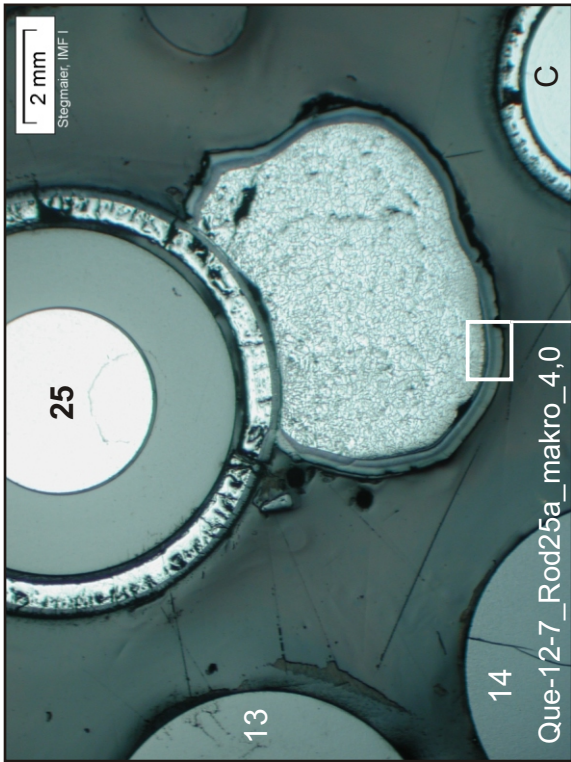


Fig. 82: QUE-12-7, level 850 mm; cladding oxidation of rod 30 (outer ring, heated).



Notice:
 Cladding scale of rod 25 shows internal dissolution trend
 Duplex microstructure of melt indicates oxygen content

Fig. 83: QUE-12-7, level 850 mm; microstructure of melt pool in contact to rod 25.



Notice:

**Thick and compact
oxide scale indicates
strong oxidation after
melt relocation**

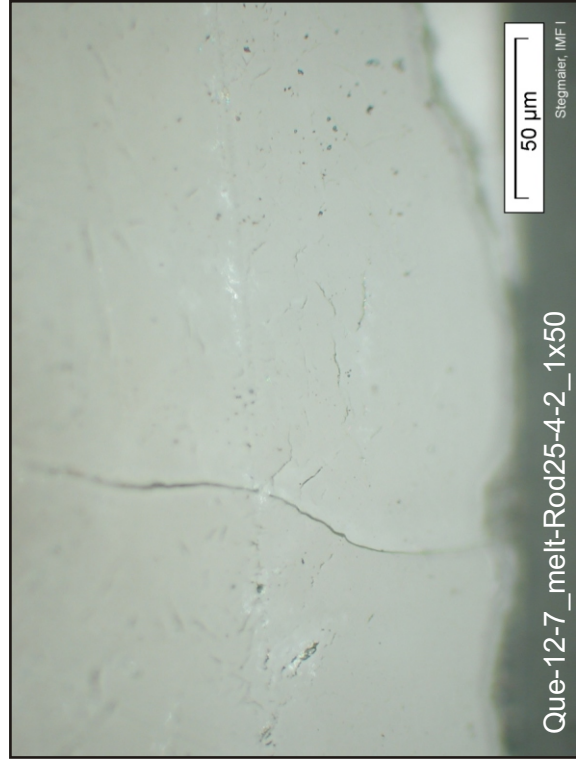
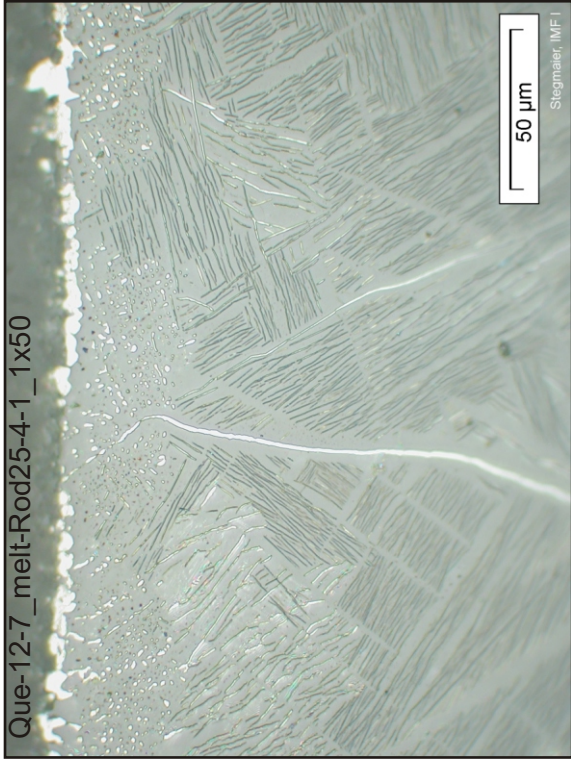


Fig. 84: QUE-12-7, level 850 mm; oxide scale around pool of relocated melt.

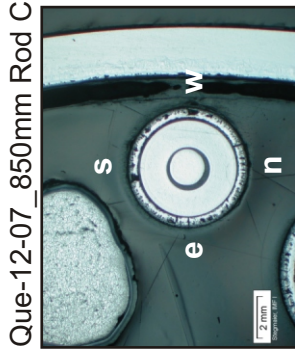
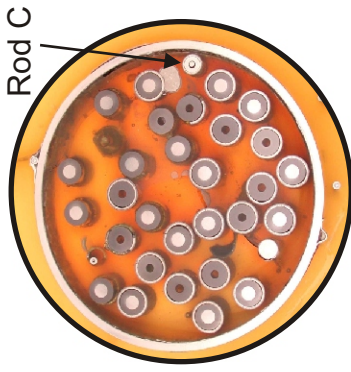
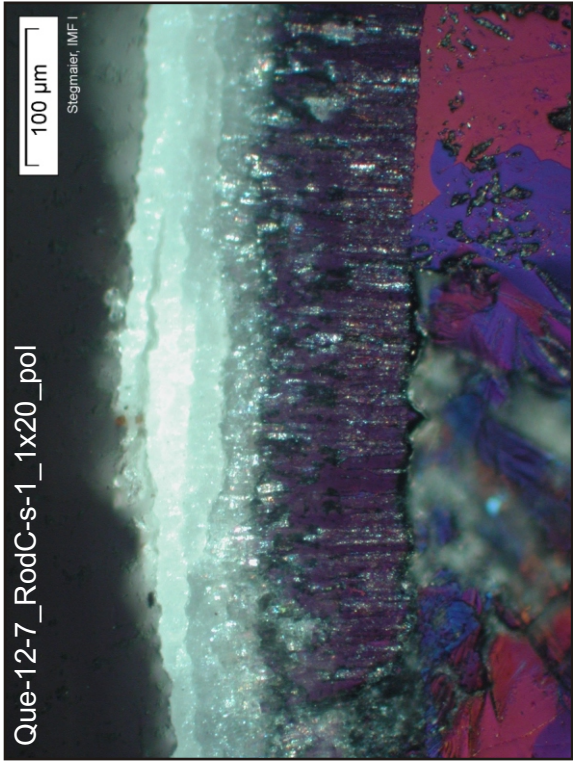
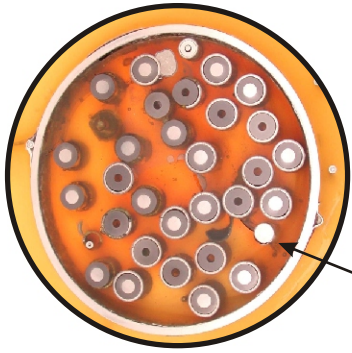
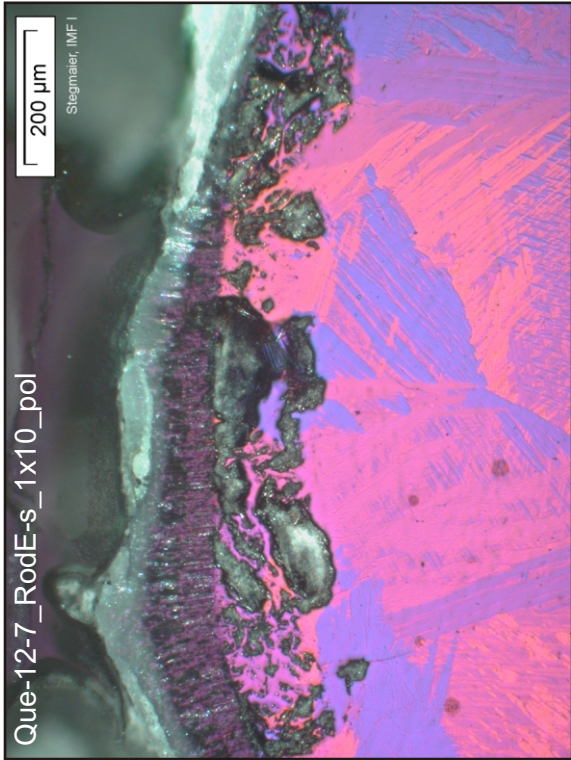


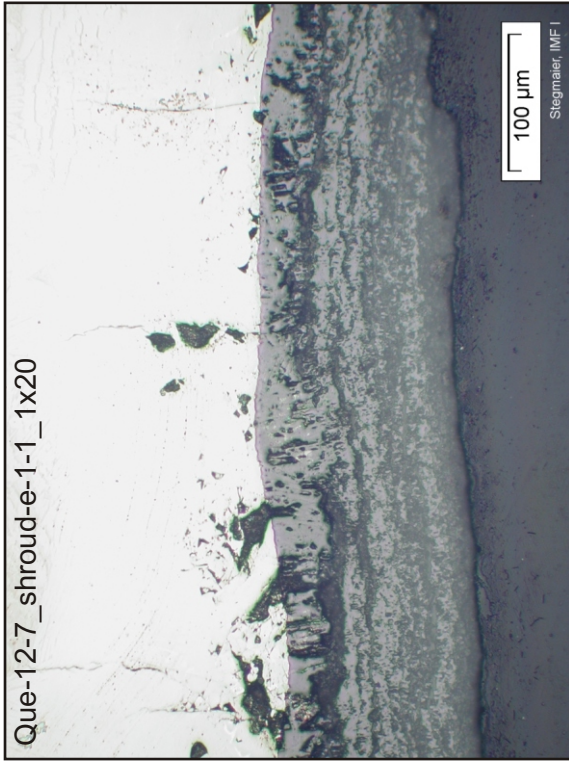
Fig. 85: QUE-12-7, level 850 mm; oxidation state of corner rod C.



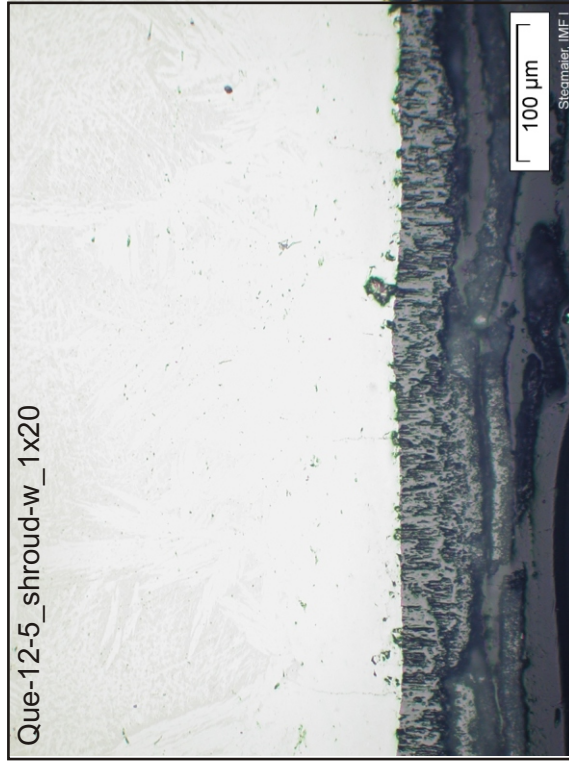
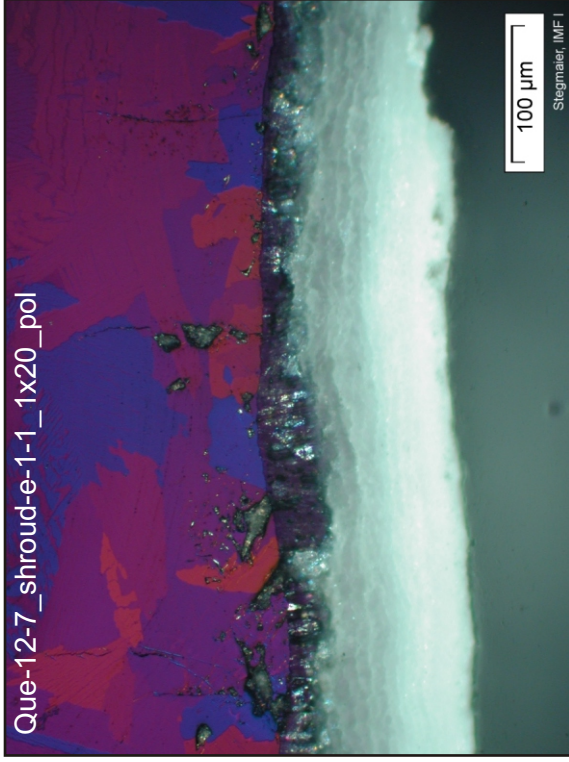
Rod E



Fig. 86: QUE-12-7, level 850 mm; oxidation state of corner rod E.



Level 850 mm



Level 750 mm

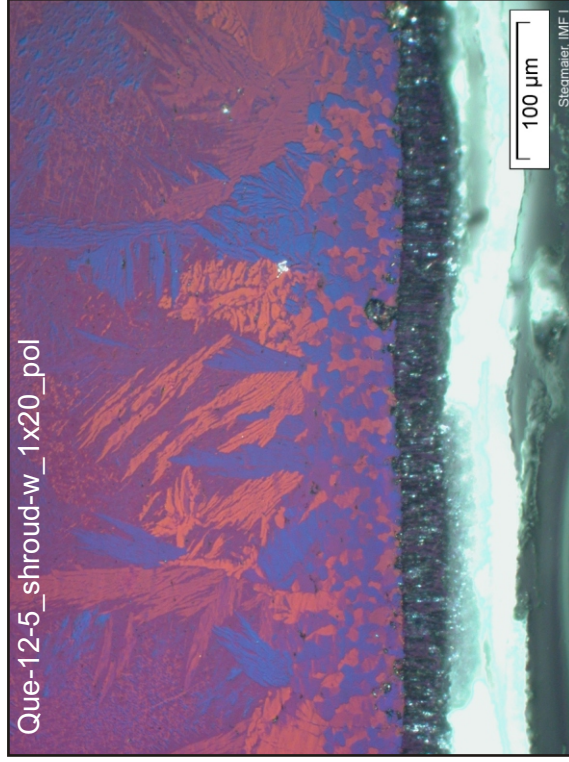
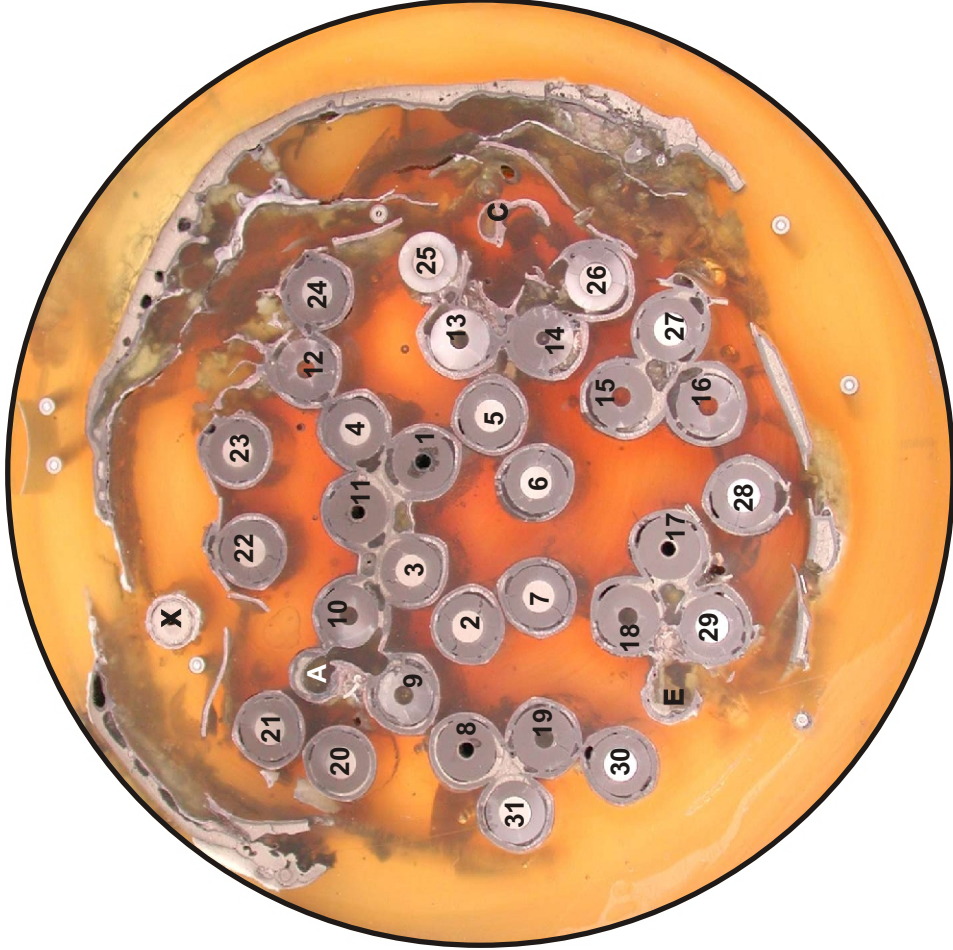


Fig. 87: QUE-12-7 and -5, levels 850 and 750 mm; oxidation of the shroud (inner side).



Elevation 950mm, top view



Elevation 934 mm, inverted to top view

Fig. 88: QUE-12-9, level 950 mm; cross section overview.

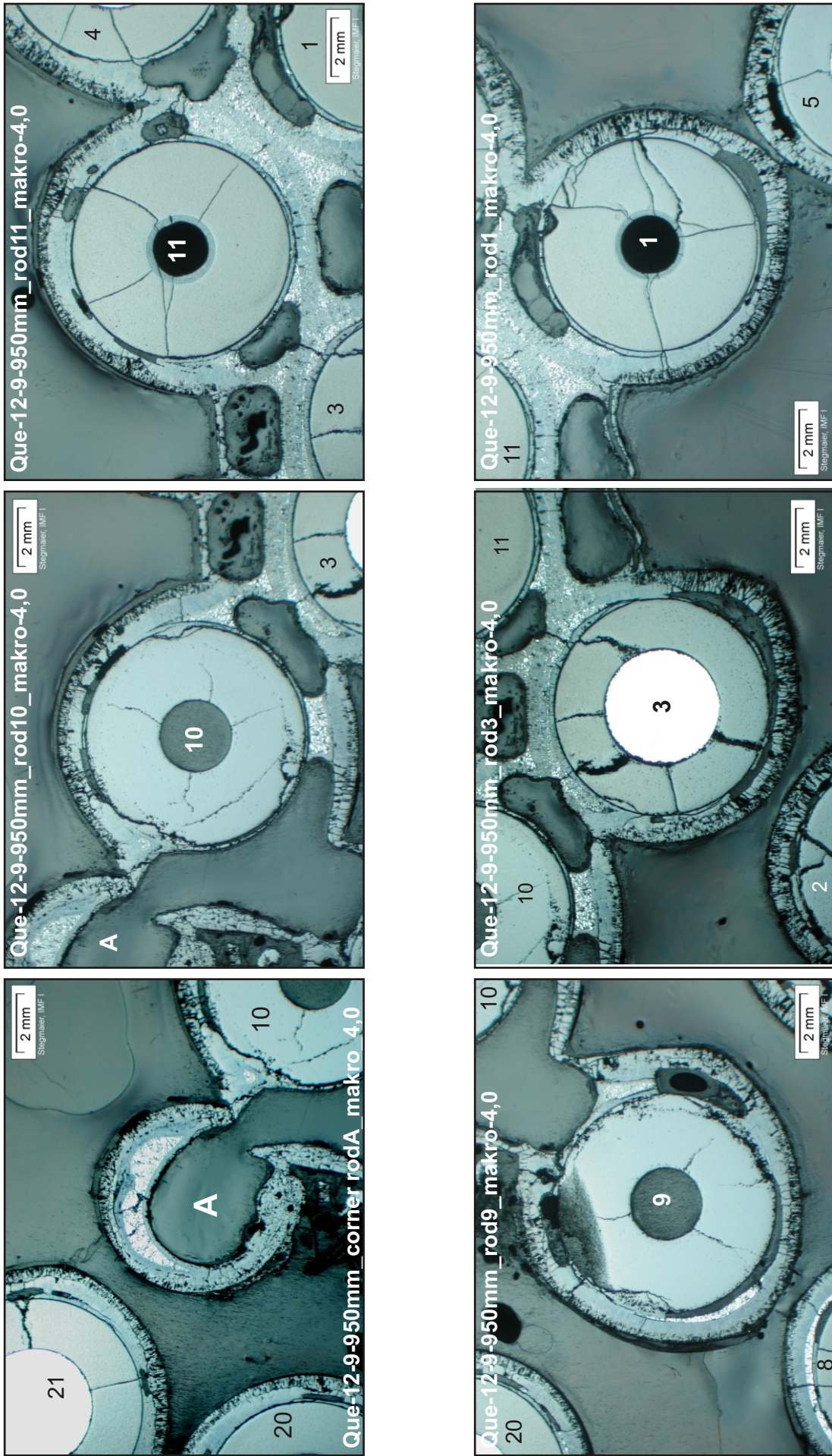


Fig. 89: QUE-12-9, level 950 mm; macrographs of rods towards S, illustrating formation and oxidation of melt pools via the necking mechanism.

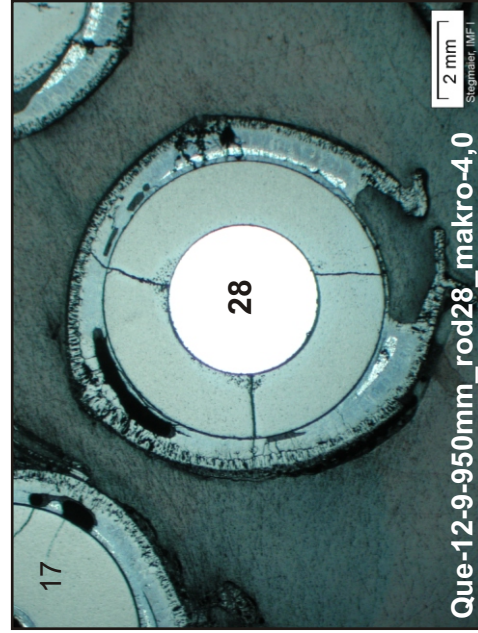
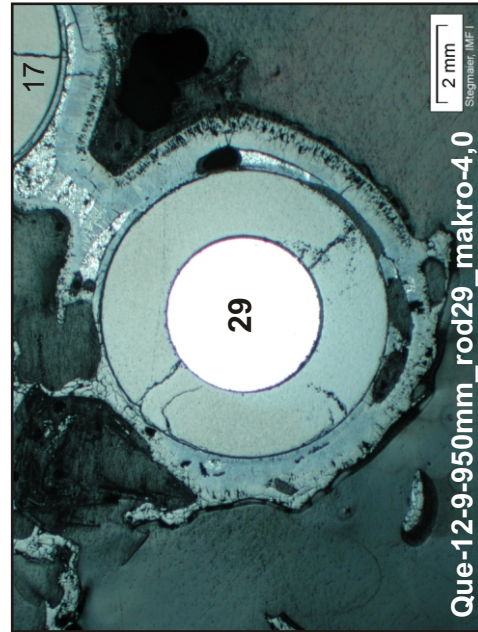
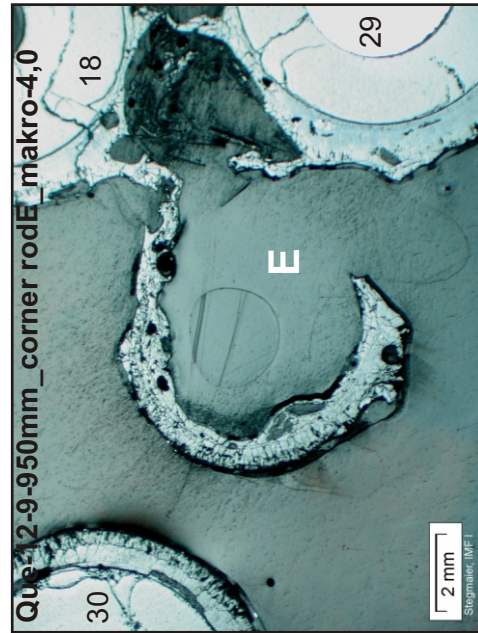
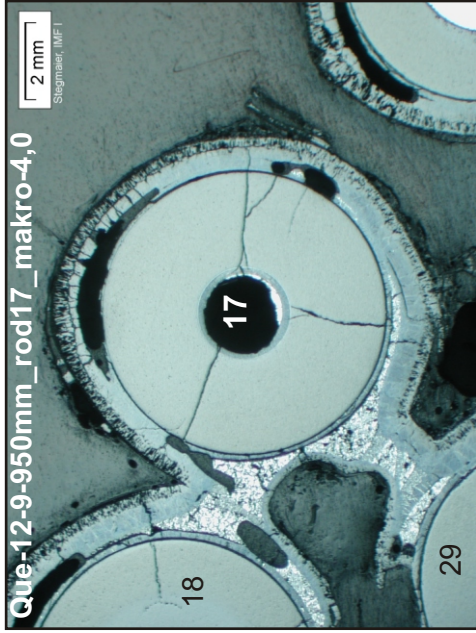
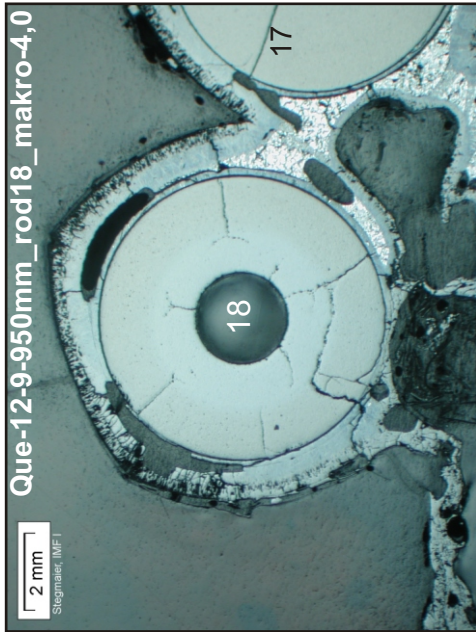
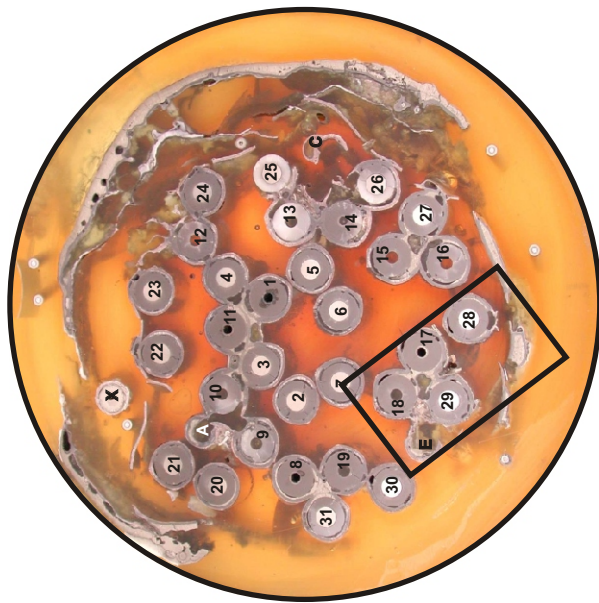


Fig. 90: QUE-12-9, level 950 mm; macrographs of rods towards N, illustrating melt pool formation and melt re-distribution.

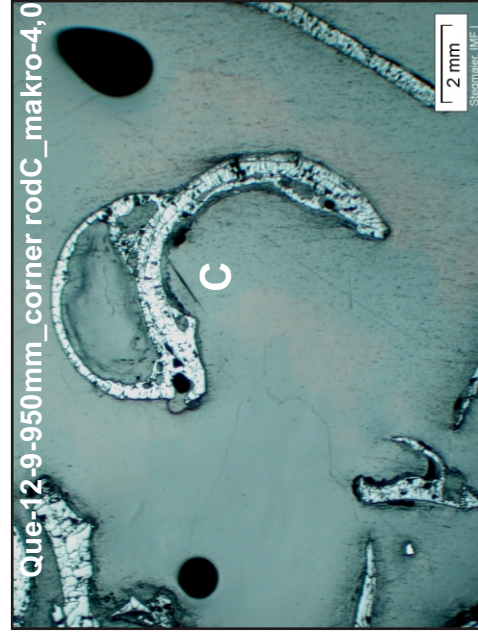
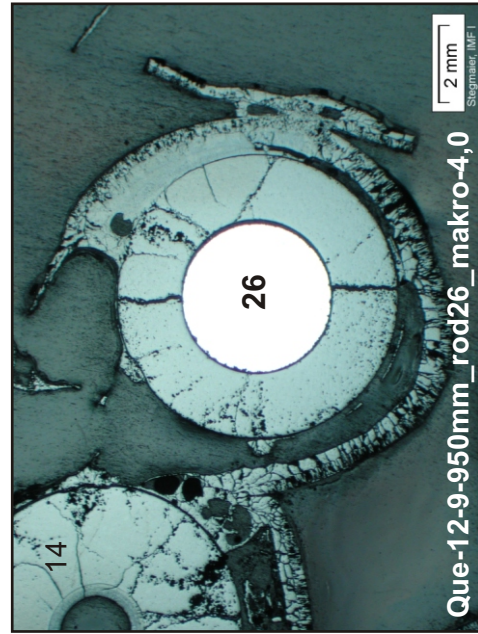
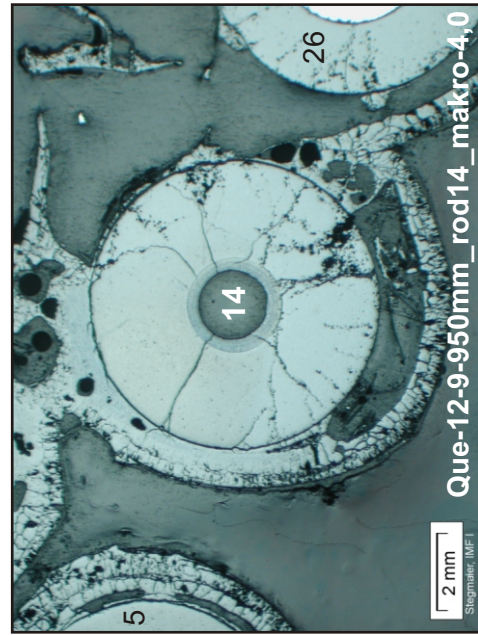
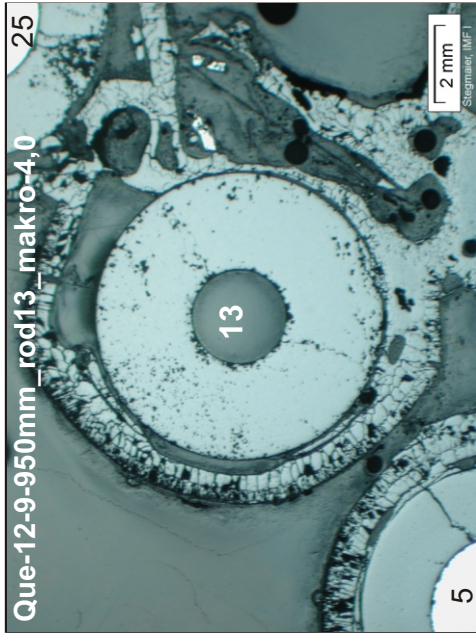
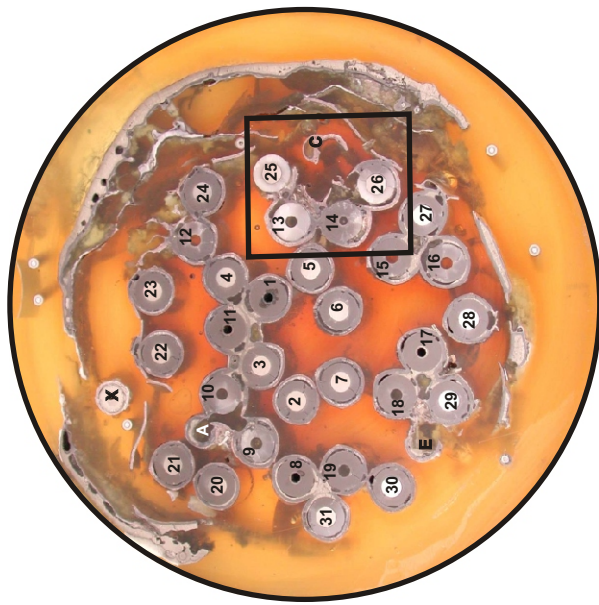


Fig. 91: QUE-12-9, level 950 mm; macrographs of rods towards W, illustrating complete oxidation of residual melt.

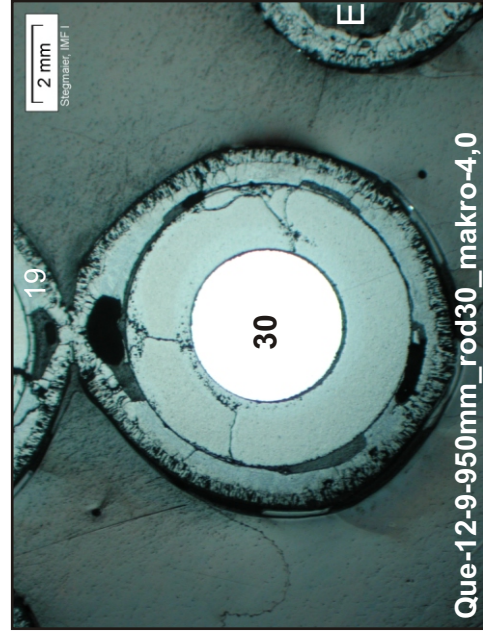
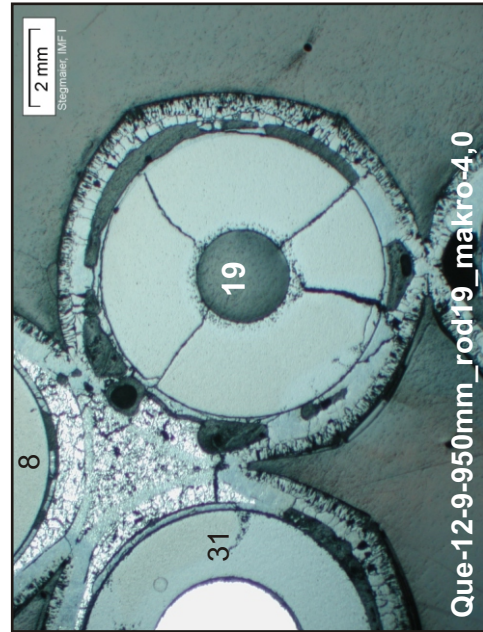
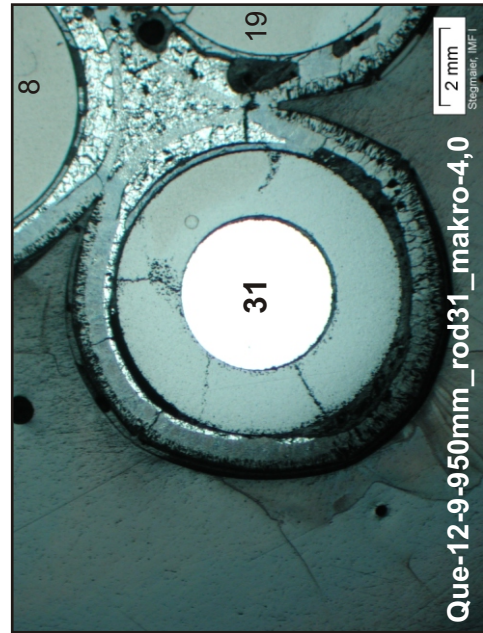
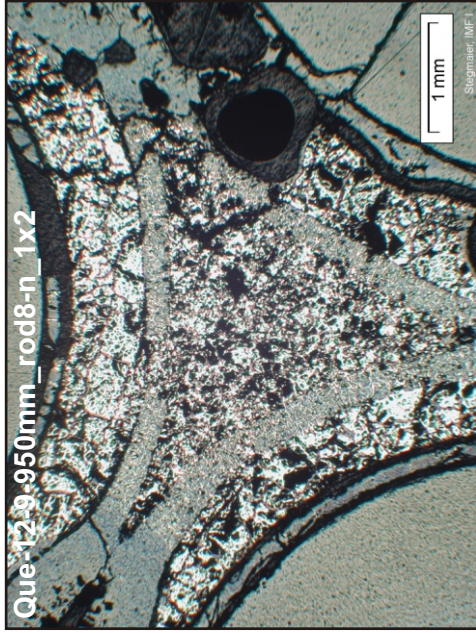
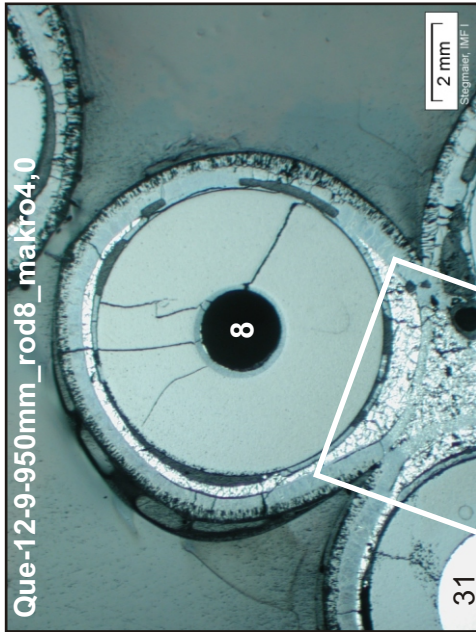
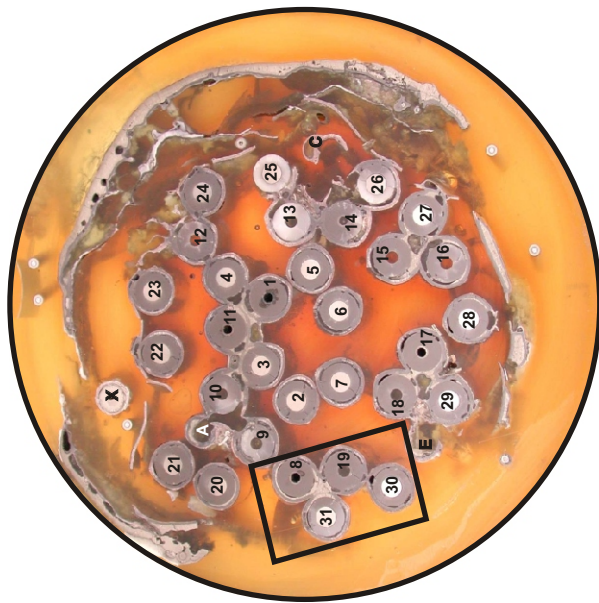


Fig. 92: QUE-12-9, level 950 mm; macrographs of rods towards E, illustrating a triangular melt pool with embedded scales and an inactive dry neck.

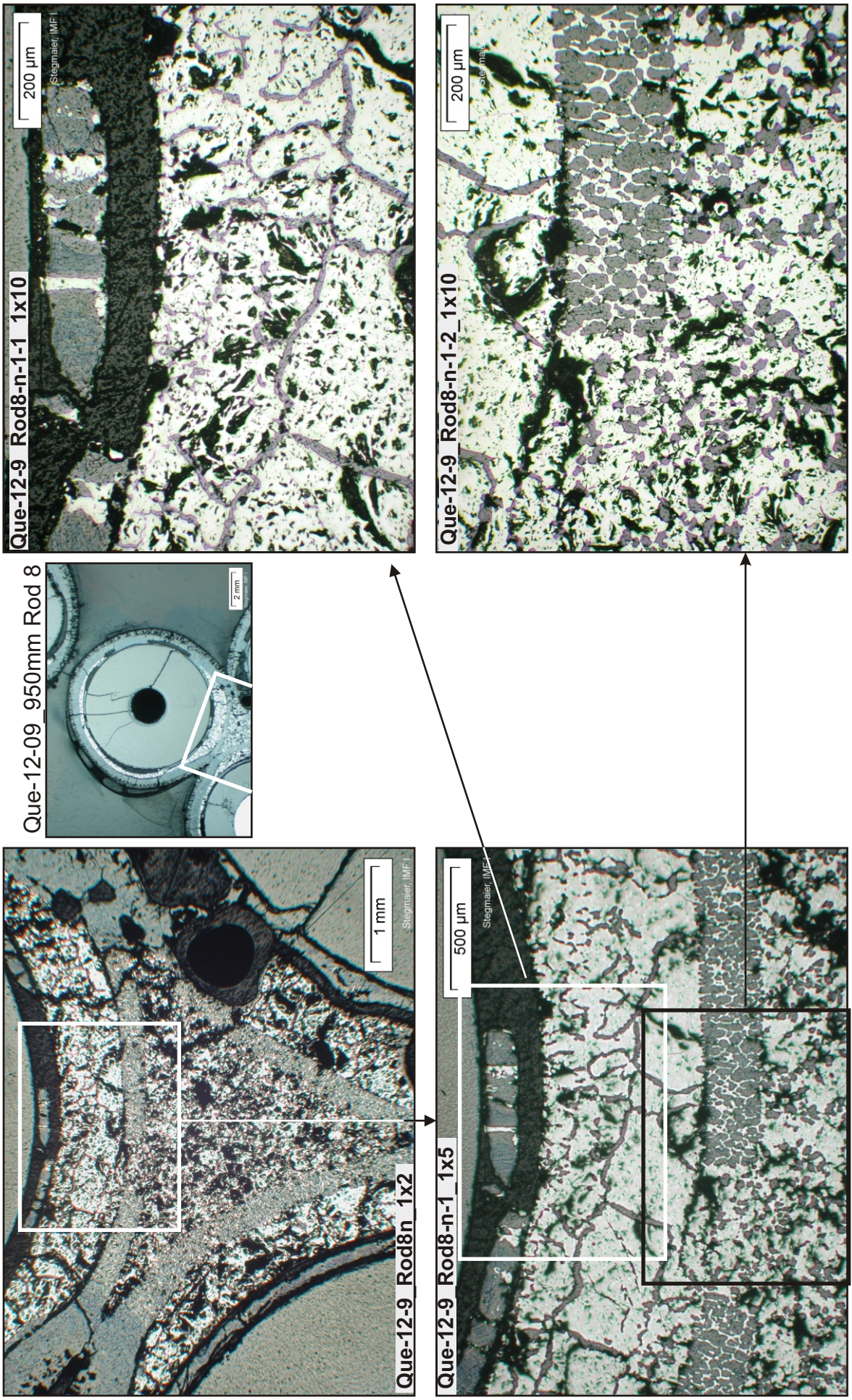


Fig. 93: QUE-12-9, level 950 mm; dissolution trend of scale of rod 8, embedded by the triangular melt pool (see previous figure).

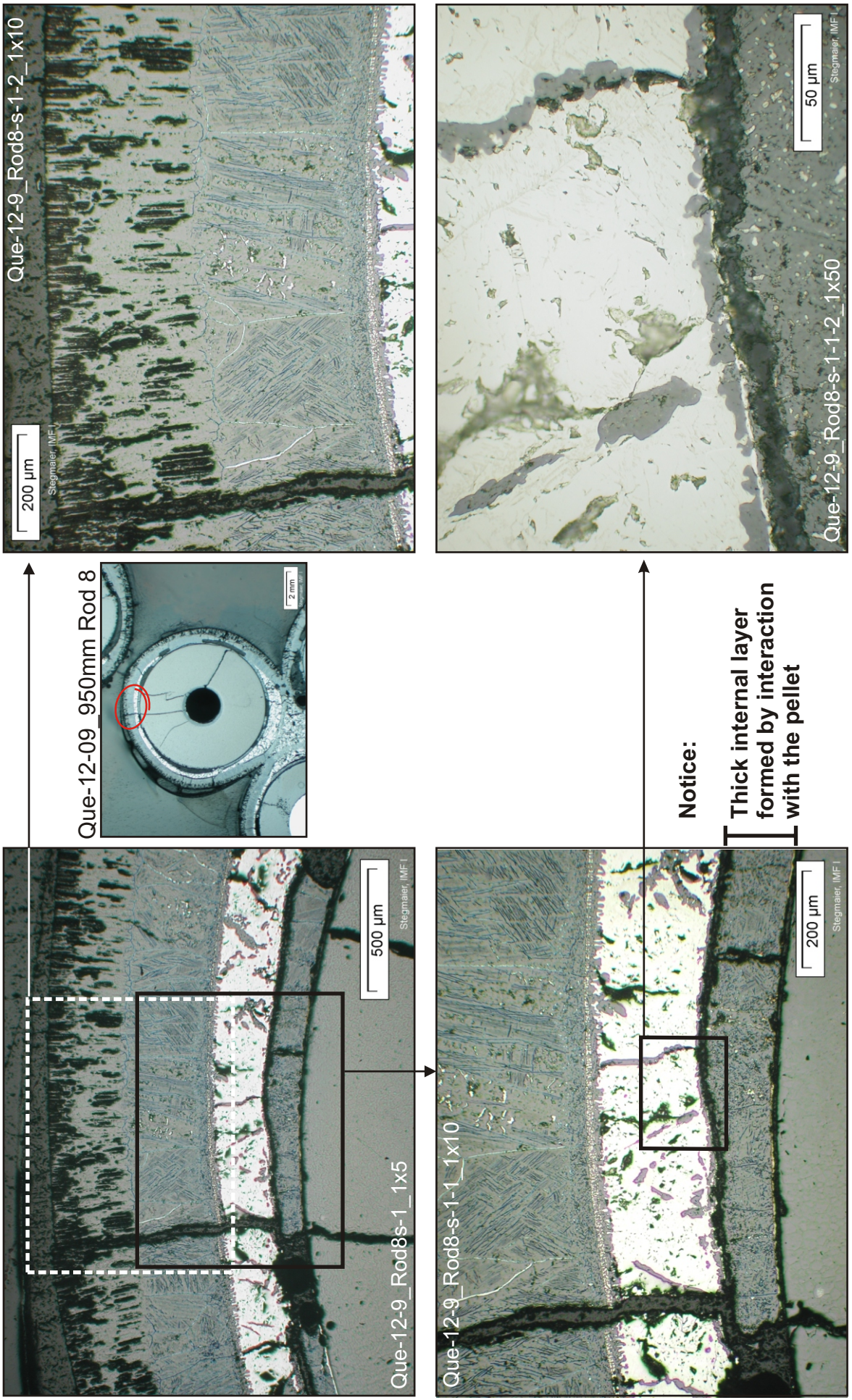


Fig. 94: QUE-12-9, level 950 mm; oxidation state of rod 8 at the steam exposed opposite side.

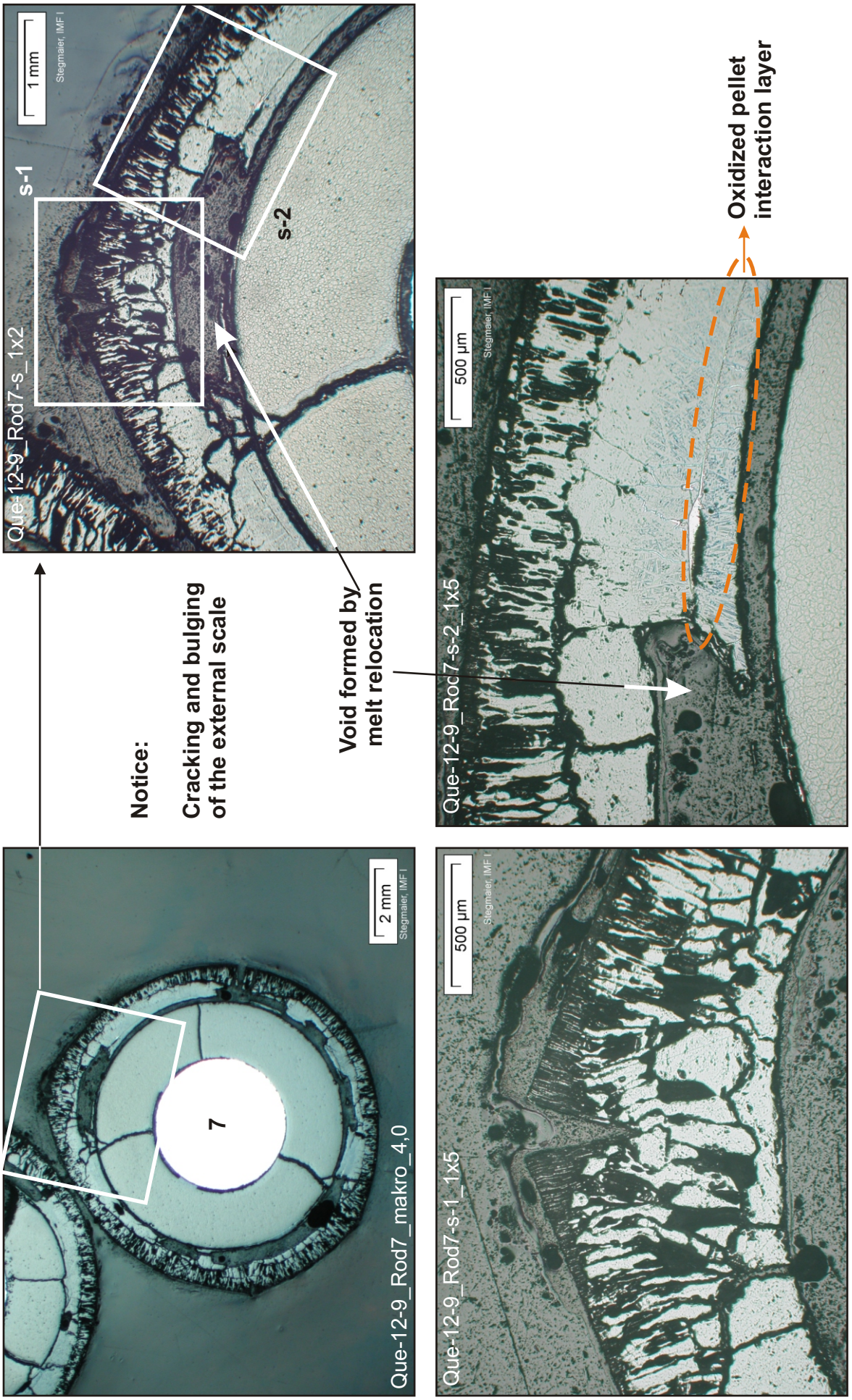


Fig. 95: QUE-12-9, level 950 mm; state of total oxidation of rod 7, indicating the history of different contributions.

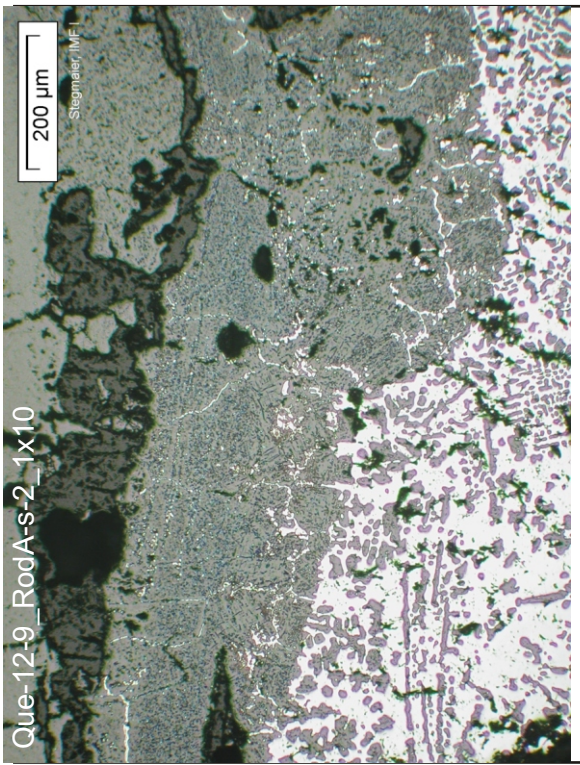
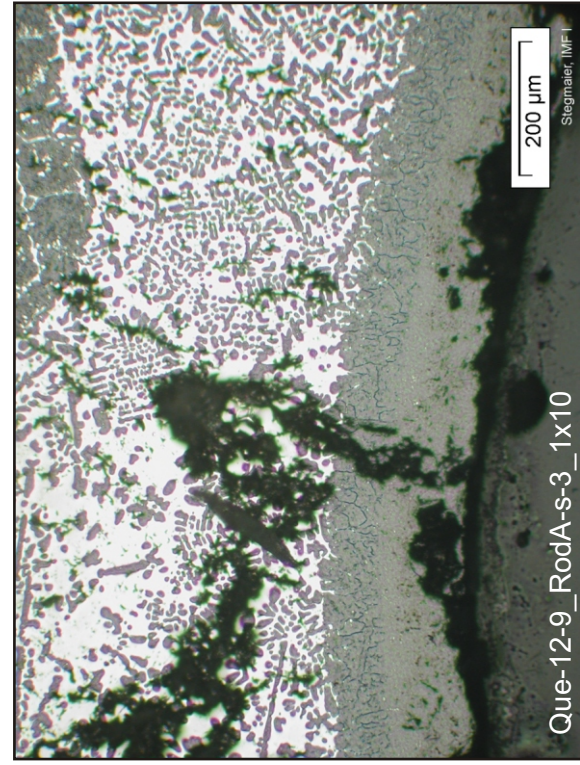
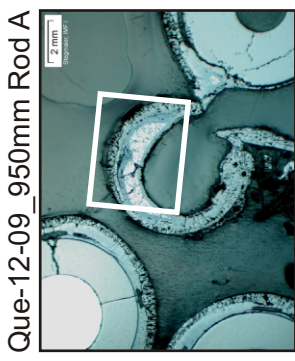
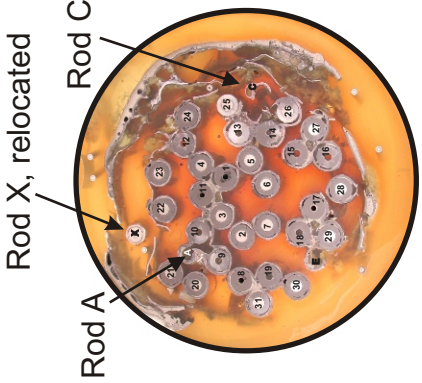
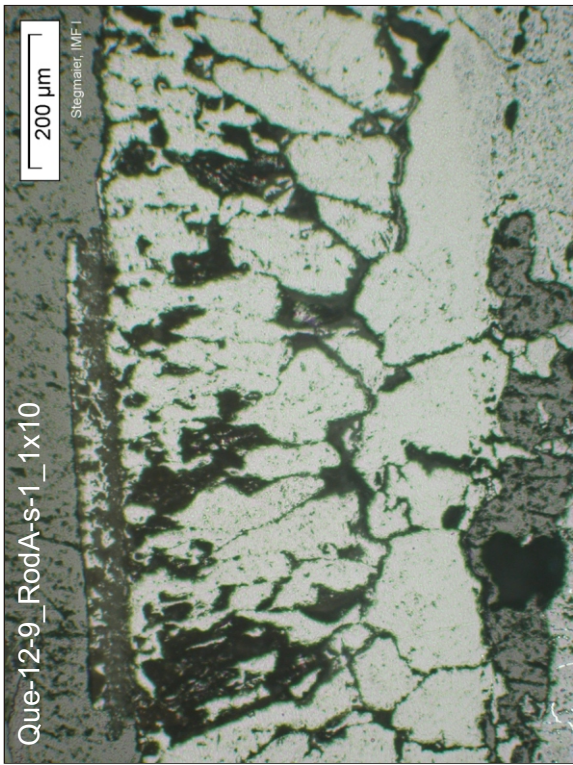
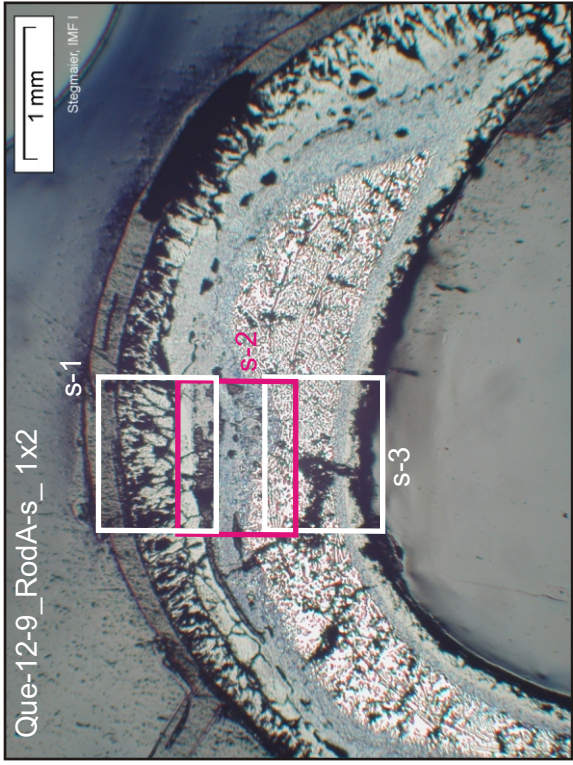


Fig. 96: QUE-12-9, level 950 mm; oxidation state of corner rod A, showing massive oxide and duplex melt microstructure.

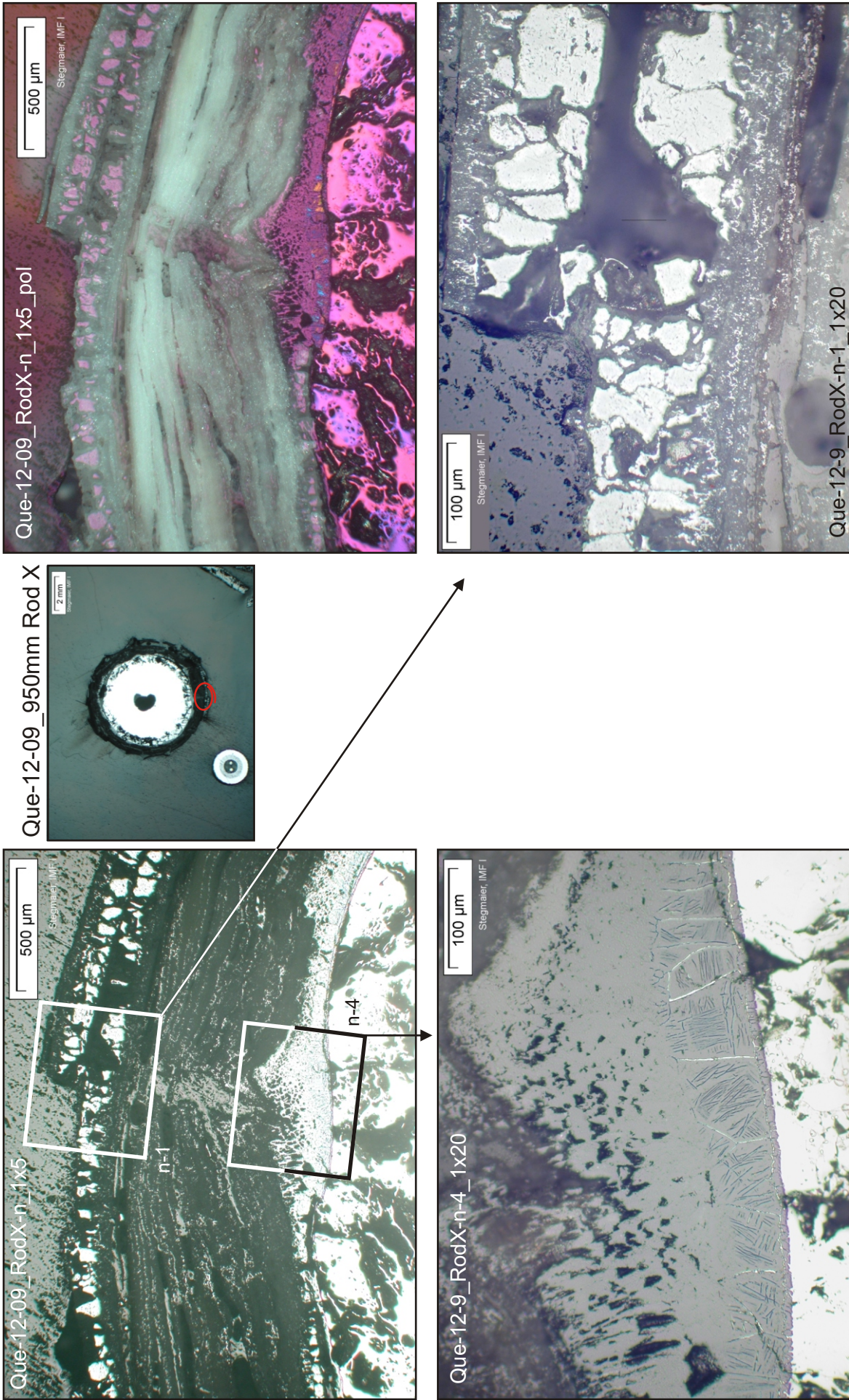


Fig. 97: QUE-12-9, level 950 mm; oxidation state of corner rod X, a massive relocated fragment, most probably of corner rod A origin.

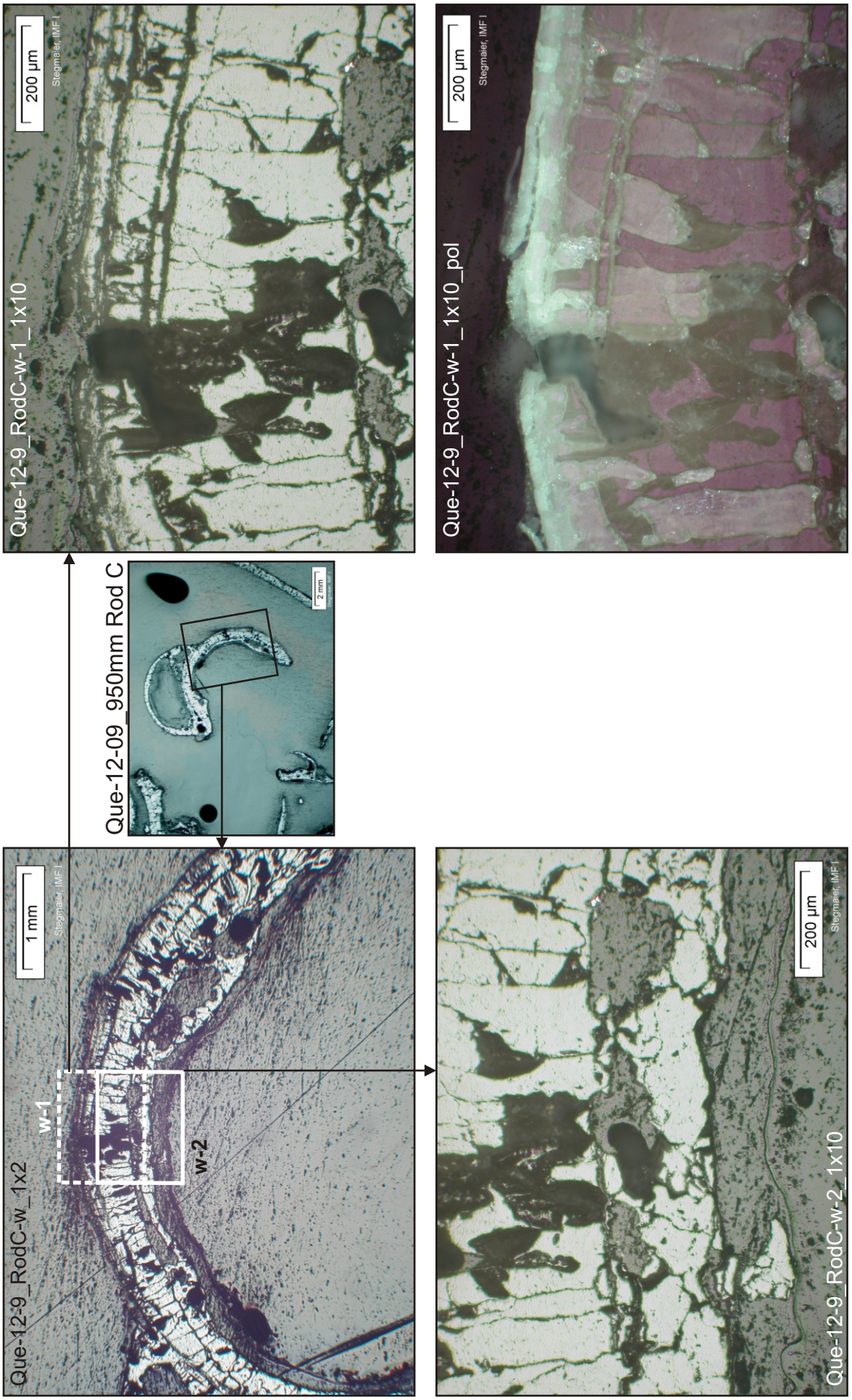


Fig. 98: QUE-12-9, level 950 mm; state of total oxidation of corner rod C remnants.

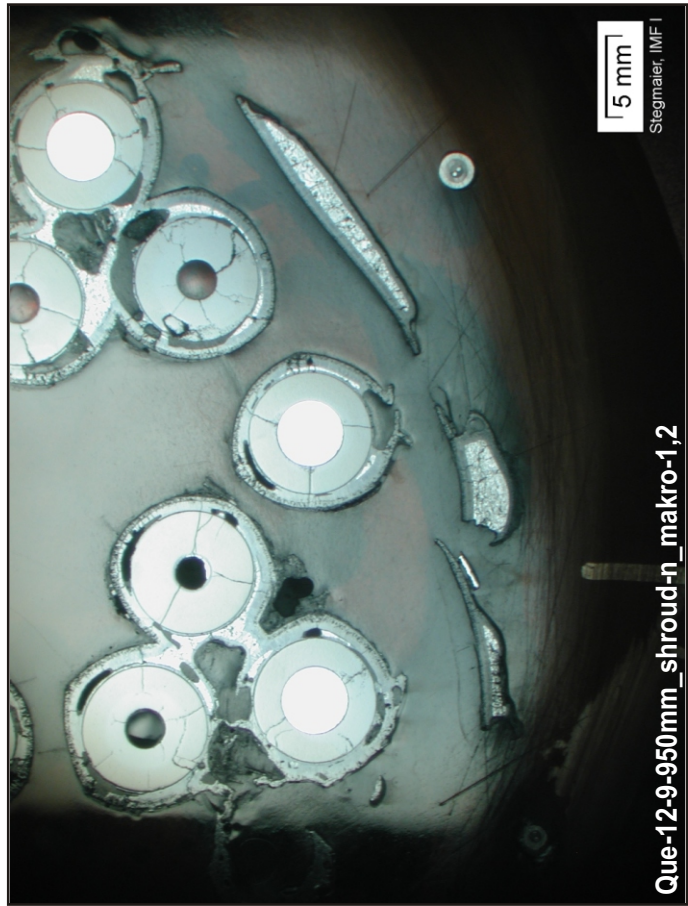
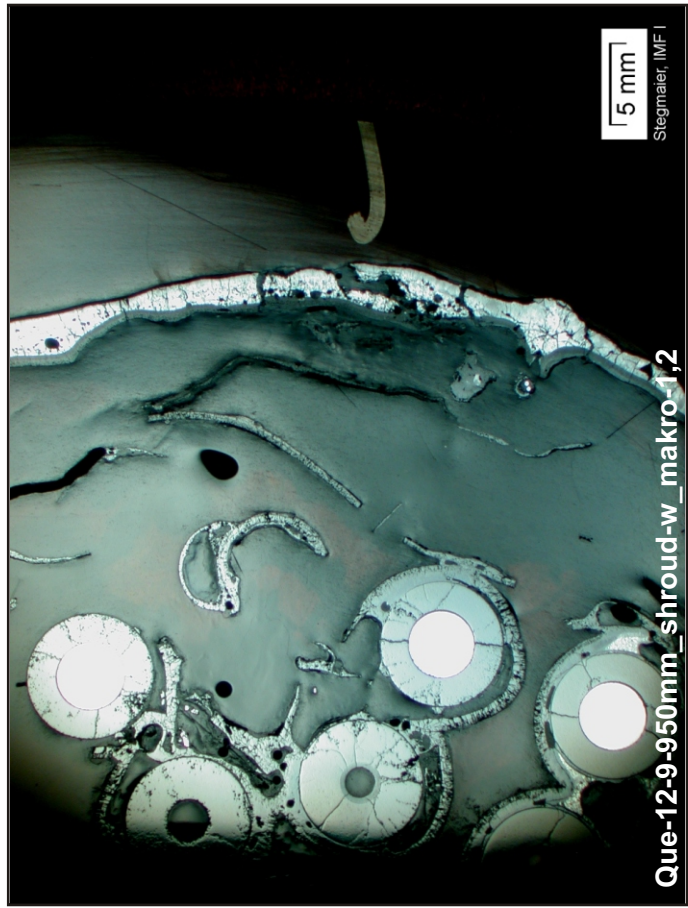
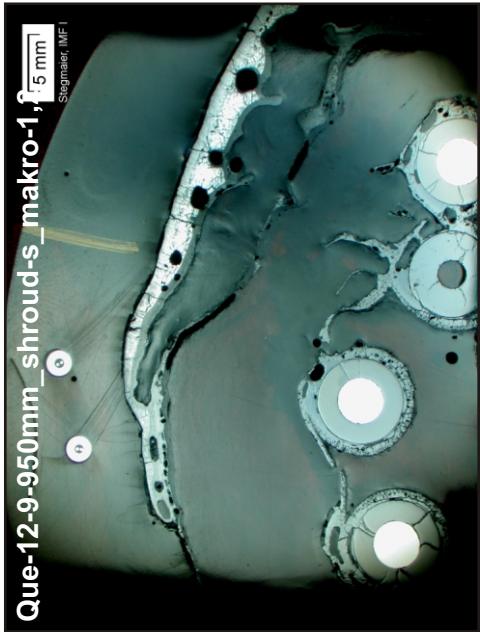


Fig. 99: QUE-12-9, level 950 mm; macrographs, depicting the remnants of the shroud.

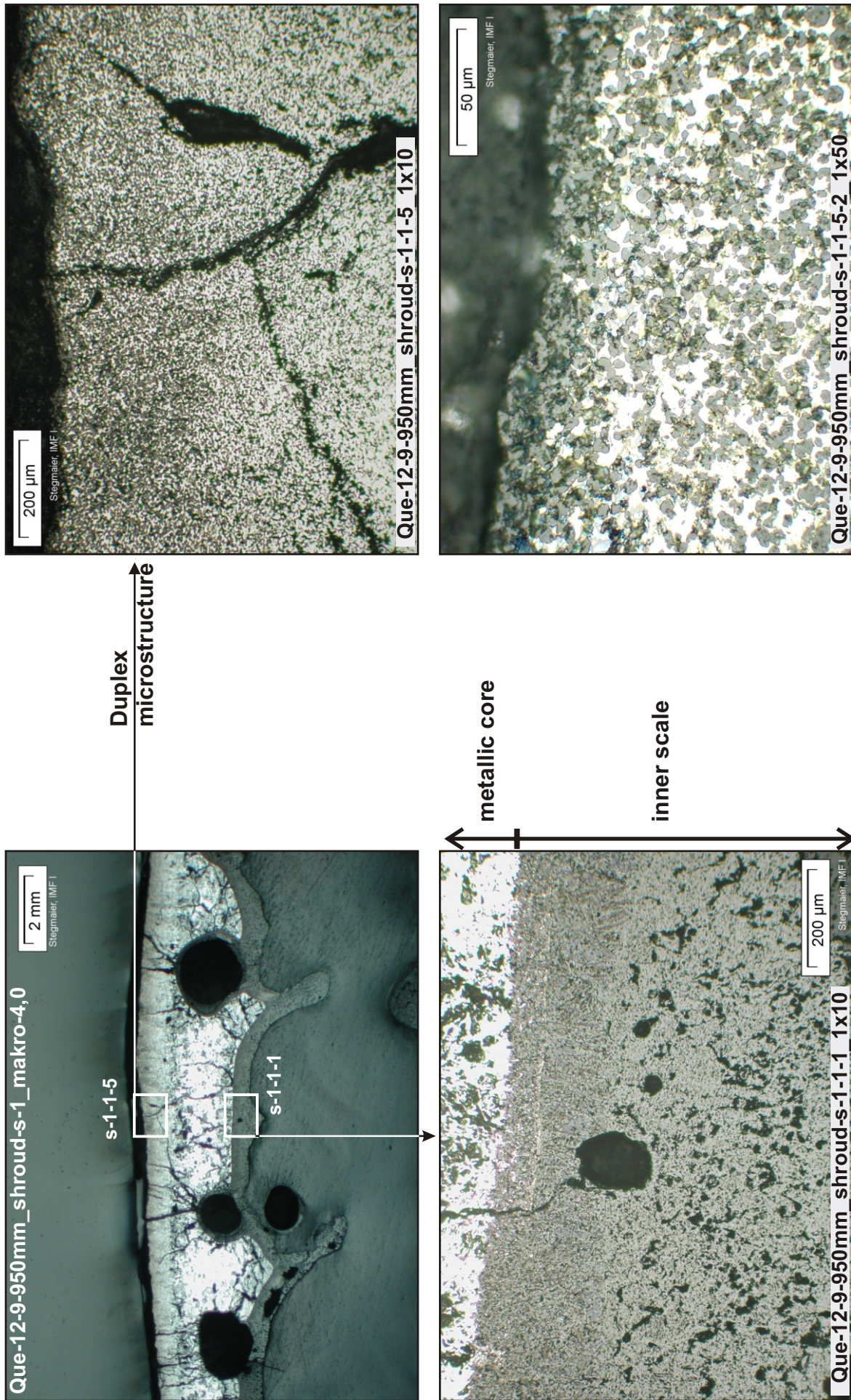


Fig. 100: QUE-12-9, level 950 mm; thick shroud remnant, composed of outer part with duplex microstructure, metallic core, and inner scale.

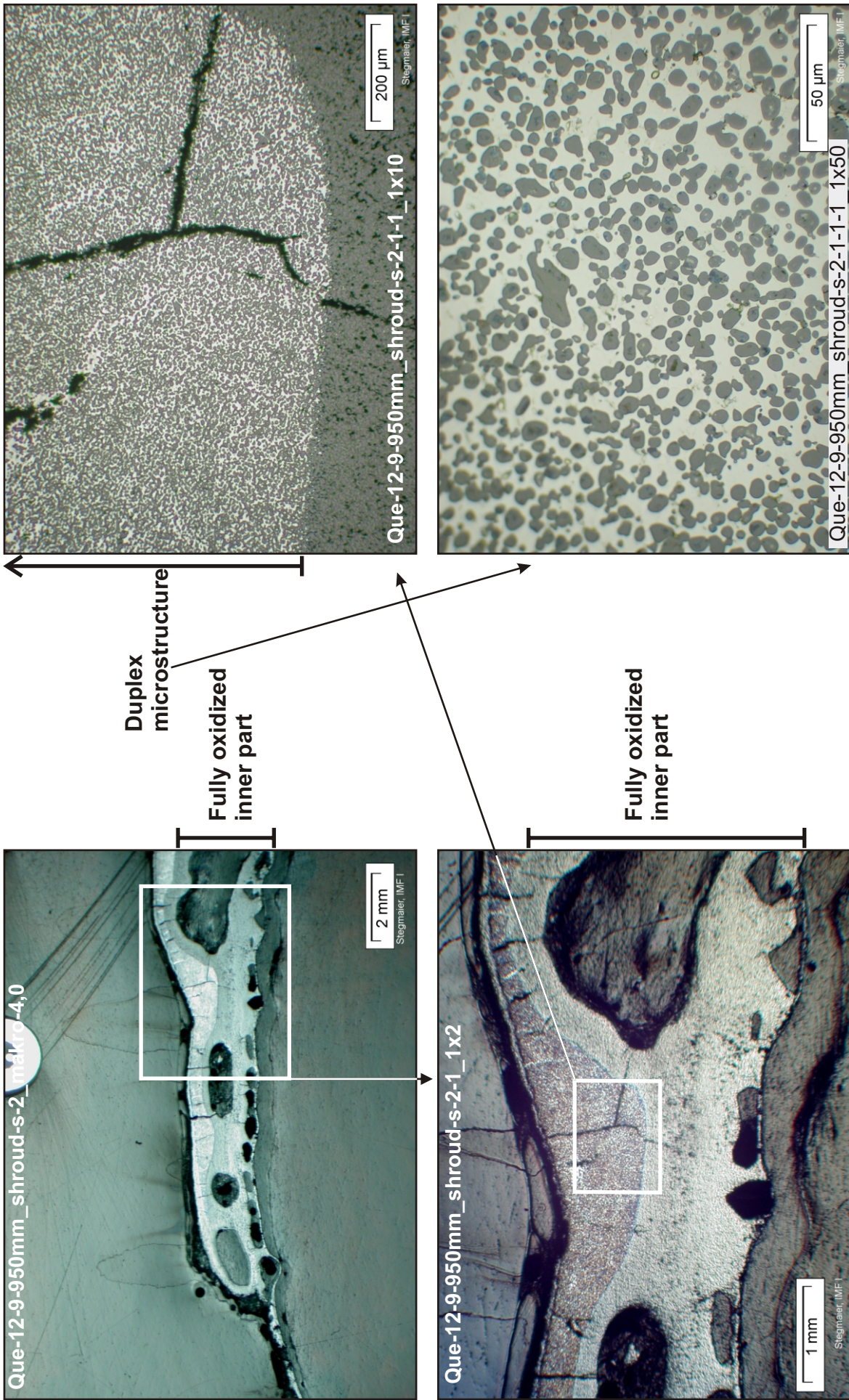


Fig. 101: QUE-12-9, level 950 mm; thin shroud remnant, composed of outer part with duplex microstructure, and fully oxidized inner part.

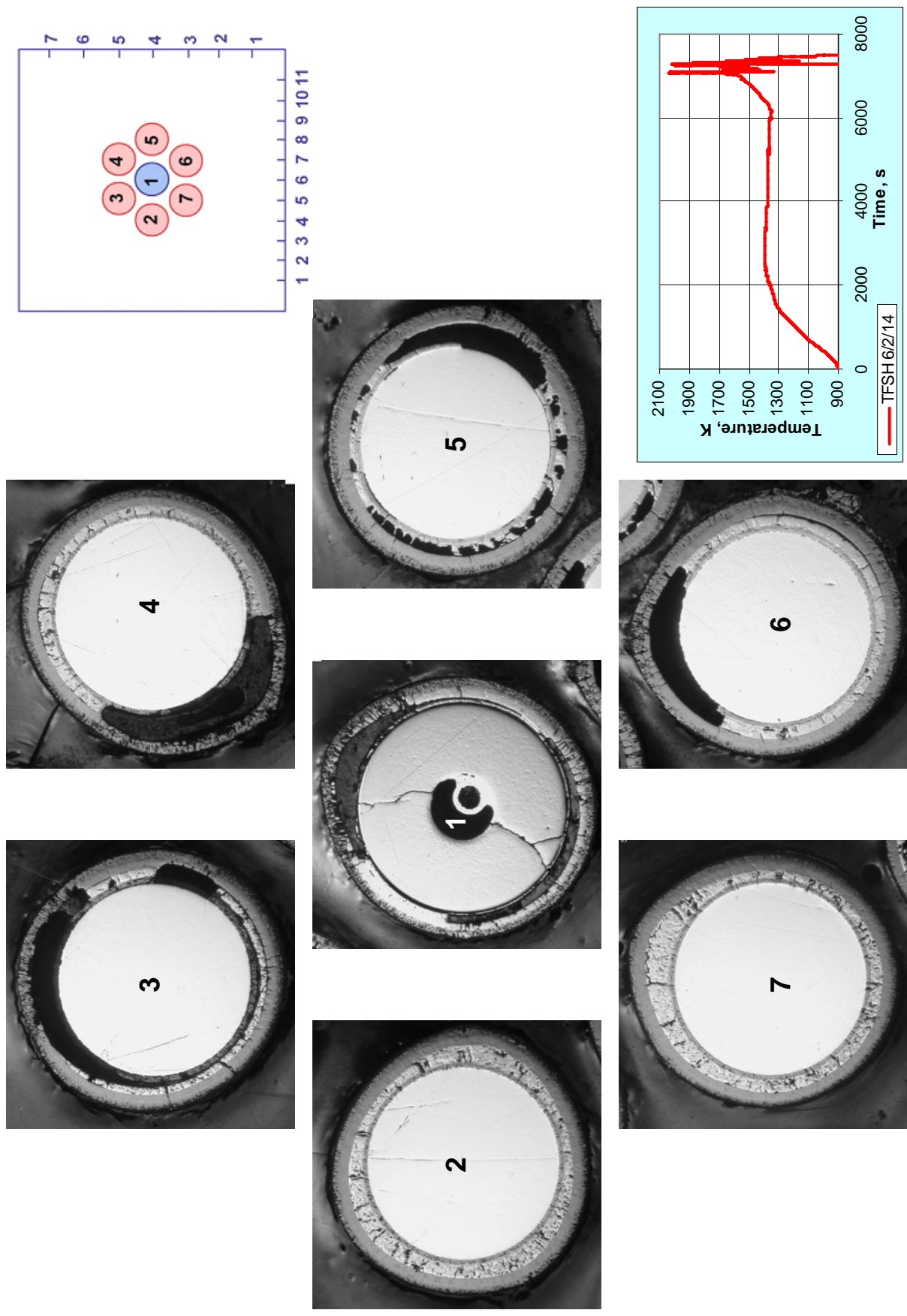


Fig. 102: QUENCH-12; Cross-sections of inner rod simulators at elevation 1050 mm

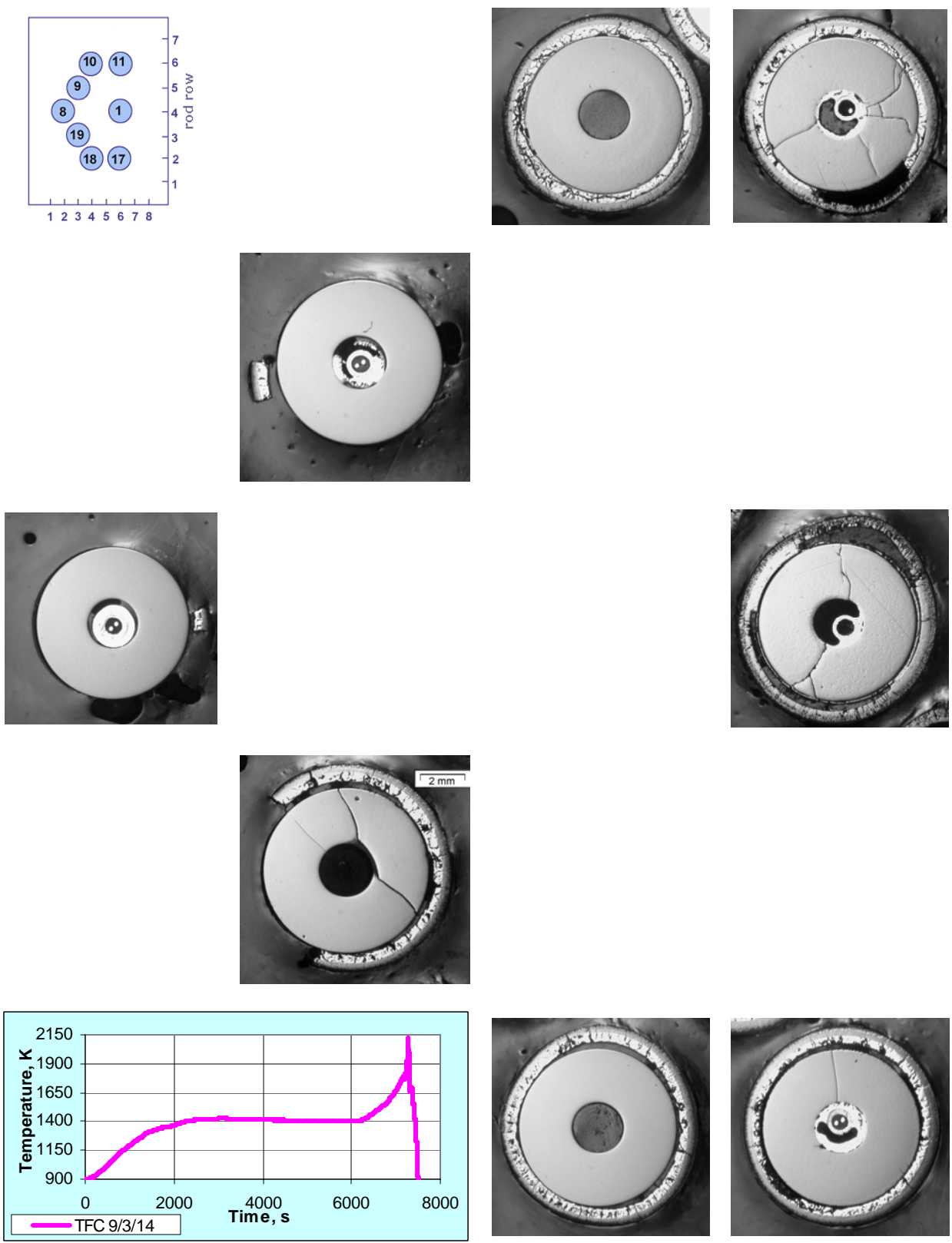


Fig. 103: QUENCH-12; Cross-sections of unheated rods (left part of the bundle) at elevation 1050 mm.

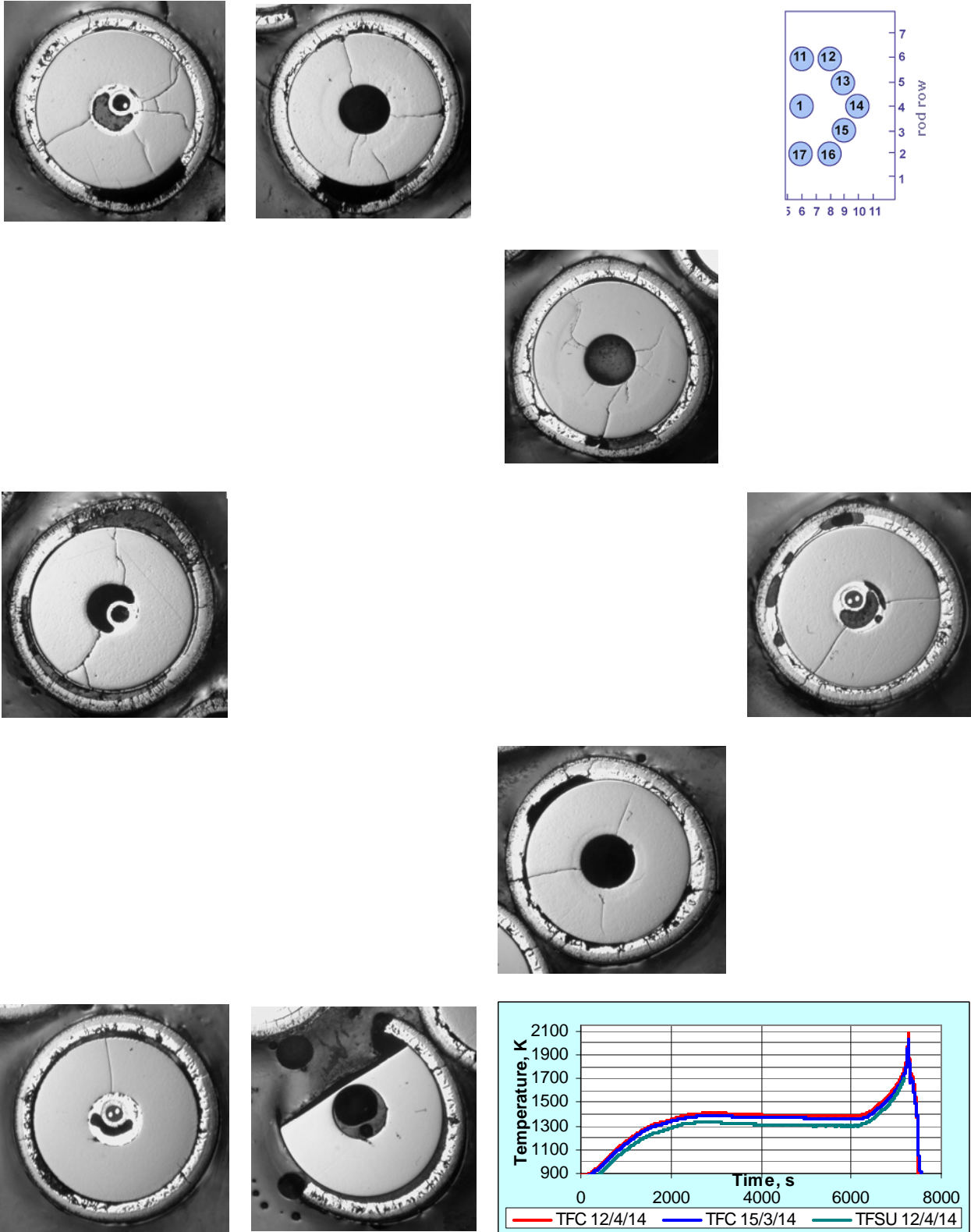


Fig. 104: QUENCH-12; Cross-sections of unheated rods (right part of the bundle) at elevation 1050 mm.

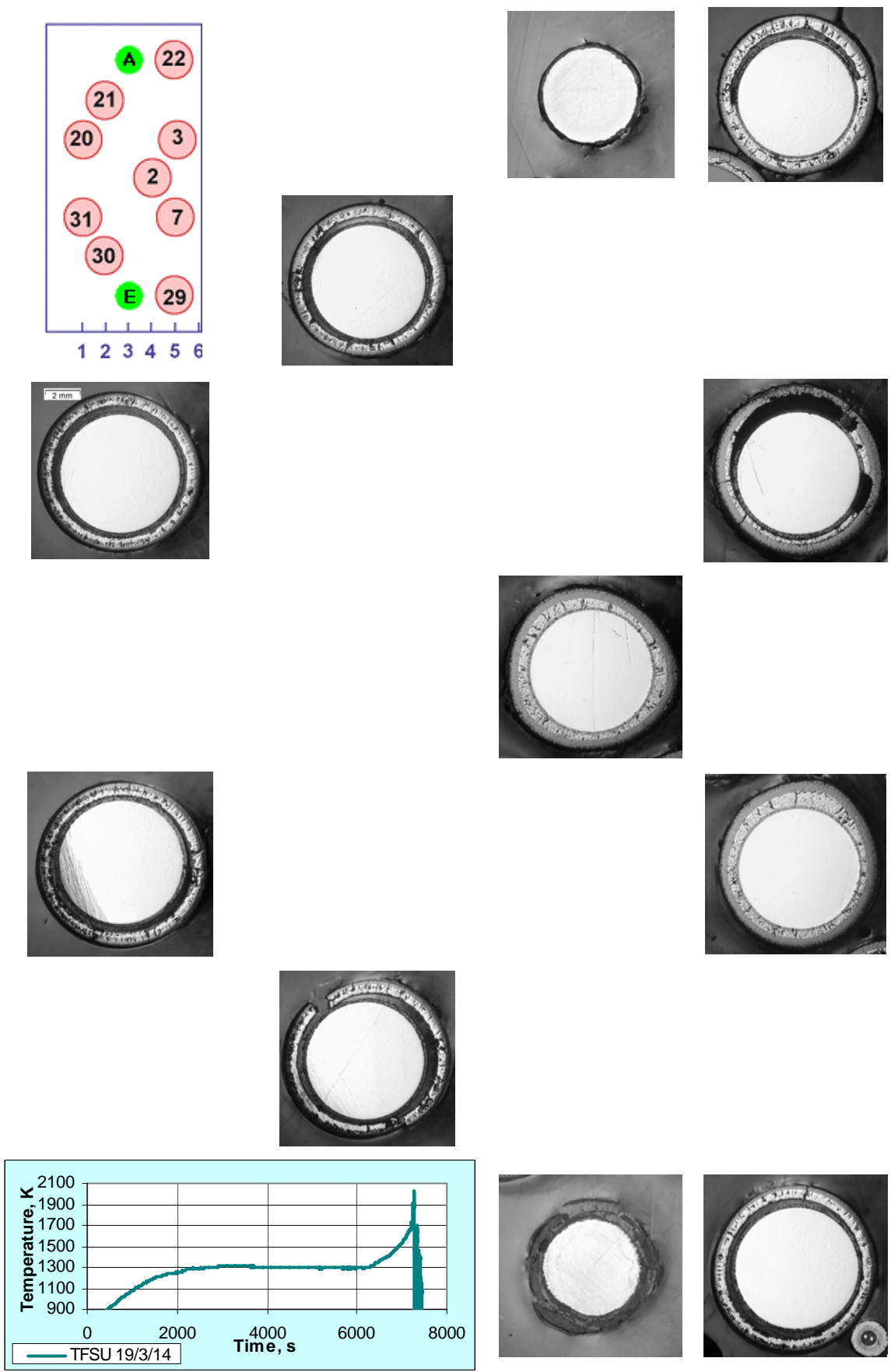


Fig. 105: QUENCH-12; Cross-sections of heated rods (left part of the bundle) at elevation 1050 mm.

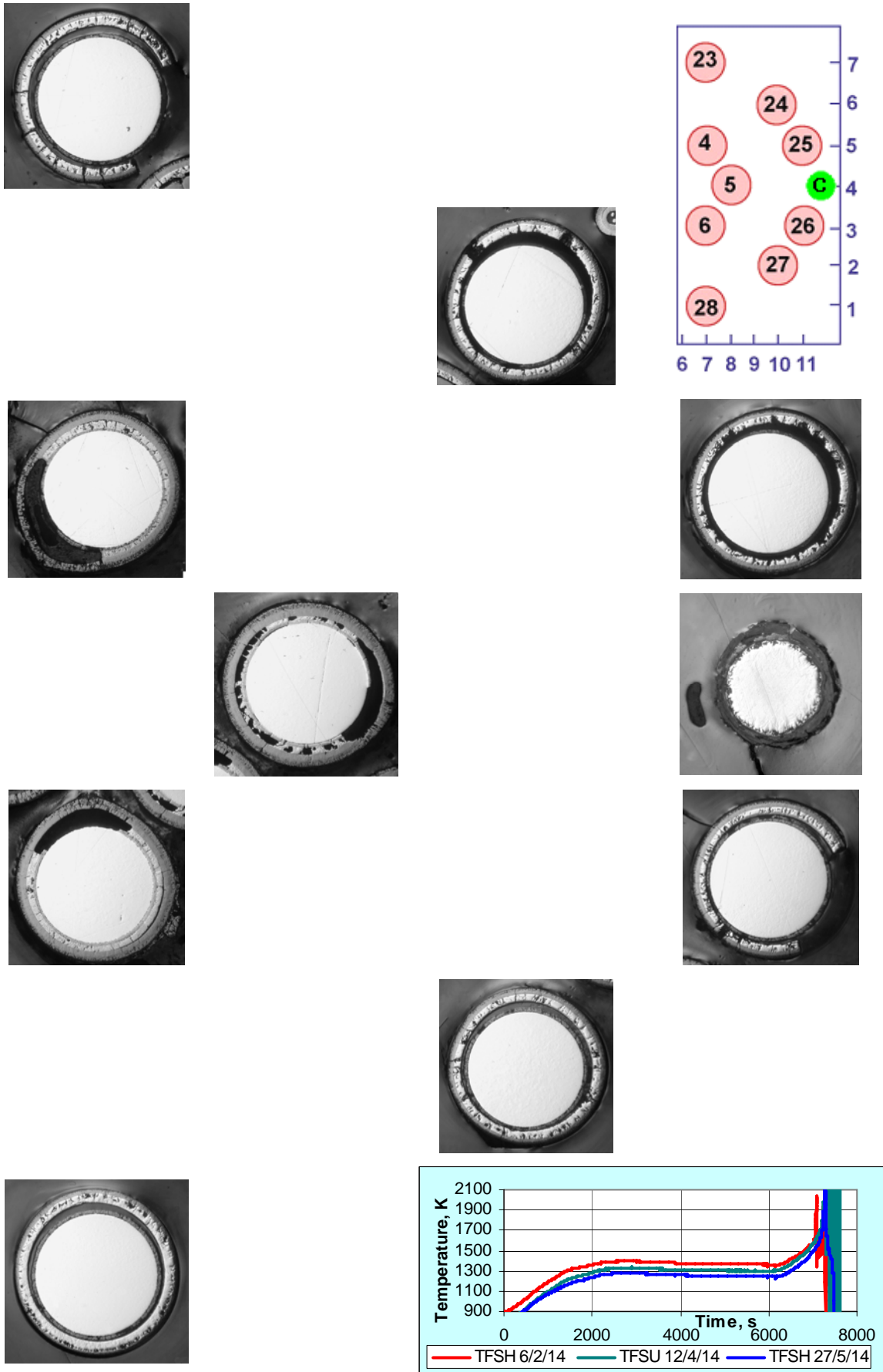
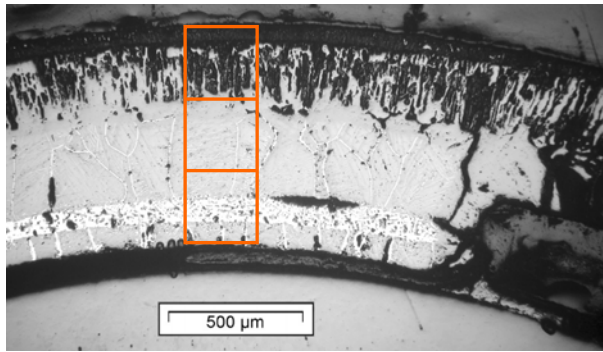
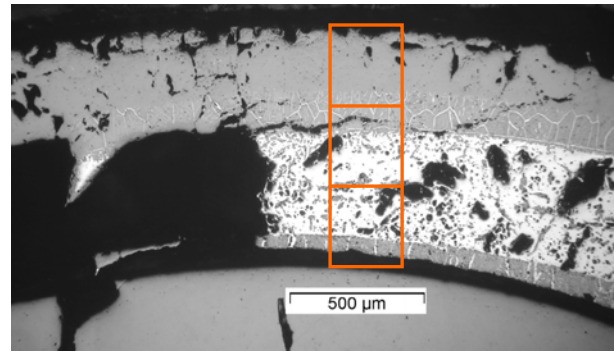


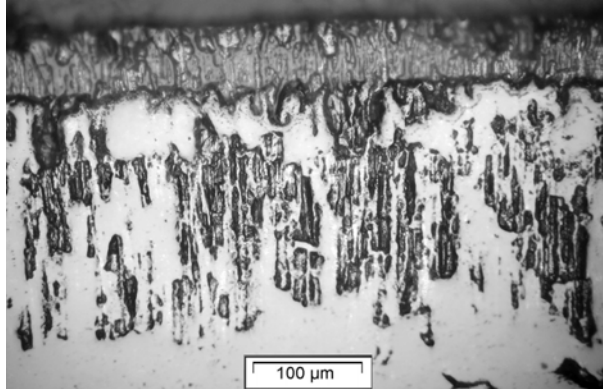
Fig. 106: QUENCH-12; Cross-sections of heated rods (right part of the bundle) at elevation 1050 mm.



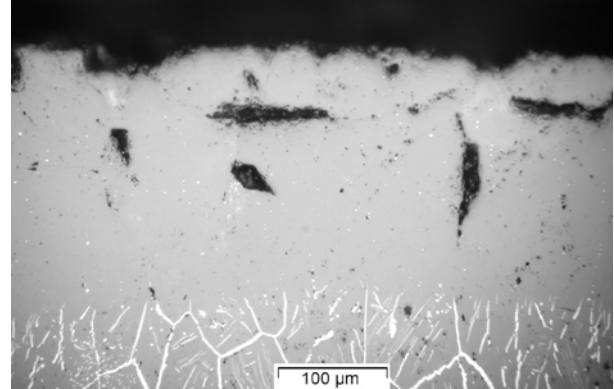
rod 1 cladding: thick external oxide layer



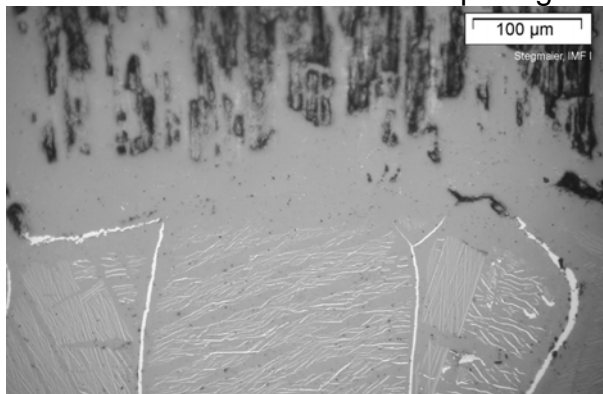
rod 13 cladding: thick melt layer



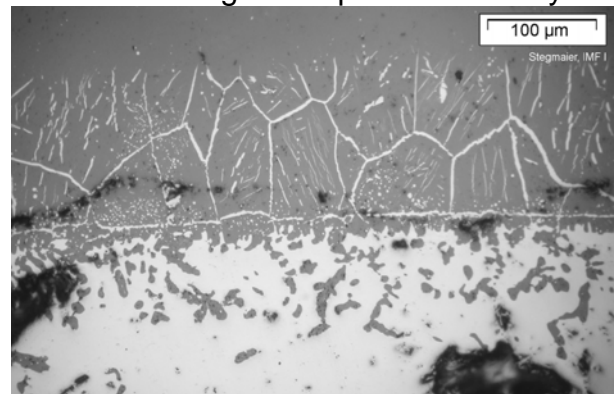
rod 1: external oxide scale spalling



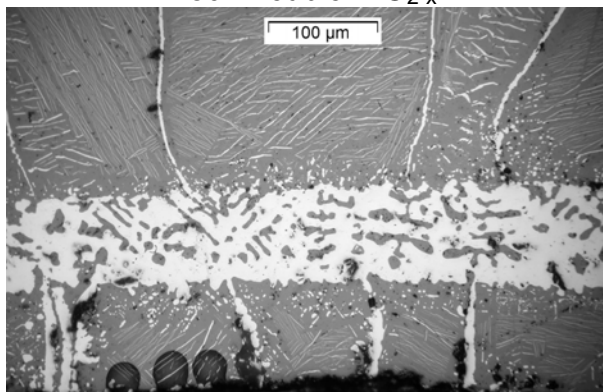
rod 13: homog. outer part of oxide layer



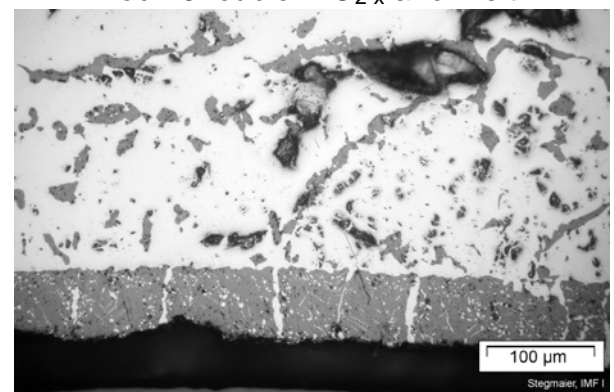
rod 1: cubic ZrO_{2-x}



rod 13: cubic ZrO_{2-x} and melt

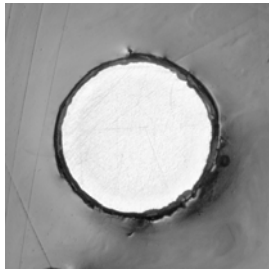


rod 1: melt and internal oxide layer

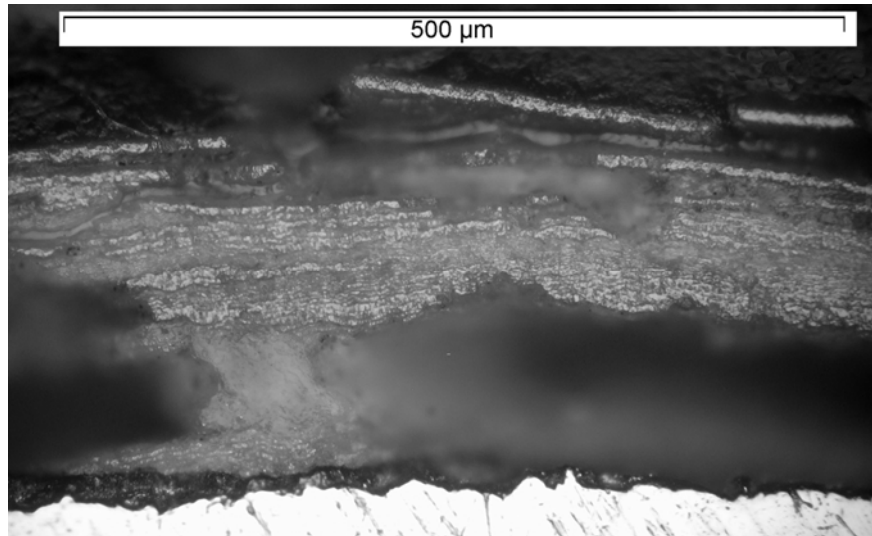


rod 13: melt and internal oxide layer

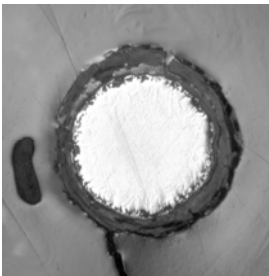
Fig. 107: QUENCH-12; microstructure of cladding tube of unheated rods 1 (intensive initial pre-oxidation; left column) and 13 (moderate initial pre-oxidation; right column) at elevation 1050 mm.



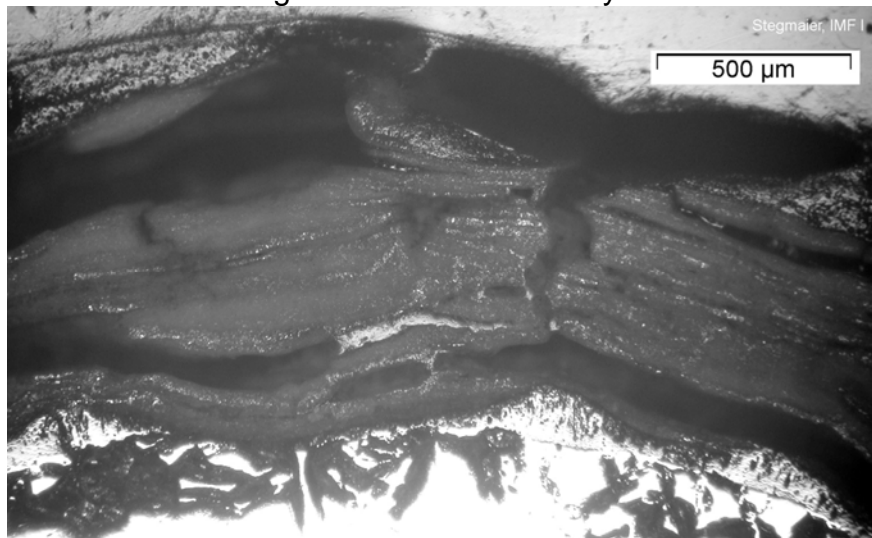
corner rod A



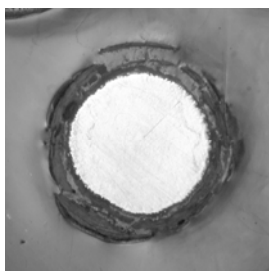
fragment of rod A oxide layer



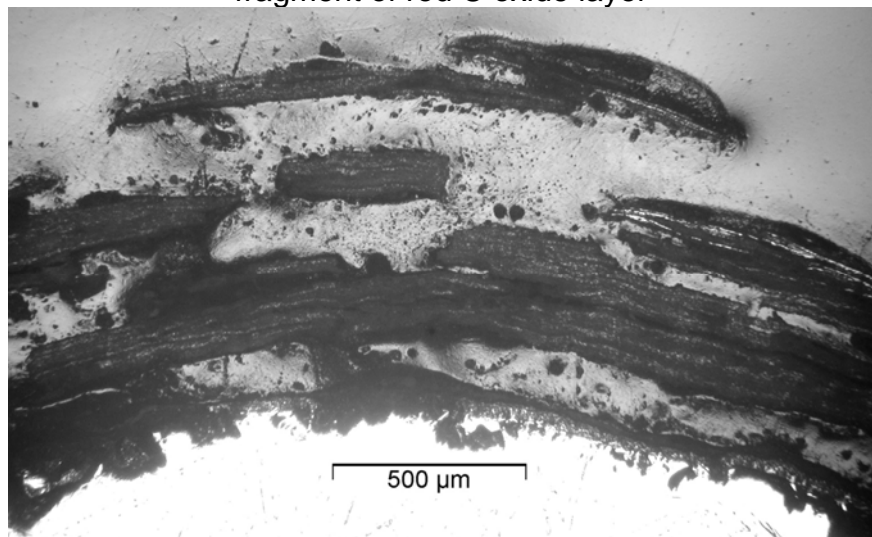
corner rod C



fragment of rod C oxide layer



corner rod E



fragment of rod E oxide layer

Fig. 108: QUENCH-12; pronounced breakaway structure of corner rods oxide layers at elevation 1050 mm; cross-section of relocated corner rod A corresponds to an upper bundle elevation.

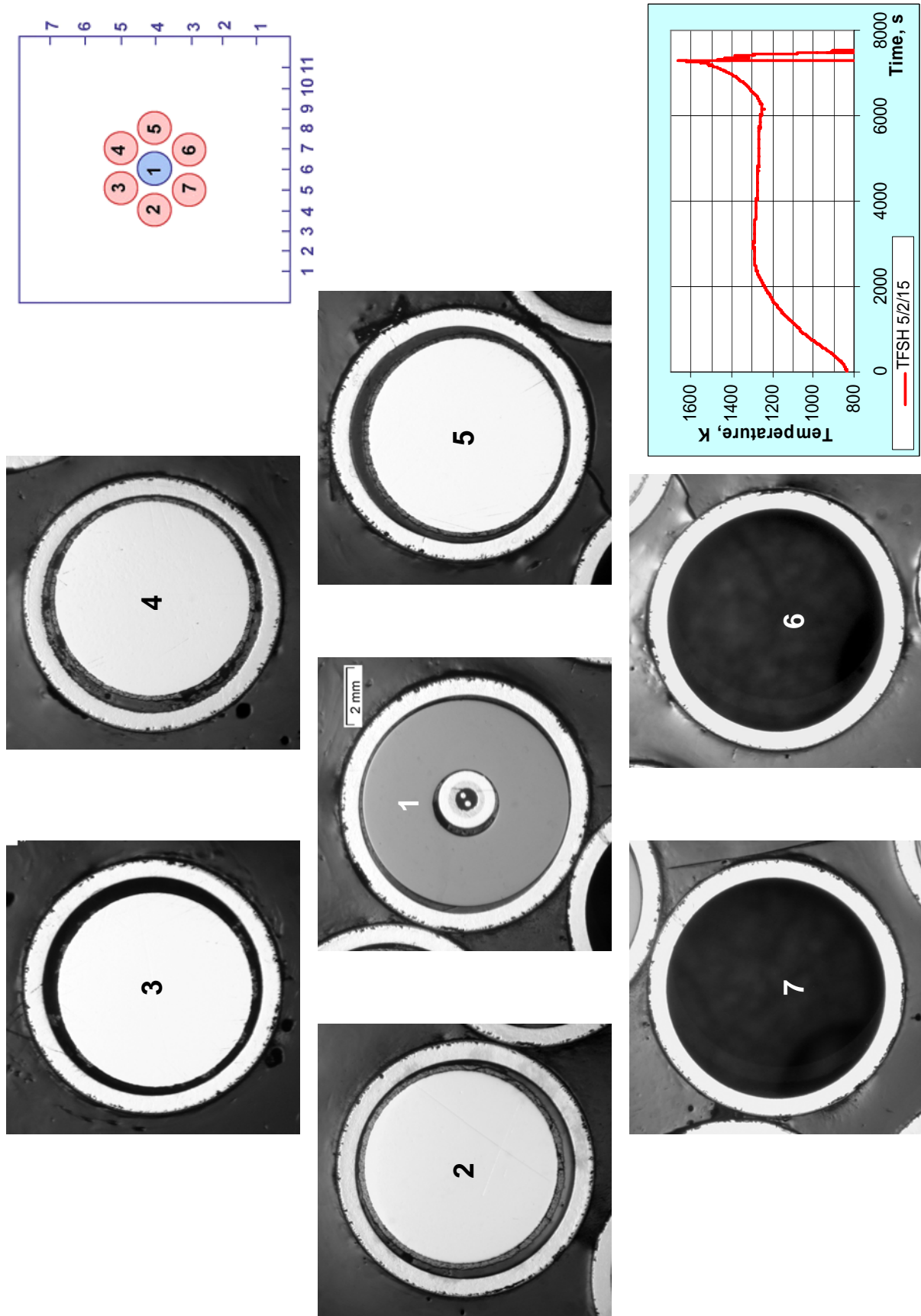


Fig. 109: QUENCH-12; Cross-sections of inner rod simulators at elevation 1150 mm.

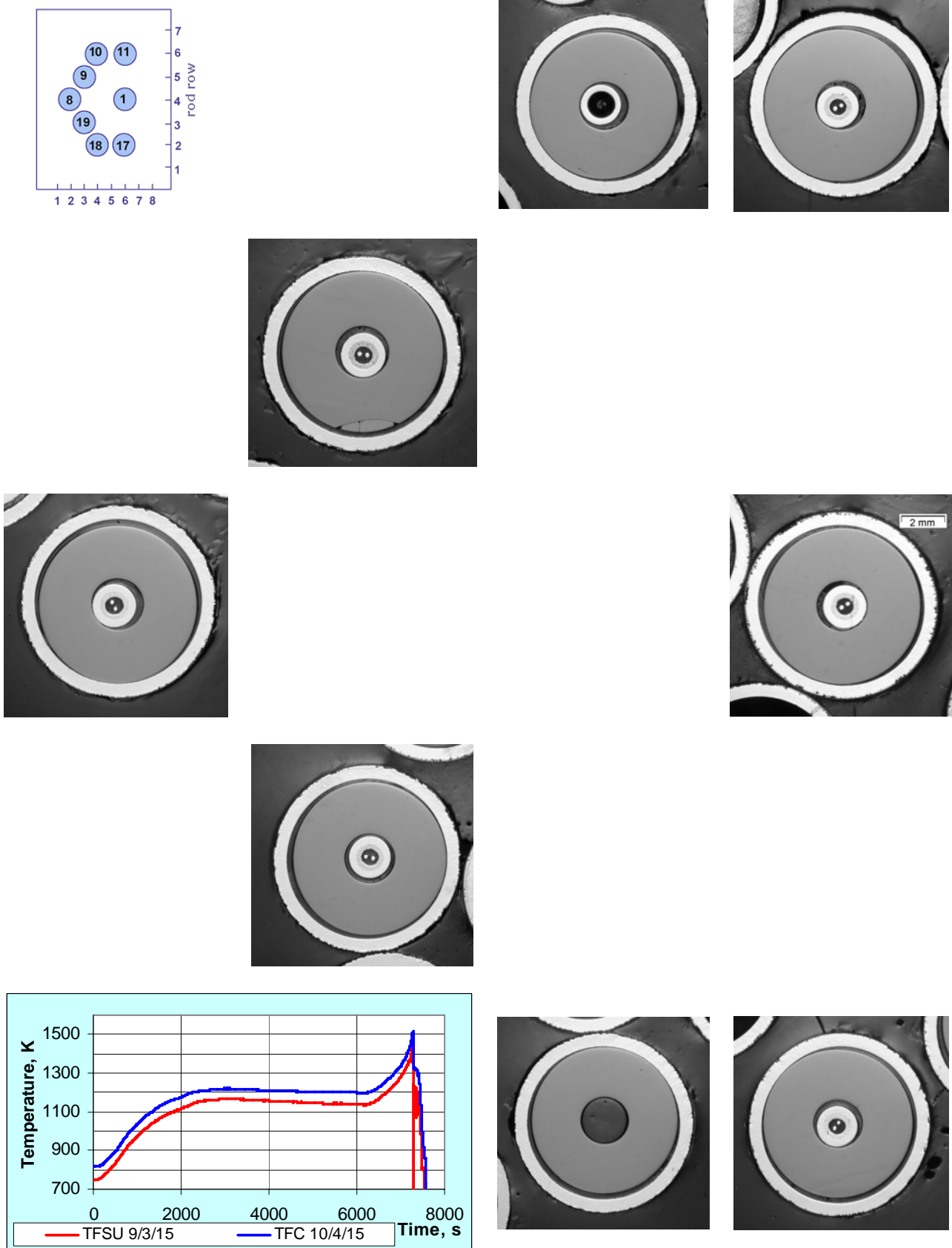


Fig. 110: QUENCH-12; cross-sections of unheated rods (left part of the bundle) at elevation 1150 mm.

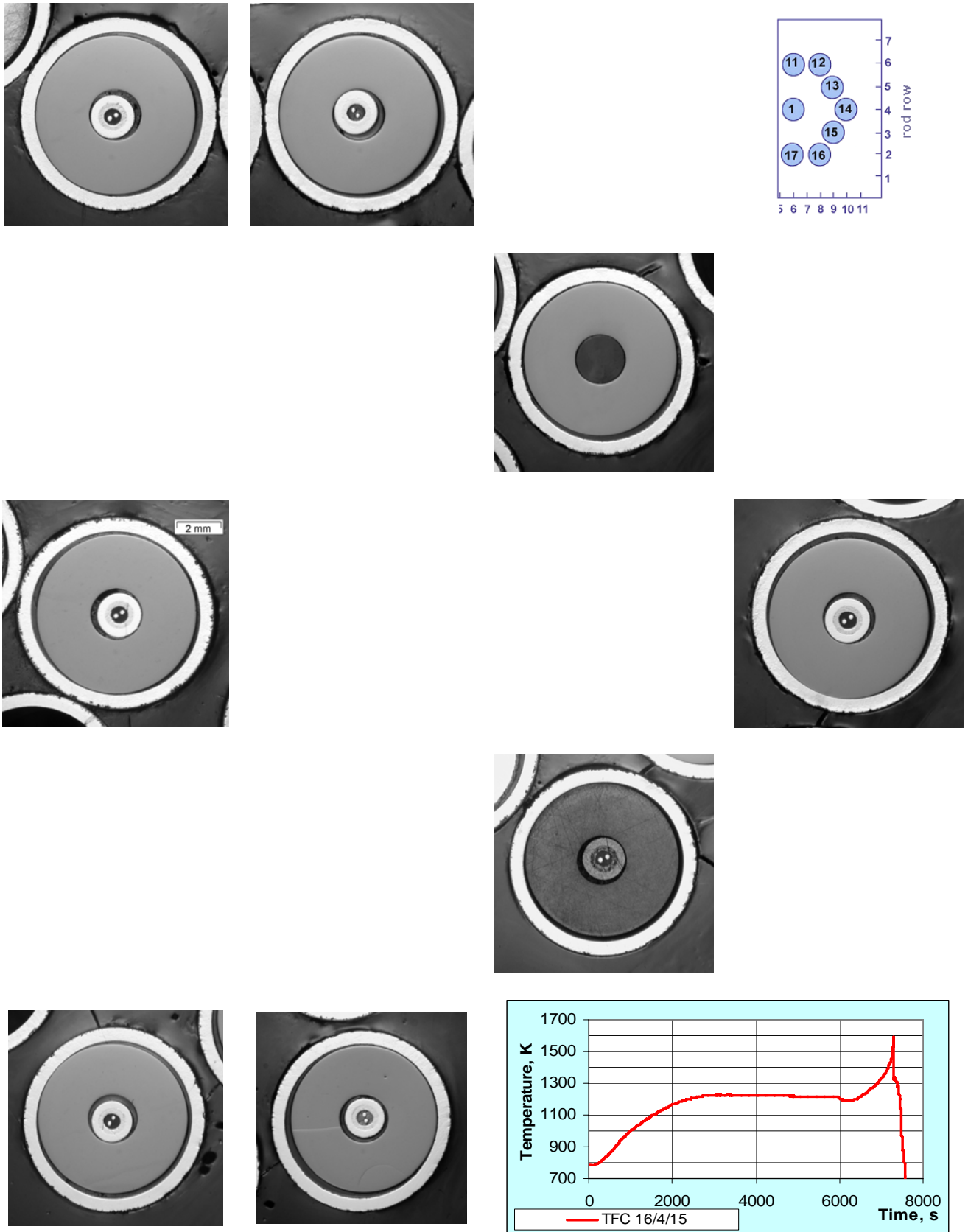


Fig. 111: QUENCH-12; Cross-sections of unheated rods (right part of the bundle) at elevation 1150 mm.

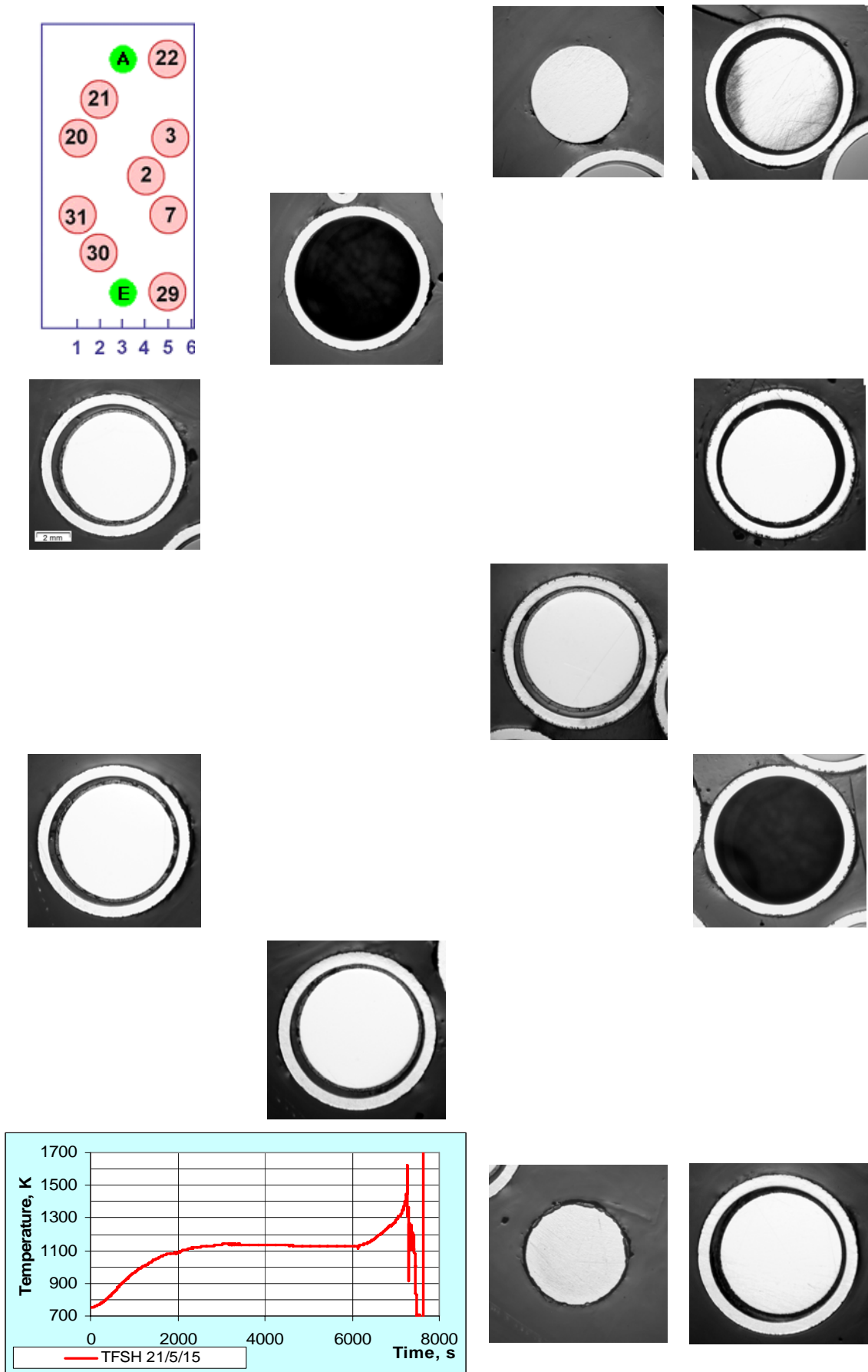


Fig. 112: QUENCH-12; Cross-sections of heated rods (left part of the bundle) at elevation 1150 mm.

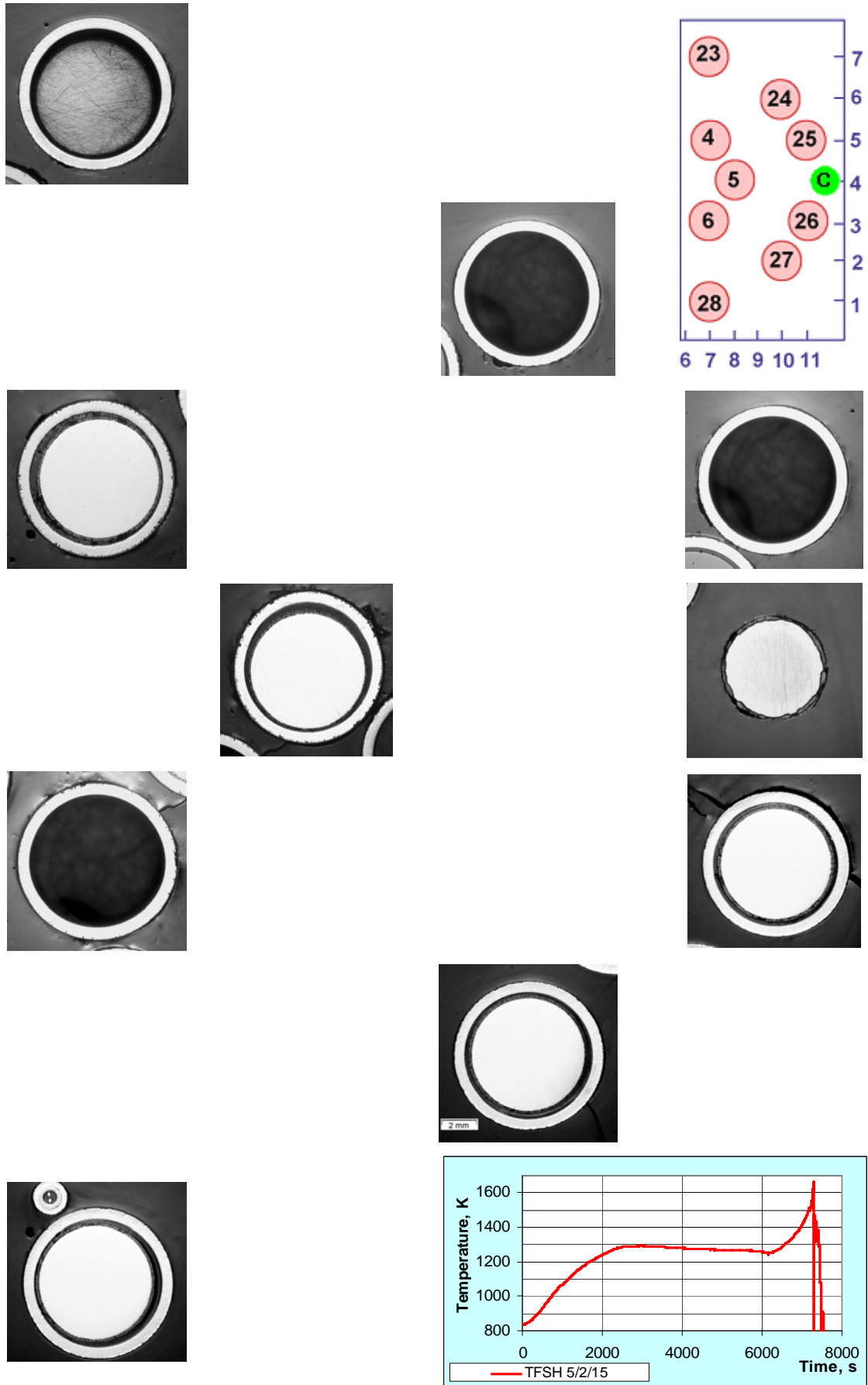
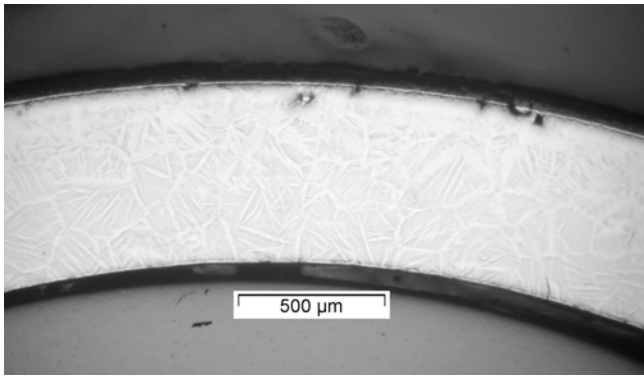
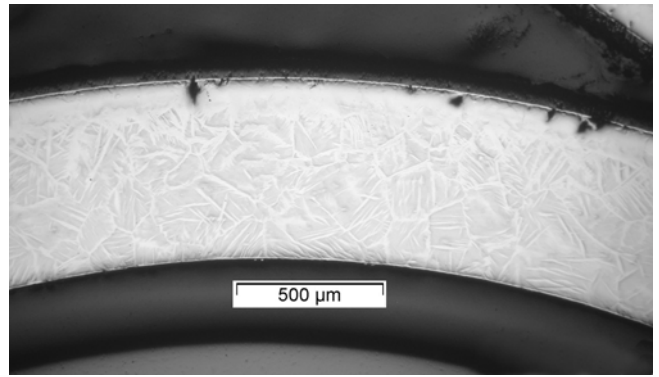


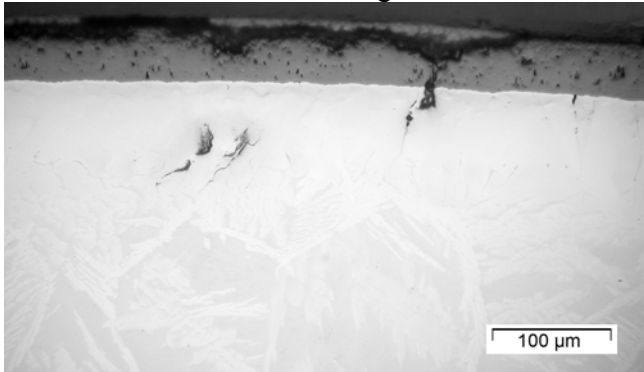
Fig. 113: QUENCH-12; Cross-sections of heated rods (right part of the bundle) at elevation 1150 mm.



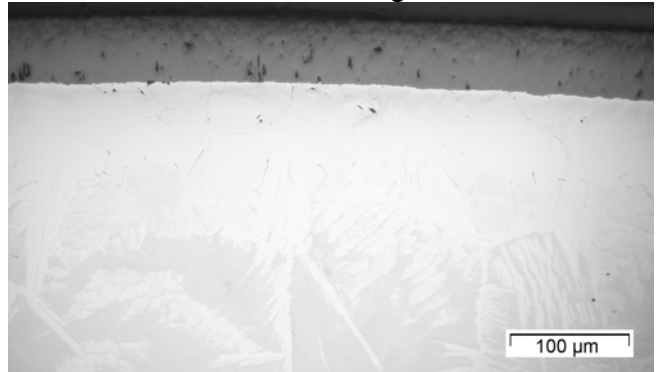
rod 12 cladding, 225°



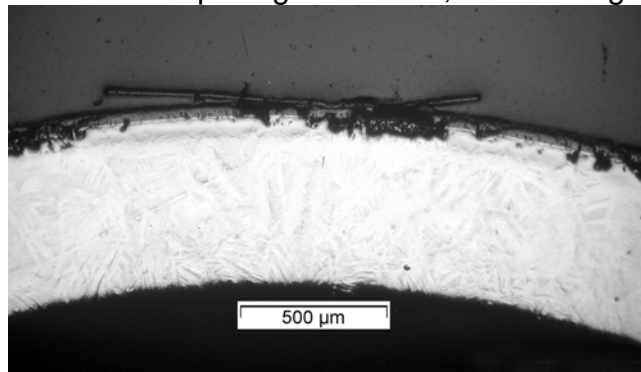
rod 12 cladding, 90°



rod 12, 225°: external oxide scale spalling



rod 12, 90°: homog. outer part of oxide layer

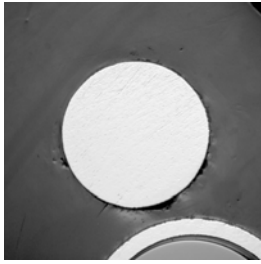


rod 21: cladding 45°

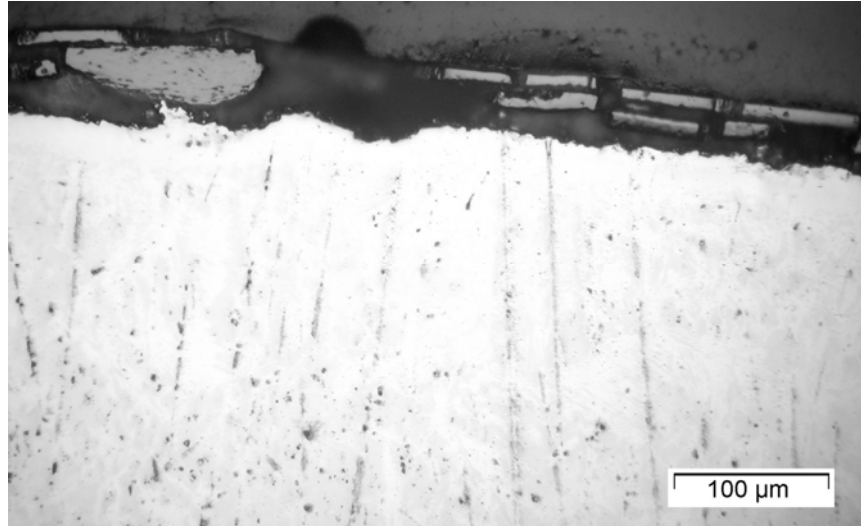


Rod 21, 45°: external oxide scale spalling

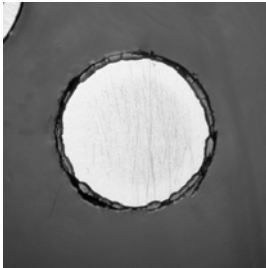
Fig. 114: QUENCH-12; Microstructure of cladding tubes of unheated rod 12 and heated rod 21 at elevation 1150 mm.



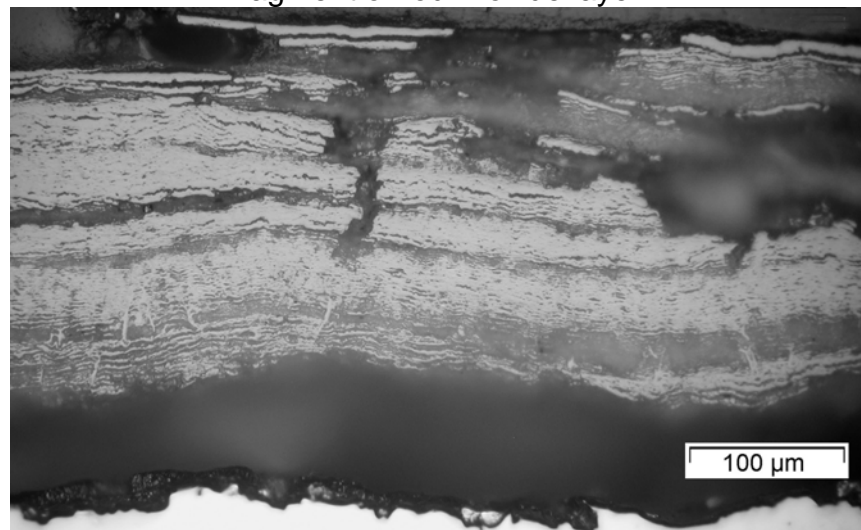
corner rod A



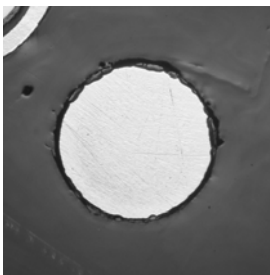
fragment of rod A oxide layer



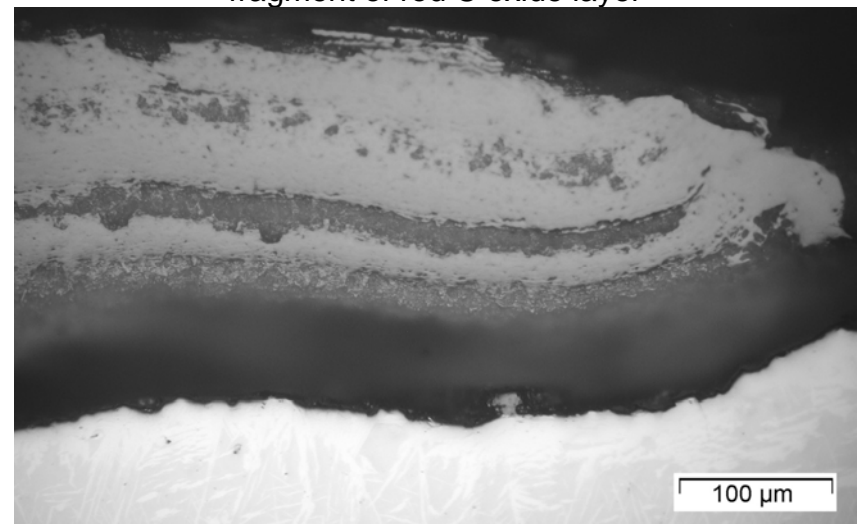
corner rod C



fragment of rod C oxide layer

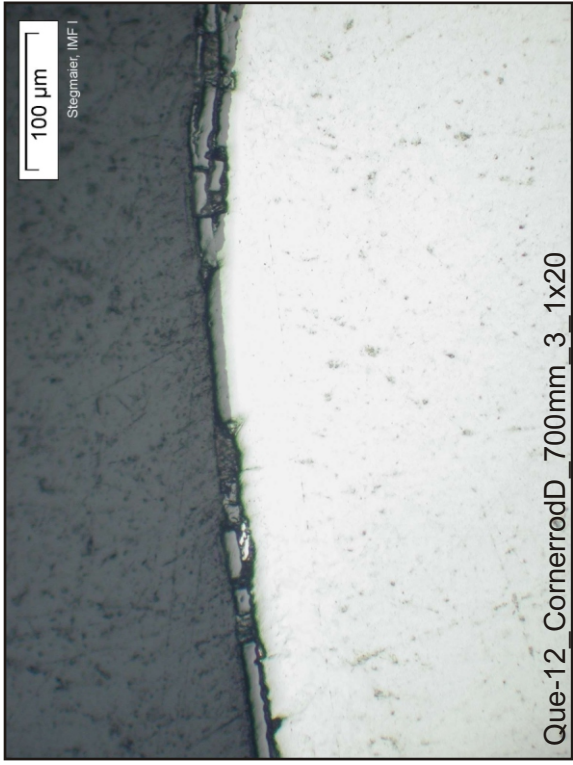


corner rod E



fragment of rod E oxide layer

Fig. 115: QUENCH-12; Pronounced breakaway structure of oxide layers of corner rods at elevation 1150 mm; cross-section of relocated corner rod A corresponds to an upper bundle elevation.



Side view of corner rod D
around 700 mm

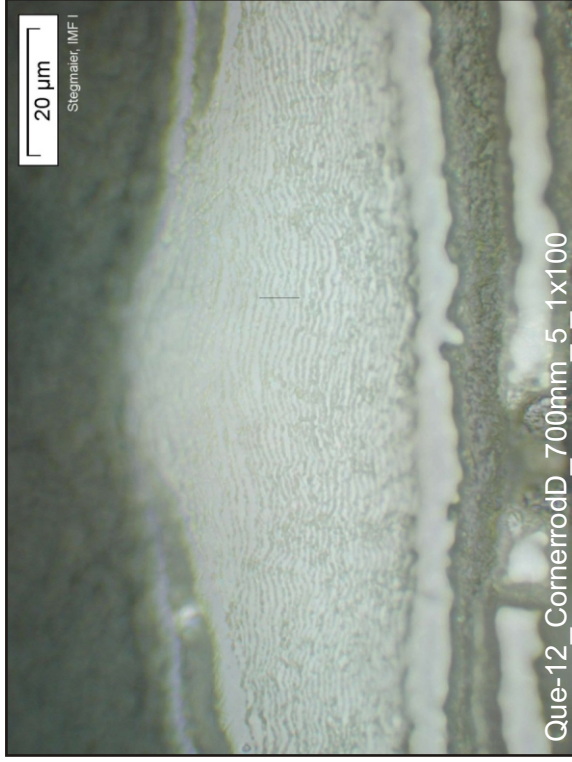
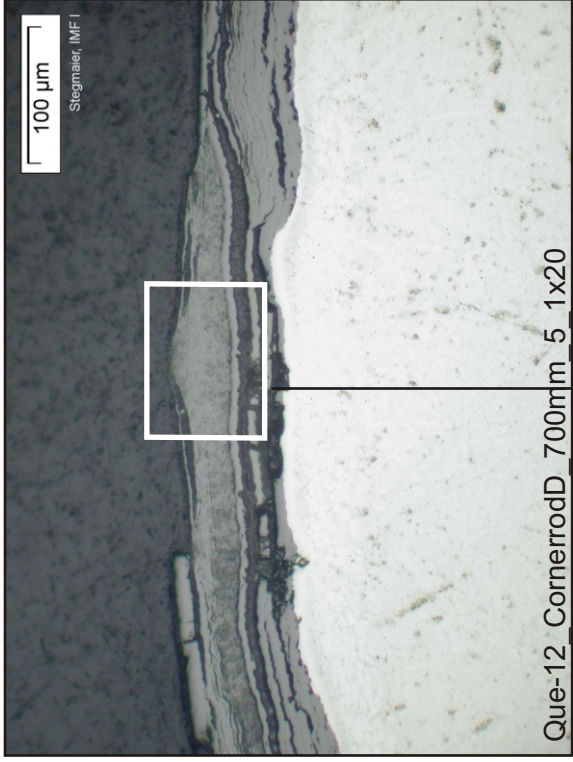
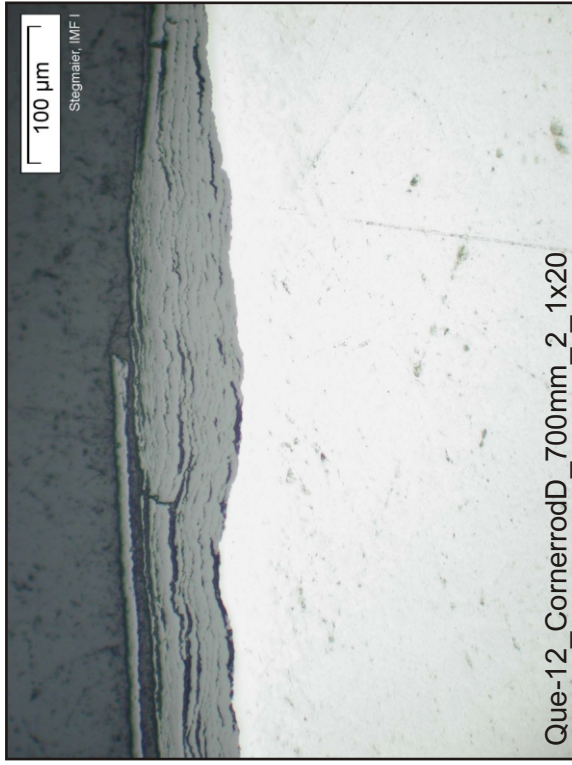
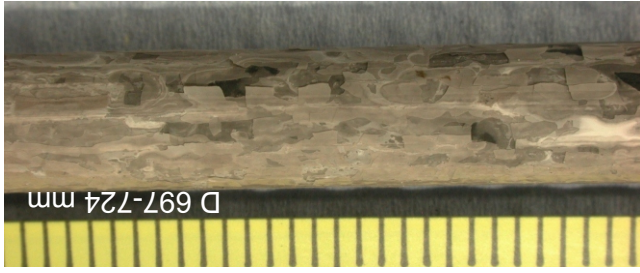
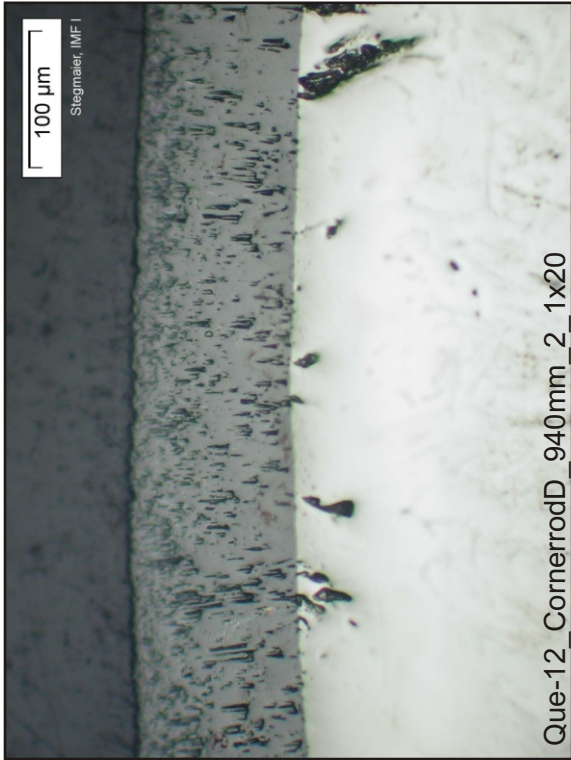


Fig. 116: QUE-12, level 700 mm; oxidation of withdrawn corner rod D, representing the end of the pre-oxidation phase.



Side view of corner rod D around 940 mm

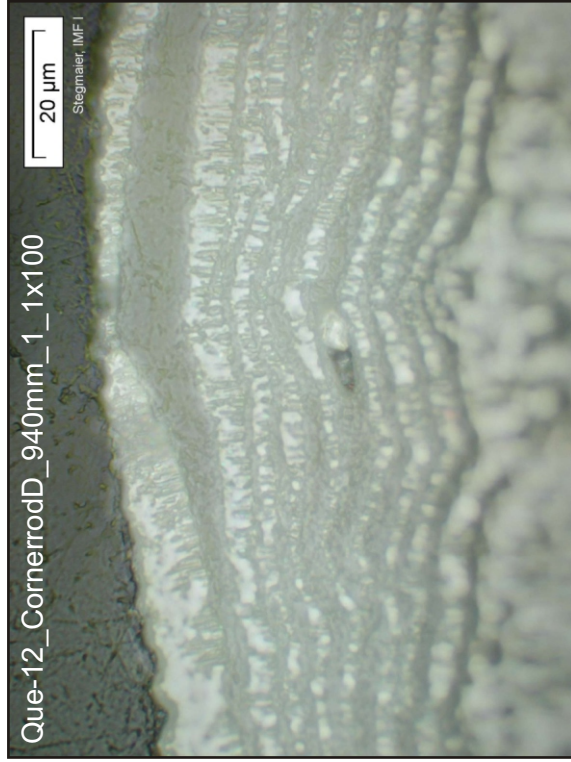
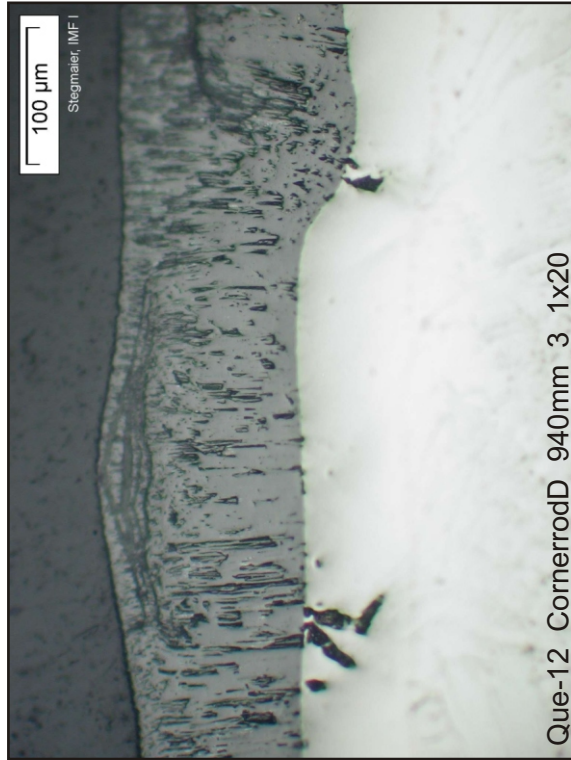
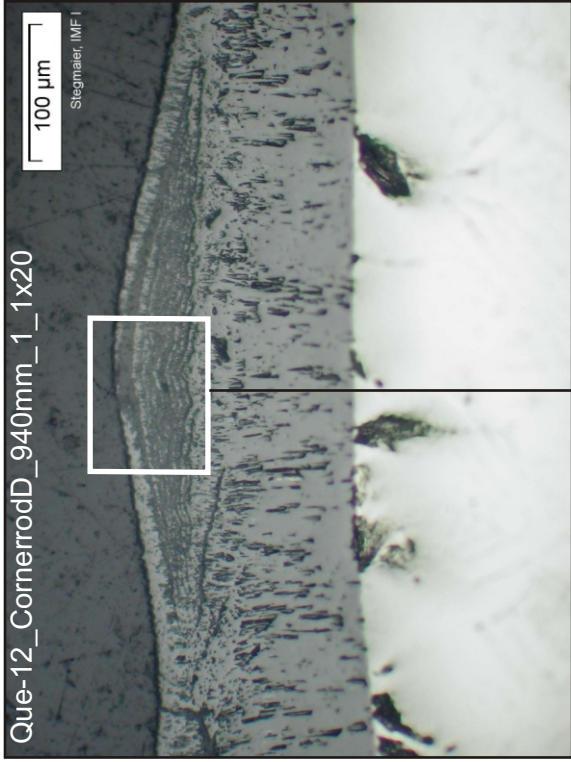
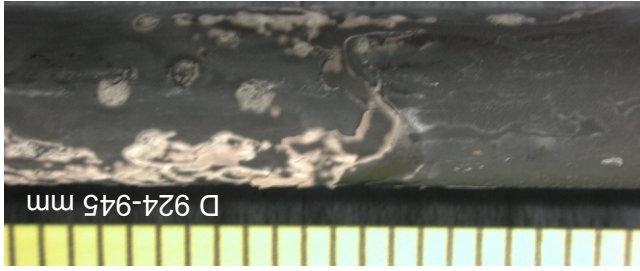
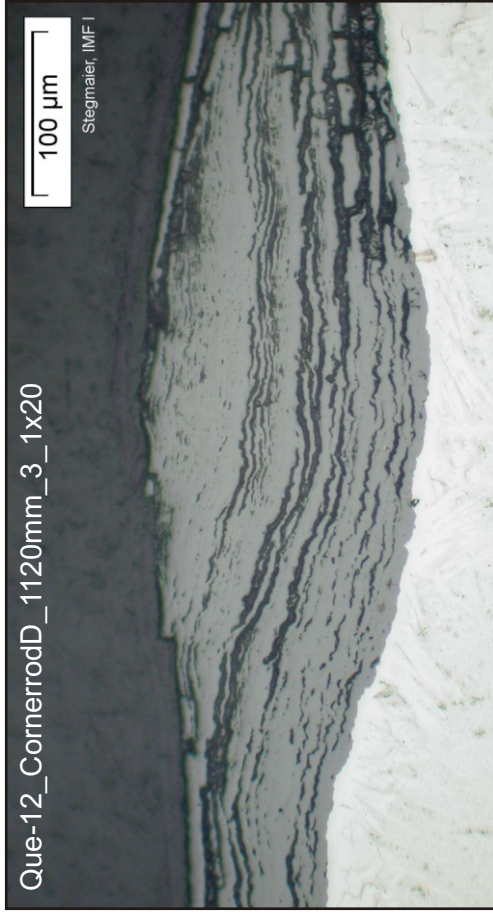
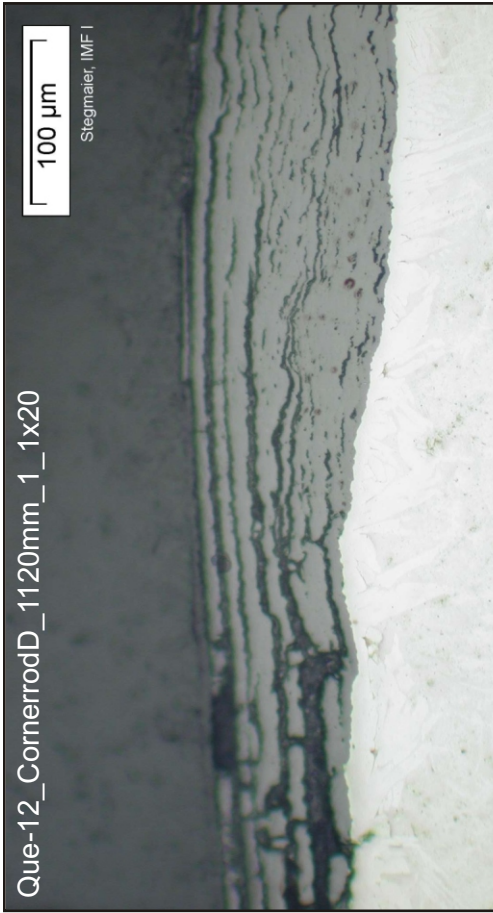
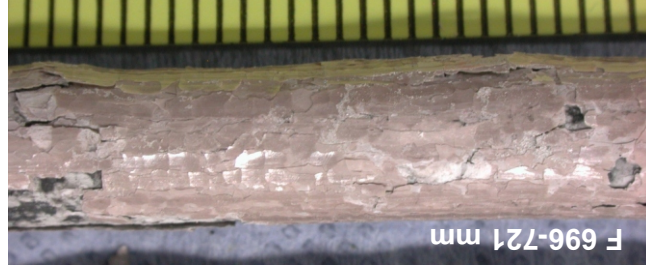
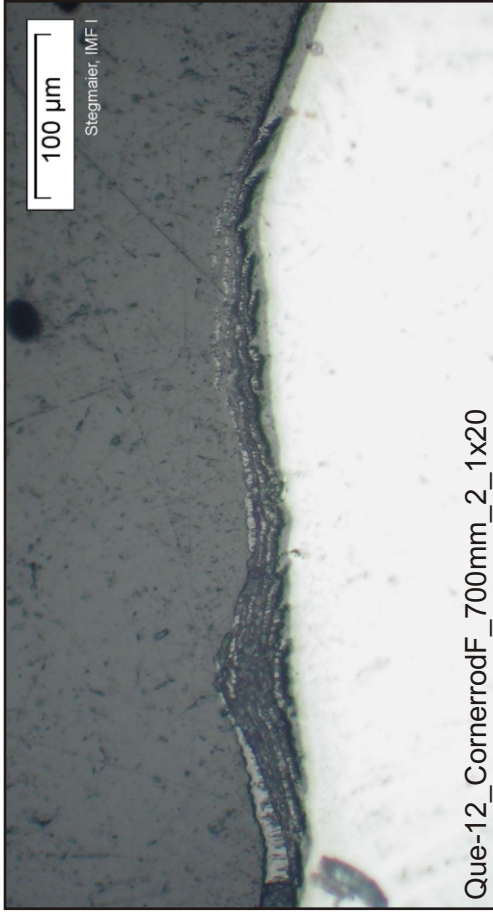
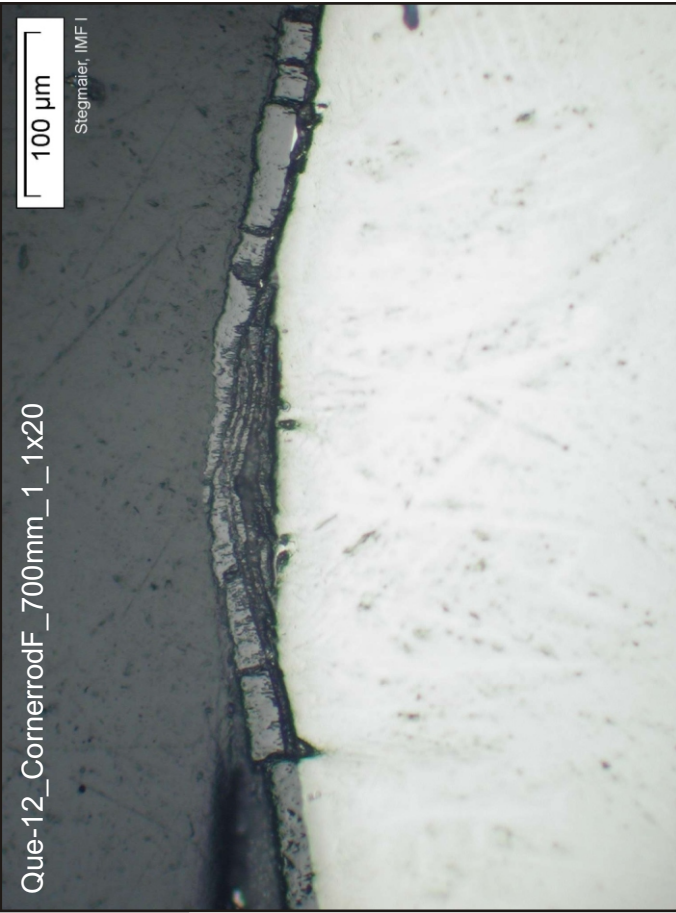
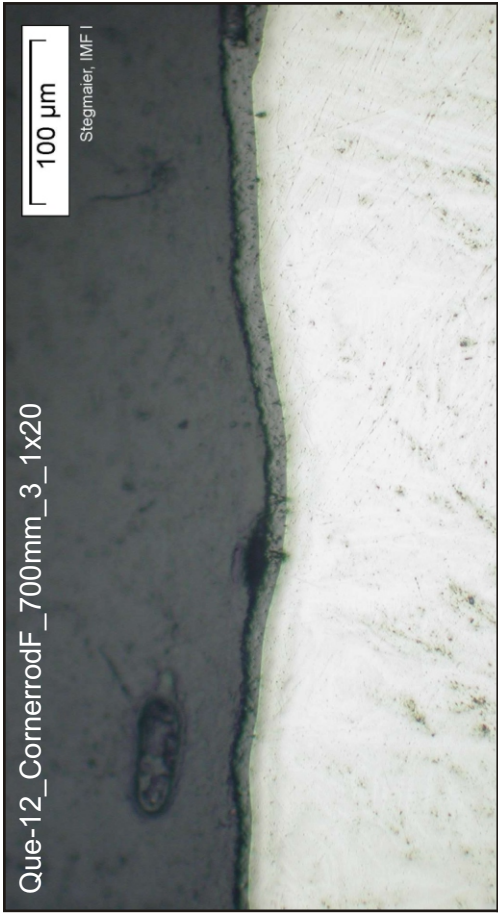


Fig. 117: QUE-12, level 940 mm; oxidation of withdrawn corner rod D, representing the end of the pre-oxidation phase.



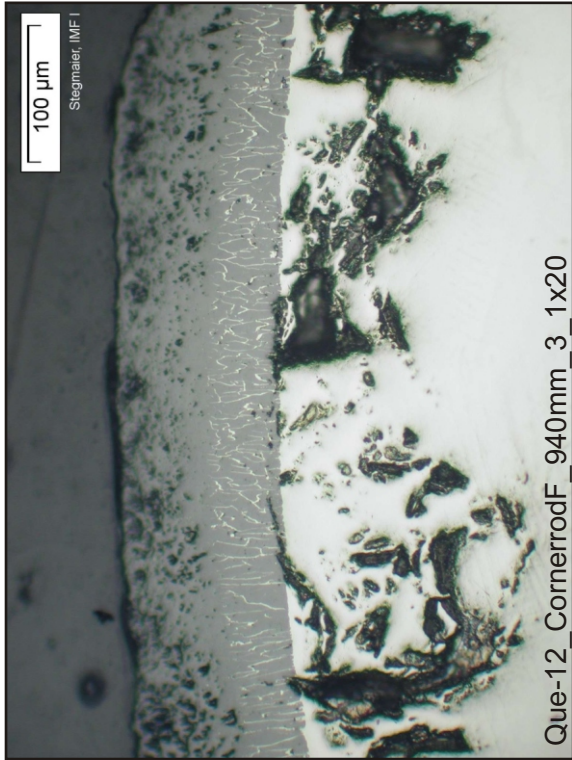
Side view of corner rod D around 1120 mm

Fig. 118: QUE-12, level 1120 mm; oxidation of withdrawn corner rod D, representing the end of the pre-oxidation phase.



Side views
of corner rod F
around 700 mm

Fig. 119: QUE-12, level 700 mm; oxidation of withdrawn corner rod F, representing the state just before quenching.



Side view of corner rod F
around 940 mm

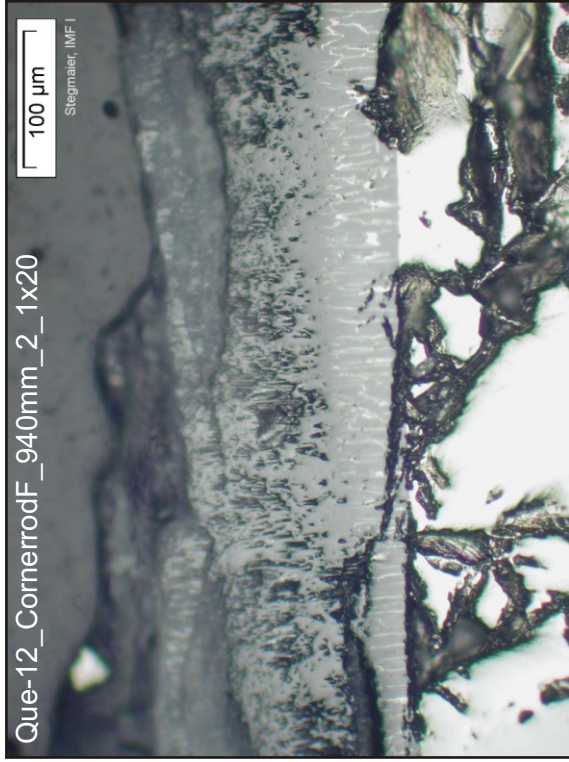
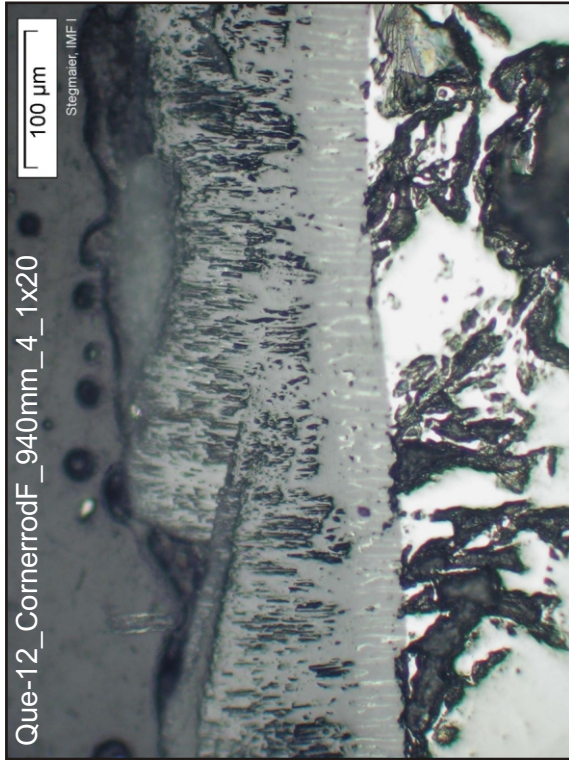
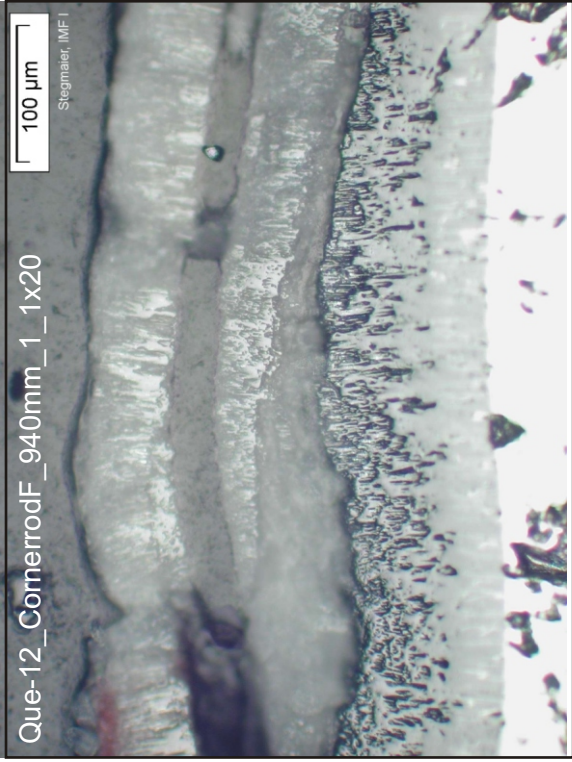
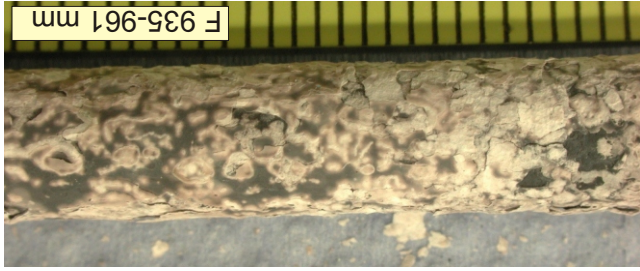
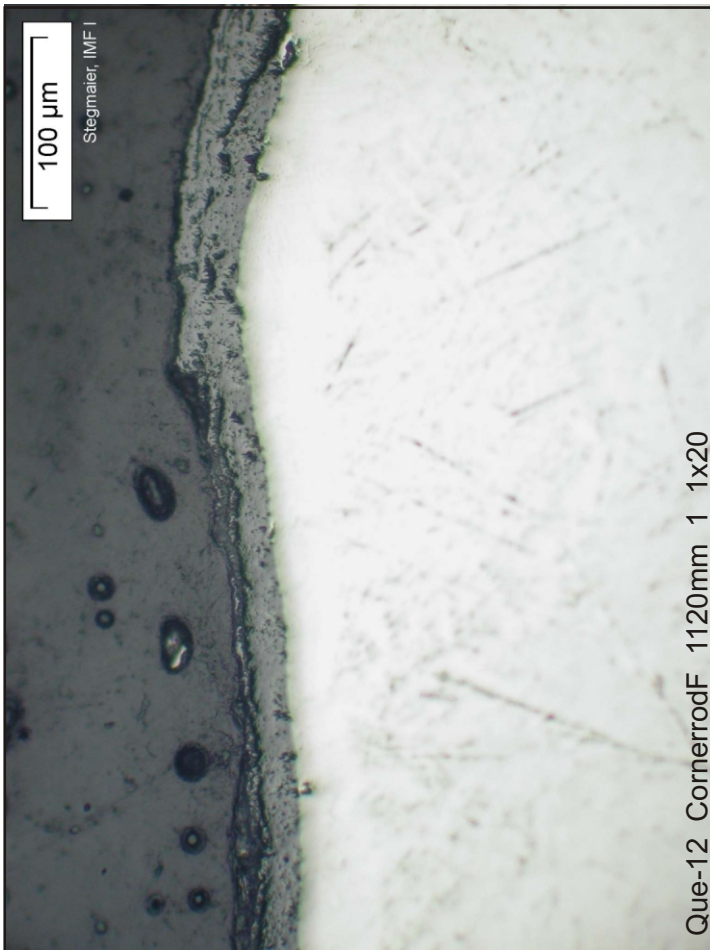


Fig. 120: QUE-12, level 940 mm; oxidation of withdrawn corner rod F, representing the state just before quenching.



Side view of corner rod F around 1120 mm



Side view of corner rod F around 1120 mm

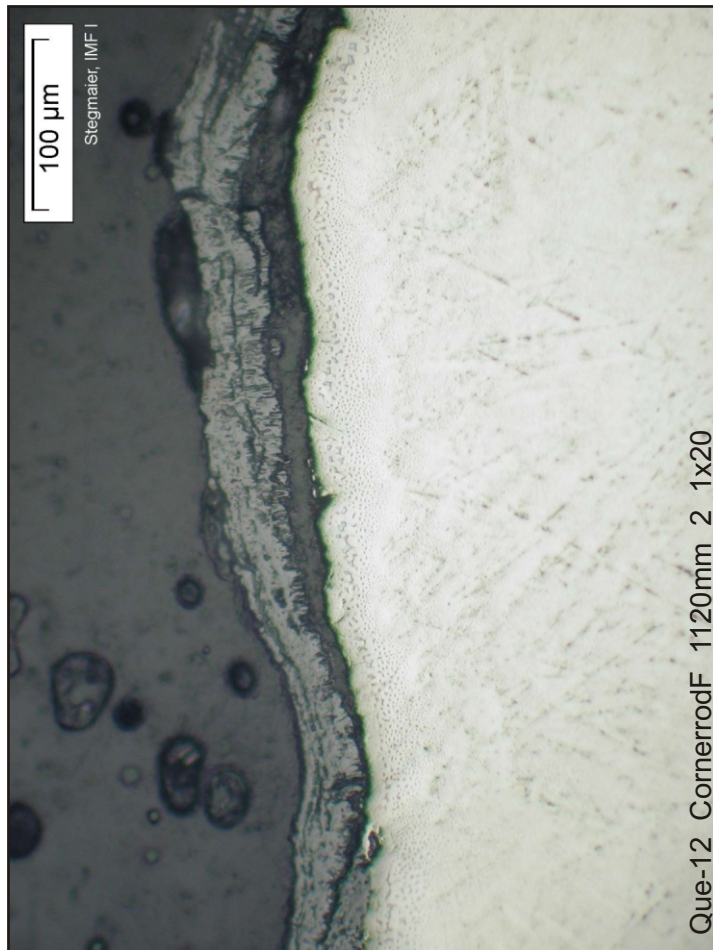
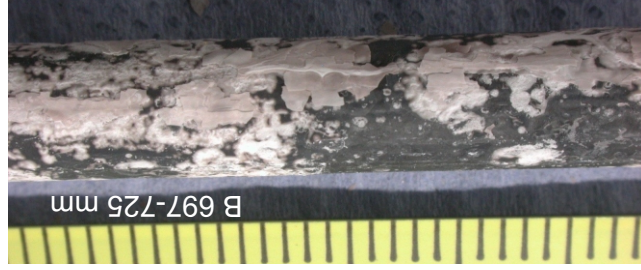
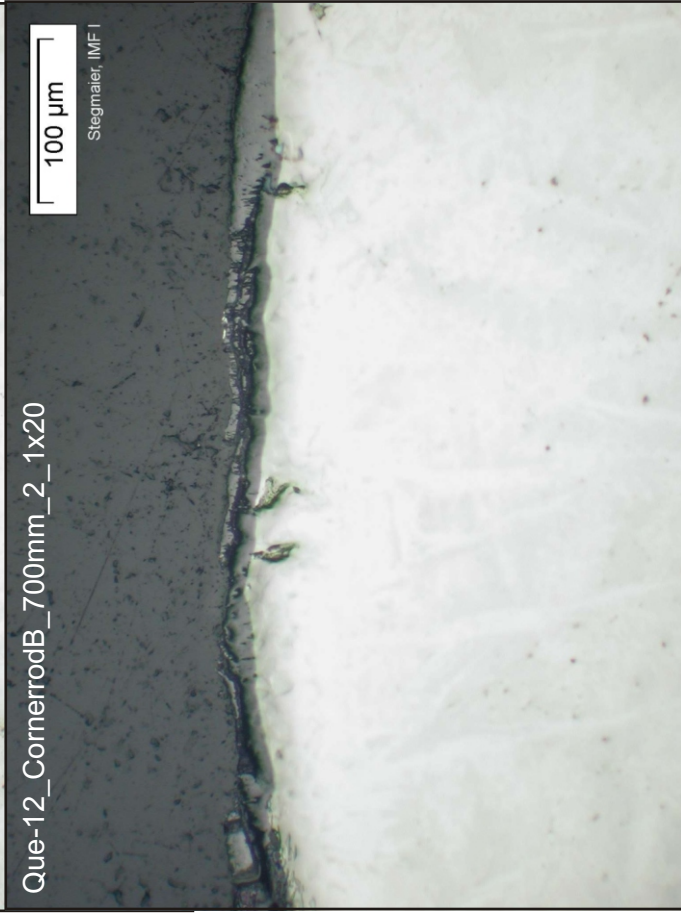
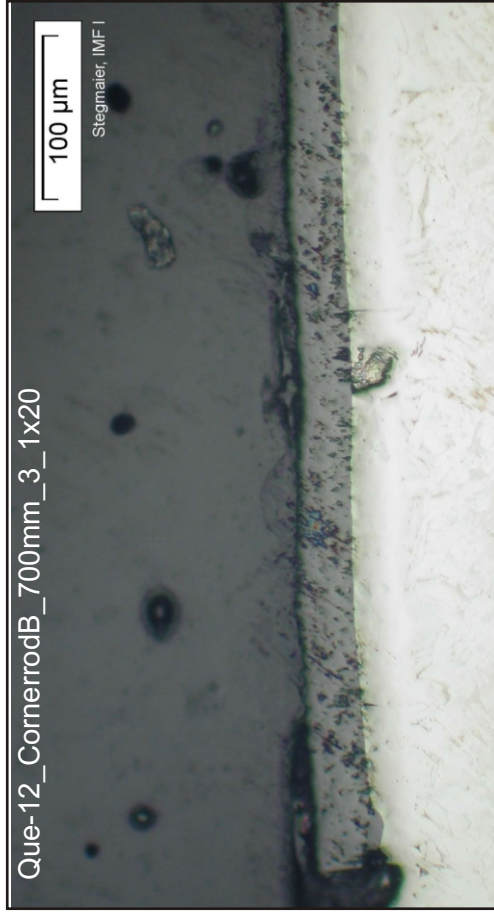
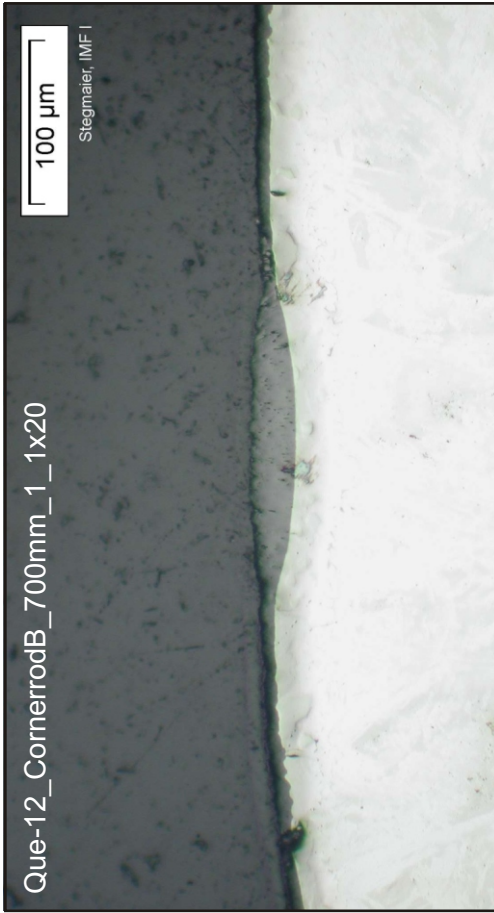
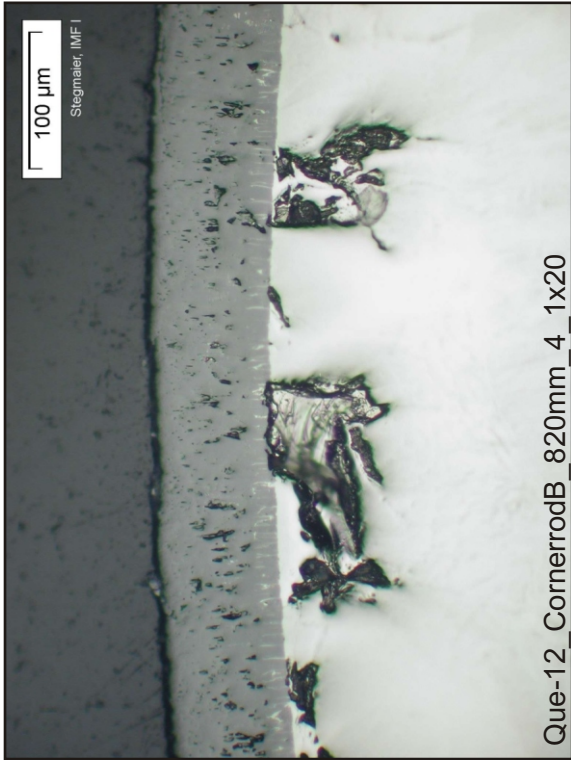


Fig. 121: QUE-12, level 1120 mm; oxidation of withdrawn corner rod F, representing the state just before quenching.



Side views
of corner rod B
around 700 mm

Fig. 122: QUE-12, level 700 mm; oxidation of withdrawn corner rod B, representing the whole test exposure.



Side view of corner rod B
around 820 mm

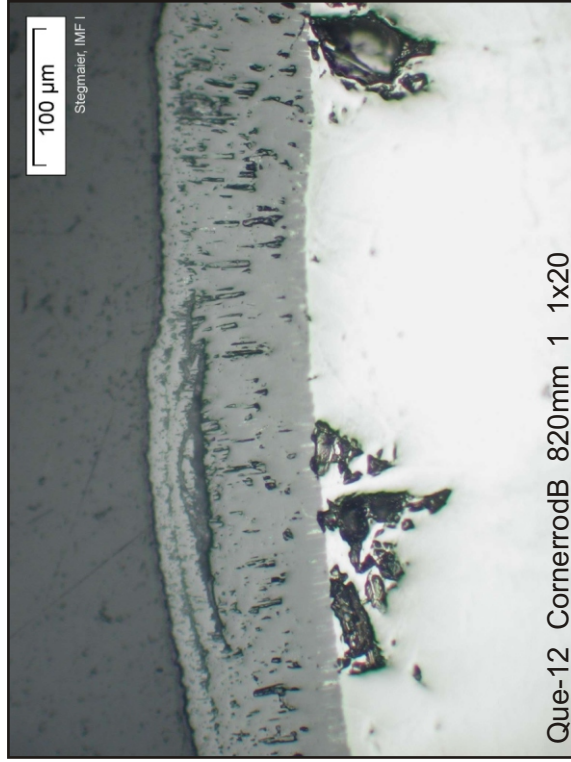
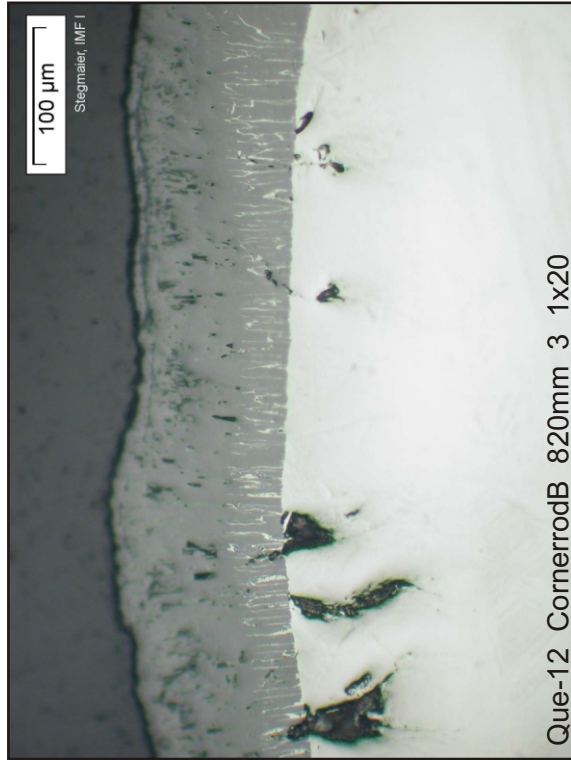
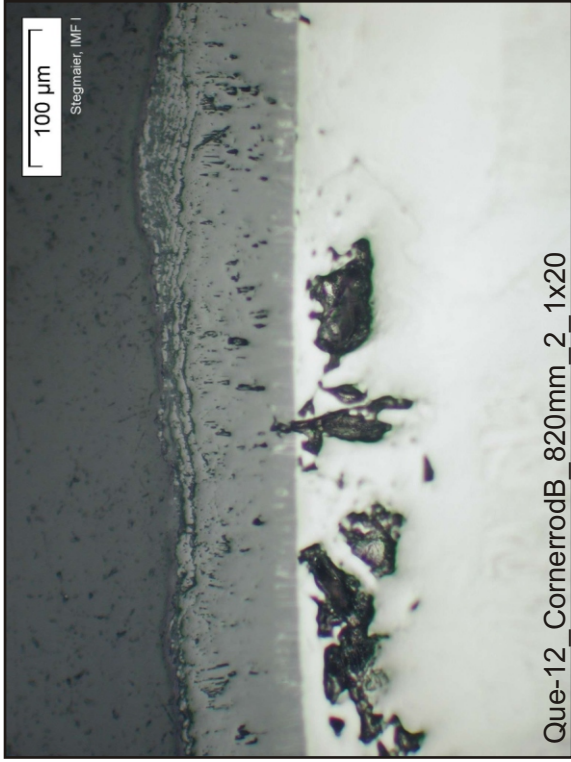
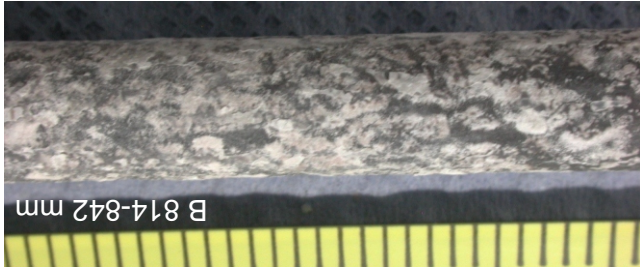


Fig. 123: QUE-12, level 820 mm; oxidation of withdrawn corner rod B, representing the whole test exposure.

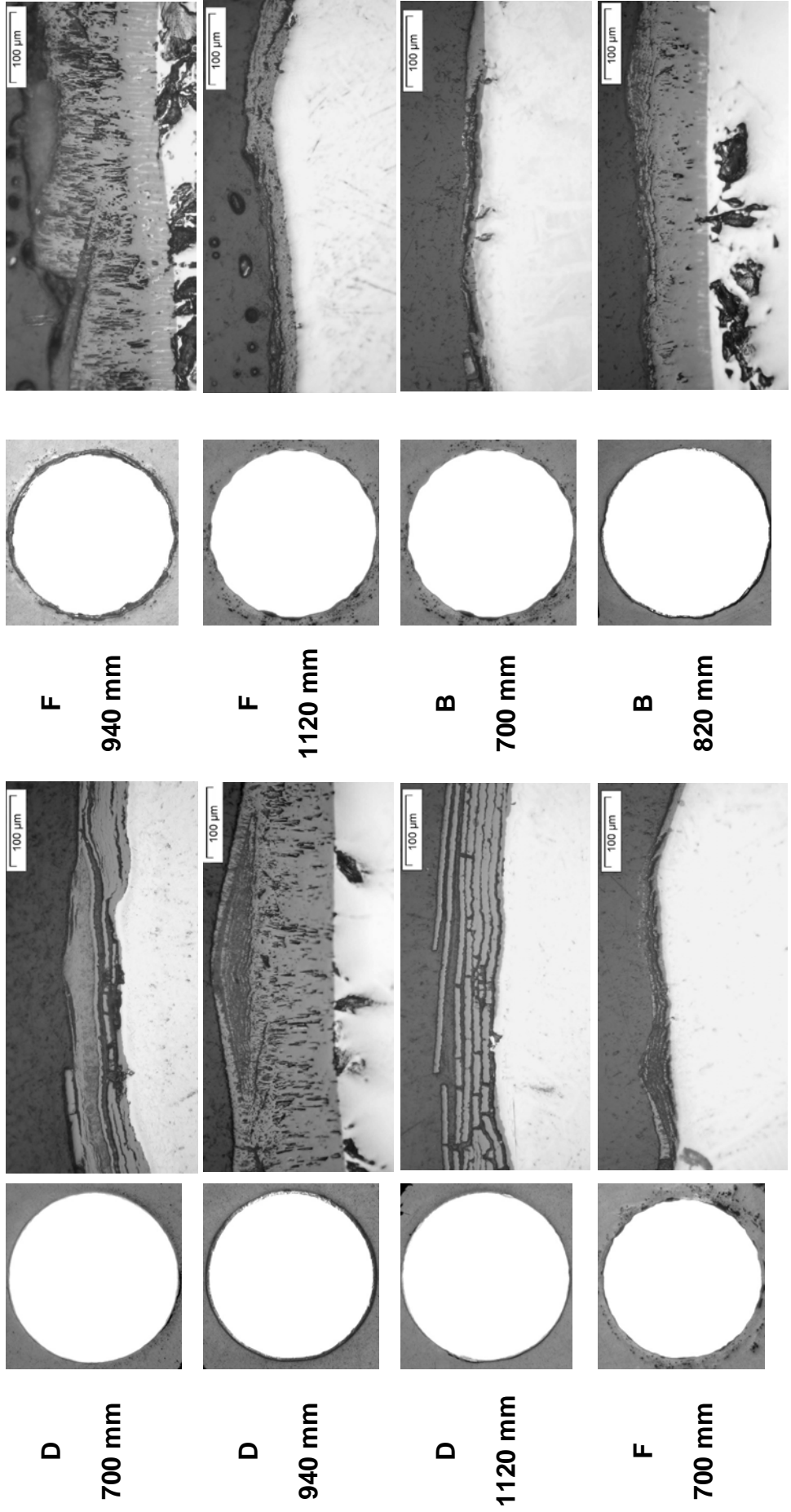


Fig. 124-QUE12-oxid layer.doc
16.06.08 – IMF

Fig. 124: QUENCH-12; Structure of the residual oxide layer on the surface of three withdrawn corner rods at different bundle elevations. Breakaway structure was formed generally during pre-oxidation by temperatures about: 850°C (at 700 mm), 1100°C (at 940 mm), 900°C (at 1120 mm).

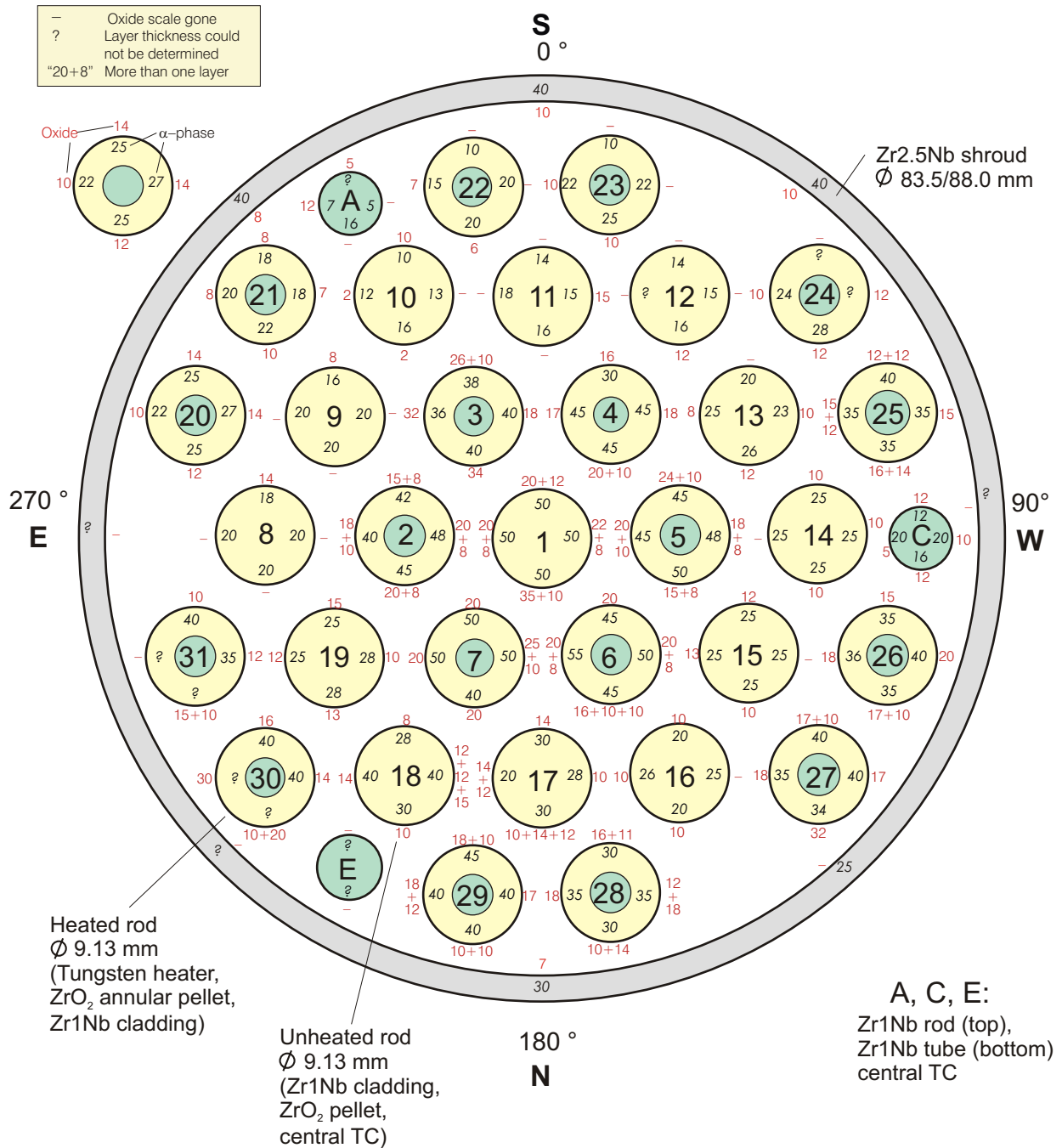


Fig. 125-QUE12 cross section 12-01.cdr
08.07.08 - IMF

Fig. 125: QUENCH-12; Oxide and α -layer thickness at bundle elevation 550 mm (Cross section QUE-12-01).

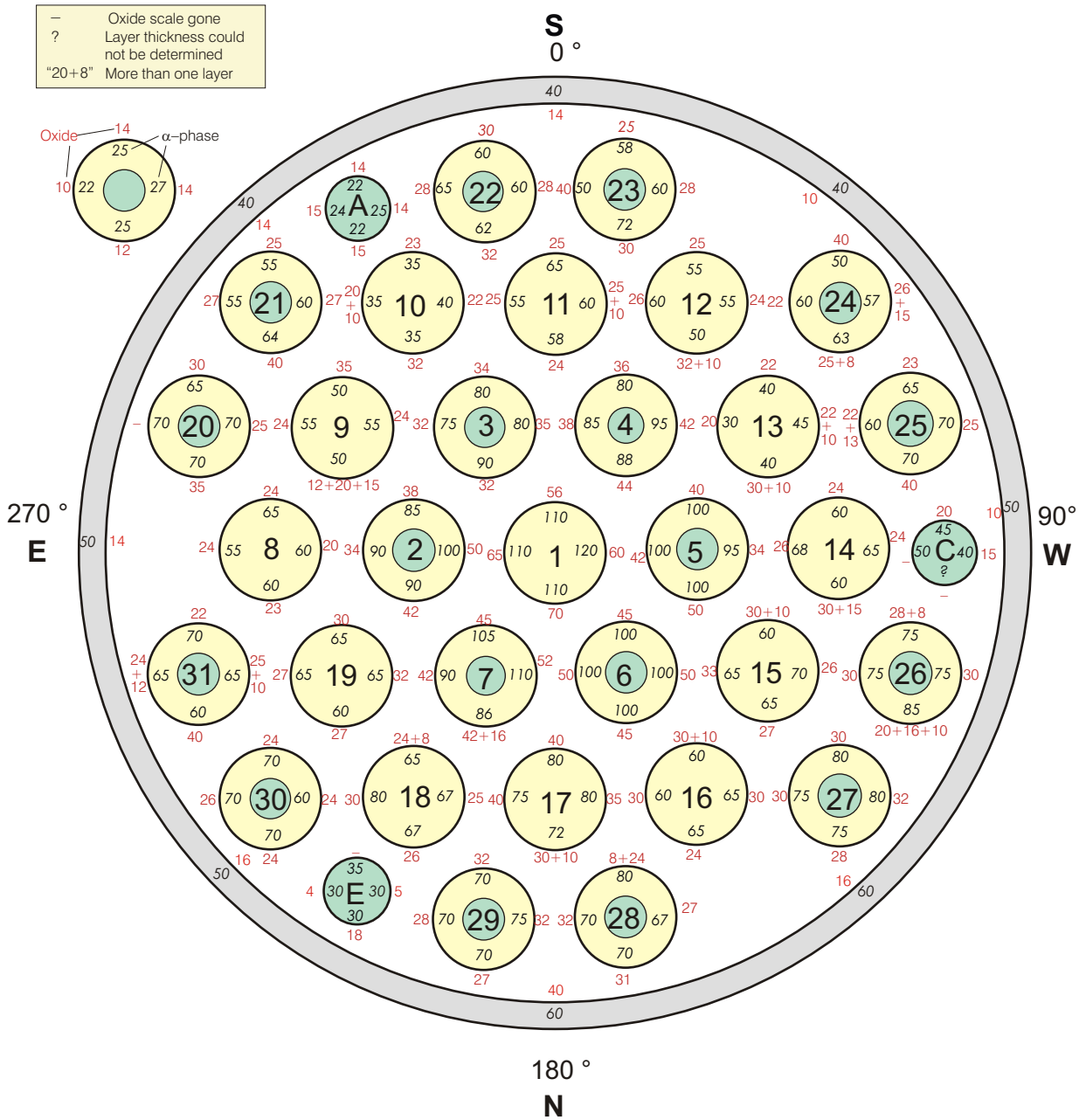


Fig. 126-QUE12 cross section 12-03.cdr
 08.07.08 - IMF

Fig. 126: QUENCH-12; Oxide and α -layer thickness at bundle elevation 650 mm (Cross section QUE-12-03).

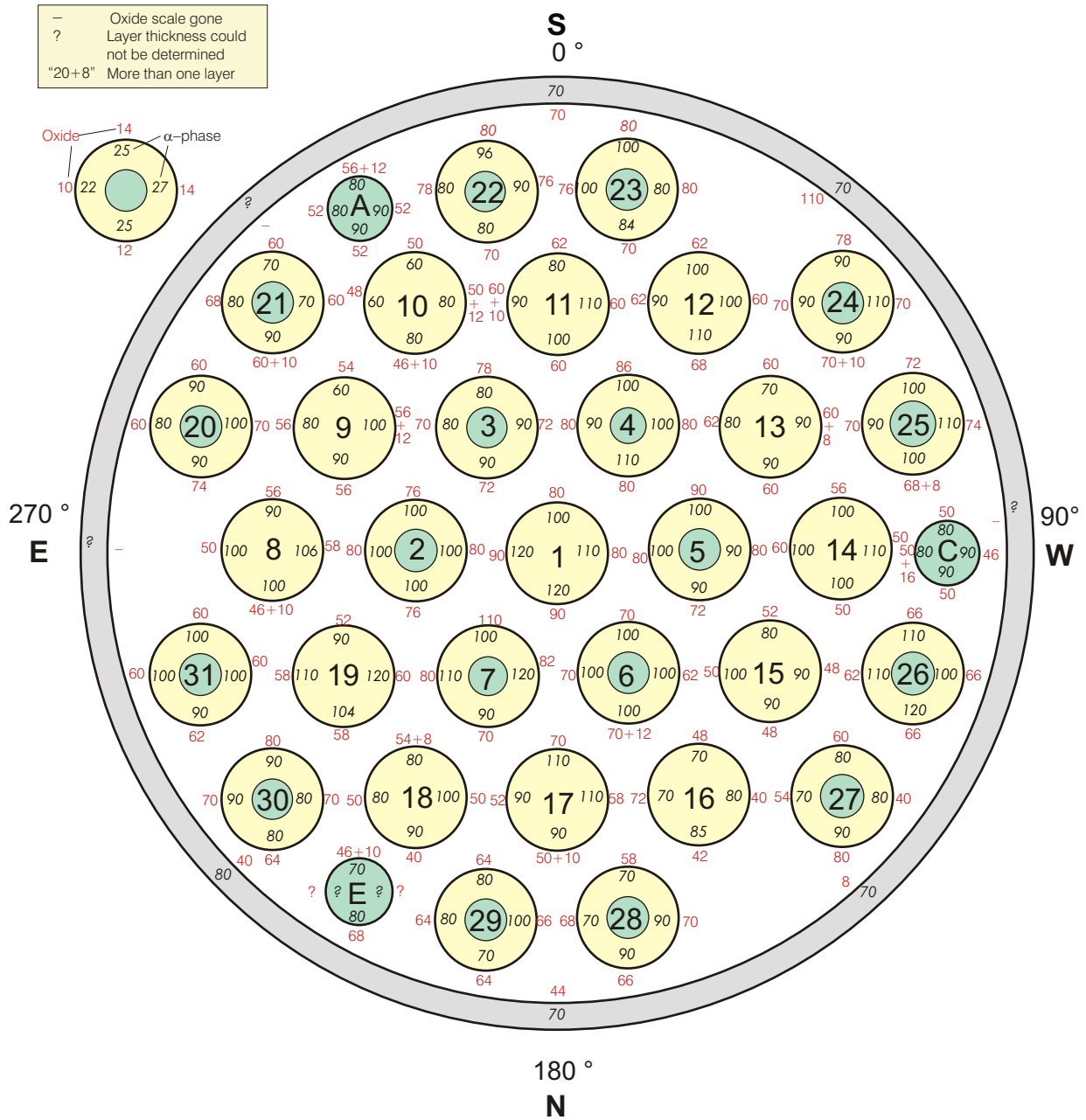


Fig. 127-QUE12 cross section 12-05.cdr
08.07.08 - IMF

Fig. 127: QUENCH-12; Oxide and α -layer thickness at bundle elevation 750 mm (Cross section QUE-12-05).

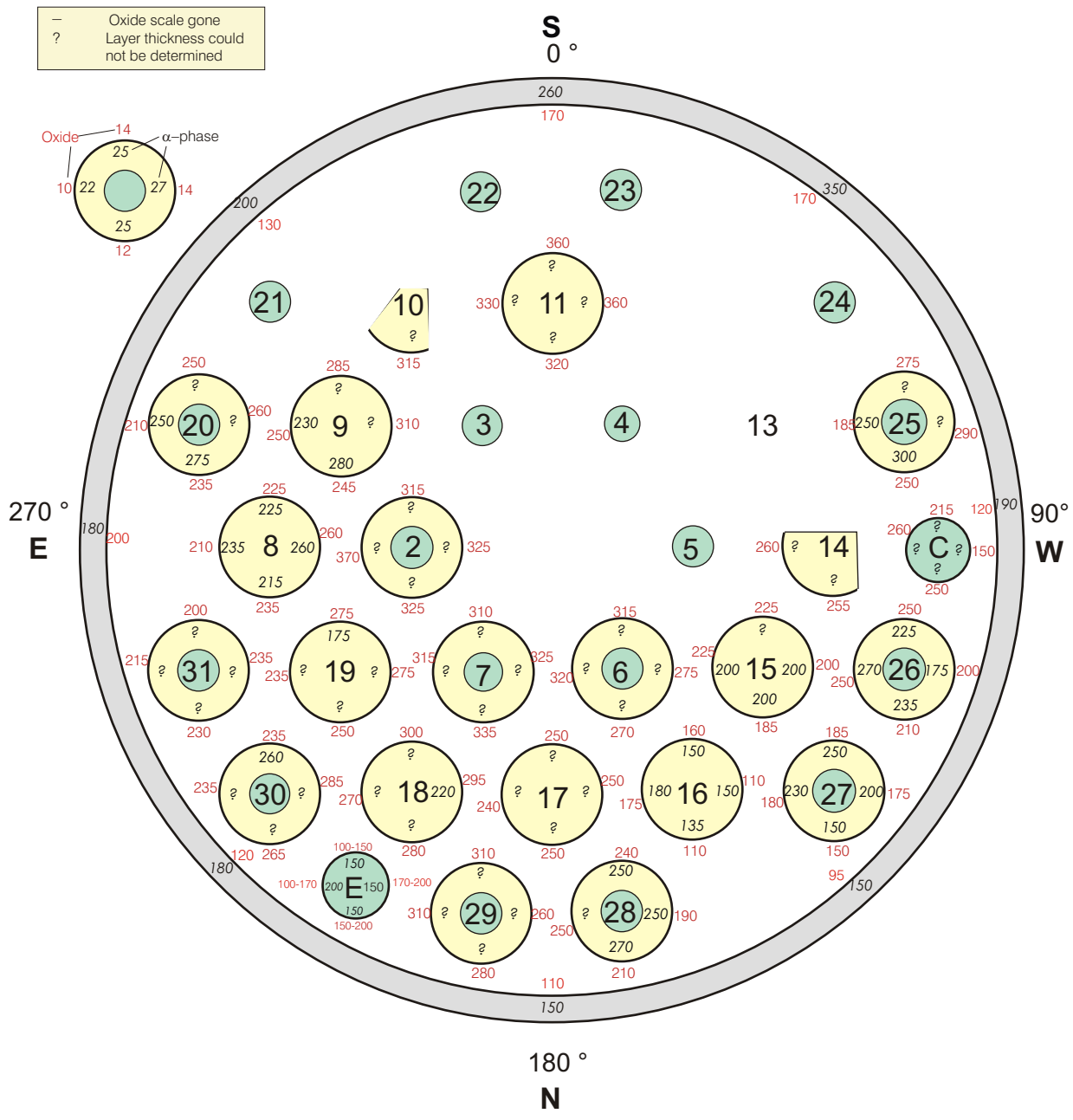


Fig. 128-QUE12 cross section 12-07.cdr
08.07.08 - IMF

Fig. 128: QUENCH-12; Oxide and α -layer thickness at bundle elevation 850 mm (Cross section QUE-12-07).

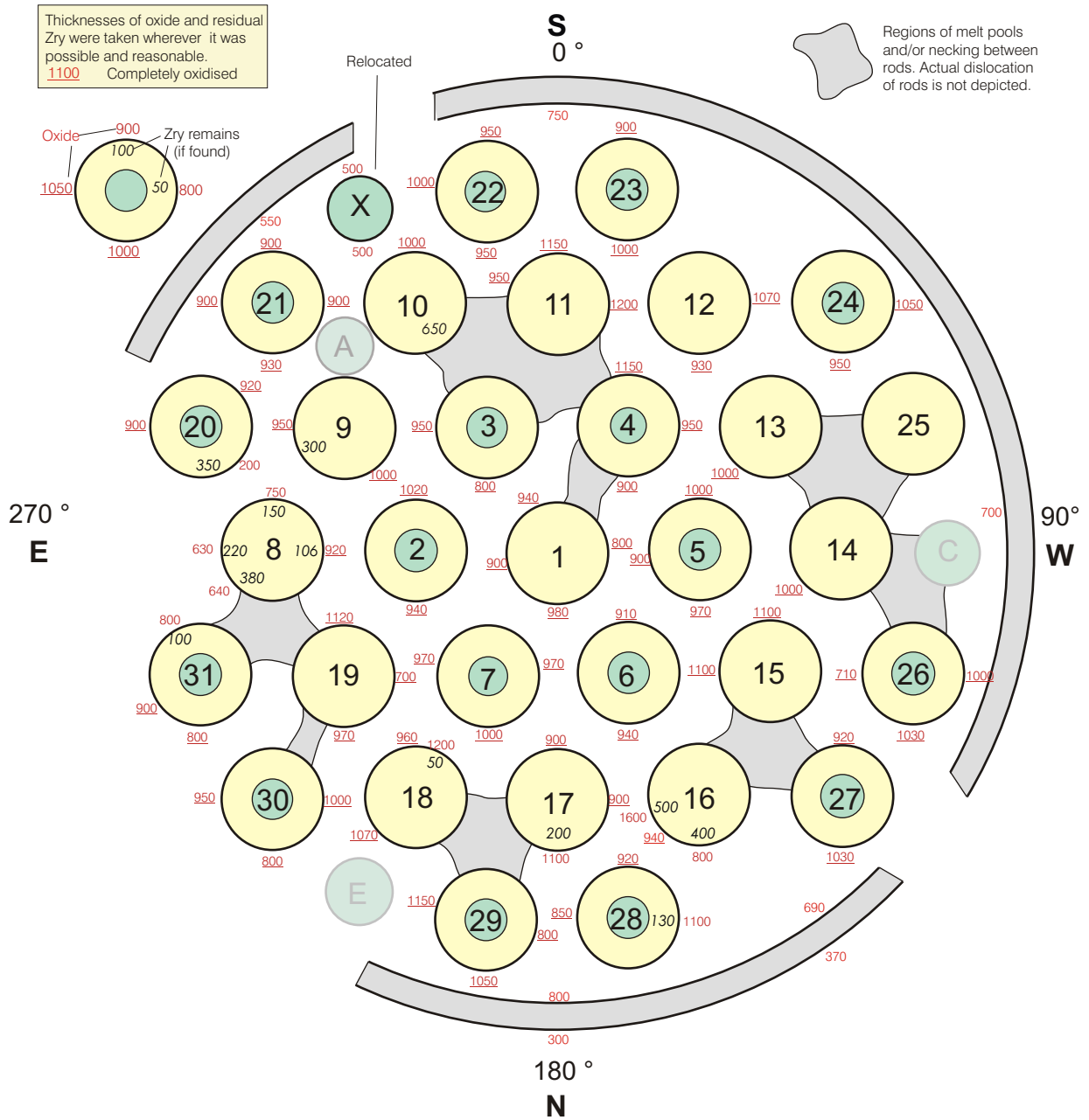


Fig. 129-QUE12 cross section 12-09.cdr
 08.07.08 - IMF

Fig. 129: QUENCH-12; Oxide and metal layer thickness at bundle elevation 950 mm (Cross section QUE-12-09).

— Scale gone
 ? Layer thickness could not be determined

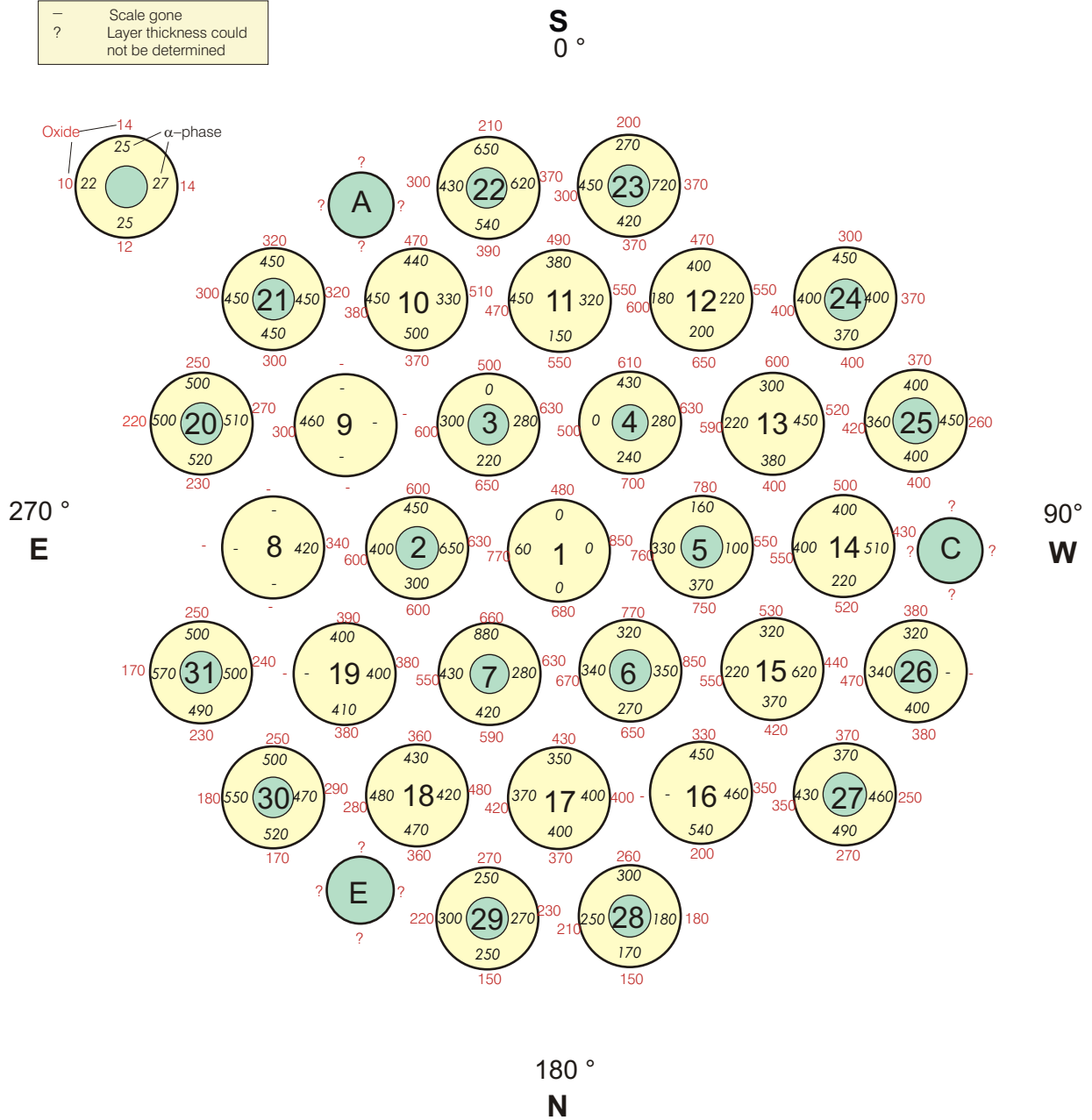


Fig. 130-QUE12 cross section 12-12.cdr
 08.07.08 - IMF

Fig. 130: QUENCH-12; Oxide and α -layer thickness at bundle elevation 1050 mm (Cross section QUE-12-12).

— Oxide scale gone
 ? Layer thickness could not be determined

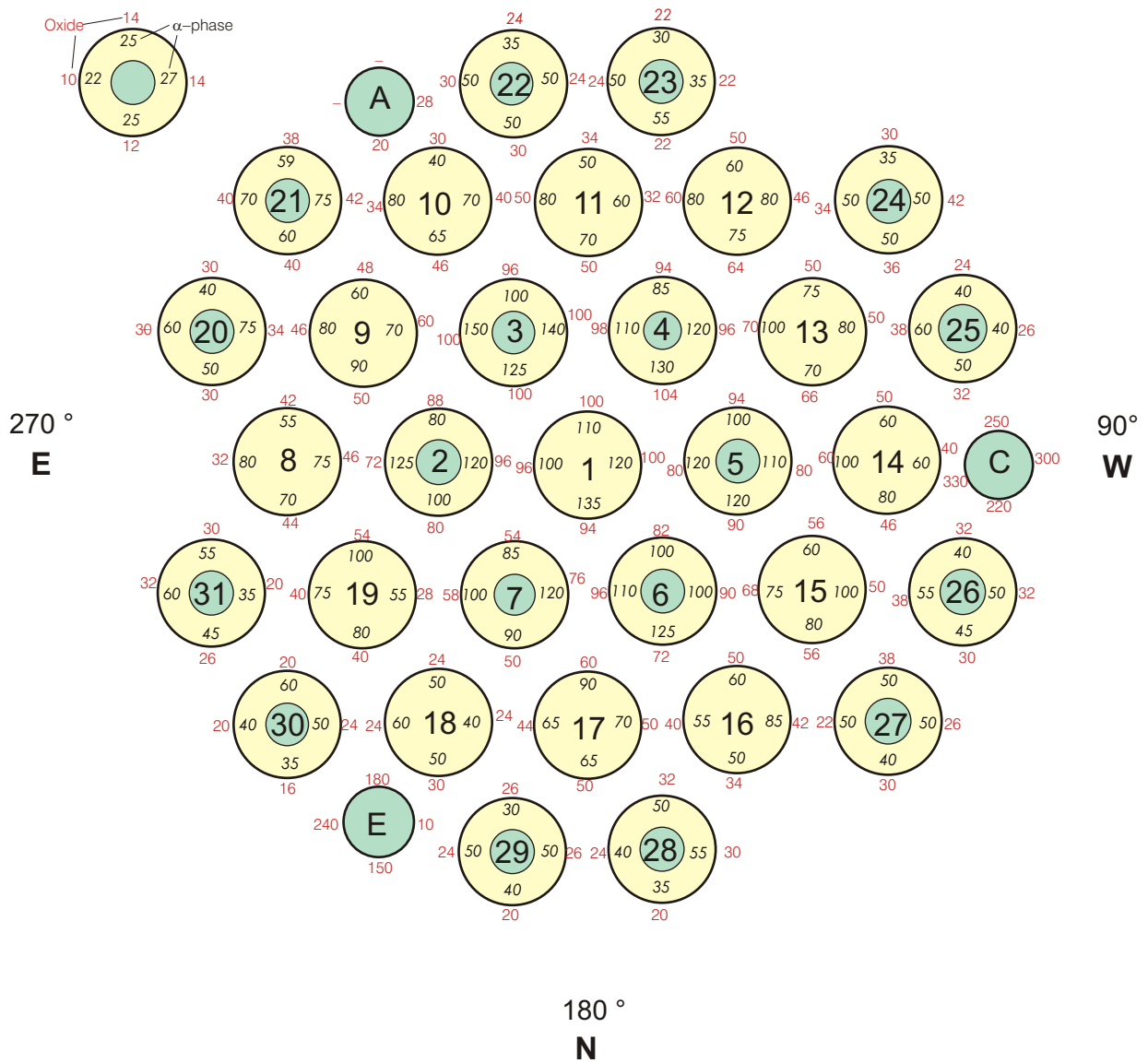


Fig. 131-QUE12 cross section 12-11.cdr
 08.07.08 - IMF

Fig. 131: QUENCH-12; Oxide and α -layer thickness at bundle elevation 1150 mm (Cross section QUE-12-11).

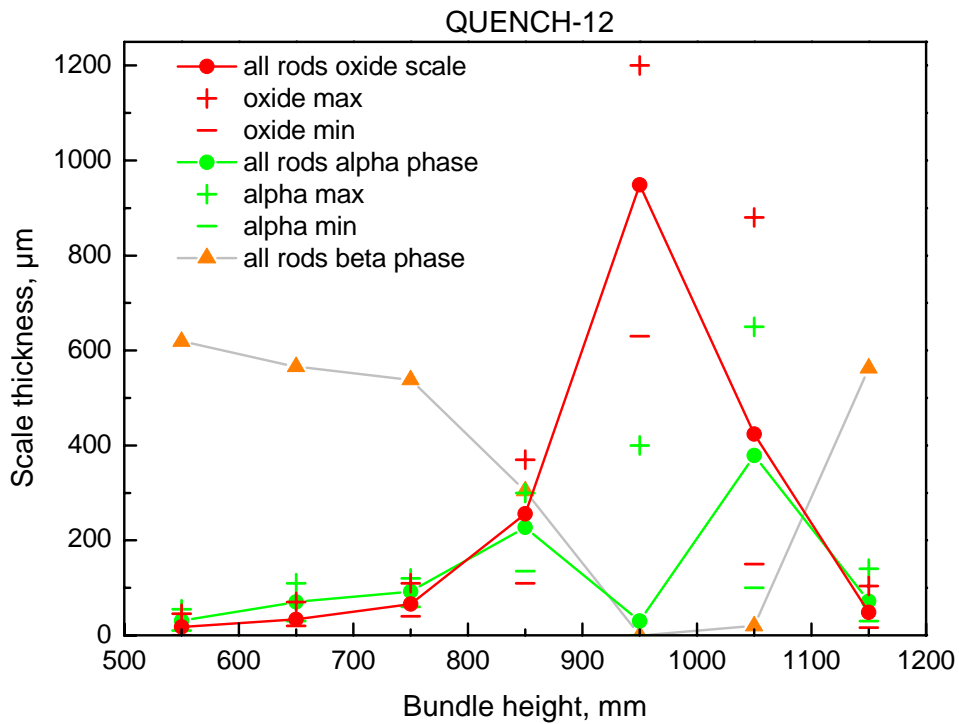
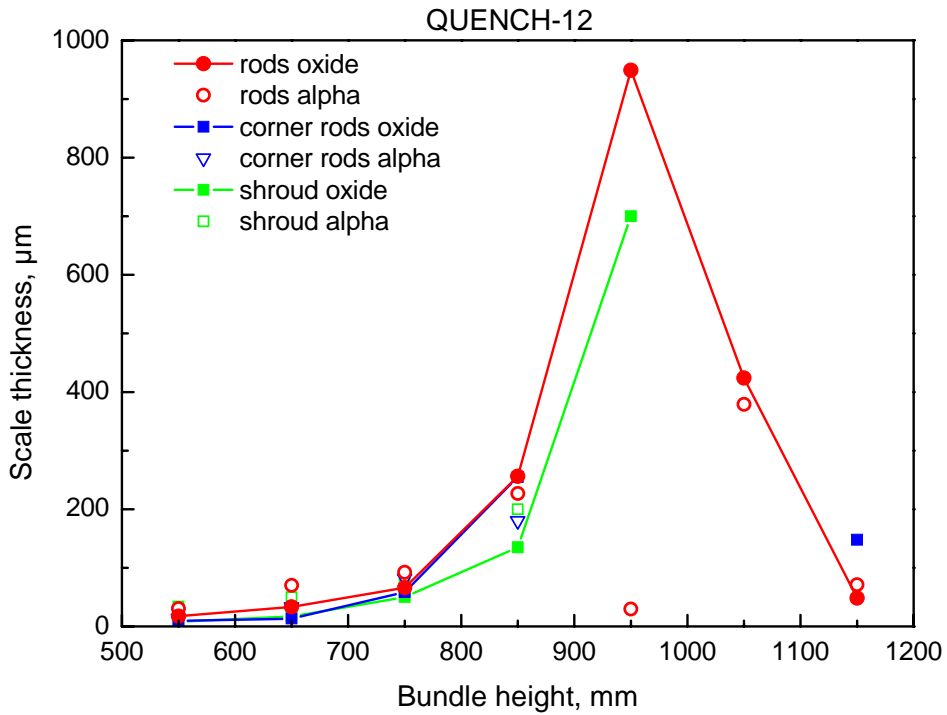


Fig. 132: QUENCH-12; Measured axial layer profiles, bundle, top, rod simulators, bottom.

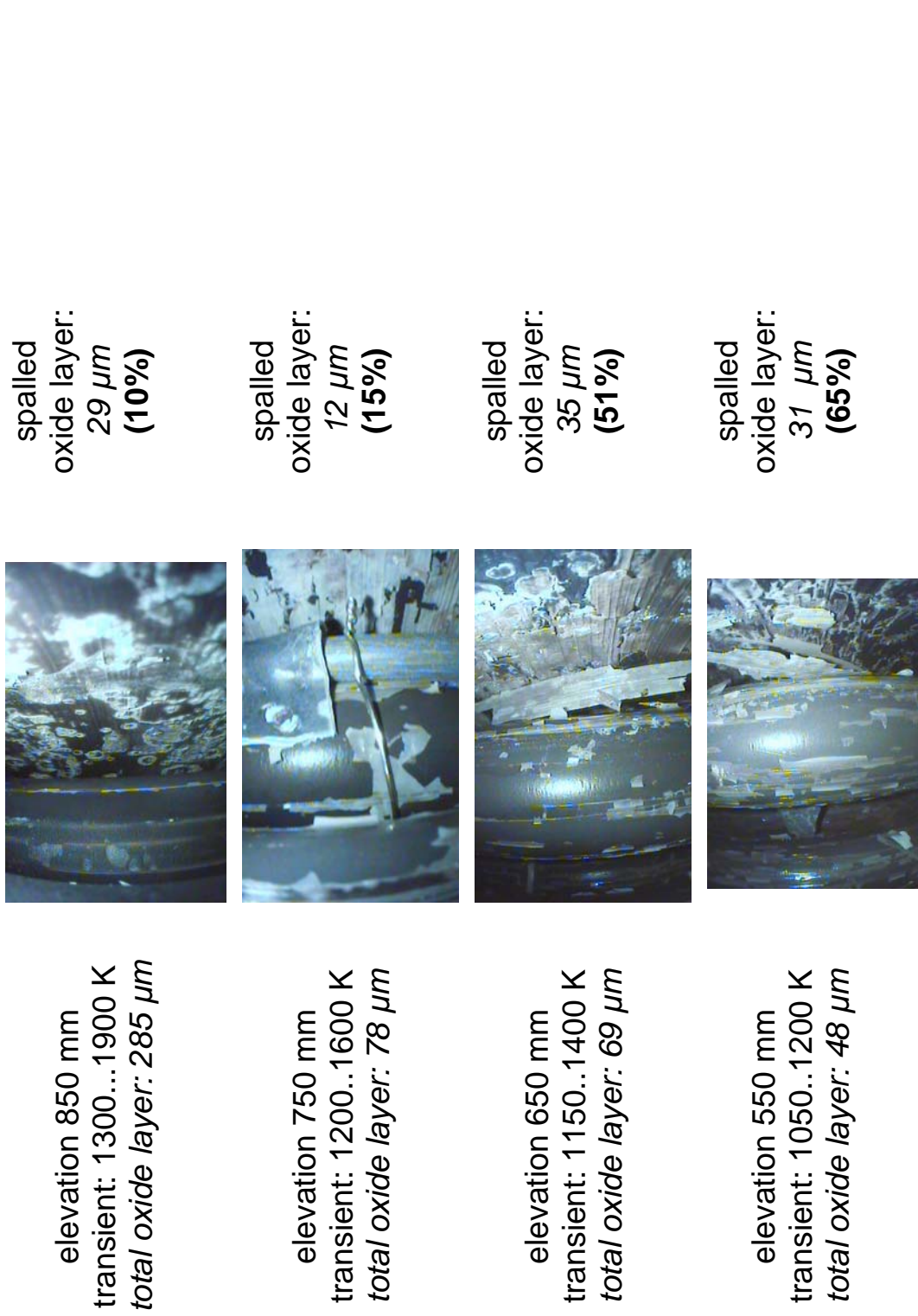


Fig. 133: QUENCH-12; degree of cladding oxide layer spalling for different bundle elevations, total oxide layer calculated on the base of residual metal.

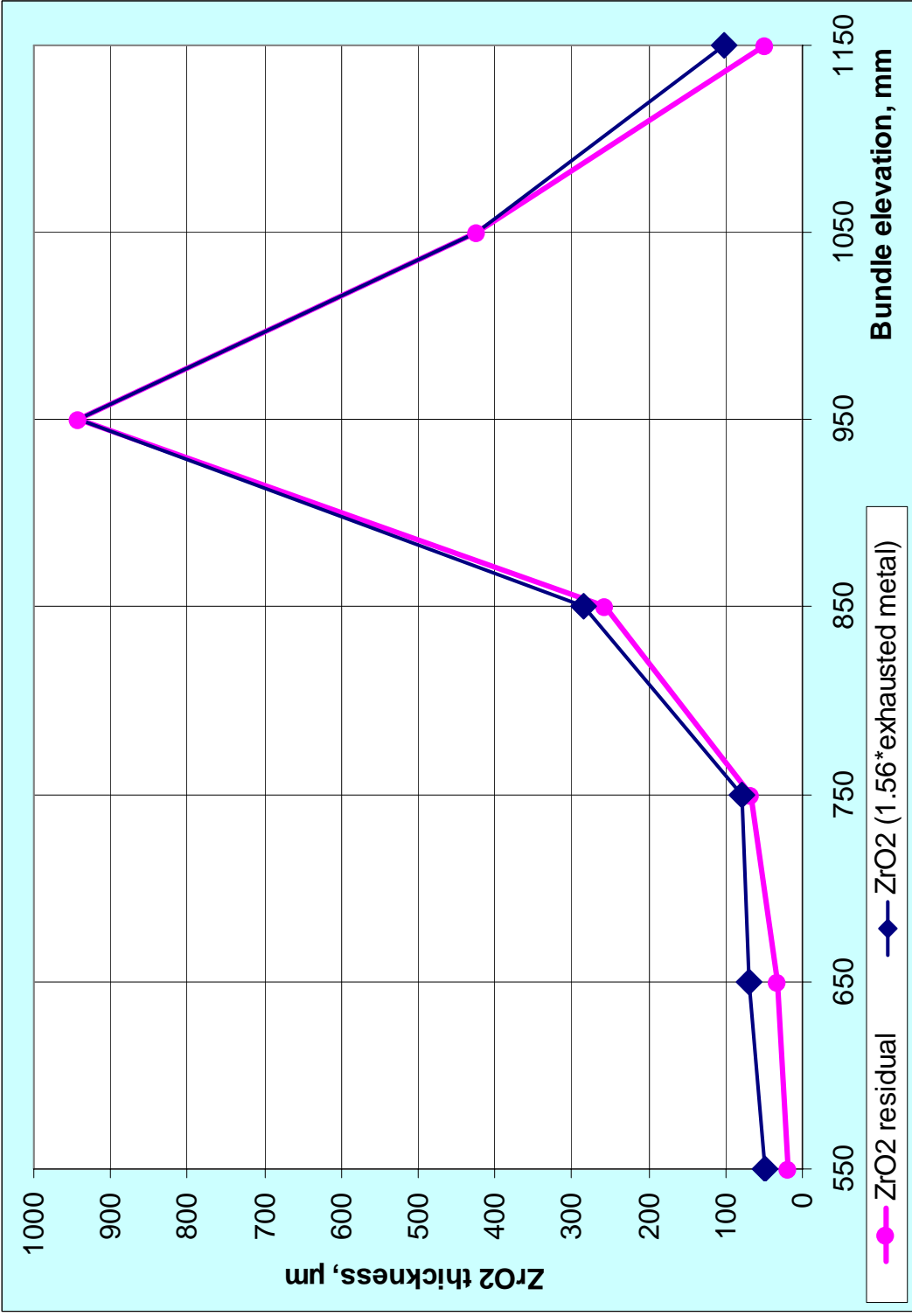
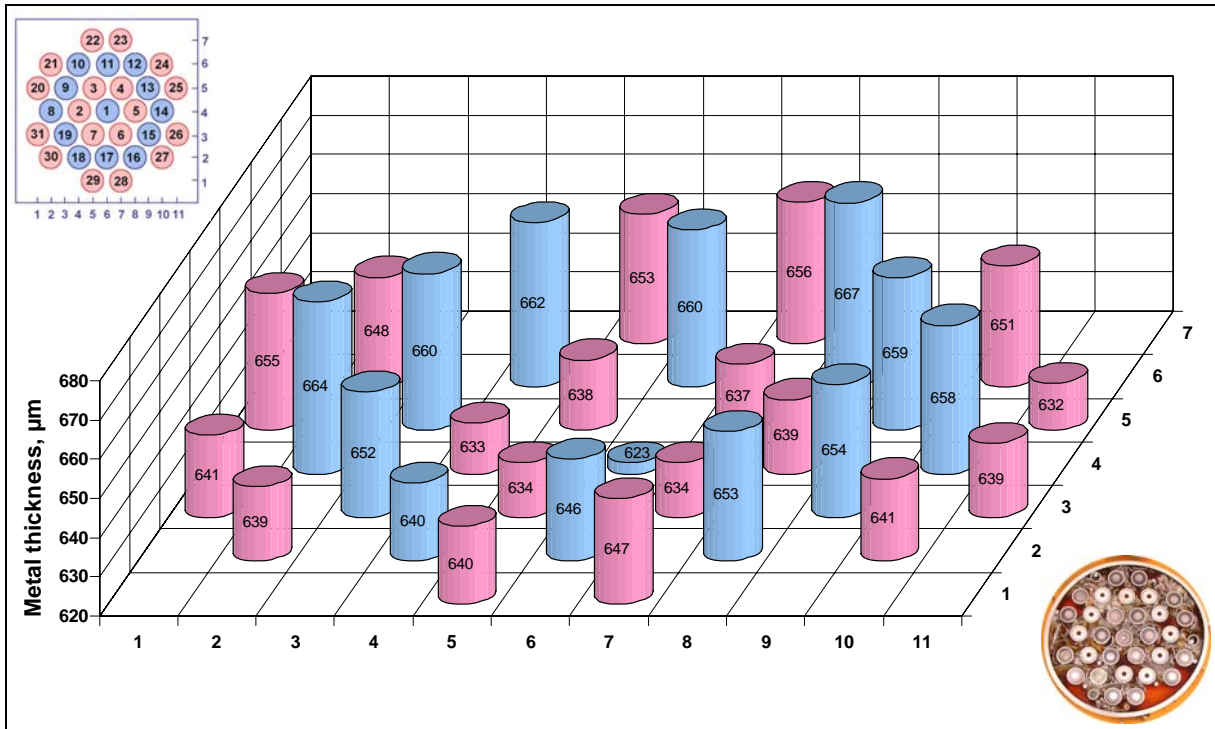
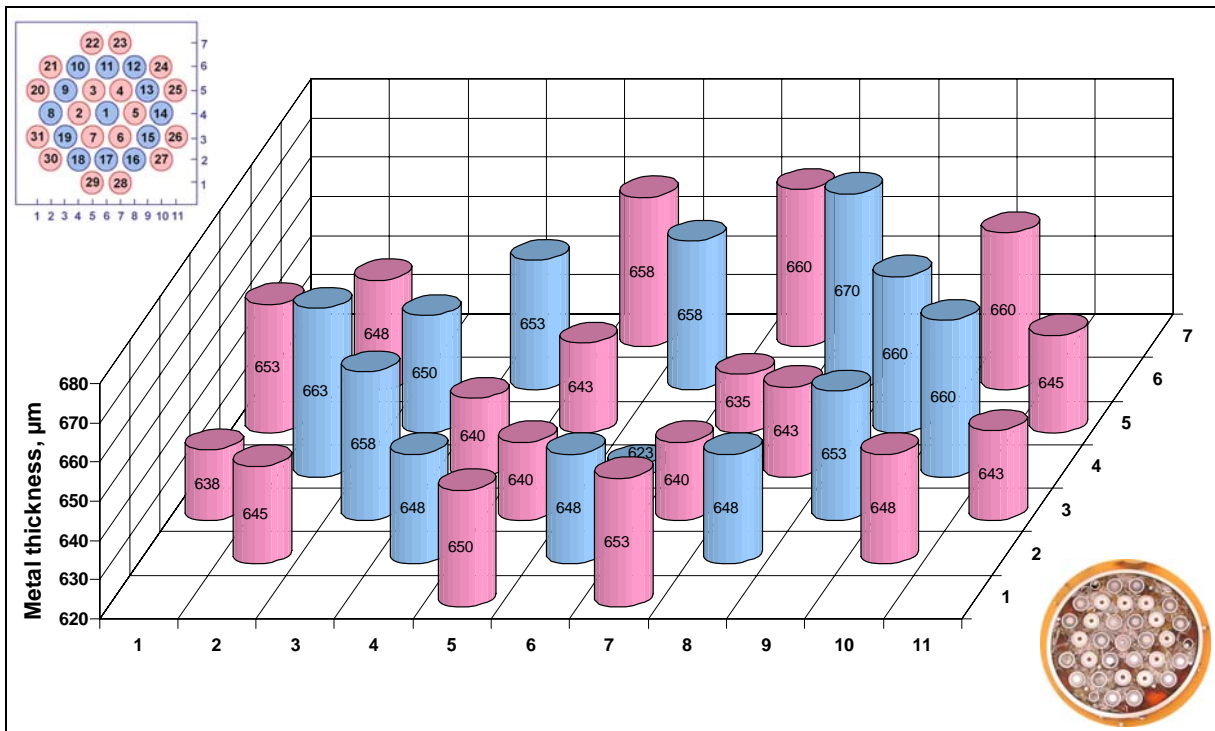


Fig. 134: QUENCH-12; Posttest axial distribution of the oxide layer of the cladding tube surfaces.

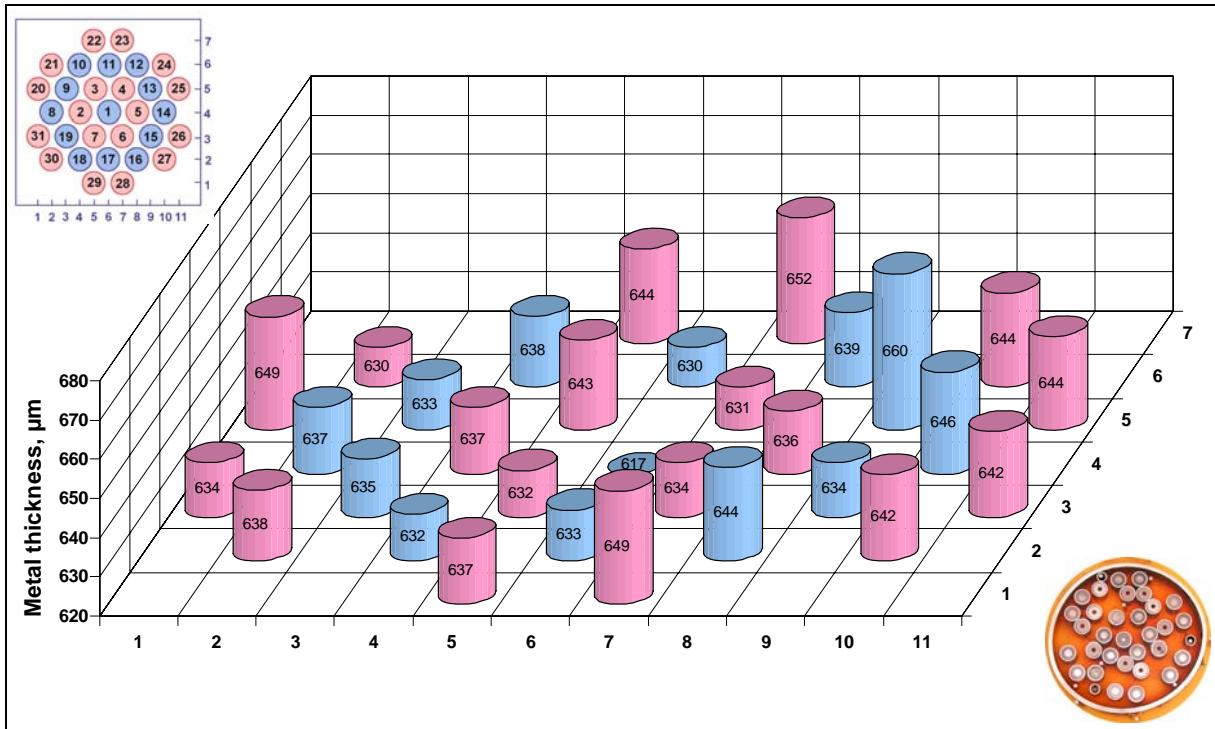


RIAR measurements at cross-section 554 mm.
 Average value and median deviation: $654 \pm 8 \mu\text{m}$ for unheated rods,
 $642 \pm 6 \mu\text{m}$ for heated rods.

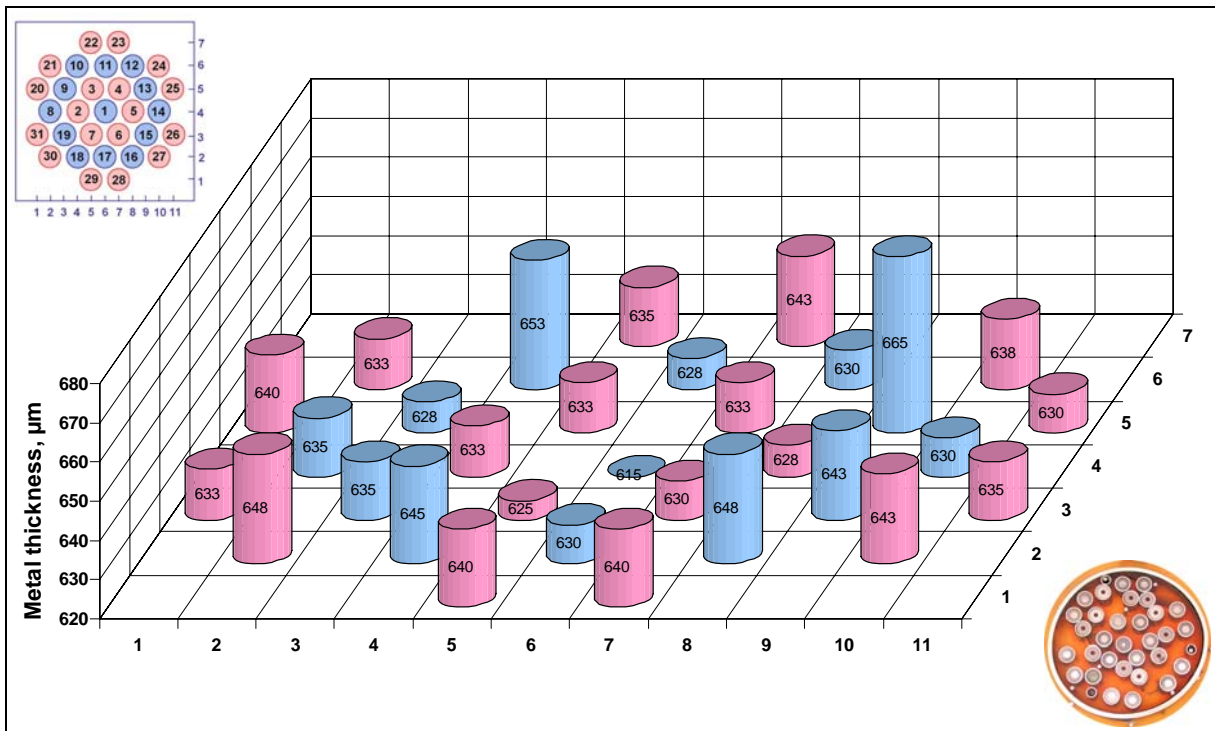


FZK measurements at cross-section 550 mm.
 Average value and median deviation: $653 \pm 8 \mu\text{m}$ for unheated rods,
 $647 \pm 6 \mu\text{m}$ for heated rods.

Fig. 135: QUENCH-12; Results of metallographical examination of residual cladding metal thickness at bundle elevation 550 mm.

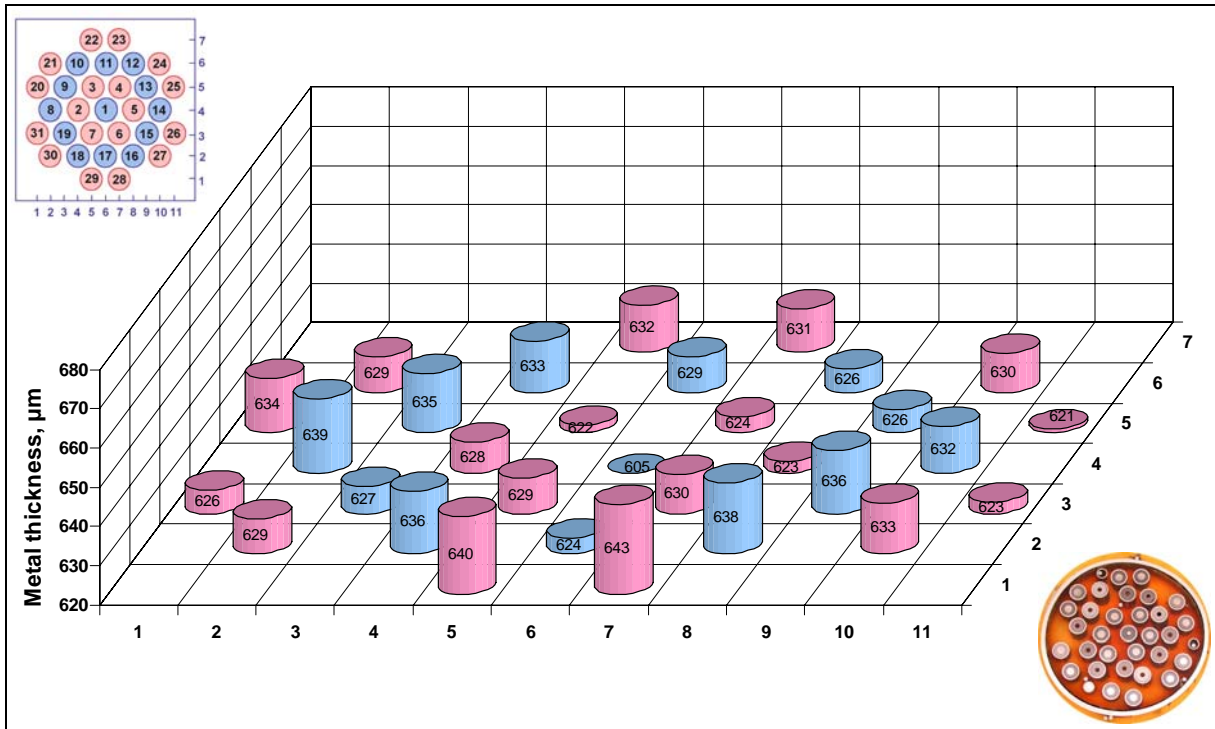


RIAR measurements at cross-section 654 mm.
 Average value and median deviation: $637 \pm 7 \mu\text{m}$ for unheated rods,
 $640 \pm 6 \mu\text{m}$ for heated rods.



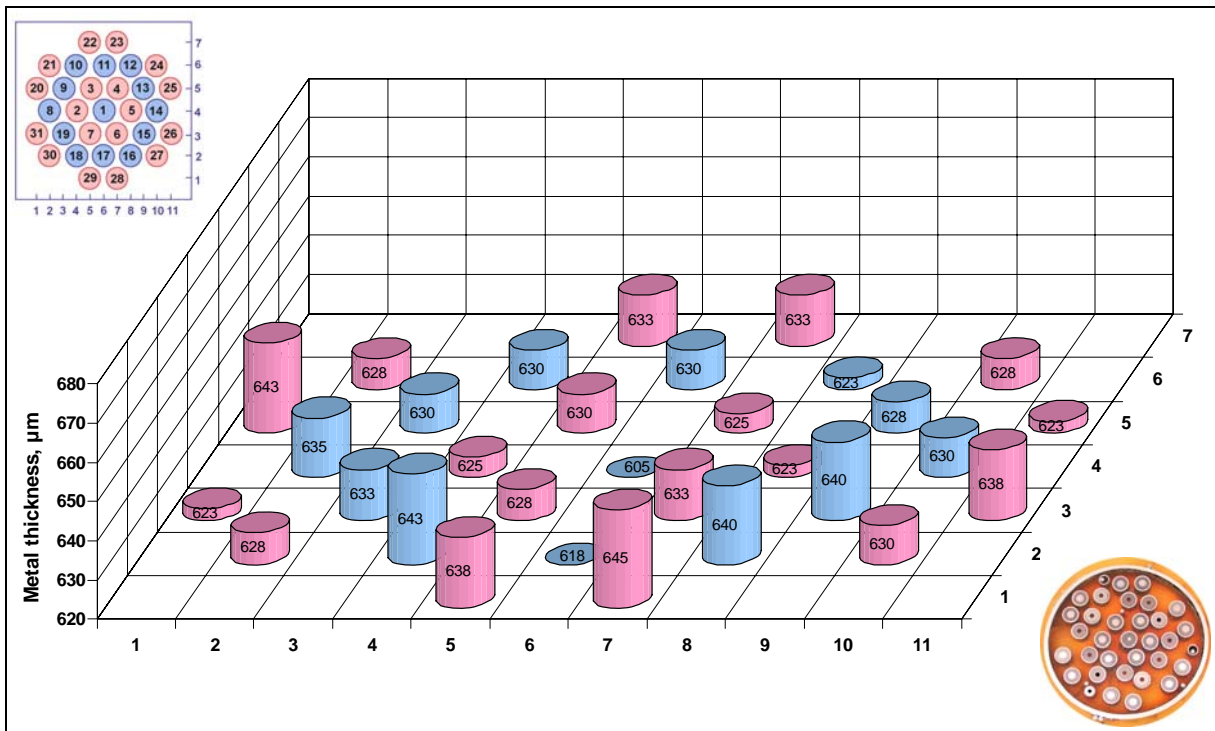
FZK measurements at cross-section 650 mm.
 Average value and median deviation: $637 \pm 10 \mu\text{m}$ for unheated rods,
 $636 \pm 5 \mu\text{m}$ for heated rods.

Fig. 136: QUENCH-12; Results of metallographical examination of residual cladding metal thickness at bundle elevation 650 mm.



RIAR measurements at cross-section 754 mm.

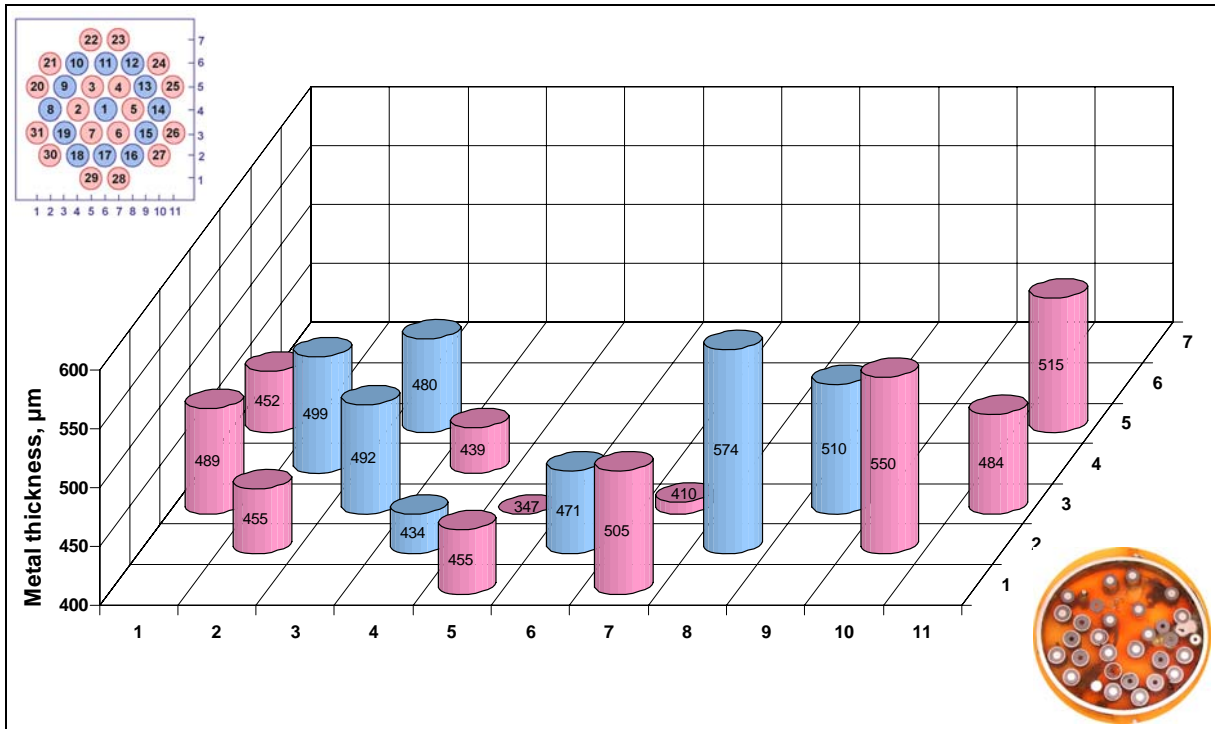
Average value and median deviation: **630 ± 6 µm** for unheated rods,
629 ± 4 µm for heated rods.



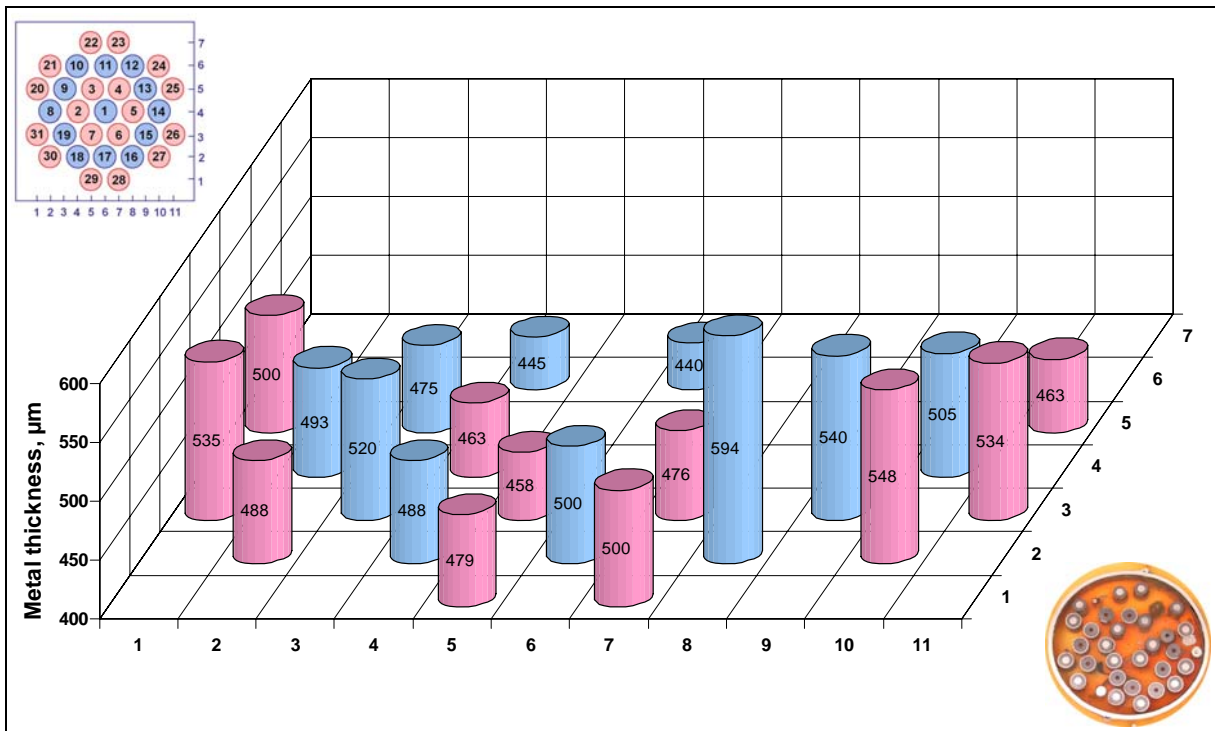
FZK measurements at cross-section 750 mm.

Average value and median deviation: **630 ± 7 µm** for unheated rods,
631 ± 5 µm for heated rods.

Fig. 137: QUENCH-12; Results of metallographical examination of residual cladding metal thickness at bundle elevation 750 mm.

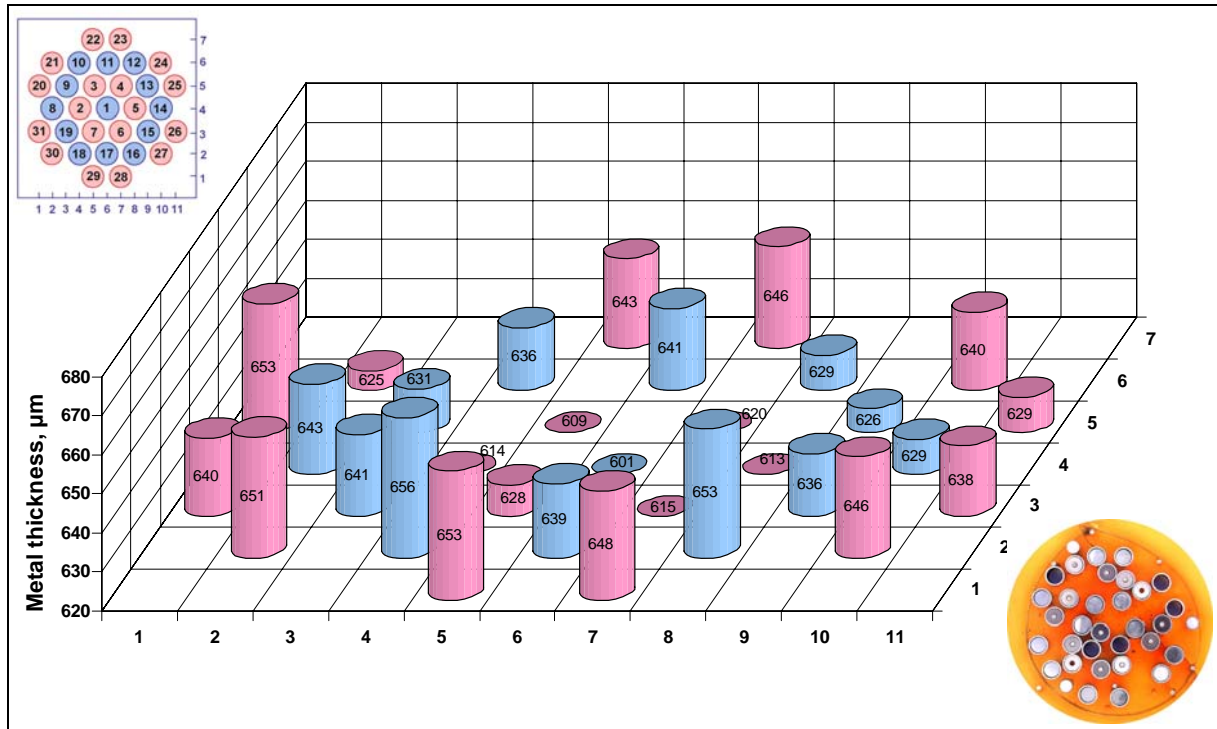


RIAR measurements at cross-section 854 mm.
 Average value and median deviation: **494 µm ± 29** for unheated rods,
464 ± 41 µm for heated rods.



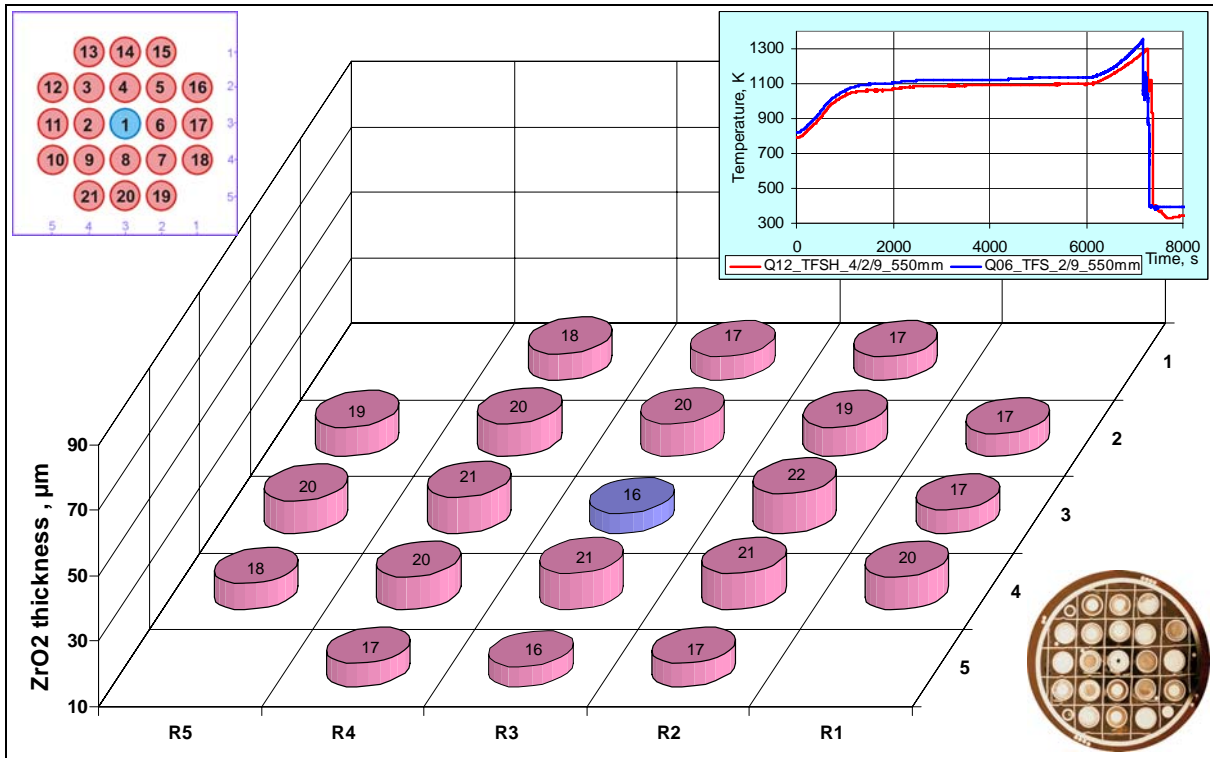
FZK measurements at cross-section 850 mm.
 Average value and median deviation: **500 ± 32 µm** for unheated rods,
495 ± 26 µm for heated rods.

Fig. 138: QUENCH-12; Results of metallographical examination of residual cladding metal thickness at bundle elevation 850 mm.

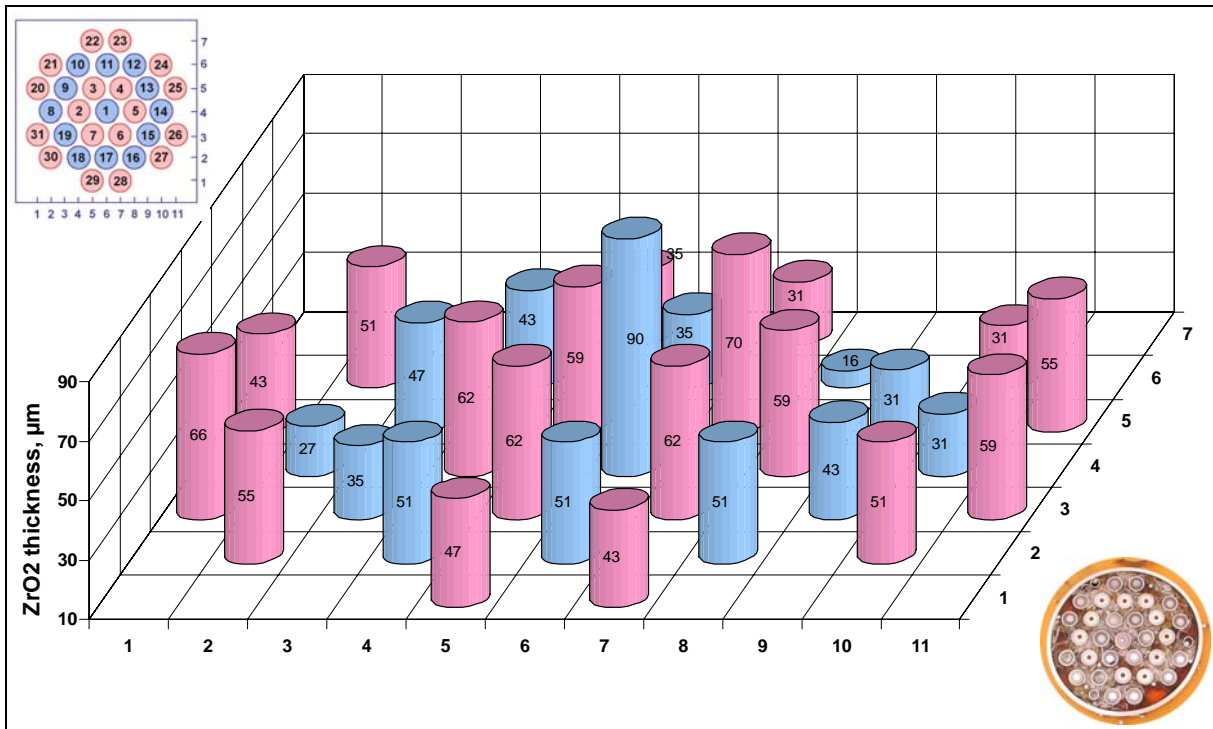


FZK measurements at cross-section 1150 mm.
 Average value and median deviation: $635 \pm 9 \mu\text{m}$ for unheated rods,
 $634 \pm 13 \mu\text{m}$ for heated rods.

Fig. 139: QUENCH-12; Results of metallographical examination of residual cladding metal thickness at bundle elevation 1150 mm.



QUENCH-06: average value and median deviation: $19 \pm 2 \mu\text{m}$ for all rods, $21 \pm 1 \mu\text{m}$ for inner heated rods; $18 \pm 1 \mu\text{m}$ for outer heated rods.



QUENCH-12: average value and median deviation: $42 \pm 12 \mu\text{m}$ for unheated rods, $52 \pm 10 \mu\text{m}$ for heated rods.

Fig. 140: Comparison of oxide thicknesses at bundle elevation 550 mm of QUENCH-12 (values estimated from residual metal) with QUENCH-06 (measured values).

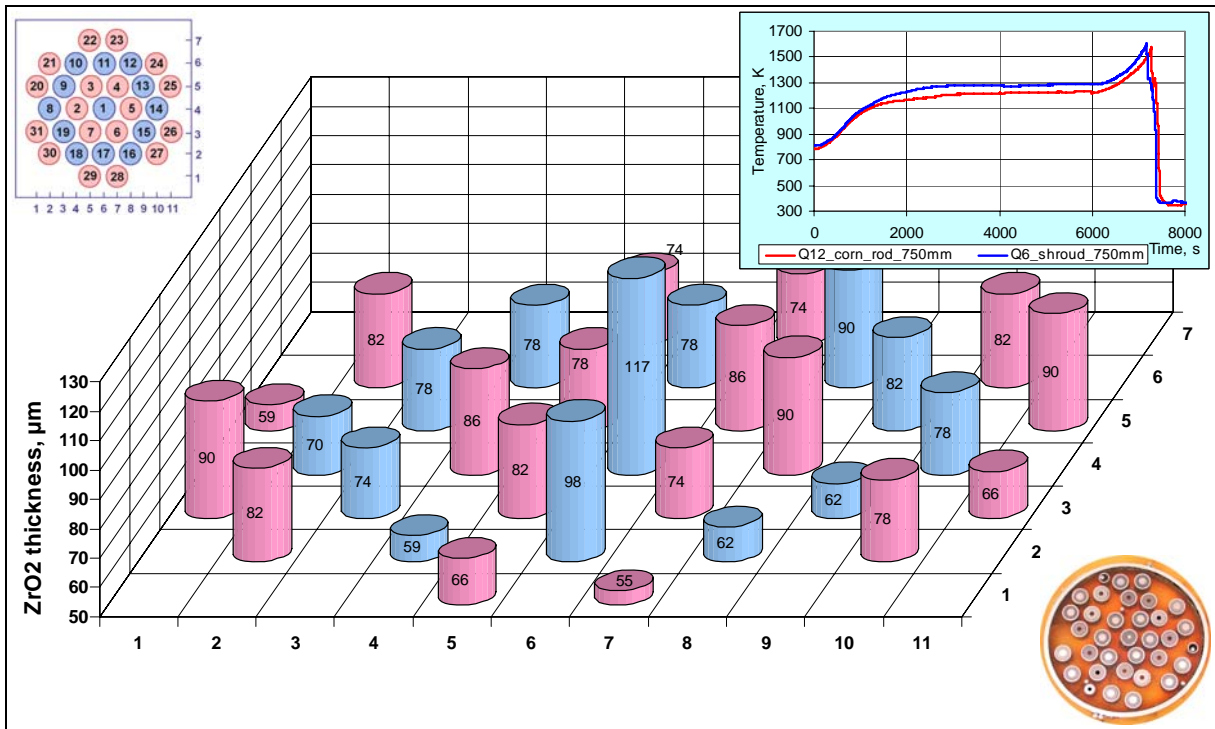
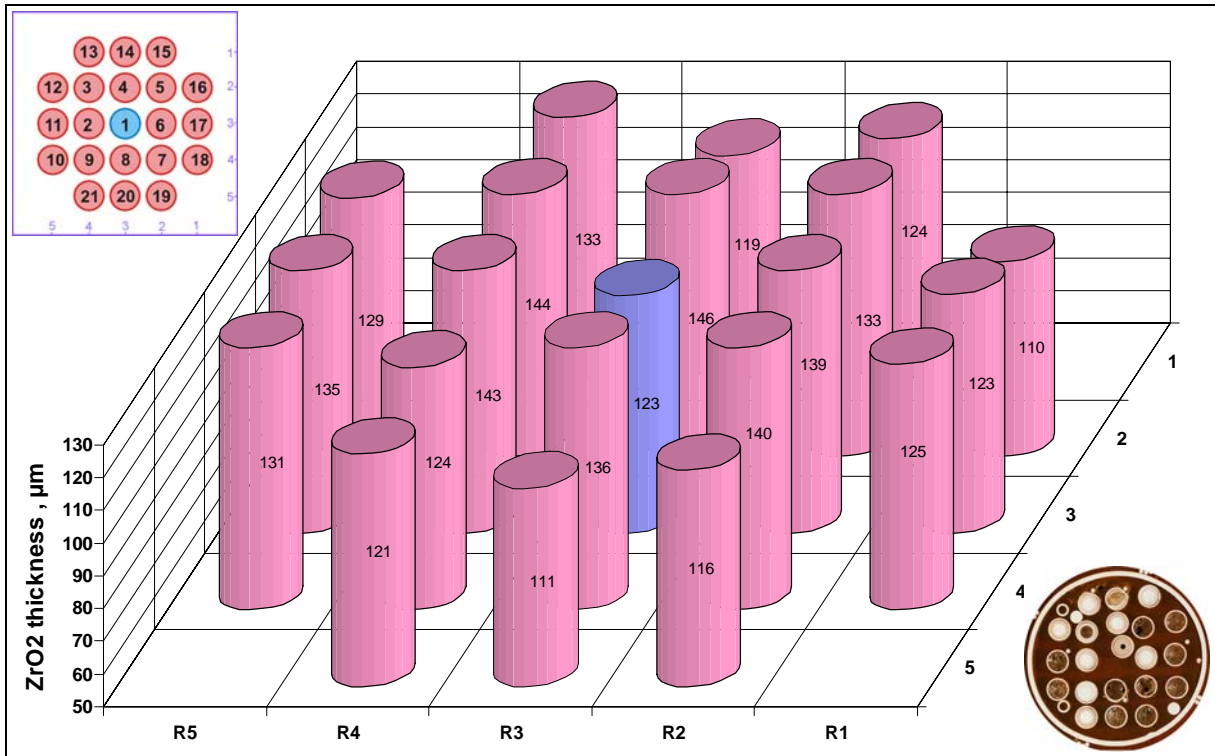
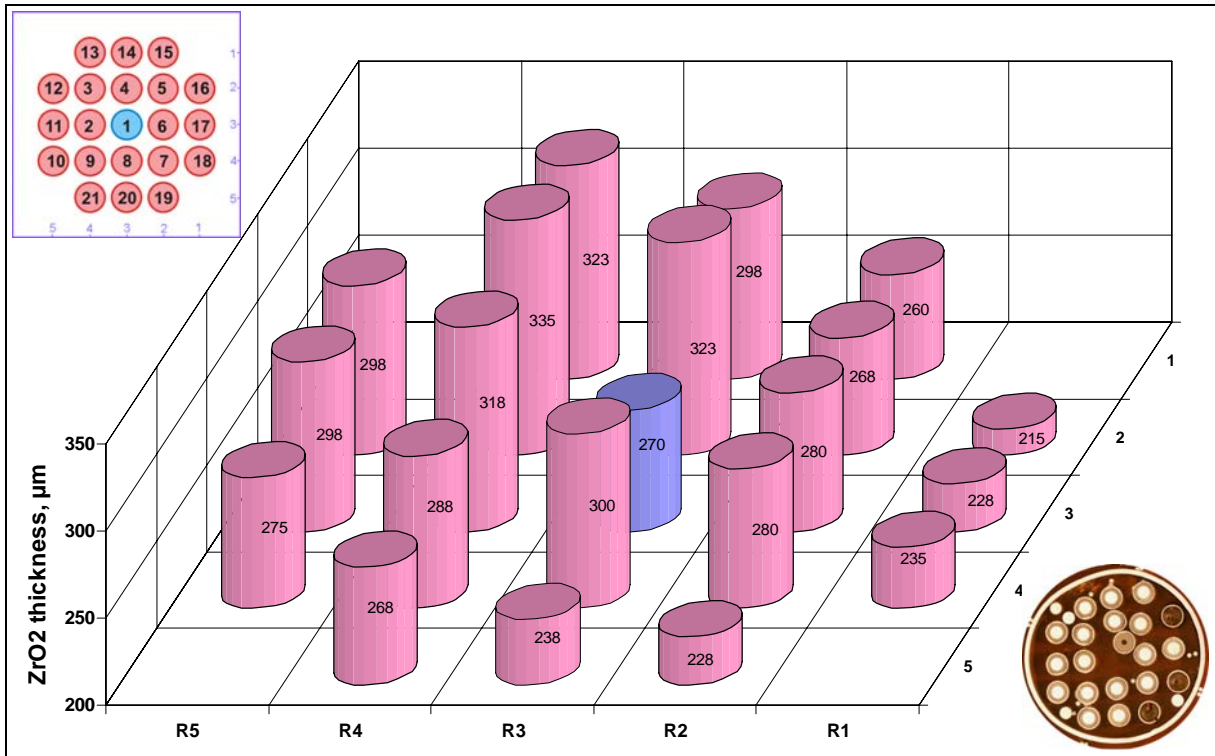
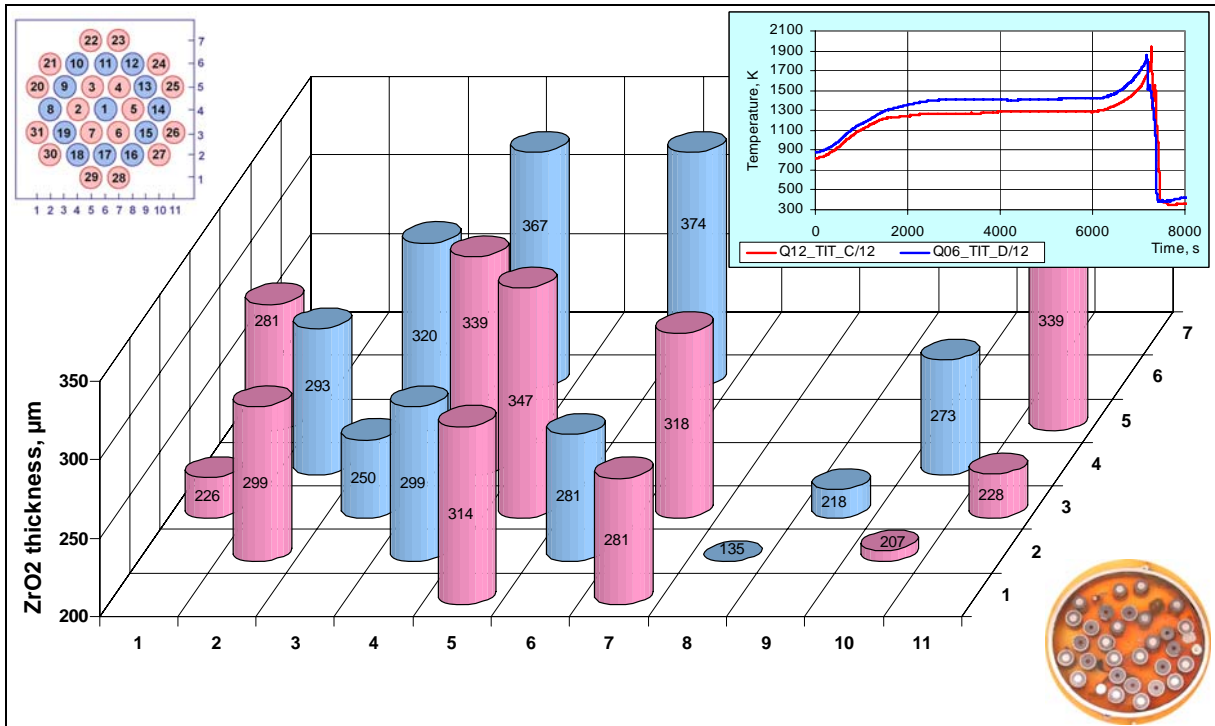


Fig. 141: Comparison of oxide thicknesses at bundle elevation 750 mm of QUENCH-12 (values estimated from residual metal) with QUENCH-06 (measured values).

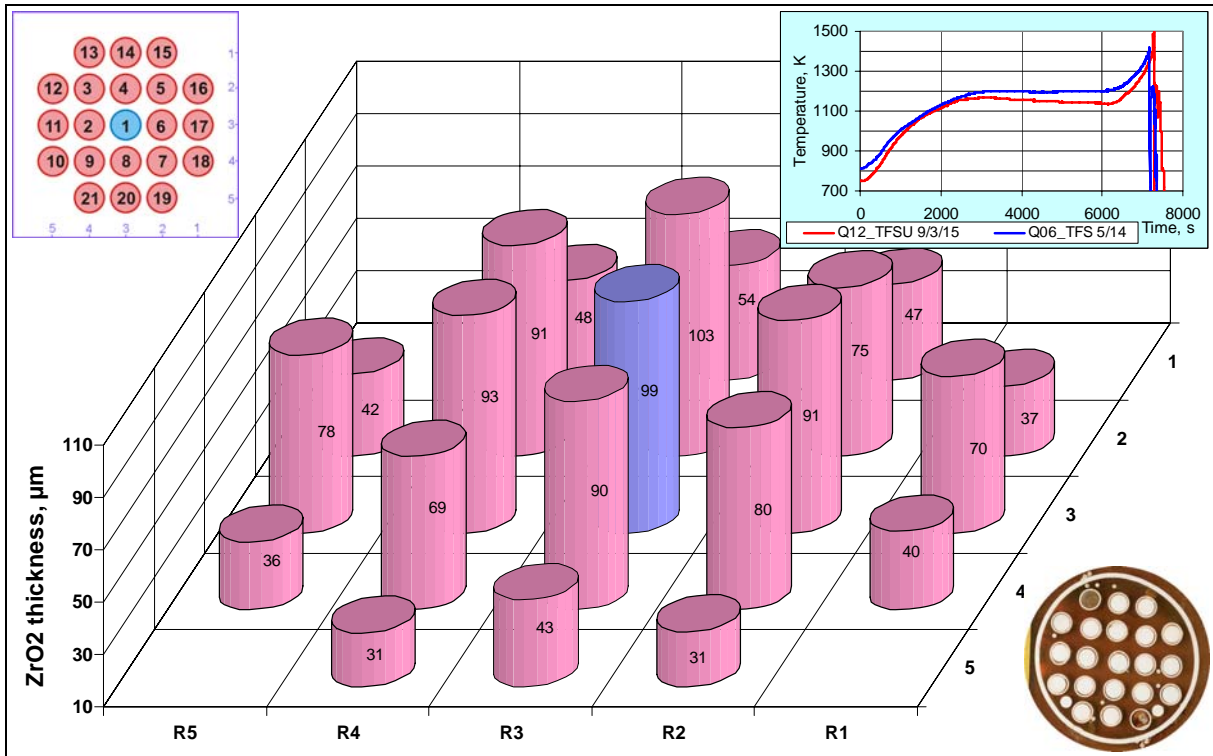


QUENCH-06: average value and median deviation: $277 \pm 28 \mu\text{m}$ for all rods, $299 \pm 20 \mu\text{m}$ for inner heated rods; $263 \pm 30 \mu\text{m}$ for outer heated rods.

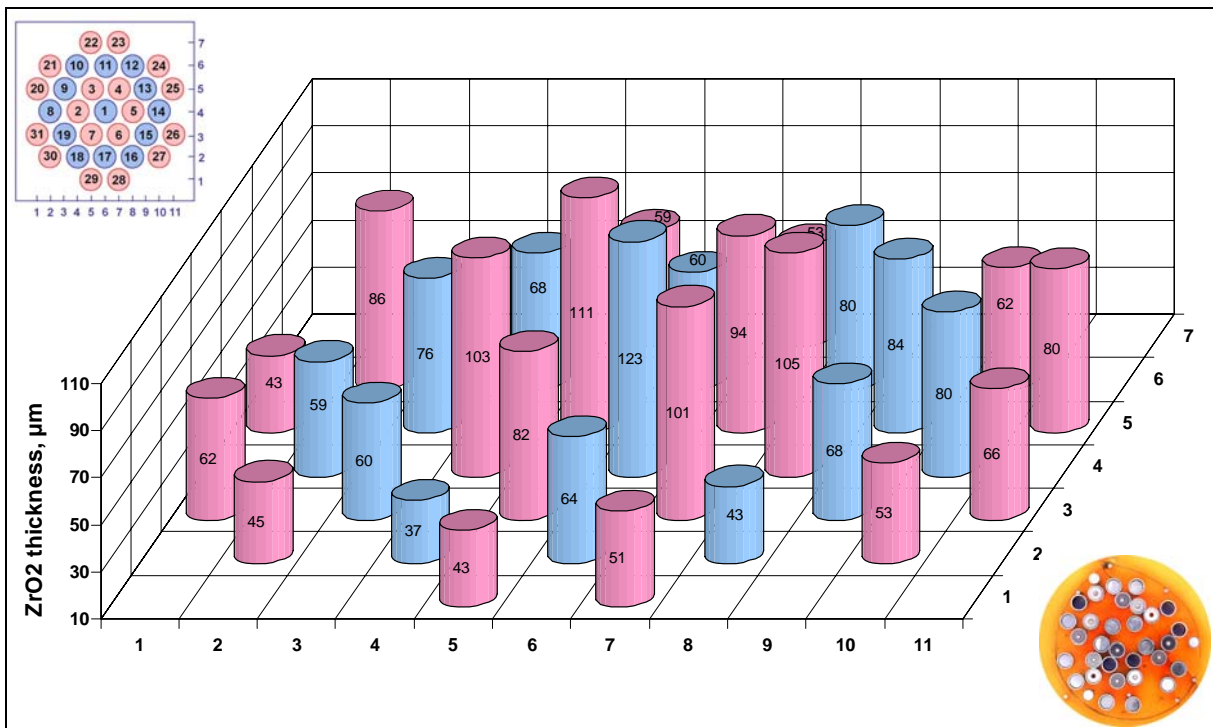


QUENCH-12: average value and median deviation: $281 \pm 50 \mu\text{m}$ for unheated rods, $289 \pm 41 \mu\text{m}$ for heated rods.

Fig. 142: Comparison of oxide thicknesses at bundle elevation 850 mm of QUENCH-12 (values estimated from residual metal) with QUENCH-06 (measured values).



QUENCH-06: average value and median deviation: $64 \pm 22 \mu\text{m}$ for all rods, $86 \pm 9 \mu\text{m}$ for inner heated rods; $46 \pm 11 \mu\text{m}$ for outer heated rods.



QUENCH-12: average value and median deviation: $69 \pm 15 \mu\text{m}$ for unheated rods, $72 \pm 21 \mu\text{m}$ for heated rods.

Fig. 143: Comparison of oxide thicknesses at bundle elevation 1150 mm of QUENCH-12 (values estimated from residual metal) with QUENCH-06 (measured values).

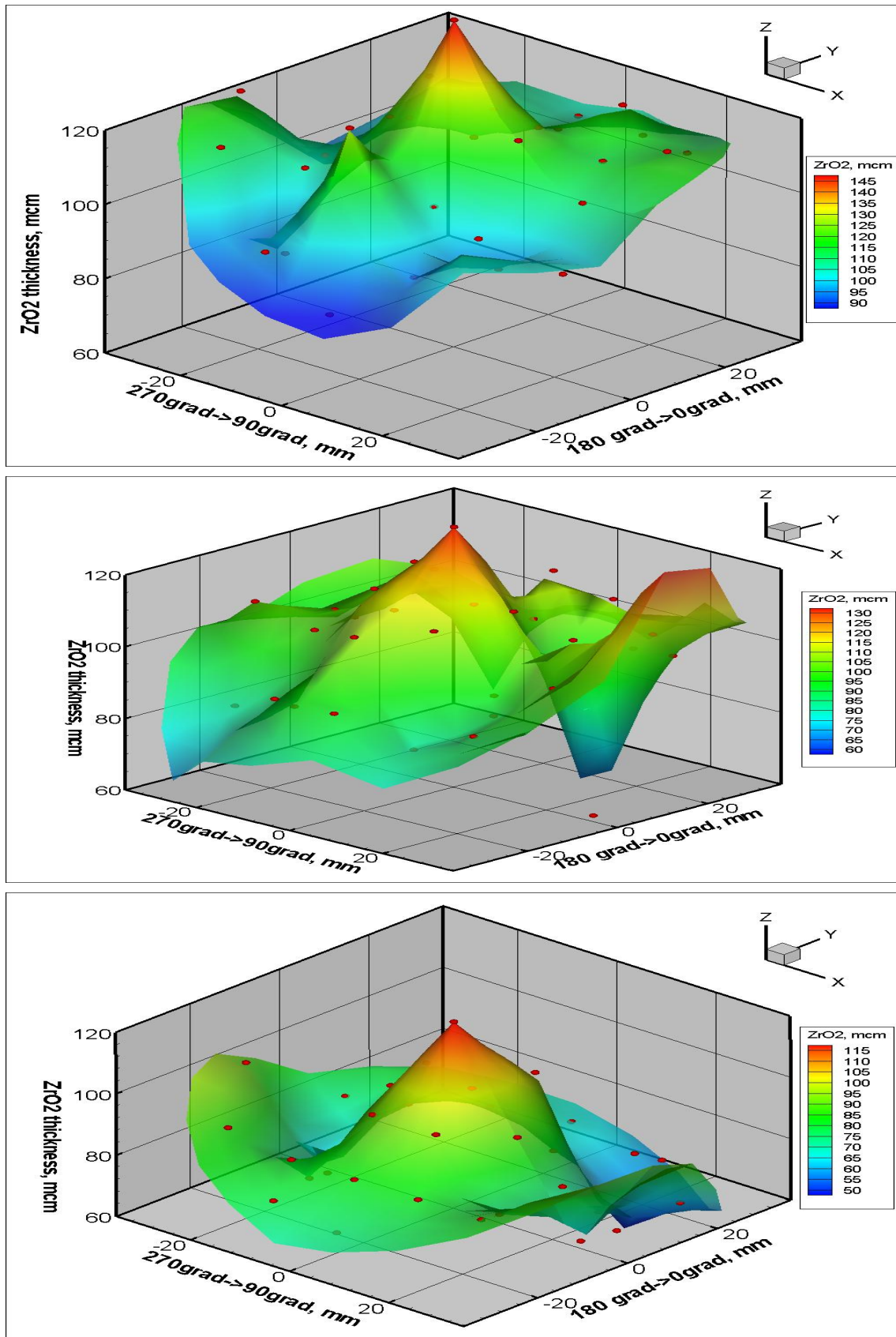


Fig. 144: QUENCH-12; Radial distribution of cladding oxide layer thicknesses calculated on the base of residual metallic layers (from bottom to top: elevations 550 mm, 650 mm, 750 mm). The distribution was received by interpolation.

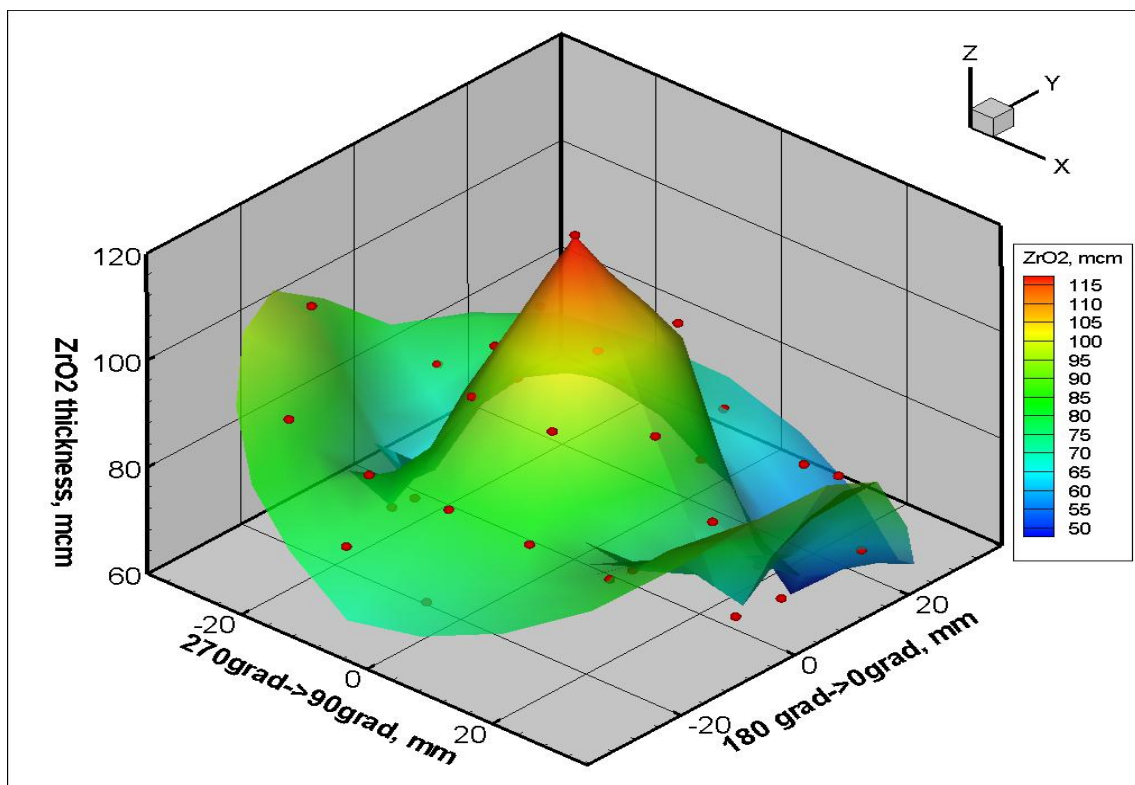
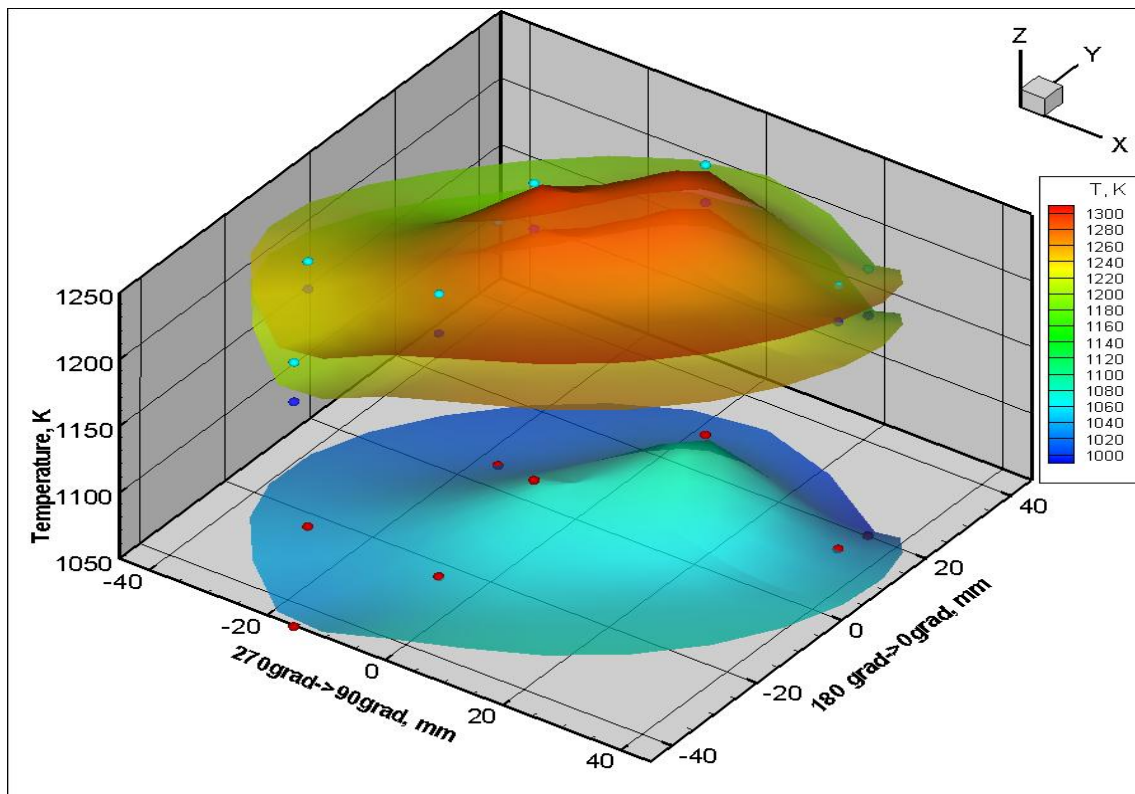
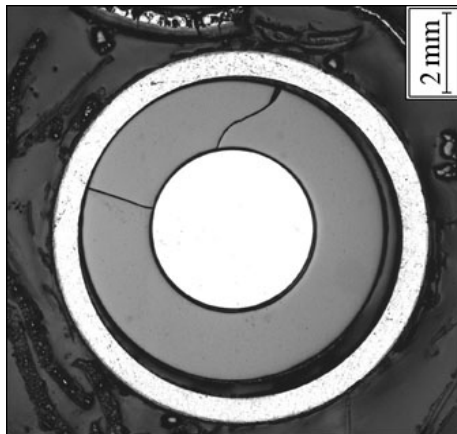


Fig. 145: QUENCH-12; Temperature distributions at elevation 550 mm for three time points (top): 1) 5960 s (corner rod D removed), 2) 7150 s (corner rod F removed), 3) 7265 s (before reflood). Corresponding distribution of cladding oxide layer thicknesses after test completion calculated on the basis of residual metallic layers (bottom).

Simulator 5



Simulator 8

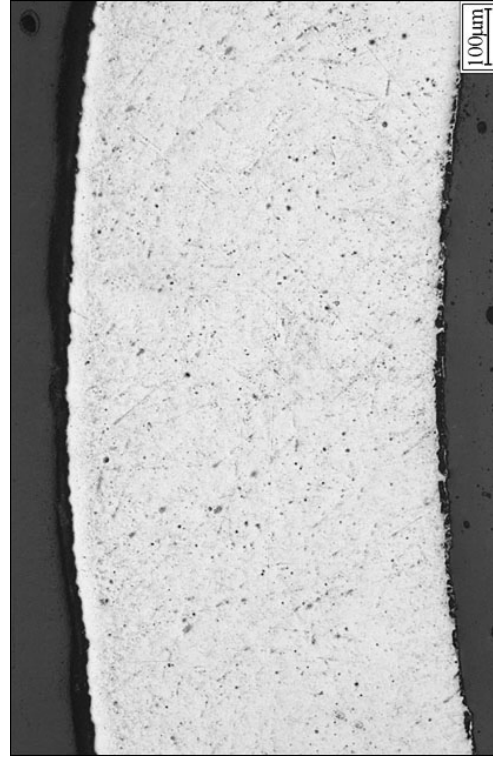
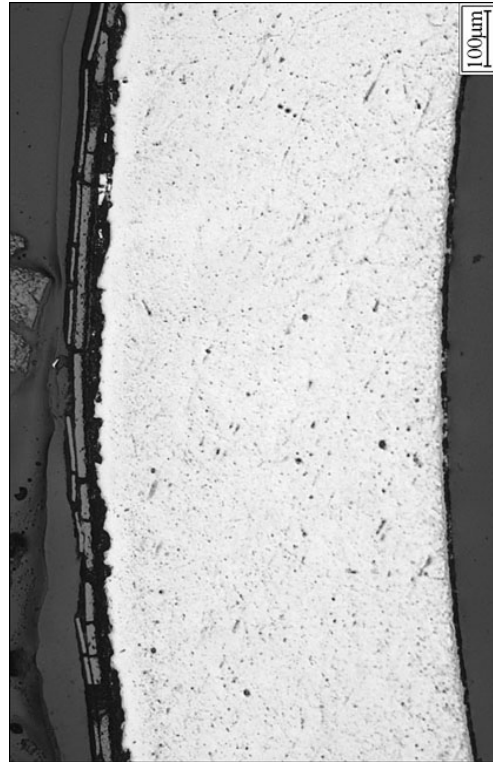
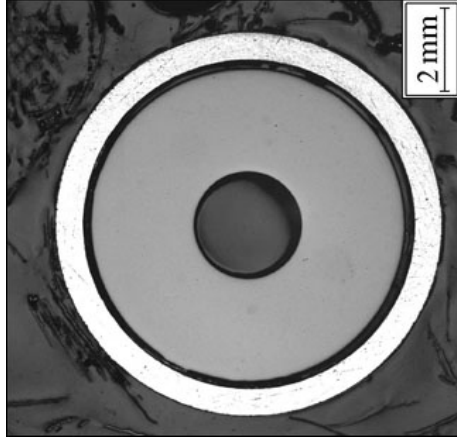
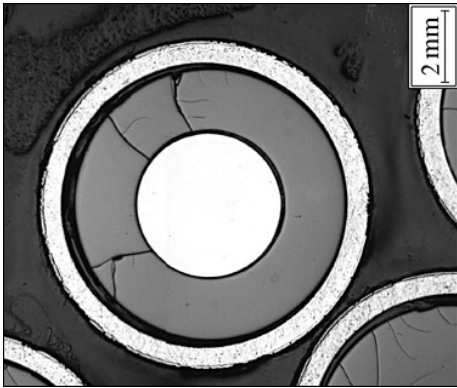


Fig. 146: QUENCH-12; Structure of the simulator claddings in cross section 554 mm (simulator 5 heated, simulator 8 unheated).

Simulator 6



Simulator 10

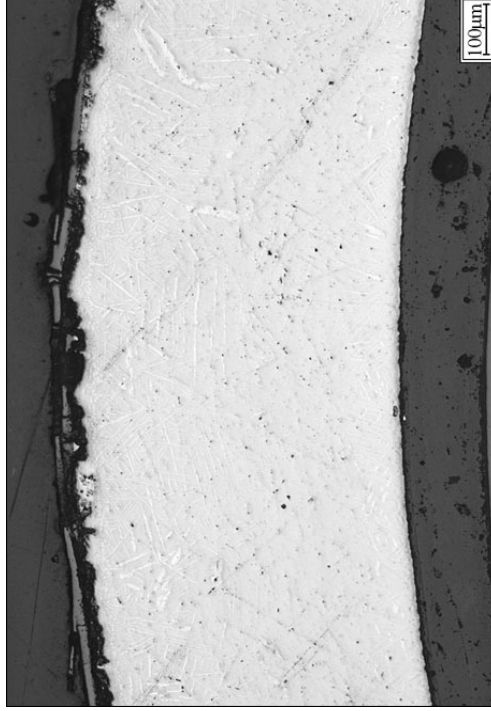
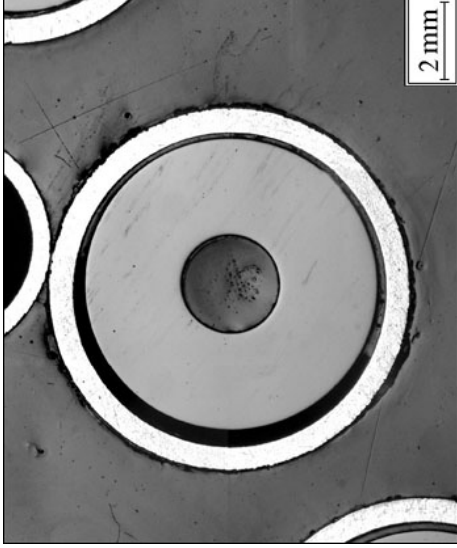
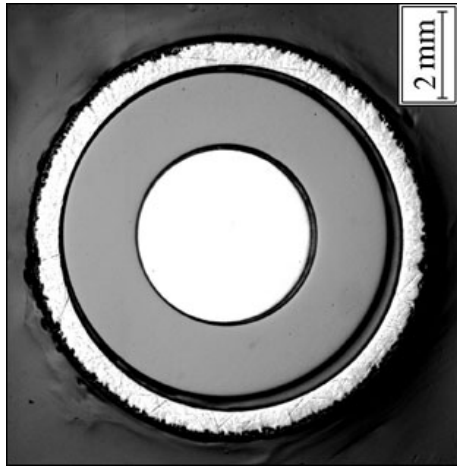


Fig. 147: QUENCH-12; Structure of the simulator claddings in cross section 654 mm (simulator 6 heated, simulator 10 unheated).

Simulator 4



Simulator 16

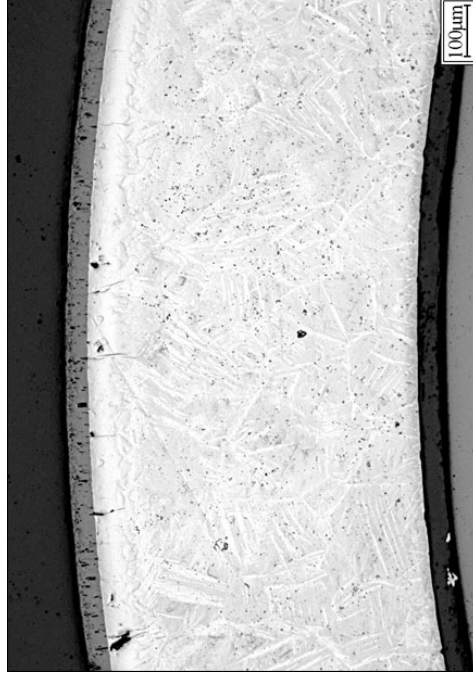
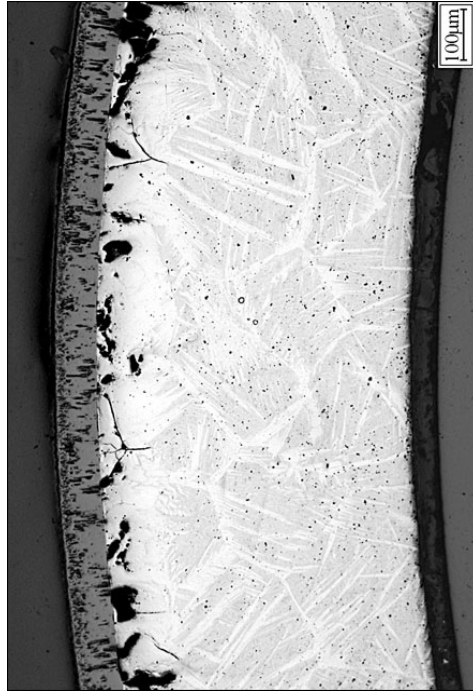
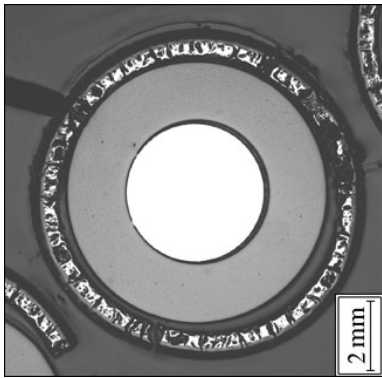


Fig. 148: QUENCH-12; Structure of the simulator claddings in cross section 754 mm (simulator 4 heated, simulator 16 unheated).

Simulator 7



Simulator 27

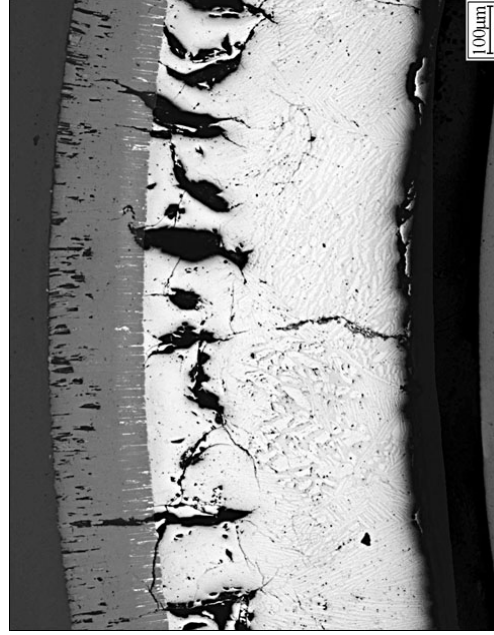
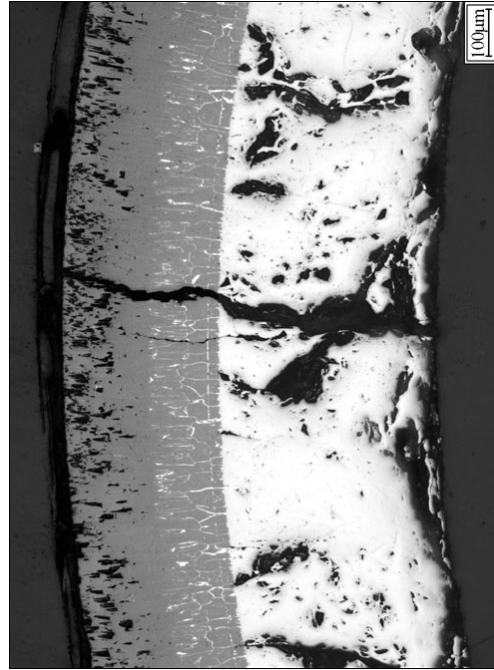
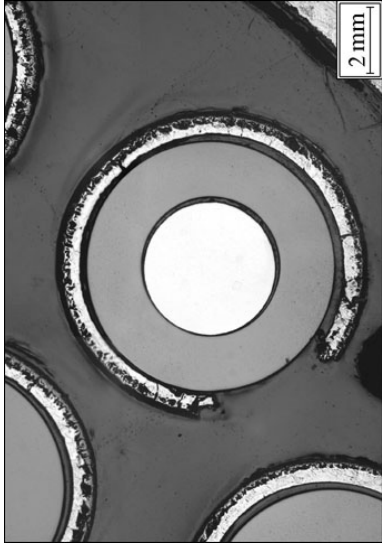
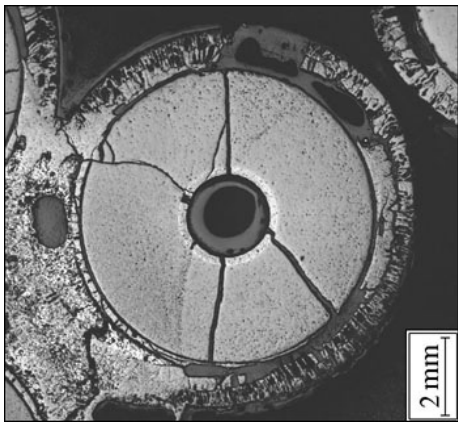
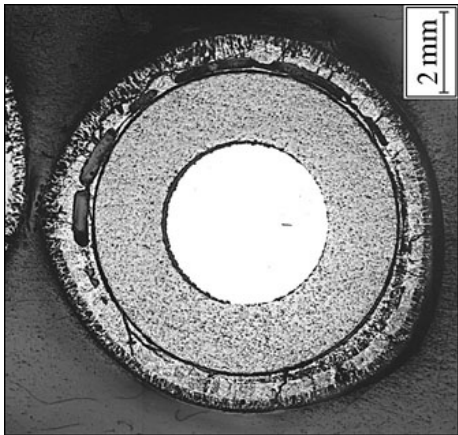


Fig. 149: QUENCH-12; Structure of the claddings of heated simulators in cross section 854 mm.

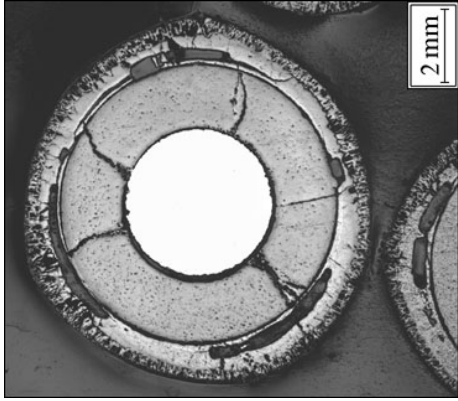
Simulator 1



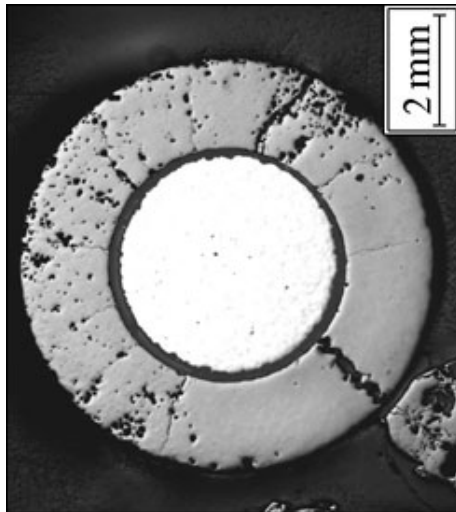
Simulator 20



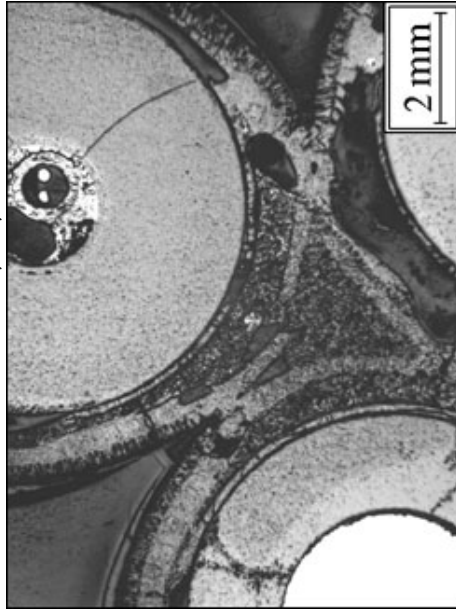
Simulator 21



Simulator 25



Simulators 8, 31, 19



Simulators 1, 4, 11

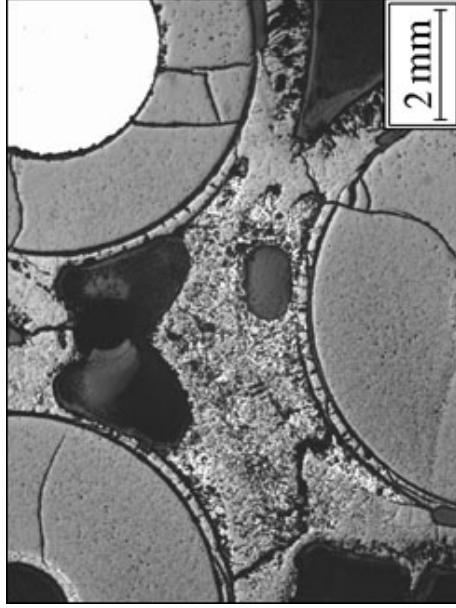
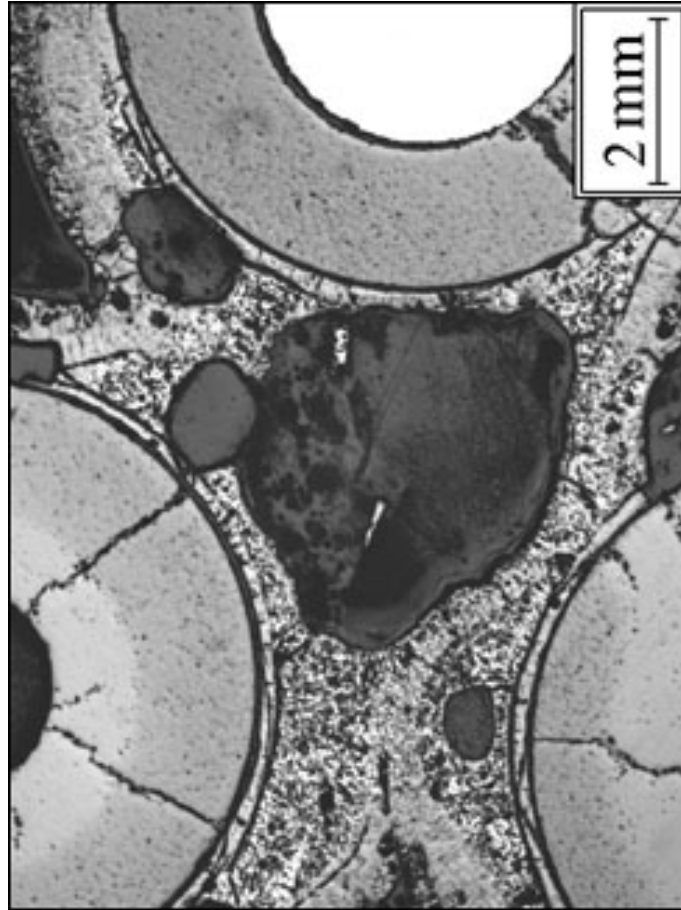


Fig. 150: QUENCH-12; Macrographs of the simulators in cross section 954 mm (simulator 20, 21 25, 31, 4 heated, simulator 1, 8, 19, 11 unheated).

Simulators 15, 16, 27



Simulator 27

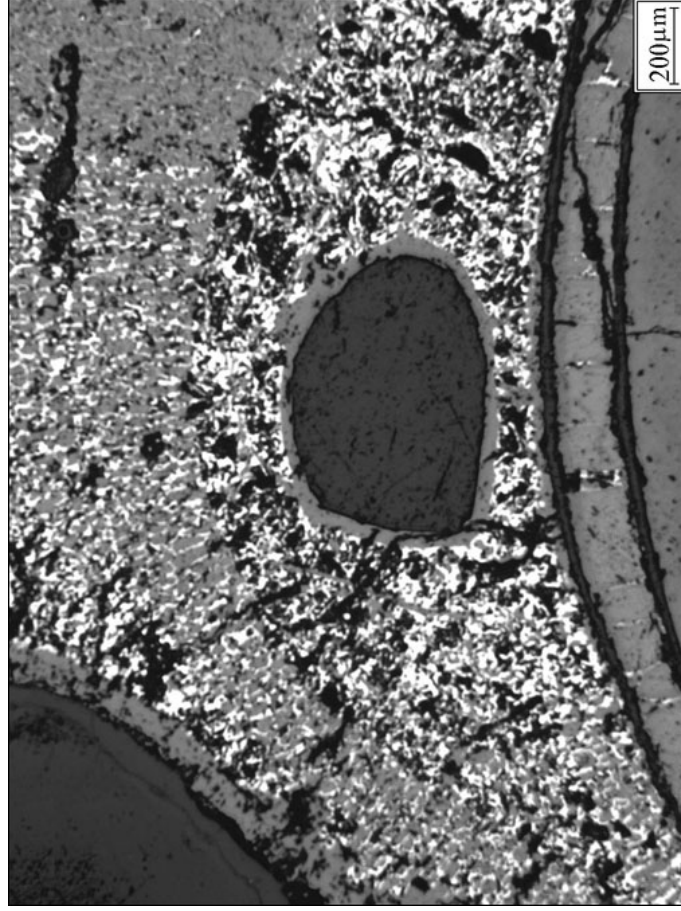


Fig. 151: QUENCH-12; Melt structure in cross section 954 mm.

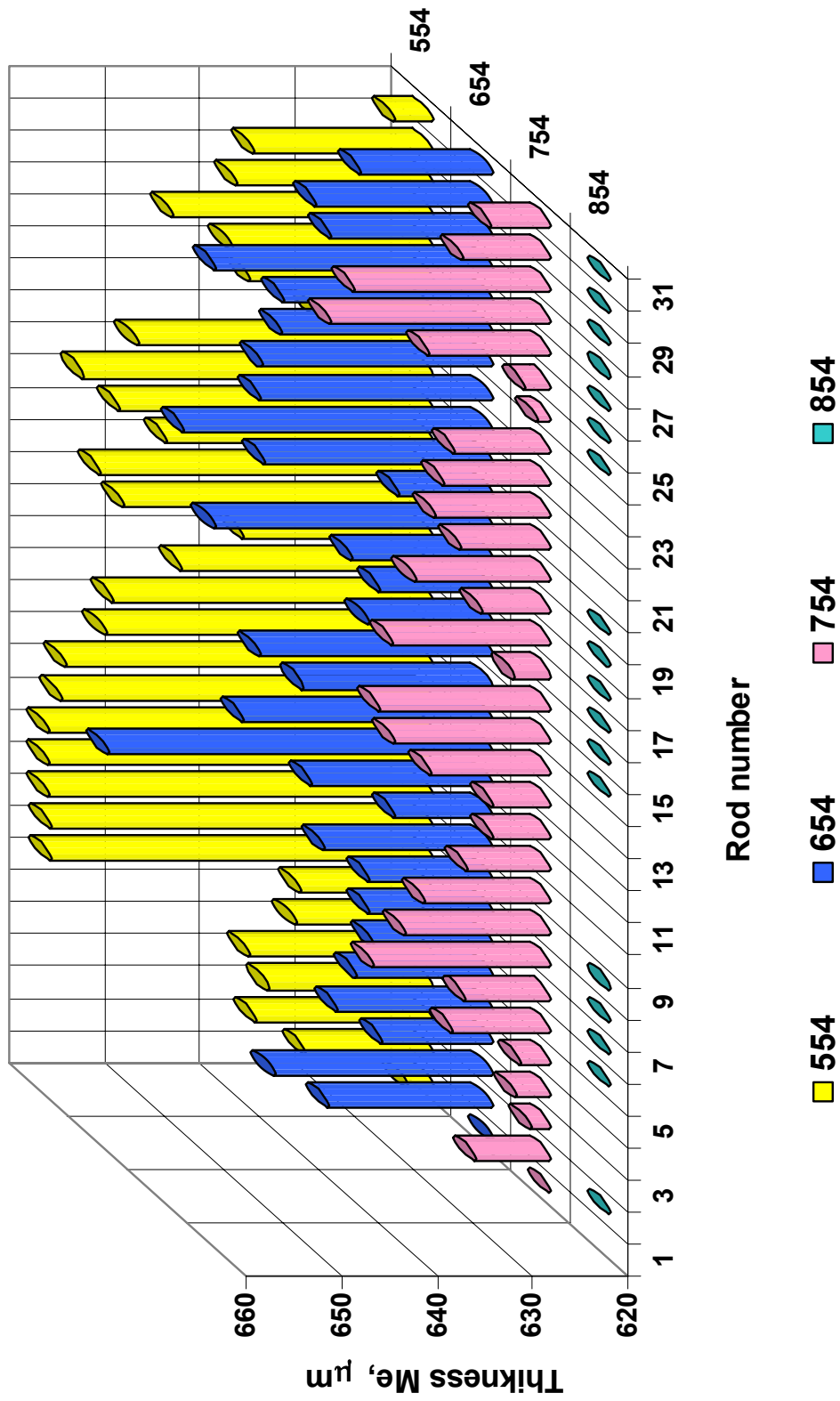


Fig. 152: QUENCH-12; Variation in the thickness of the metal part of the simulator claddings in the examined cross sections.

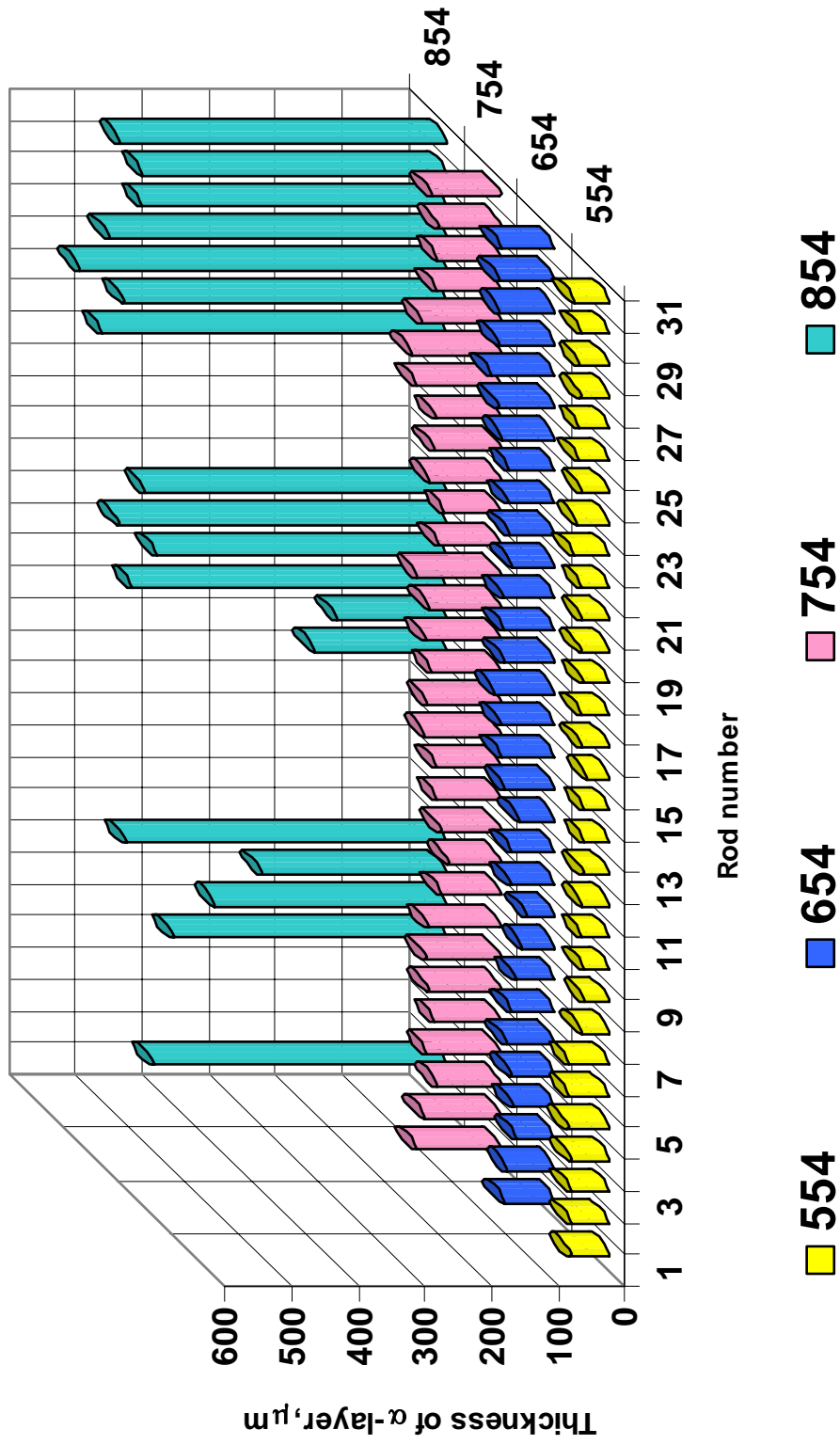


Fig. 153: QUENCH-12; Variation in thickness of α -Zr(O) in the examined cross sections.

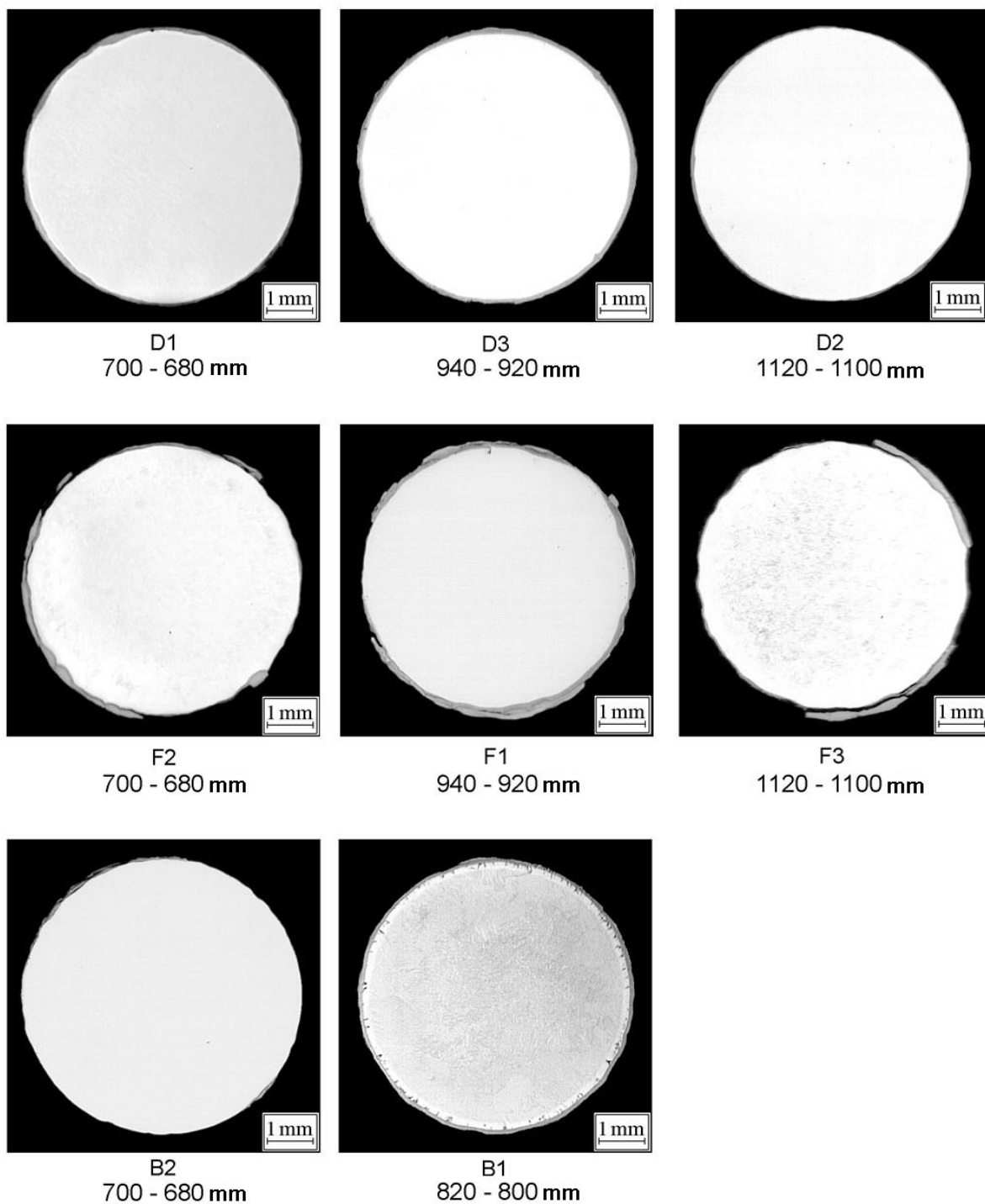
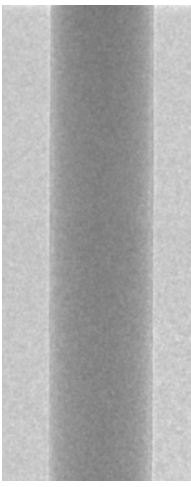


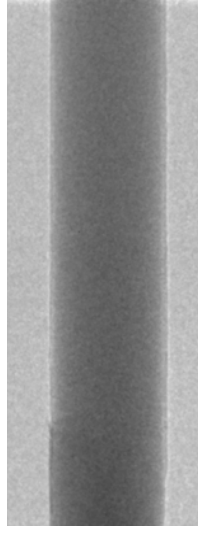
Fig. 154: QUENCH-12; Pictures of corner rod cross sections from 20 mm segments (polished at top) examined by RIAR.



z = 801 - 829 mm



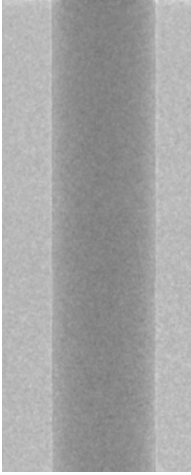
z = 801 - 827 mm



z = 1081 - 1109 mm



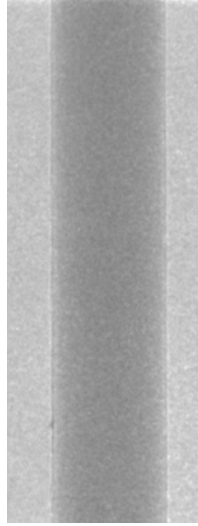
z = 1086 - 1112 mm



z = 693 - 721 mm



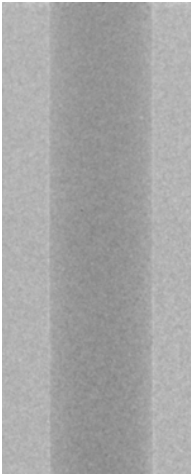
z = 697 - 724 mm



z = 1001 - 1029 mm



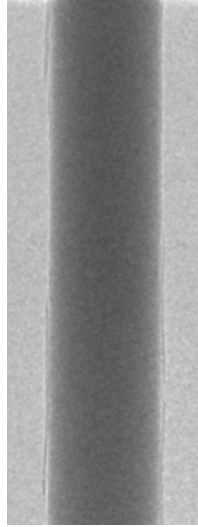
z = 1003 - 1024 mm



z = 590 - 619 mm



z = 597 - 625 mm



z = 861 - 889 mm



z = 860 - 885 mm

Fig. 155: QUENCH-12; Neutron radiographs and visual appearance of selected axial positions of corner rod D.

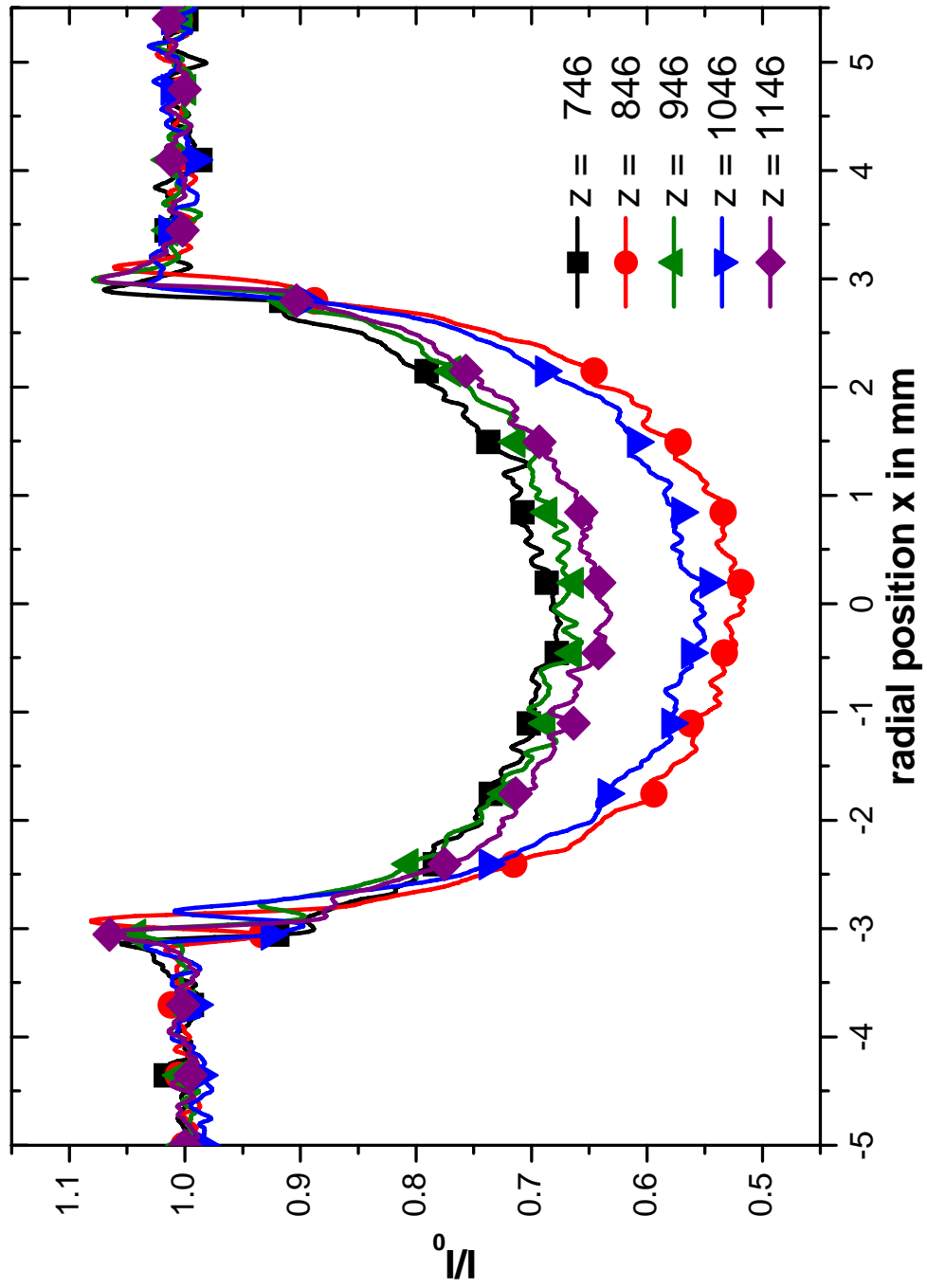


Fig. 156: QUENCH-12; Normalized radial intensity distribution of five axial positions of corner rod D.

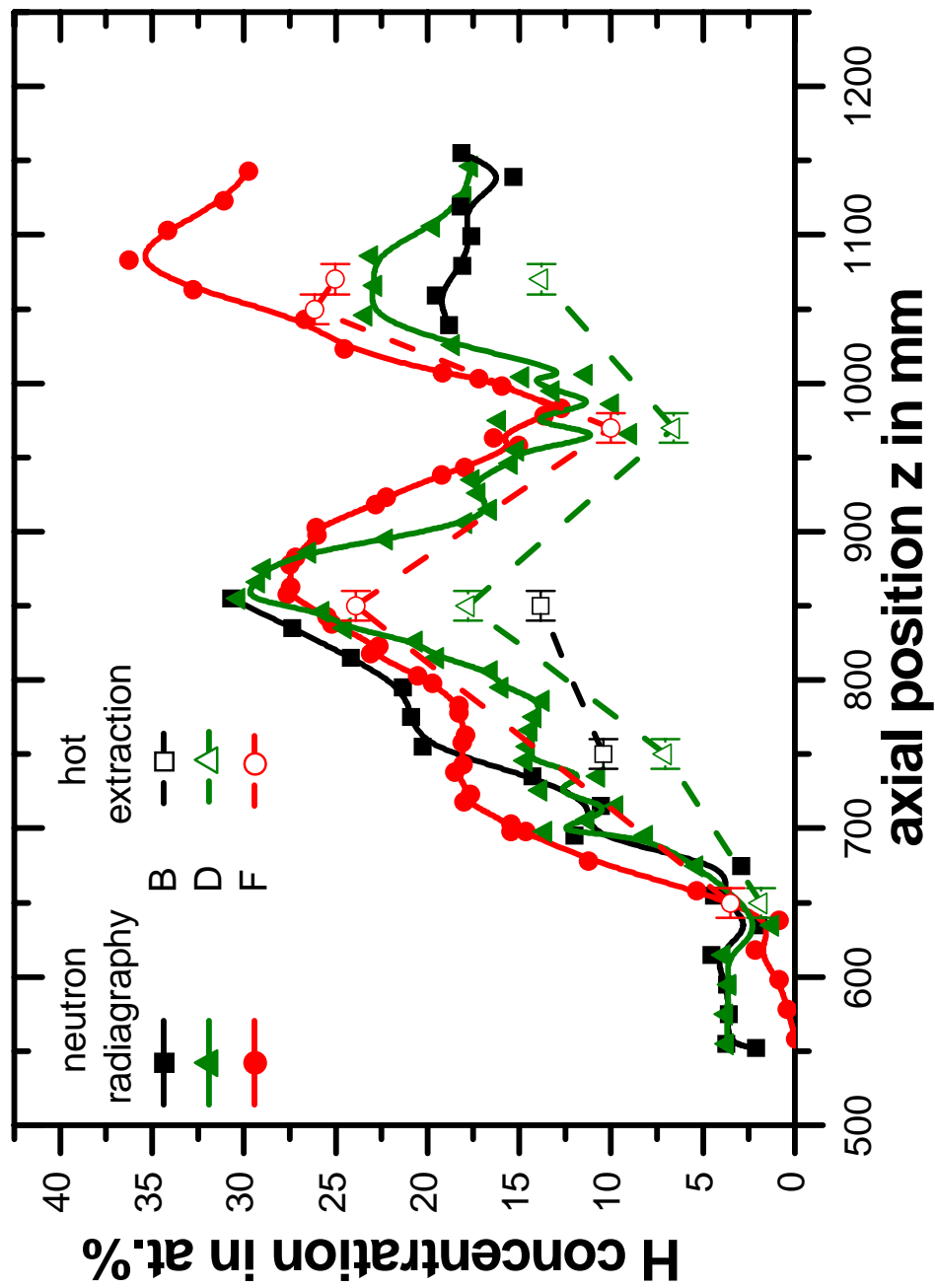


Fig. 157: QUENCH-12; Axial distribution of the hydrogen content for the three investigated corner rods.

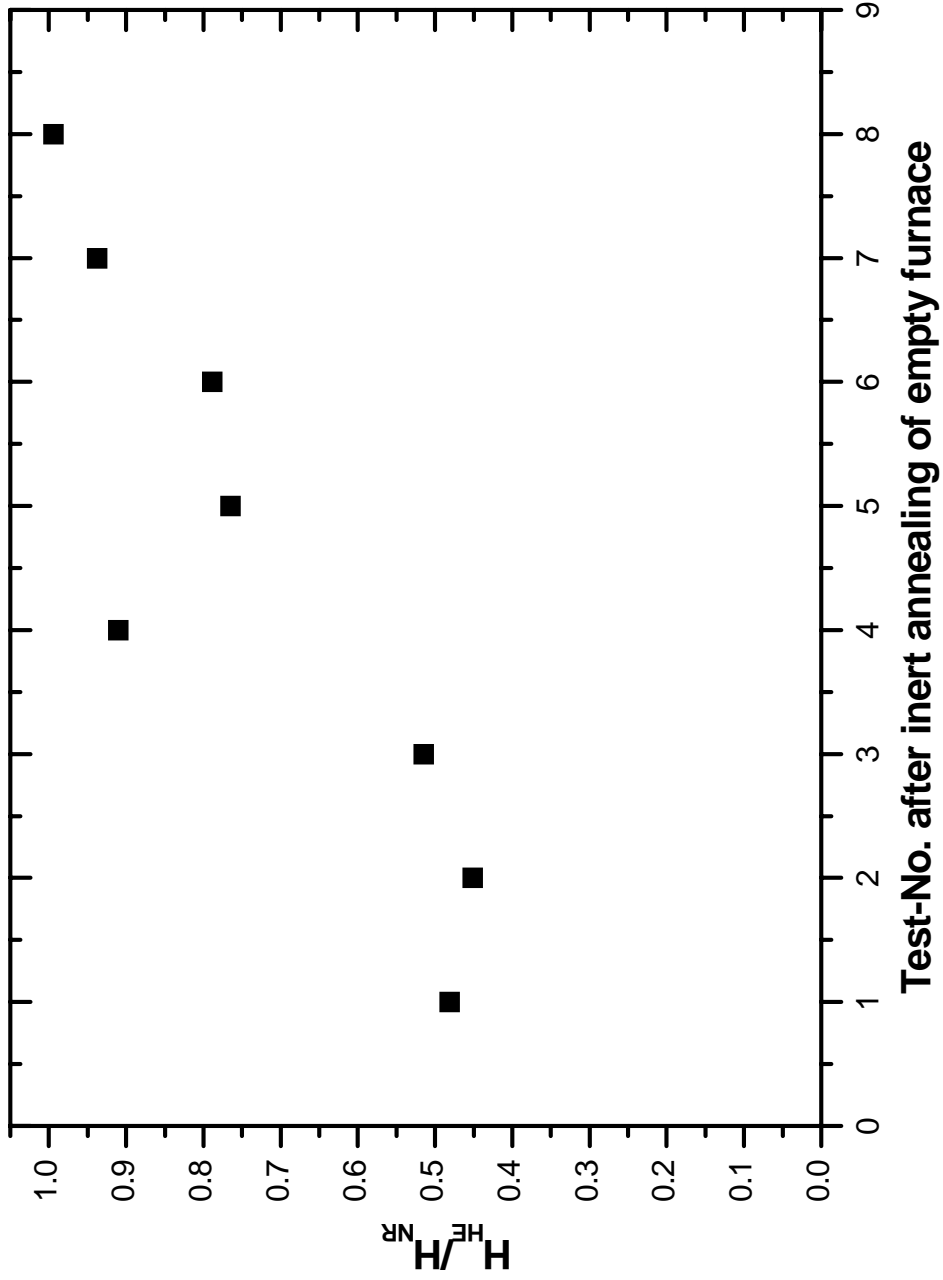


Fig. 158: QUENCH-12; Ratio between the values of hydrogen concentration determined by hot extraction (HE) and neutron radiography (NR) for withdrawn corner rods.

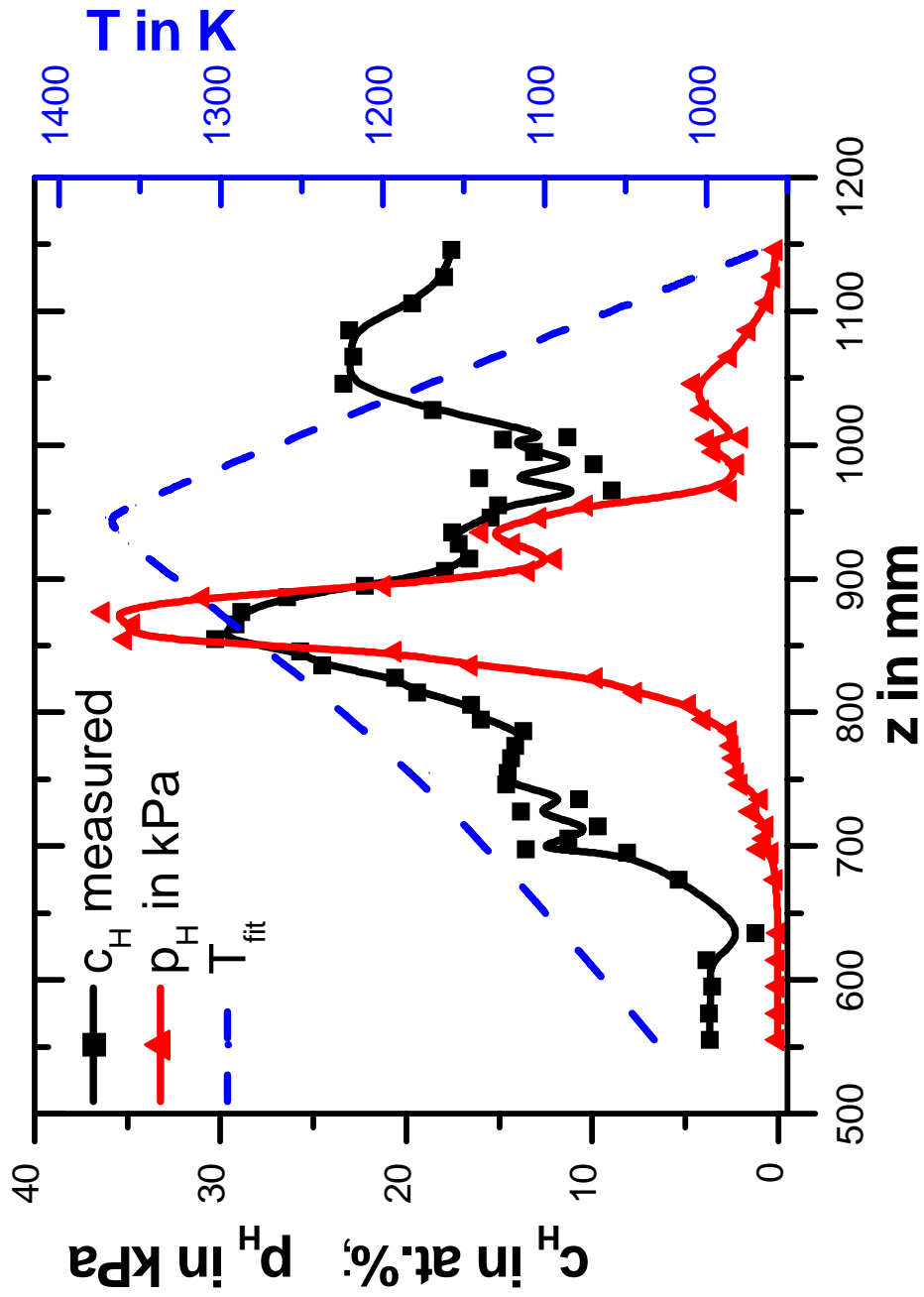
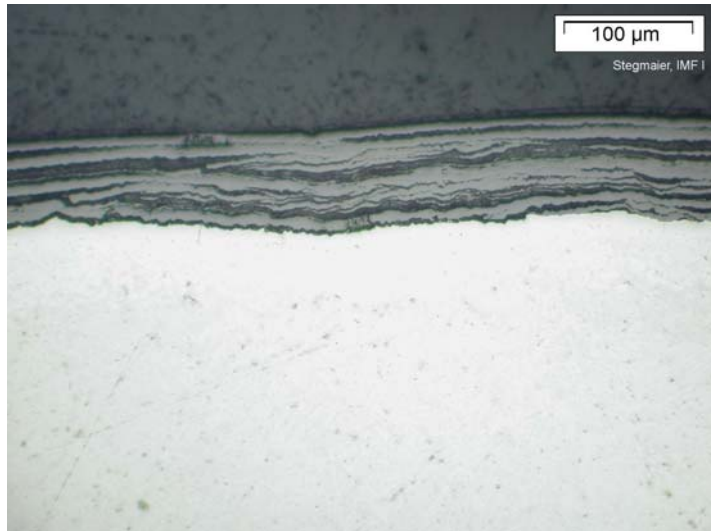
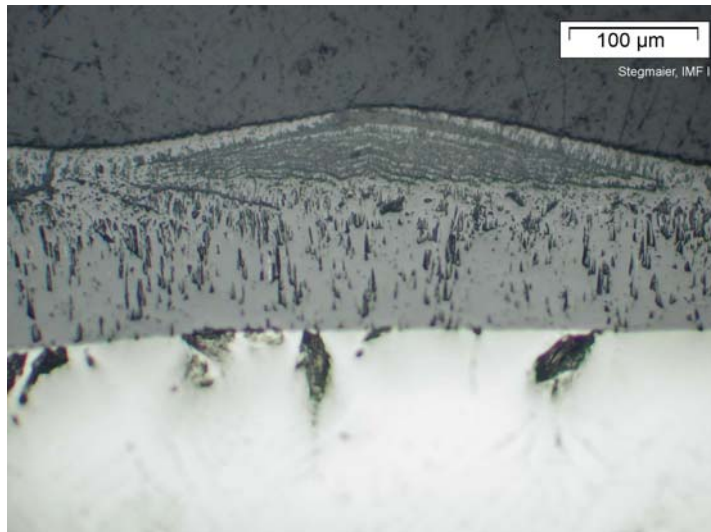


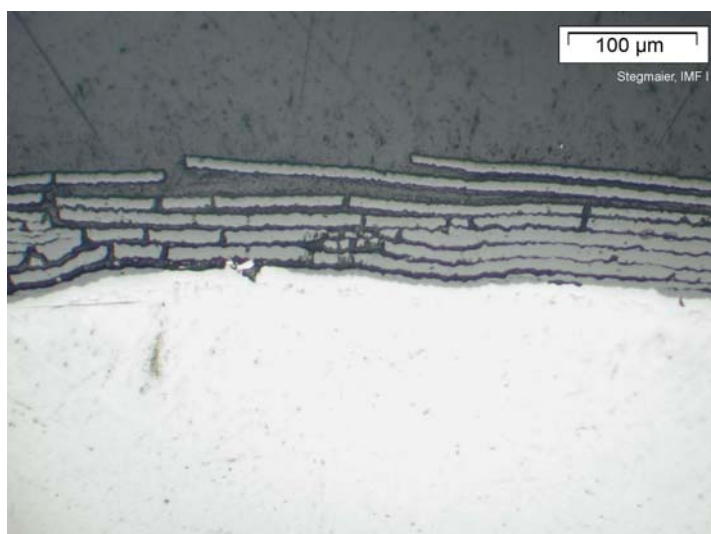
Fig. 159: QUENCH-12; Fit of axial temperature distribution (dashed blue line), determined hydrogen content (black solid line with symbol), and calculated hydrogen partial pressure (red solid line with symbol) for corner rod D.



$z = 700 \text{ m}$



$z = 940 \text{ mm}$



$z = 1120 \text{ mm}$

Fig. 160: QUENCH-12; Micrographs of details taken from cross sections at different axial positions of corner rod D.

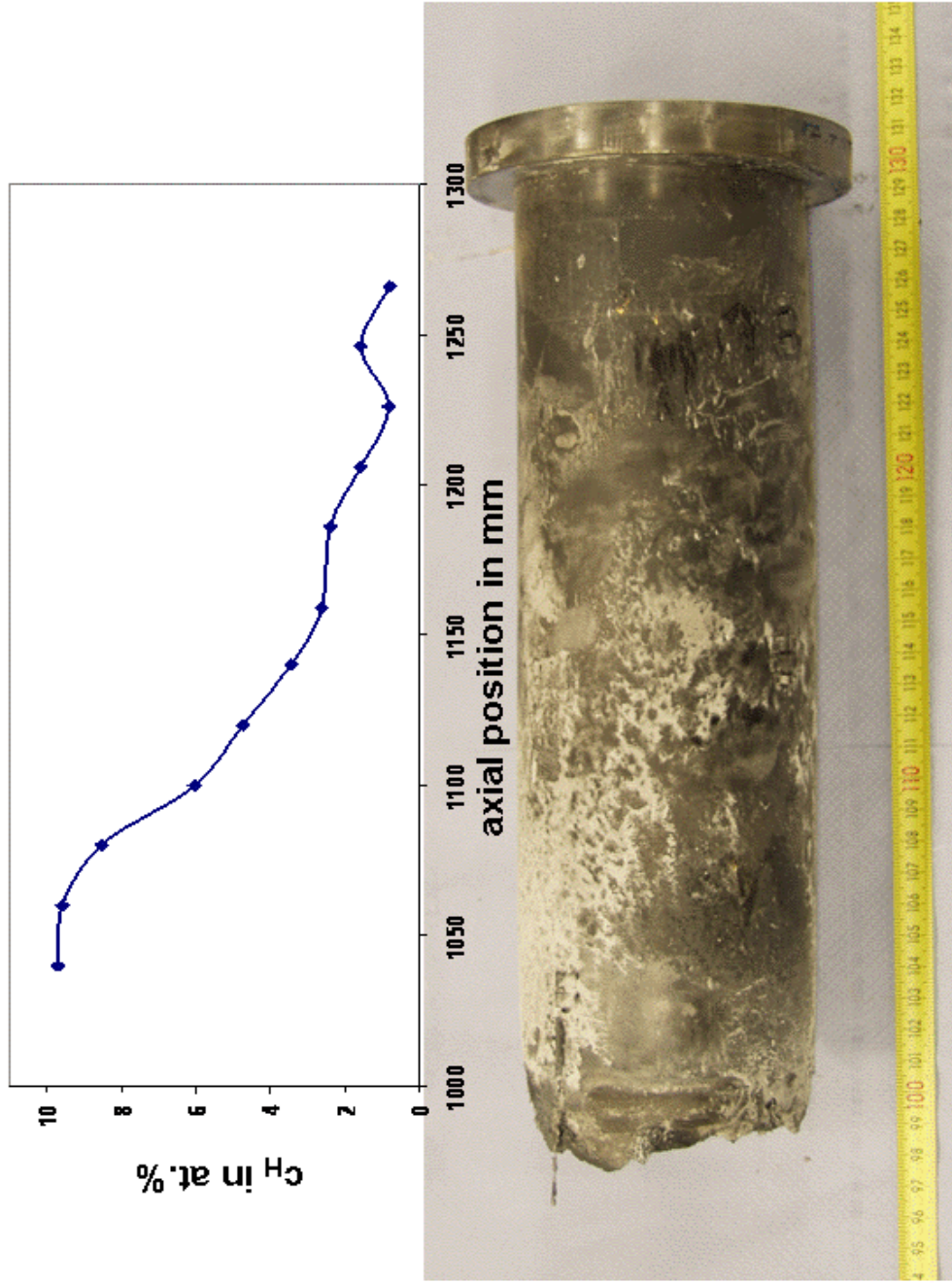


Fig.: 161 QUENCH-12; Comparison of axial variation of the hydrogen content and the macroscopic appearance of the upper part of the shroud.

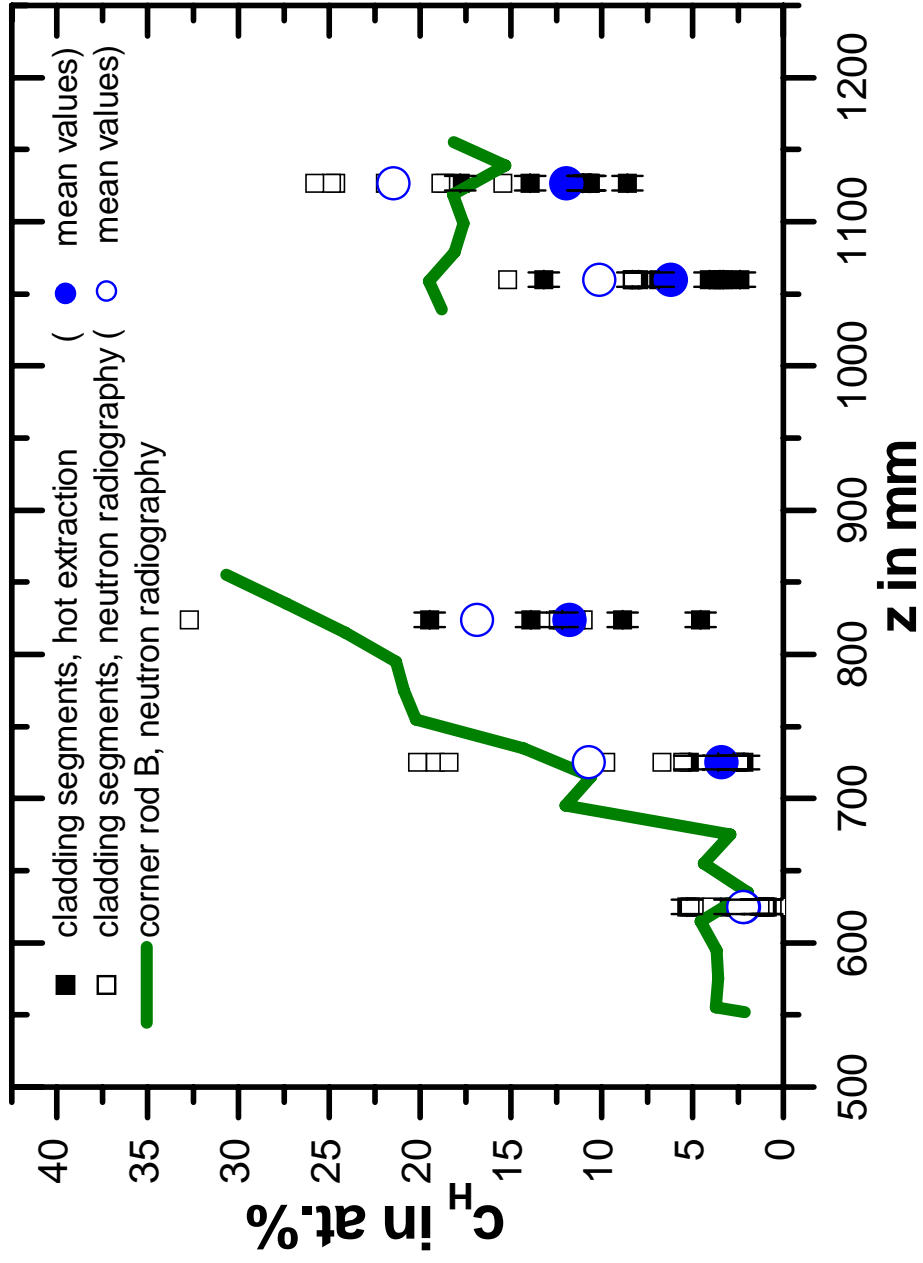


Fig.: 162 QUENCH-12; Comparison of the hydrogen concentrations in cladding rod segments and in corner rod B.

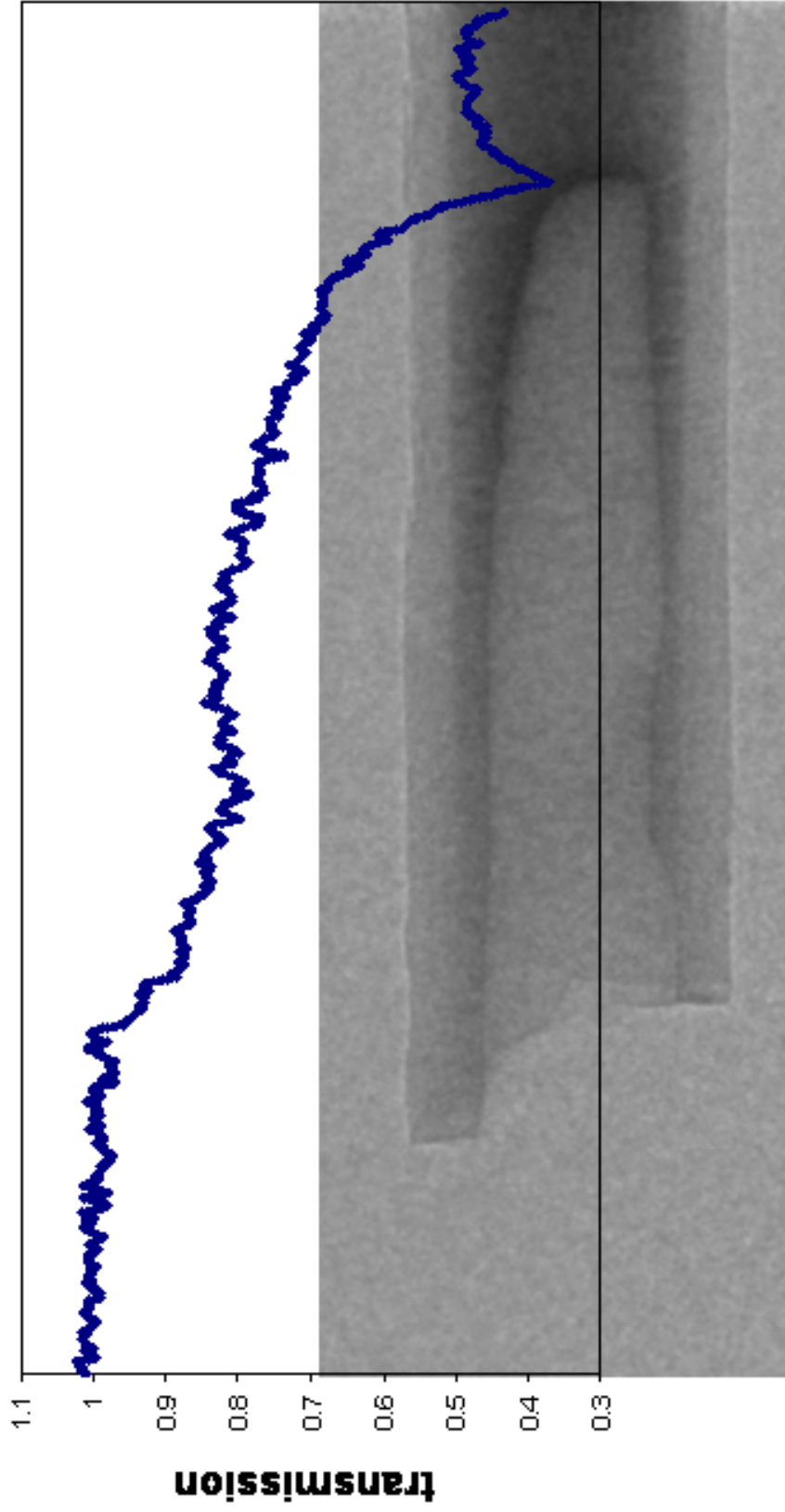


Fig. 163: QUENCH-12; Neutron radiograph of the upper end of the lower part of corner rod B (x axis is the position of the transmission graph).

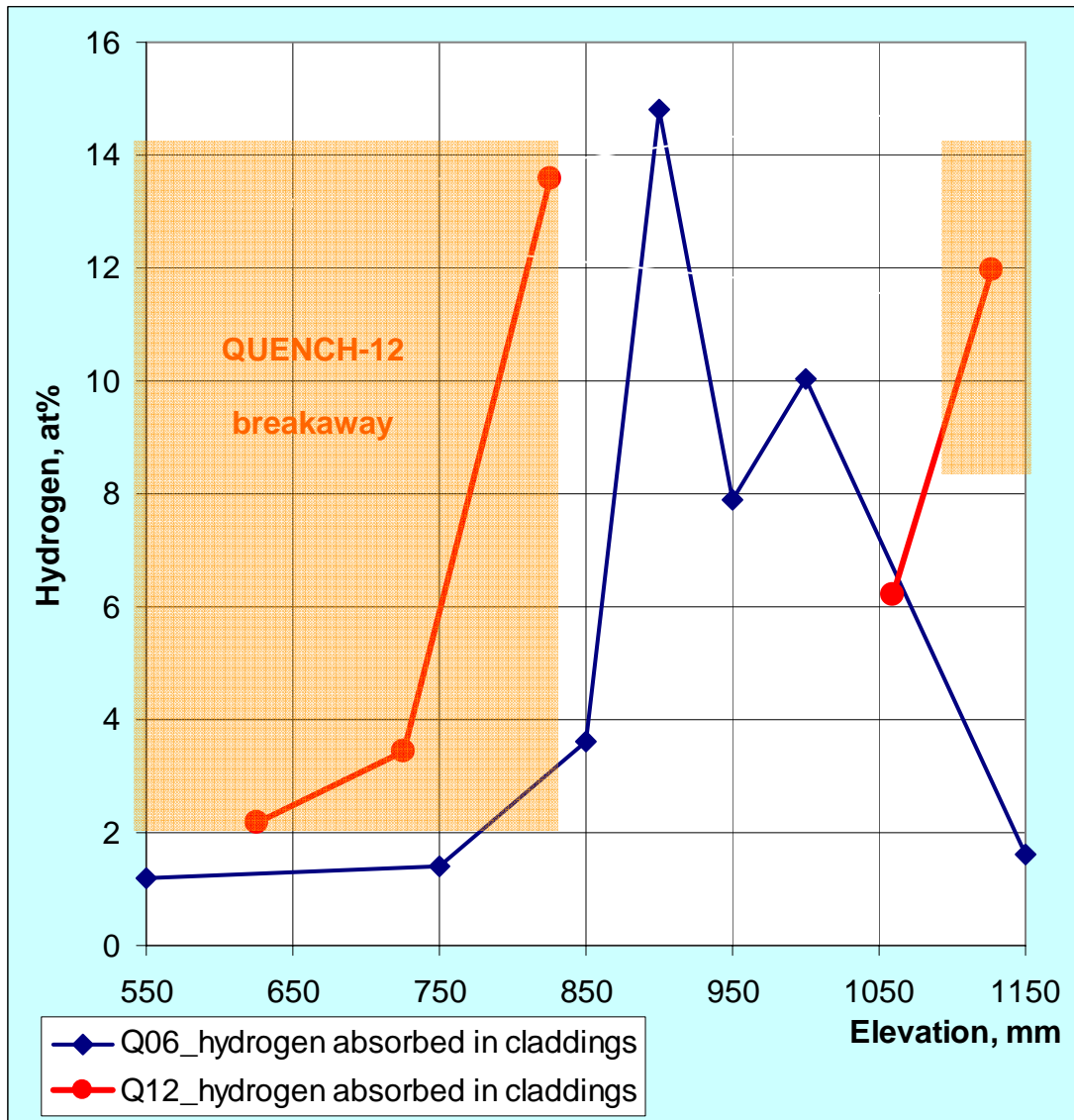


Fig. 164: Comparison of hydrogen absorbed by cladding during QUENCH-12 and QUENCH-06 tests.